



UNIVERSITÀ DEGLI STUDI DI NAPOLI
FEDERICO II

itee^{PhD}
information technology
electrical engineering



Università degli Studi di Napoli Federico II

Ph.D. Program in
Information Technology and Electrical Engineering
XXXV Cycle

THESIS FOR THE DEGREE OF DOCTOR OF PHILOSOPHY

Cardio-respiratory monitoring via Forcecardiography

by
Jessica Centracchio

Advisor: Prof. Paolo Bifulco



SCUOLA POLITECNICA E DELLE SCIENZE DI BASE
DIPARTIMENTO DI INGEGNERIA ELETTRICA E DELLE TECNOLOGIE DELL'INFORMAZIONE

CARDIO-RESPIRATORY MONITORING VIA FORCECARDIOGRAPHY

Ph.D. Thesis presented
for the fulfillment of the Degree of Doctor of Philosophy
in Information Technology and Electrical Engineering

by

Jessica Centracchio

January 2023



Approved as to style and content by

Paolo Bifulco

Prof. Paolo Bifulco, Advisor

Università degli Studi di Napoli Federico II

Ph.D. Program in Information Technology and Electrical Engineering

XXXV cycle - Chairman: Prof. Stefano Russo



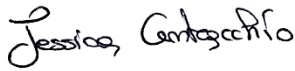
<http://itee.dieti.unina.it>

Candidate's declaration

I hereby declare that this thesis submitted to obtain the academic degree of Philosophiæ Doctor (Ph.D.) in Information Technology and Electrical Engineering is my own unaided work, that I have not used other than the sources indicated, and that all direct and indirect sources are acknowledged as references.

Parts of this dissertation have been published in international journals and/or conference articles (see list of the author's publications at the end of the thesis).

Napoli, January 23, 2023



Jessica Centracchio

Abstract

To date, Seismocardiography (SCG) is the most widespread technique for cardio-mechanical monitoring. SCG measures infrasonic cardiac-induced mechanical vibrations via accelerometers placed on the chest. The SCG signal is mainly used to locate important cardiac cycle events, thus allowing the estimation of cardiac time intervals of clinical relevance. Very recently, a novel, non-invasive technique, namely Forcecardiography (FCG), has been introduced to record the weak forces induced onto the chest wall by the mechanical activity of the beating heart via broadband force sensors. FCG sensors proved capable of capturing signals with much richer information content as compared to SCG. Indeed, the FCG signal consists of two infrasonic components, namely low-frequency FCG (LF-FCG) and high-frequency FCG (HF-FCG), and a sonic component corresponding to the heart sounds. In this thesis, a deeper investigation on the information content of FCG signals was carried out, and the performance of FCG was assessed against reference techniques. To this aim, FCG and SCG signals were acquired simultaneously on a cohort of healthy subjects, along with Electrocardiography recordings. Results of the experimental tests showed that the HF-FCG shares a very high similarity with the SCG signal and provides very accurate localization of aortic valve opening and closure events and estimates of inter-beat interval, pre-ejection period and left ventricular ejection time. The LF-FCG reflects heart walls motion, thus potentially carrying information on ventricular volume variations. This low-frequency component is generally not visible in SCG recordings. In this thesis, a specific numerical procedure was proposed to recover this information from SCG. However, despite its high similarity with the LF-FCG, this low-frequency SCG component has not very high consistency within the cardiac cycle, thus leading to inaccuracies in inter-beat intervals estimation. In addition to the cardiac components, a large, very low-frequency component related to respiration, referred to as the Forcerespirogram (FRG), was observed in FCG signals. The FRG captures the forces impressed onto the chest wall by the expansions and releases of the ribcage during the breathing acts. For this reason, FCG signals were acquired simultaneously with reference respiration signals. The FRG signals achieved high accuracy and precision in respiratory acts detection and inter-breath intervals measurement. In addition, cardio-respiratory interactions have been shown to cause amplitude modulations of the LF-FCG and

HF-FCG components, as well as changes in various parameters of heartbeat morphology. Finally, FCG sensors were used to monitor finger pulse waves. In conclusion, FCG stands as a very promising cardio-respiratory monitoring technique.

Keywords: forcecardiography, seismocardiography, cardio-mechanical signals, cardio-respiratory monitoring, cardiac time intervals, pulse wave

Sintesi in lingua italiana

La Seismocardiography (SCG) è attualmente la tecnica più diffusa per il monitoraggio cardio-meccanico. La SCG misura le vibrazioni meccaniche infrasoniche indotte dal cuore attraverso accelerometri posizionati sul torace. Il segnale SCG viene utilizzato principalmente per localizzare eventi importanti del ciclo cardiaco, consentendo così di stimare intervalli di tempo cardiaci di rilevanza clinica. Recentemente è stata introdotta una nuova tecnica non invasiva, denominata Forcecardiography (FCG), per registrare le deboli forze indotte sul torace dall'attività meccanica del cuore mediante sensori di forza a banda larga. È stato dimostrato che i sensori FCG catturano segnali con un contenuto informativo molto più ricco rispetto alla SCG. Infatti, il segnale FCG è costituito da due componenti infrasoniche, ovvero FCG a bassa frequenza (LF-FCG) e FCG ad alta frequenza (HF-FCG), e da una componente sonora corrispondente ai suoni cardiaci. In questa tesi, è stata condotta un'indagine più approfondita sul contenuto informativo dei segnali FCG e sono state valutate le prestazioni della FCG rispetto a tecniche di riferimento. A tal fine, i segnali FCG e SCG sono stati acquisiti simultaneamente su una coorte di soggetti sani, insieme a registrazioni elettrocardiografiche. I risultati dei test sperimentali hanno mostrato che la componente HF-FCG ha un'elevata somiglianza con il segnale SCG e fornisce accuratamente la localizzazione degli eventi di apertura e chiusura della valvola aortica e le stime dell'intervallo inter-battito, del periodo di pre-eiezione e del tempo di eiezione del ventricolo sinistro. La componente LF-FCG riflette il movimento delle pareti cardiache e fornisce potenzialmente informazioni sulle variazioni del volume ventricolare. Questa componente a bassa frequenza non è generalmente visibile nelle registrazioni SCG. In questo lavoro di tesi, è stata proposta una procedura numerica specifica per recuperare questa informazione dalla SCG. Tuttavia, nonostante l'elevata somiglianza con la componente LF-FCG, questa componente SCG a bassa frequenza non ha una consistenza molto elevata all'interno del ciclo cardiaco, causando imprecisioni nella stima degli intervalli inter-battito. In aggiunta alle componenti cardiache, nei segnali FCG è stata osservata un'ampia componente a frequenza molto bassa legata alla respirazione, denominata Forcerespirogram (FRG). La componente FRG registra le forze impresse sul torace dalle espansioni e dai rilassamenti della gabbia toracica durante gli atti respiratori.

Per questo motivo, i segnali FCG sono stati acquisiti contemporaneamente a segnali respiratori di riferimento. I segnali FRG hanno ottenuto un'elevata accuratezza e precisione nel rilevamento degli atti respiratori e nella misurazione degli intervalli inter-respiro. È stato inoltre dimostrato che le interazioni cardio-respiratorie causano modulazione di ampiezza delle componenti LF-FCG e HF-FCG, nonché variazioni di vari parametri della morfologia del battito cardiaco. Infine, i sensori FCG sono stati utilizzati per monitorare le onde sfigmiche del dito. In conclusione, la FCG è una tecnica di monitoraggio cardio-respiratorio molto promettente.

Parole chiave: forcecardiography, seismocardiography, segnali cardio-meccanici, monitoraggio cardio-respiratorio, intervalli di tempo cardiaci, onde sfigmiche

Contents

Abstract..... i

Sintesi in lingua italiana..... iii

Acknowledgements x

List of Acronyms xii

List of Symbols xvii

List of Figures..... xxi

List of Tables xxx

1 Introduction1

2 Anatomy and physiology of the cardiovascular system.....7

2.1 The cardiovascular system7

2.2 The heart9

2.2.1 The location of the heart.....9

2.2.2 The anatomy of the heart.....10

2.2.3 The conduction system of the heart16

2.2.4 The cardiac cycle.....19

2.3 Physiological parameters.....24

2.3.1 Heart rate.....24

2.3.2 Stroke volume.....25

2.3.3 Cardiac output.....26

2.3.4	Blood flow	27
2.3.5	Blood pressure	30
2.3.6	Pulse.....	32
2.3.7	Heart sounds.....	33
2.3.8	Cardiac time intervals	34
2.4	Pathologies of the cardiovascular system	36
3	Cardiac monitoring techniques	39
3.1	Reference techniques	39
3.1.1	Electrocardiography.....	40
3.1.2	Echocardiography	42
3.1.3	Impedance cardiography.....	44
3.2	Cardio-mechanical monitoring techniques.....	47
3.2.1	Phonocardiography	49
3.2.2	Apexcardiography.....	52
3.2.3	Applications of PCG and ACG in the estimation of CTIs	56
3.2.4	Ballistocardiography	62
3.2.5	Seismocardiography	66
3.2.6	Gyrocardiography	75
4	Forcecardiography	79
4.1	The FCG signal.....	79
5	The effect of respiration on FCG signals.....	89
5.1	Respiration monitoring via FCG sensors.....	89
5.1.1	The piezoresistive FCG sensor	90

5.1.2	Electro-resistive band for respiration monitoring	91
5.1.3	Sensor placement and measurement setup	92
5.1.4	Signal processing and analysis	94
5.1.5	Discussion	102
5.2	Respiratory-induced amplitude modulation of FCG signals	102
5.2.1	The piezoelectric FCG sensor	103
5.2.2	Sensor placement and measurement setup	104
5.2.3	Signal processing and analysis	105
5.2.4	Discussion	116
5.3	Changes in FCG heartbeat morphology induced by cardio-respiratory interactions	117
5.3.1	Signal pre-processing	117
5.3.2	Extraction of the LVET and MSi trends	118
5.3.3	Analysis of consistency within the respiratory cycle	120
5.3.4	Discussion	127
6	Localization of cardiac cycle events in FCG signals	129
6.1	Detection of aortic valve opening and estimation of PEP in FCG signals	129
6.1.1	Measurement setup and protocol	129
6.1.2	Signal processing	132
6.1.3	Morphological comparison between FCG and SCG signals	133
6.1.4	Statistical analyses on PEP estimates	136
6.1.5	Discussion	141
6.2	Heartbeats localization in FCG signals via template matching	142
6.2.1	Measurement setup and protocol	142

6.2.2	Signal pre-processing	143
6.2.3	Heartbeats localization via template matching.....	144
6.2.4	Statistical analyses on inter-beat intervals	146
6.2.5	Discussion.....	148
7	Comparison between LF-FCG signal and double integration of seismocardiogram.....	149
7.1	Measurement setup and protocol	150
7.2	Signals processing.....	151
7.2.1	FCG signals processing.....	151
7.2.2	SCG signals processing.....	152
7.3	Morphological comparison between LF-FCG and LF-DSCG signals	152
7.3.1	LF-FCG vs LF-DSCG during apneas.....	152
7.3.2	LF-FCG vs LF-DSCG during quiet breathing	154
7.4	Statistical analyses on inter-beat intervals.....	156
7.4.1	Inter-beat intervals from LF-FCG and LF-DSCG signals acquired during apneas	156
7.4.2	Inter-beat intervals from LF-FCG and LF-DSCG signals acquired during quiet breathing.....	160
7.5	Discussion.....	163
8	Multimodal finger pulse wave sensing: comparison of FCG and PPG sensors	165
8.1	Photoplethysmography.....	165
8.2	Multimodal PW sensor.....	168
8.3	Measurement setup and protocol	169
8.4	Signal processing and analysis.....	170

8.4.1	Pre-processing.....	170
8.4.2	Detection of fiducial points.....	171
8.4.3	Extraction of PW morphological parameters	171
8.4.4	Normalized cross-correlation.....	179
8.4.5	Statistical analyses on morphological parameters.....	179
8.5	Discussion.....	184
9	Conclusions	187
	Bibliography.....	192
	Author's Publications.....	217

Acknowledgements

First of all, I would like to thank my supervisor, Prof. Paolo Bifulco, for the trust he placed in me. I would not have achieved the results reported in this thesis without his valuable teachings. I am extremely grateful for the support he gave me during the three years of my Ph.D., as well as for his helpfulness and care towards me.

Special thanks go to my colleagues, Dr. Emilio Andreozzi and Dr. Daniele Esposito, who welcomed me into the Biomedical Engineering group from the beginning and supported me in every moment of my Ph.D.

Finally, I would like to show my gratitude to Prof. Gaetano D. Gargiulo for the great opportunity to collaborate with him.



List of Acronyms

3D	three-dimensional
AC	aortic valve closure
ACG	apexcardiography
AO	aortic valve opening
AV	atrioventricular
BCG	ballistocardiography
BF	blood flow
BMI	body mass index
BP	blood pressure
BSA	body surface area
CI	cardiac index
CNS	central nervous system
CO	cardiac output
CTI	cardiac time interval
CVD	cardiovascular disease
CVS	cardiovascular system
DBP	diastolic blood pressure
DSCG	displacement SCG signal
DTI	diastolic time interval
ECG	electrocardiography

ECHO	echocardiography
EDV	end-diastolic volume
EMD	electromechanical delay
ESV	end-systolic volume
FCG	forcecardiography
FHR	fetal heart rate
FN	number of false negatives
FP	number of false positives
FRG	forcerespirogram
FSR	force-sensing resistor
GCG	gyrocardiography
HF-FCG	high-frequency component of FCG signal
HR	heart rate
HRV	heart rate variability
HS-FCG	heart-sound component of FCG signal
ICG	impedance cardiography
IMU	inertial measurement unit
IVCT	isovolumetric contraction time
IVRT	isovolumetric relaxation time
KCG	kinocardiography
LF-DSCG	low-frequency component of DSCG signal

LF-FCG	low-frequency component of FCG signal
LoA	limits of agreement
LVEF	left ventricular ejection fraction
LVET	left ventricular ejection time
LVFT	left ventricular filling time
MAP	mean arterial blood pressure
MEMS	micro-electromechanical system
MPI	myocardial performance index
MSi	morphological similarity index
NCC	normalized cross-correlation
NCCF	normalized cross-correlation function
NIBP	non-invasive blood pressure
NS	non-significant
PAT	pulse arrival time
PCG	phonocardiography
PEP	pre-ejection period
PMI	point of maximal impulse
PNS	parasympathetic nervous system
PPG	photoplethysmography
PPG-IR	infrared PPG signal
PPG-R	red PPG signal

PPV	positive predictive value
PTT	pulse transit time
PZT	lead-zirconate-titanate piezoelectric sensor
PW	pulse wave
R-FCG	respiratory component of FCG signal, i.e., the FRG
R-R	inter-beat interval from ECG signal
RVFT	rapid ventricular filling time
SA	sinoatrial
SBP	systolic blood pressure
SCG	seismocardiography
SD	standard deviation
SNS	sympathetic nervous system
SNR	signal-to-noise ratio
STI	systolic time interval
SV	stroke volume
SVR	systemic vascular resistance
TDI	tissue doppler imaging
TP	number of true positives
TST	total systolic time
US	ultrasound
WHF	world heart federation



List of Symbols

ΔP	pressure difference (introduced in Section 2.3.4)
$\Delta Z(t)$	thoracic electrical impedance variation, i.e., blood volume curve (introduced in Section 3.1.3)
η	blood viscosity (introduced in Section 2.3.4)
bpm	beats per minute
Ca^{2+}	calcium ion (introduced in Section 2.2.3)
cm	centimeters
$(dP/dt)_{\max}$	maximum of the first temporal derivative of left intraventricular pressure (introduced in Section 3.2.3)
$dZ(t)/dt$	first temporal derivative of $\Delta Z(t)$, i.e., blood velocity curve (introduced in Section 3.1.3)
dps	degrees per second
g	grams
h	hours
h_1	systolic peak height with respect to the foot of PPG signal (introduced in Section 8.4.3)
h_2	dicrotic notch height with respect to the foot of PPG signal (introduced in Section 8.4.3)
h_3	diastolic peak height with respect to the foot of PPG signal (introduced in Section 8.4.3)

h_2/h_1	ratio of the dicrotic notch to the systolic peak heights of PPG signal (introduced in Section 8.4.3)
h_3/h_1	ratio of the diastolic to systolic peaks heights of PPG signal (introduced in Section 8.4.3)
Hz	Hertz
K^+	potassium ion (introduced in Section 2.2.3)
kg	kilograms
kHz	10^3 Hertz
L	blood vessel length (introduced in Section 2.3.4)
L	liters
m^2	square meters
min	minute
mg	10^{-3} g (where g is the gravitational acceleration)
mL	milliliters
mmHg	millimeters of mercury
ms	milliseconds
NCC_E	normalized cross-correlation related to the ECG-triggered ensemble averages (introduced in Section 7.3.1)
NCC_{MEAN}	mean of the normalized cross-correlation related to single heartbeats (introduced in Section 7.3.1)

\mathbf{NCC}_{SD}	SD of the normalized cross-correlation related to single heartbeats (introduced in Section 7.3.1)
\mathbf{NCC}_{W}	normalized cross-correlation related to the whole signals (introduced in Section 7.3.1)
\mathbf{r}	blood vessel internal radius (introduced in Section 2.3.4)
\mathbf{R}	blood flow resistance (introduced in Section 2.3.4)
\mathbf{R}^2	coefficient of determination (introduced in Section 5.1.4)
\mathbf{S}_1	1 st heart sound (introduced in Section 2.3.7)
\mathbf{S}_2	2 nd heart sound (introduced in Section 2.3.7)
\mathbf{S}_3	3 rd heart sound (introduced in Section 2.3.7)
\mathbf{S}_4	4 th heart sound (introduced in Section 2.3.7)
\mathbf{SpO}_2	saturation of peripheral oxygen (introduced in Section 8)
\mathbf{T}	time distance between two consecutive feet of PPG signal (introduced in Section 8.4.3)
\mathbf{t}_i	time distance between the foot and the dicrotic notch of PPG signal (introduced in Section 8.4.3)
\mathbf{t}_{up}	time distance between the foot and the systolic peak of PPG signal (introduced in Section 8.4.3)
$\mathbf{t}_{\text{up}}/\mathbf{T}$	ratio of foot time distances from the systolic peak and from subsequent foot of PPG signal (introduced in Section 8.4.3)



List of Figures

Figure 1. The circulatory system. The circulatory system is divided into two circuits, both originating from the heart and returning to the heart: the pulmonary circulation, which allows blood flow from and to the lungs, and the systemic circulation, which supports blood flow from and to body tissues [24].....	8
Figure 2. The location of the heart. The heart is located within the thorax, in a space between the lungs, called the mediastinum. It is placed posterior to the sternum and anterior to the vertebral column, resting on the diaphragm. It is surrounded by the pericardium [23].....	10
Figure 3. Blood flow through the heart. The right atrium receives deoxygenated blood from the inferior vena cava and superior vena cava which is then pumped into the pulmonary trunk by the right ventricle. Oxygenated blood returning from the lungs is collected by the left atrium through the pulmonary veins and then pumped into the aorta by the left ventricle [24].....	11
Figure 4. Anterior view of the heart showing the four chambers, the valves, the major vessels and their primary branches [23].	12
Figure 5. Internal anatomy of the heart: (a) transverse section (the atrioventricular valves are closed, while the semilunar valves are open); (b) frontal section (the aortic valve is open, while the mitral valve is closed to prevent blood backflow into the left atrium) [23].	13
Figure 6. Internal anatomy of the heart: (a) transverse section (the atrioventricular valves are open, while the semilunar valves are closed); (b) frontal section (the aortic valve is closed to prevent blood backflow into the aorta, while the mitral valve is closed) [23].	13
Figure 7. Auricles and coronary circulation of the heart: (a) anterior view [26]; (b) posterior view [27].....	14
Figure 8. Heart wall. The heart wall consists of the epicardium (outer layer), the myocardium (middle layer) and the endocardium (inner layer) [23].....	15
Figure 9. The myocardium: (a) configuration of cardiac muscle fibers; (b) ventricular muscle thickness [23].....	16

Figure 10. The conduction system of the heart. The conduction system of the heart consists of the SA node, the AV node, the AV bundle, the AV bundle branches, and the Purkinje fibers [23].....	17
Figure 11. The action potential of a conductive myocardial cell [23].	18
Figure 12. The action potential of a contractile myocardial cell [23].....	19
Figure 13. Wiggers' diagram showing blood pressure and blood volume curves along with Electrocardiography and Phonocardiography tracings [28].	20
Figure 14. The cardiac cycle. The cardiac cycle is the alternated and coordinated sequence of contractions (systoles) and relaxation (diastoles) of atria and ventricles [23].....	22
Figure 15. ECG waveform and its relation to the phases in the cardiac cycle [23].	23
Figure 16. ECG waves, intervals and segments [23].	24
Figure 17. Blood vessels. Blood from the heart flows through arteries, arterioles and capillaries towards body tissues; blood from body tissues flows through capillaries, venules and veins towards the heart [24].	28
Figure 18. Structure of a blood vessel: (a) comparison between artery and vein lumen [23], (b) the tunics of blood vessel wall [24].	29
Figure 19. Typical arterial blood pressure waveform [29].....	31
Figure 20. Pulse sites on the human body [23].	32
Figure 21. Heart sounds recording along with pressure curves [23].	33
Figure 22. Representation of cardiac time intervals on Wiggers' diagram, along with Electrocardiography and Phonocardiography tracings [28].	35
Figure 23. Einthoven's triangle. I, II and III indicate the ECG bipolar leads defined by Einthoven. aVF, aVL and aVR indicate the ECG augmented unipolar leads due to Goldberger [37].	41
Figure 24. Examples of ECHO images: (a) M-mode; (b) Blood flow from ECHO Doppler. AVO and AVC indicate aortic valve opening and closure events, while MVO and MVC indicate mitral valve opening and closure events. Max and min subscripts represent the start and the end points of ECHO ranges for these events [38].	44
Figure 25. ICG acquisition configuration: electrodes placement [40].	45
Figure 26. First derivative of thoracic electrical impedance, $dZ(t)/dt$, along with simultaneous ECG and PCG recordings. Q refers to the Q-wave in the ECG signal;	

B marks the onset of left ventricular ejection on $dZ(t)/dt$; X indicates the closure of the aortic valve on $dZ(t)/dt$. PEP is the time interval from the Q wave to the B-point. LVET is the time interval from the B-point to the X-point [41].....	46
Figure 27. Heart motion during the cardiac cycle. (a) During the isovolumic contraction phase, an equally distributed pressure is exerted on the walls of the left ventricle and no movement can be appreciated; (b) when the aortic valve opens, the ejection of blood into the aorta induces the heart to move downward, since the force applied against the apex is no longer balanced by an equal reaction; (c) during blood ejection, the aortic arch straightens under the recoil effect that causes the left ventricle to move upward and forward towards the chest wall; (d) the upward and downward movement of the left ventricle generates the apical impulse [44].....	48
Figure 28. Example of PCG signal (blue line) along with a simultaneous electrocardiogram (red line) [65]......	52
Figure 29. Measurement setup for apexcardiogram recording [66].	53
Figure 30. ACG waveform along with schematic PCG signal. The typical ACG waveform is represented on the top. A = a wave that reflects ventricular filling due to atrial contraction; C = systolic wave due to ventricular contraction; E-point = peak of the systolic wave; O-point = onset of the rapid filling wave (AV valves opening); F = onset of slow filling wave (diastasis). A schematic PCG signal is depicted on the bottom. A _o = aortic valve closure; P = pulmonary valve closure [67].	54
Figure 31. BCG signal obtained from Henderson’s apparatus, along with carotid pulse tracing. Four waves can be recognized: D _s , which is a slight upward movement at the onset of systole; D _r , which is a rapid and considerable downward movement due to blood ejection; D _h , which is a large upward movement caused by blood flowing toward the feet; and D _d , which is a large downward movement during diastole, followed by an upward wave of slight amplitude [84].	63
Figure 32. (a) Example of a typical BCG signal with its characteristic waves. The arrow indicates the timing of the QRS complex onset in the electrocardiogram; (b) Aortic arch and force vectors coming from blood ejection by the left ventricle [97].	65
Figure 33. Mounsey’s precordial ballistocardiogram, along with simultaneous ECG and PCG signals [99].	67

Figure 34. SCG signal annotation by Crow, along with a simultaneous electrocardiogram [103].	69
Figure 35. SCG signal along with a simultaneous electrocardiogram. MC = mitral valve closure; IM = isovolumic movement; AO = aortic valve opening; RE = rapid ejection; AC = aortic valve closure; MO = mitral valve opening; RF = rapid filling; AS = atrial systole [102].	71
Figure 36. Example of experimental SCG signal. From bottom to top: the acceleration of aortic blood derived from Doppler ultrasound, SCG and its 95% higher and lower confidence intervals, ICG, Doppler velocity ultrasound, and ECG. AO: aortic valve opening, AC: aortic valve closure, RE: rapid ejection, SCG-min: global minimum of SCG, Doppler- max: global maximum of the Doppler blood acceleration signal [127].	72
Figure 37. GCG signal annotation, along with a simultaneous electrocardiogram [138].	76
Figure 38. Simultaneous recordings of ECG, SCG (z-axis), GCG (y-axis), and PCG signals captured in the supine position. MC = mitral valve closure; AO = aortic valve opening; AC = aortic valve closure; MO = mitral valve opening [16].	77
Figure 39. Main cardio-mechanical monitoring techniques.	78
Figure 40. An excerpt of ECG signal (black line) and FCG signal (brown line), along with LF-FCG (blue line), HF-FCG (orange line) and HS-FCG (green line) components. The pink asterisks mark R-peaks locations.	80
Figure 41. An excerpt of FCG (blue line) and SCG (red line) signals, along with the simultaneous ECG signal (green line). The dashed vertical lines indicate R-peaks locations [20].	81
Figure 42. An excerpt of LF-FCG (blue line) and LF-SCG (red line) signals, along with the simultaneous ECG signal (green line). The dashed vertical lines indicate R-peaks locations [20].	82
Figure 43. Some excerpts of ECG (green line), HF-SCG (red/orange line) and HF-FCG (blue line) signals [20]-[21]. The dashed vertical lines in panel (a) indicate R-peaks locations.	83
Figure 44. Some examples of ECG-triggered ensemble averages of ECG (green line), HF-SCG (red line) and HF-FCG (blue line), synchronized with the R-peaks [20]-[21]. The dashed lines in panel (a) indicate standard deviation (SD) intervals.	85

Figure 45. Some excerpts of ECG signal (green line), (a) LF-FCG signal (blue line) with its largest negative peak (red cross) marked as heartbeat fiducial point and (b) HF-FCG signal (blue line) with its positive peak (red cross) marked as heartbeat fiducial point. The dashed vertical lines indicate R-peaks locations [20].	86
Figure 46. HS-FCG (blue line), PCG (orange line) and ECG (green line) signals: (a) an excerpt; (b) an example of ECG-triggered ensemble averages [21].	88
Figure 47. The piezoresistive FCG sensor used in the experimental tests.	90
Figure 48. Conditioning circuit for the FSR-based sensor [143].	91
Figure 49. The electro-resistive band used in the experimental tests.	92
Figure 50. Example of ERB and FCG sensor placement on the chest of subject #7: (a) FCG sensor mounted on patient’s chest by means of medical adhesive tape; (b) FCG secured on the chest via a belt fastened around the thorax, and the ERB mounted on the upper chest, so as not to interfere with the FCG sensor.	93
Figure 51. (a) An excerpt of raw FCG, ERB and ECG signals acquired from subject #7; (b) respiratory (R-FCG) and cardiac (C-FCG) components extracted from FCG signal depicted in panel (a).	96
Figure 52. Examples of ERB, R-FCG and EDR signals extracted from data acquired on subject #3: (a) quiet breathing; (b) forced breathing at higher rate; (c) forced breathing at lower rate.	98
Figure 53. Statistical analyses on inter-breath intervals estimated from EDR and ERB: (a) results of correlation analysis; (b) results of Bland–Altman analysis.	100
Figure 54. Statistical analyses on inter-breath intervals estimated from FCG and ERB: (a) results of correlation analysis; (b) results of Bland–Altman analysis.	101
Figure 55. The piezoelectric FCG sensor used in the experimental tests: (a) schematic representation; (b) conditioning circuit for the PZT sensor [21].	104
Figure 56. Piezoelectric FCG sensor placement.	104
Figure 57. Some excerpts of FRG signal (blue line), LF-FCG signal (violet line) and its linear envelope (orange line) from: (a) subject #4; (b) subject #5.	107
Figure 58. Some excerpts of FRG signal (blue line) and the linear envelope of LF-FCG signal (orange line) from: (a) subject #4; (b) subject #5.	108
Figure 59. Some excerpts of FRG signal (blue line), HF-FCG signal (red line) and its linear envelope (green line) from: (a) subject #4; (b) subject #5.	109

Figure 60. Some excerpts of FRG signal (blue line) and the linear envelope of HF-FCG signal (green line) from: (a) subject #4; (b) subject #5.	110
Figure 61. Some excerpts of FRG signal (blue line), the linear envelope of LF-FCG signal (orange line) and the linear envelope of HF-FCG (green line) from: (a) subject #4; (b) subject #5.	111
Figure 62. Statistical analyses of inter-breath intervals: (a) results of regression and correlation analyses; (b) results of Bland–Altman analysis for LF-FCG signals.	114
Figure 63. Statistical analyses of inter-breath intervals: (a) results of regression and correlation analyses; (b) results of Bland–Altman analysis for HF-FCG signals.	115
Figure 64. Example of FRG (blue line), dHF-FCG (orange line) and ECG (purple line) signals. The FRG signal captures the expansion and relaxation of the thorax during breathing and allows accurate monitoring of respiration. The dHF-FCG is a high-frequency component of the FCG signal, which is very similar to the seismocardiogram and provides information about the heart mechanical function. The ECG is a well-established signal that provides information about the heart electrical function.....	118
Figure 65. Example of LVET and MSi estimation in dHF-FCG signals (orange lines) from: (a) subject #2; (b) subject #4. ECG signals (blue lines) are also reported as a time reference for the cardiac cycle.	120
Figure 66. Some excerpts of FRG signal (blue line) and LVET trend (orange line) from: (a) subject #2; (b) subject #4.	121
Figure 67. Some excerpts of FRG signal (blue line) and MSi trend (green line) from: (a) subject #2; (b) subject #4.	122
Figure 68. Statistical analyses on inter-breath intervals extracted from FRG and LVET time trend: (a) results of linear regression; (b) results of Bland-Altman analysis.	125
Figure 69. Statistical analyses on inter-breath intervals extracted from FRG and MSi time trend: (a) results of linear regression; (b) results of Bland-Altman analysis.	126
Figure 70. Sensors assembly: piezoelectric FCG sensor with a dome and MMA7361 accelerometer.	130

Figure 71. Sensors assembly placement on a subject: (a) frontal view; (b) lateral view.....	131
Figure 72. Examples of HF-FCG (violet line), dHF-FCG (blue line), SCG (orange line) and ECG (green line) signals from: (a) subject #1; (b) subject #3.....	133
Figure 73. Ensemble averages of: (a) HF-FCG, SCG and ECG of subject #1; (b) dHF-FCG, SCG and ECG of subject #1; (c) HF-FCG, SCG and ECG of subject #3; (d) dHF-FCG, SCG and ECG of subject #3. The ensemble averages are depicted as solid lines, while the limits of the \pm SD ranges are depicted as dashed lines.....	136
Figure 74. Statistical analyses on PEP estimates related to signals acquired during apneas: (a) results of regression and correlation analyses; (b) results of Bland–Altman analysis.	139
Figure 75. Statistical analyses on PEP estimates related to signals acquired during quiet breathing: (a) results of regression and correlation analyses; (b) results of Bland–Altman analysis.	140
Figure 76. Piezoelectric FCG sensor applied on a subject’s chest.....	143
Figure 77. Example of a template (red line) selected within a dHF-FCG signal (blue line).	145
Figure 78. dHF-FCG signal (blue line) with the NCC (red line) obtained via the template depicted in Figure 77, and the heartbeat markers (black dots) located in the NCC.....	146
Figure 79. Statistical analyses on inter-beat interval estimates: (a) results of regression and correlation analyses; (b) results of Bland–Altman analysis.	148
Figure 80. (a) Lateral view of sensors assembly applied on the chest of a subject; (b) frontal view of sensors positioning area on the chest (green dashed line).	151
Figure 81. LF-FCG, LF-DSCG and ECG signals acquired during apneas from subject #2. Black points indicate R-peaks locations.	153
Figure 82. FRG, LF-FCG, LF-DSCG and ECG signals acquired during quiet breathing from subject #2. Black points indicate R-peaks locations.....	155
Figure 83. Statistical analyses on inter-beat intervals extracted from LF-FCG signals during apneas. (a) Results of regression and correlation analyses; (b) results of Bland–Altman analysis.....	158

Figure 84. Statistical analyses on inter-beat intervals extracted from LF-DSCG signals during apneas. (a) Results of regression and correlation analyses; (b) results of Bland-Altman analysis.....	159
Figure 85. Statistical analyses on inter-beat intervals extracted from LF-FCG signals during respiration. (a) Results of regression and correlation analyses; (b) results of Bland-Altman analysis.	161
Figure 86. Statistical analyses on inter-beat intervals extracted from LF-DSCG signals during respiration. (a) Results of regression and correlation analyses; (b) results of Bland-Altman analysis.	162
Figure 87. Schematic representation showing the components of the multimodal PW sensor placed on a subject's finger, namely MAX30102 PPG sensor, piezoelectric FCG sensor, and a flat cylinder acting as a mechanical coupler to ensure reasonable force transduction from the PPG sensor to the FCG sensor.....	169
Figure 88. Graphical example of PW fiducial points and morphological parameters.	172
Figure 89. Example of PW signals acquired by the PPG sensor (red and infrared) and the piezoelectric FCG sensor, along with the concurrently acquired ECG lead I. ECG R-peaks and the four fiducial markers located in PW signals are also depicted. A delay between the PPG and FCG sensor signals can be clearly observed. (a) Signals acquired in subject #1; (b) signals acquired in subject #3; (c) detail on four heart beats from the signal shown in panel (a) with the localized fiducial markers; (d) detail on four heartbeats from the signal shown in panel (b) with the localized fiducial markers.....	175
Figure 90. Comparison of PW signals and related first and second derivatives, acquired by the PPG sensor (red and infrared photodetectors) and the piezoelectric FCG sensor, along with the concurrently acquired ECG lead I. Signals acquired in subjects #1 and #3 are depicted in the first and second columns, respectively. The original PW signal, first derivative, and second derivative of both subjects are depicted in the first (a),(b), second (c),(d), and third (e),(f) rows, respectively.	178



List of Tables

Table 1. Respiratory acts detected in the ERB, R-FCG and EDR signals. The missed and spurious acts are reported for the R-FCG and EDR signals with reference to the acts detected in the ERB signal.	98
Table 2. Sensitivity and PPV of respiratory acts detection in the R-FCG and EDR signals.	99
Table 3. Results of regression, correlation and Bland–Altman analyses for R-FCG and EDR signals. Non-significant bias is indicated as “NS”.	102
Table 4. Respiratory acts detected in the FRG signal and the linear envelopes of LF-FCG and HF-FCG signals per subject. The missed and spurious acts are reported for the linear envelopes of LF-FCG and HF-FCG signals with reference to the acts detected in the FRG signal.	112
Table 5. Sensitivity and PPV of respiratory acts detection in the linear envelopes of LF-FCG and HF-FCG signals.	113
Table 6. Results of regression, correlation and Bland–Altman analyses for LF-FCG and HF-FCG signals. Non-significant bias is indicated as “NS”.	113
Table 7. Respiratory acts detected in the FRG signal and the LVET and MSi trends per subject. The missed and spurious acts are reported for the LVET and MSi trends with reference to the acts detected in the FRG signal.	123
Table 8. Sensitivity and PPV of respiratory acts detection in the LVET and MSi trends.	123
Table 9. Results of regression, correlation and Bland–Altman analyses for LVET and MSi trends. Non-significant bias is indicated as “NS”.	124
Table 10. NCC indices and time lags between the ensemble averages of HF-FCG vs. SCG and dHF-FCG vs. SCG for each subject. Positive time lags corresponded to FCG signals delayed with respect to SCG.	136
Table 11. Number of heartbeats in ECG and of missed AO events in SCG and in dHF-FCG for each subject in apnea conditions.	137
Table 12. Number of heartbeats in ECG and of missed AO events in SCG and in dHF-FCG for each subject in quiet breathing conditions.	138
Table 13. Sensitivity and PPV of AO events detection in SCG and dHF-FCG signals.	138

Table 14. Results of regression, correlation and Bland–Altman analyses for dHF-FCG vs SCG signals acquired during apnea and quiet breathing conditions.....	141
Table 15. Results of regression, correlation and Bland–Altman analyses for dHF-FCG signals. Non-significant bias is indicated as “NS”.	147
Table 16. NCC indices of the LF-FCG and LF-DSCG signals acquired during apneas. The correlation indices were computed between the whole signals, between single corresponding heartbeats (mean and SD of correlation indices are reported) and between the ECG-triggered ensemble averages.....	154
Table 17. NCC indices of the LF-FCG and LF-DSCG signals acquired during quiet breathing. The correlation indices were computed between the whole signals, between single corresponding heartbeats (mean and SD of correlation indices are reported) and between the ECG-triggered ensemble averages.....	155
Table 18. Results of regression, correlation and Bland–Altman analyses for LF-FCG vs LF-DSCG signals acquired during apneas. Non-significant bias is indicated as “NS”.	157
Table 19. Results of regression, correlation and Bland–Altman analyses for LF-FCG vs LF-DSCG signals acquired during quiet breathing. Non-significant bias is indicated as “NS”	160
Table 20. Subjects’ demographics.	170
Table 21. Mean and SD of time delays (in milliseconds) between PW fiducial markers of FCG and PPG.	173
Table 22. Mean and SD of beat-by-beat NCCs between PW signals acquired by FCG and PPG-R sensors.....	180
Table 23. NCCs and time lags between whole PW signals acquired by FCG and PPG-R sensors.....	180
Table 24. Morphological parameters extracted from PW signals acquired by FCG and PPG sensors.....	181
Table 25. Results of the regression, correlation, and Bland–Altman analyses that were carried out to compare the morphological parameters of PW signals provided by FCG and PPG sensors for each subject. Intercept, bias, and LoA for t_{up} , t_i , and T are expressed in milliseconds. Non-significant bias is indicated as “NS”	182

Table 26. Results of the regression, correlation, and Bland–Altman analyses that were carried out to compare the morphological parameters of PW signals provided by FCG and PPG sensors for each subject.....183

Table 27. Results of the regression, correlation, and Bland–Altman analyses that were carried out to compare the morphological parameters of PW signals provided by FCG and PPG sensors for all subjects. Intercept, bias, and LoA for t_{up} , t_i , and T are expressed in milliseconds. Non-significant bias is indicated as “NS”.184

Table 28. Results of the regression, correlation, and Bland–Altman analyses that were carried out to compare the morphological parameters of PW signals provided by FCG and PPG sensors for all subjects.....184



Introduction

Cardiac monitoring is a vital task in health condition assessment, especially considering the current burden of cardiovascular diseases (CVDs). Indeed, CVDs (e.g., coronary artery disease, myocardial infarction, heart failure, stroke, cardiomyopathies, heart valve disfunctions, arrhythmias) are the leading cause of death worldwide. According to the World Heart Federation (WHF), 18.6 million people globally die of CVD every year, accounting for 33 % of all global deaths. Moreover, the number of CVD deaths is expected to exceed 22.2 million in 2030 and 32.3 million in 2050, thus resulting in increased healthcare costs [1]-[2]. For these reasons, cardiac monitoring plays a key role in the early diagnosis of CVDs, as well as in the follow-up of chronic patients, to improve personal care and reduce CVDs mortality rate.

Electrocardiography (ECG) is widely considered as the gold standard for non-invasive measurement of the heart electrical activity and is undoubtedly one of the most widespread techniques in clinical practice for cardiac monitoring. Indeed, many CVDs are associated with alterations in cardiac electrical pattern, thus in the typical ECG waveform. However, this technique does not provide information about the heart mechanical function. Therefore, ECG is usually combined with other clinical examinations to obtain a more comprehensive evaluation of the cardiac function. ECG signals are often acquired simultaneously with Impedance cardiography (ICG) recordings by taking advantage of electrodes placed on the body surface. ICG measures changes in thoracic electrical impedance due to blood volume variations and allows the estimation of various parameters of cardiac function, such as

myocardial contractility, stroke volume, cardiac output, cardiac time intervals, etc. Abnormalities in ICG waveform provide valuable information for the diagnosis of CVDs. However, both ECG and ICG are not well suited to long-term monitoring, particularly in home settings, and early detection of CVDs because signs of heart dysfunction are often evident only in advanced pathological conditions [3]-[4]. Moreover, they intrinsically involve electrical risks [5].

The heart accomplishes its function of pumping blood through the cardiovascular system via the contraction of atria and ventricles. The mechanical activity of the beating heart generates weak forces on the thoracic surface and the whole body. On one hand, the pulsatile force developed by the heart contraction propagates through various chest tissues and reaches the surface, thus causing small movements of the chest wall that can be felt by contact with the hands (this practice is known as palpation). On the other hand, the blood flowing into the great vessels generates recoil forces that result in subtle displacements of the body's center of mass, mainly along the superior-inferior axis (i.e., head to feet direction).

The quantitative, non-invasive assessment of the mechanical aspects of cardiac function dates back to the second half of the 19th century. Since then, several methods and apparatuses have been introduced to record the vibrations of the precordium and the whole body, by leveraging different physical principles. Phonocardiography (PCG) [6]-[7], Apexcardiography (ACG) [8]-[9], Ballistocardiography (BCG) [10]-[11], and Seismocardiography (SCG) [11]-[13] have been the most successful, among the techniques proposed at the outset, thus gaining sufficient attention to be extensively investigated as valuable tools for CVDs discrimination. PCG captures the sonic components of precordial vibrations, commonly known as heart sounds, while both ACG and SCG record the infrasonic components. In particular, ACG monitors chest wall displacements at the apex of the heart, while SCG measures precordial accelerations. On the contrary, BCG records the whole-body vibrations induced by displacements of the body's center of mass due to blood flowing towards the feet. However, they all originally had in common the use of cumbersome instrumentation and uneasiness of signals interpretation, which made them lose their appeal as practical indirect methods for the evaluation of the cardiac function, especially with the emergence of ultrasound imaging technologies, which brought outstanding diagnostic capabilities by allowing

physicians to actually look inside the human body. In particular, Echocardiography (ECHO) enables the visualization of cardiac events (e.g., opening and closure of heart valves) almost in real-time, and the analysis of blood flow through the heart and great vessels, providing useful information for the estimation of hemodynamic parameters. However, this technique is expensive, cumbersome, operator-dependent and not suitable for continuous, long-term monitoring. These factors make it feasible only in clinical settings [14].

In the last decade, the availability of small and lightweight accelerometers based on micro-electromechanical systems (MEMS) technologies gave rise to a new research trend that largely focused on SCG [11]-[13], particularly to develop wearable applications for continuous, long-term monitoring of both healthy and pathological subjects. Indeed, the typical SCG signal is composed of infrasonic oscillations, which feature various peaks and valleys that have a temporal relationship with important cardiac cycle events, such as heart valves opening and closure, isovolumic contraction, blood ejection, etc. From these fiducial markers, different cardiac time intervals can be estimated (e.g., inter-beat interval, isovolumic contraction time, pre-ejection period, left ventricular ejection time, isovolumic relaxation time, etc.), which provide clinically relevant information for the diagnosis and management of various cardiac pathologies [12]-[13]. For this reason, SCG is currently considered as the mechanical counterpart of ECG. Furthermore, SCG is often performed via small inertial measurement units (IMUs). Since IMUs usually also include gyroscopes, new techniques have recently been proposed, such as Gyrocardiography (GCG), which captures the rotational components of local cardiac-induced mechanical vibrations [15]-[16]. In addition to SCG, GCG has also proven useful as wearable surrogate for ECHO in estimating cardiac time intervals. The joint use of SCG and GCG, even from multiple sites, has further been investigated [17]-[18]. Moreover, they have also been combined with BCG, as in the case of the recent Kinocardiography [19].

Lately, Forcercardiography (FCG) has been proposed as a novel technique to measure the cardiac-induced vibrations of the chest wall via force sensors [20]-[21]. To this aim, specific force sensors have been employed, based on both the piezoresistive and the piezoelectric effect, which have been equipped with dome-shaped mechanical couplers to optimize the transduction of forces from tissues to sensors. In the first place, FCG signals have been acquired via piezoresistive force

sensors based on force-sensing resistors (FSRs) [20]. Very recently, a novel piezoelectric sensor with a specific conditioning circuit has been proposed for FCG recordings [21], which showed superior performance as compared to piezoresistive ones. FCG sensors are characterized by a wide bandwidth and have been proven capable of capturing infrasonic cardiac vibrations and heart sounds, all simultaneously from a single site on the chest. Indeed, the raw signal provided by the FCG sensor features both a sonic component (i.e., HS-FCG) corresponding to the heart sounds, and two infrasonic components, namely the low-frequency FCG (LF-FCG) and high-frequency FCG (HF-FCG). In detail, the HF-FCG has been shown to carry similar information to SCG, while the LF-FCG reflects the forces impressed on the chest wall by the emptying and filling actions of heart chambers, thus potentially carrying information on stroke volume variations. This low-frequency component of the precordial vibrations cannot be directly observed in common SCG recordings [20]. Both LF-FCG and HF-FCG are strongly correlated with heart contractions, thus providing accurate estimates of inter-beat intervals, while HS-FCG has been shown to share very high similarity with PCG signals in terms of morphology, as well as acoustic impression [20]-[21].

By considering the recent introduction of FCG, the primary goals are the analysis of accuracy and the optimization of performance, then proceeding towards the standardization, as in the case of other well-established techniques. Therefore, this thesis aims to perform a more in-depth investigation on clinically relevant information that can be extracted from FCG signals in order to disclose the potentialities of FCG as compared to existing cardio-mechanical monitoring techniques, particularly SCG. To this end, FCG recordings were carried out on a cohort of healthy subjects in different experimental conditions, along with reference signals for comparison purposes.

In detail, **Chapter 2** provides a brief description of anatomy and physiology of the cardiovascular system, along with its most relevant physiological parameters, and finally an overview of the main CVDs.

Chapter 3 briefly outlines three well-established techniques in clinical practice, i.e., ECG, ECHO and ICG, which are commonly adopted as references for the characterization of cardio-mechanical signals. Then, it describes the main techniques for non-invasive cardio-mechanical monitoring, i.e., PCG, ACG, BCG, SCG and

GCG (it is worth underlining that this thesis is focused on contact-based methods), with particular attention to signals interpretation and cardiac parameters extraction.

Chapter 4 presents FCG technique, specifically by illustrating the main components of the raw FCG sensor signal.

Chapters 5 to 8 describe the materials and methodologies adopted for the experimental tests and report the results obtained. In particular, **Chapter 5**, which is organized in three different studies, investigates the effect of breathing activity on FCG signals. The first study aims to demonstrate the suitability of FCG sensors for accurate, continuous and unobtrusive monitoring of respiration. To this end, FCG recordings were acquired simultaneously with reference respiration signals. The second study explores the respiratory-related amplitude modulation of LF-FCG and HF-FCG signals, while the third study analyses changes in FCG heartbeat morphology induced by cardio-respiratory interactions.

Chapter 6 is focused on the localization of cardiac cycle events in FCG signals. Specifically, a first study addresses the detection of aortic valve opening events in HF-FCG signals and the estimation of pre-ejection periods, while also performing a performance comparison with simultaneous SCG signals. Moreover, a novel template matching approach for heartbeats localization in HF-FCG signals is proposed in a further study.

Chapter 7 demonstrates the feasibility of extracting the same information on ventricular emptying and filling events, as captured by the LF-FCG component, from SCG recordings, by implementing a method based on numerical double integration of accelerometric SCG signals.

Chapter 8 presents a true multimodal pulse wave sensor, obtained by integrating a piezoelectric FCG sensor and a Photoplethysmography (PPG) sensor, thus enabling simultaneous mechanical-optical measurements of pulse waves from the same site on the body.

Finally, conclusions and future perspectives are discussed in **Chapter 9**.



Chapter 2

Anatomy and physiology of the cardiovascular system

This chapter provides some basics of anatomy and physiology of the cardiovascular system [22]-[24], along with a brief description of its most relevant physiological parameters [22]-[24], and finally an overview of the main cardiovascular diseases [22]-[23],[34]. It should not be considered an exhaustive exposition of this topic. For a deeper study, anatomy and physiology books are highly recommended.

2.1 The cardiovascular system

The cardiovascular system (CVS) consists of three main components, the blood, blood vessels and heart, which are intimately organized in a closed-loop system. The CVS is primarily responsible for transporting nutrients to the cells of body tissues, while removing waste products of the metabolism. The heart acts as a dual-system pump to eject blood into the vascular system. As shown in **Figure 1**, blood vessels are divided into two main branches, both originating from the heart and returning to the heart: the pulmonary circulation, which allows blood flow from and to the lungs, and the systemic circulation, which supports blood flow from and to body tissues. Pulmonary venules and veins carry oxygenated blood from the lungs to the left heart which is pumped into the systemic circuit through the aorta, then passing

into arteries, arterioles and capillaries where nutrients, metabolic end products and other substances are exchanged with the surrounding body tissues. On the contrary, deoxygenated blood returns to the right heart through venules and veins in the systemic circuit and then is pumped into the lungs through the pulmonary arteries. Here it is enriched with oxygen and deprived of carbon dioxide. Hence, the CVS guarantees the body cells to survive.

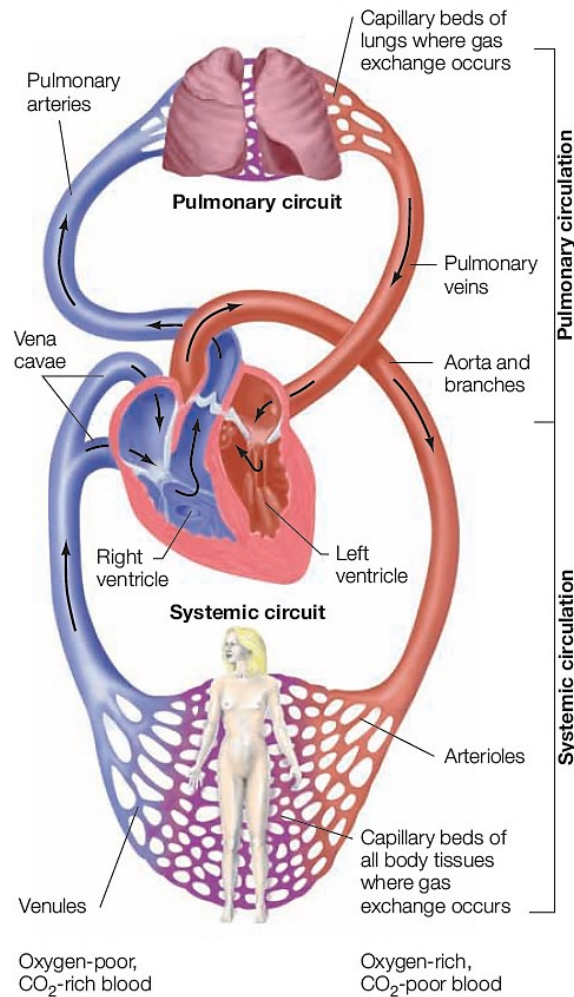


Figure 1. The circulatory system. The circulatory system is divided into two circuits, both originating from the heart and returning to the heart: the pulmonary circulation, which allows blood flow from and to the lungs, and the systemic circulation, which supports blood flow from and to body tissues [24].

2.2 The heart

The human heart is a hollow, cone-shaped muscular organ of varying size. It can be considered approximately the size of a man's clenched fist, about 12 cm in length, 8 cm in wide and 6 cm in thickness. Its weight varies with gender. Indeed, a female heart weighs about 250-300 g, while a male heart weighs about 300-350 g. The heart contracts and relaxes cyclically to accomplish its function of pumping blood through the CVS. It contracts on average 75 times per minute, 108000 times in a day, by ejecting 70 mL of blood per contraction. This results in approximately 5.25 L of blood pumped by the heart per minute and thus 7000 L every day.

2.2.1 The location of the heart

The heart is located within the thoracic cavity, in a space between the pleural cavities which contain the lungs, called the medial mediastinum (see **Figure 2**). It is placed posterior to the sternum and anterior to the vertebral column, resting on the superior surface of the diaphragm. A protective double-layer membrane, the pericardium (also known as pericardial sac), surrounds the heart and separates it from the other mediastinal structures, bounding the pericardial cavity. The pericardium consists of an outer fibrous layer made of dense connective tissue, namely the fibrous pericardium, and an inner serous layer, namely the serous pericardium. The latter is further divided into two continuous membranes: the outer parietal pericardium, which lines the internal surface of the fibrous pericardium, and the inner visceral pericardium or epicardium, which is attached to the heart. The cavity between these two layers is filled with a serous fluid that lubricates the surface of the heart, reducing friction when it contracts. The heart is placed in an oblique position, in a plane that roughly extends from the right shoulder to the left nipple. Its long axis is tilted approximately 45° to the left with respect to the midline of the thoracic sagittal plane [25]. The upper portion of the heart, the base, is located at the level of the third costal cartilage, while the lower portion ends in a blunt point, the apex, which lies within the fifth intercostal space along the midclavicular line.

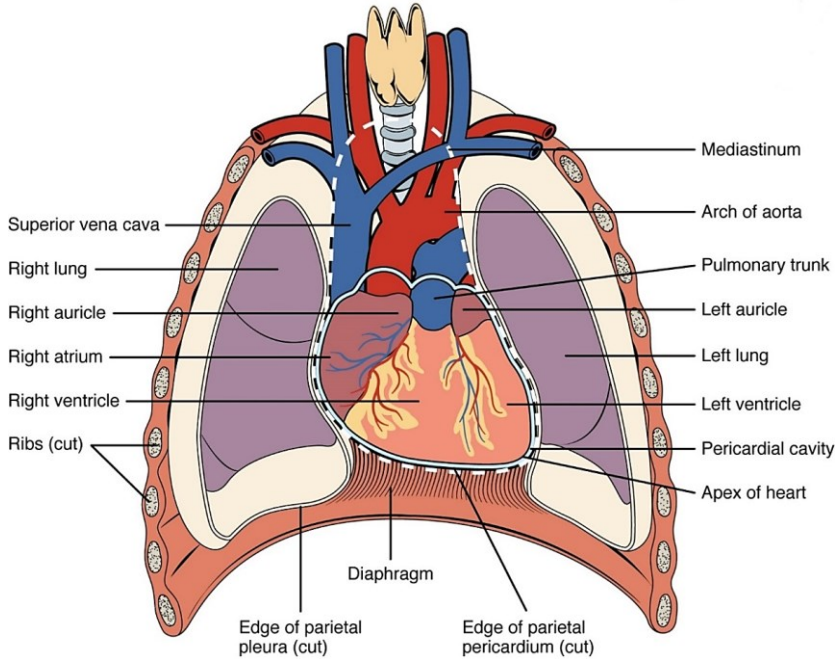


Figure 2. The location of the heart. The heart is located within the thorax, in a space between the lungs, called medial mediastinum. It is placed posterior to the sternum and anterior to the vertebral column, resting on the diaphragm. It is surrounded by the pericardium [23].

2.2.2 The anatomy of the heart

The inside of the heart is composed of two upper chambers, the atria, and two lower chambers, the ventricles. Longitudinally, the heart can be divided into right side and left side, each consisting of an atrium-ventricle pump. The right atrium receives deoxygenated blood from two large veins in the systemic circuit, the inferior vena cava (carrying blood from the lower portion of the body) and the superior vena cava (carrying blood from the upper portion of the body), and the coronary sinus (which drains blood from the coronary veins into the cardiac muscle). Deoxygenated blood is then pumped into the pulmonary trunk (which bifurcates into right and left pulmonary arteries supplying blood to the lungs) by the right ventricle. Oxygenated blood returning from the lungs is collected by the left atrium through the pulmonary veins. Finally, the left ventricle pumps it into the aorta and once again in the systemic circulation (see **Figure 3**).

2.2 THE HEART

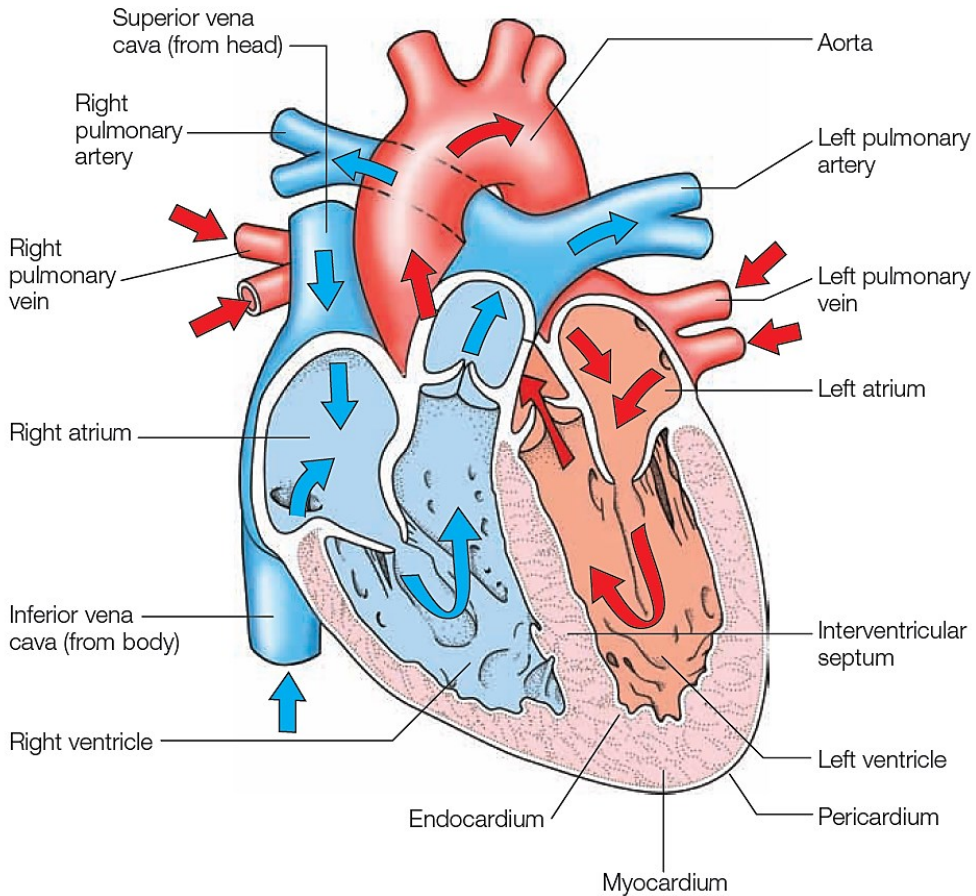


Figure 3. Blood flow through the heart. The right atrium receives deoxygenated blood from the inferior vena cava and superior vena cava which is then pumped into the pulmonary trunk by the right ventricle. Oxygenated blood returning from the lungs is collected by the left atrium through the pulmonary veins and then pumped into the aorta by the left ventricle [24].

Atria and ventricles are separated by solid wall-like structures, namely the interatrial septum (between the atria), the interventricular septum (between the ventricles) and the atrioventricular (AV) septum (between the atria and ventricles). The latter has four openings through which blood flows, where the heart valves are located. Heart valves ensure unidirectional blood flow and can be grouped into AV valves (between the atria and ventricles) and semilunar valves (between the heart and pulmonary or systemic circulation). The AV valves include the tricuspid valve (or right AV valve), which is placed between the right atrium and right ventricle, and the mitral valve (or left AV valve), which is placed between the left atrium and

left ventricle. The semilunar valves are the pulmonary valve, located between the right ventricle and the pulmonary trunk, and the aortic valve, located between the left ventricle and the aorta (see **Figure 4**).

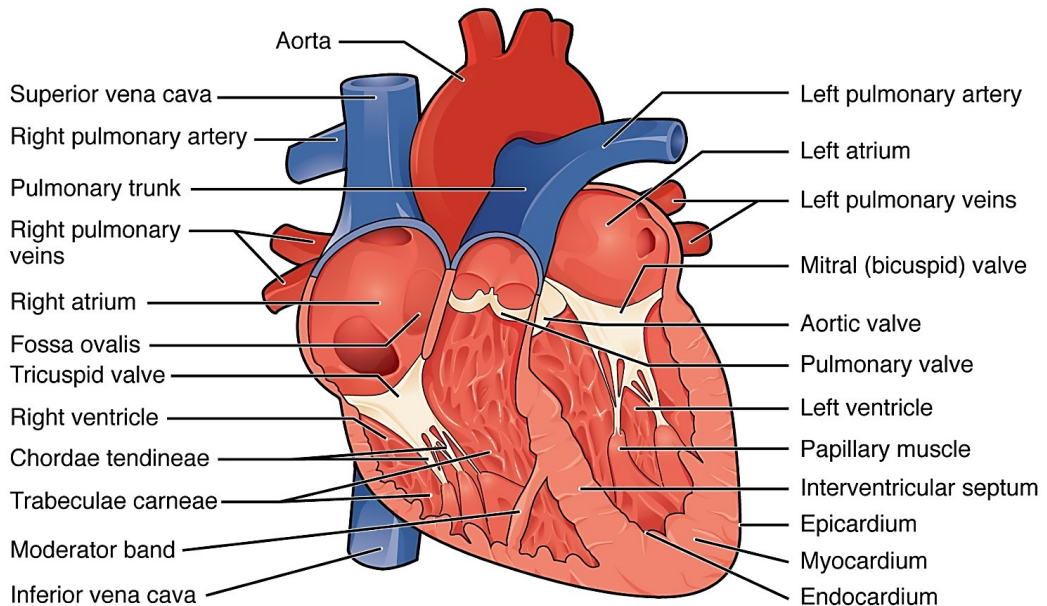


Figure 4. Anterior view of the heart showing the four chambers, the valves, the major vessels and their primary branches [23].

All valves present three leaflets or flaps, known as cusps, except for the mitral valve, which has only two cusps (therefore it is also known as bicuspid valve). The cusps of AV valves are linked by fibers of connective tissue, the chordae tendineae, to the ventricular papillary muscles, which keep the valves closed during contraction and prevent blood from flowing back into the atria (indeed, the papillary muscles contract together with the ventricles and cause the chordae tendineae to stretch). The semilunar valves, instead, do not have chordae tendineae, nor associated papillary muscles, and their cusps form a pocket-shape configuration. Heart valves are showed in **Figure 5** and **Figure 6**. Because of the presence of heart valves, the AV septum is supported by a reinforcement made of dense connective tissue, namely the cardiac skeleton, which surrounds the valves.

2.2 THE HEART

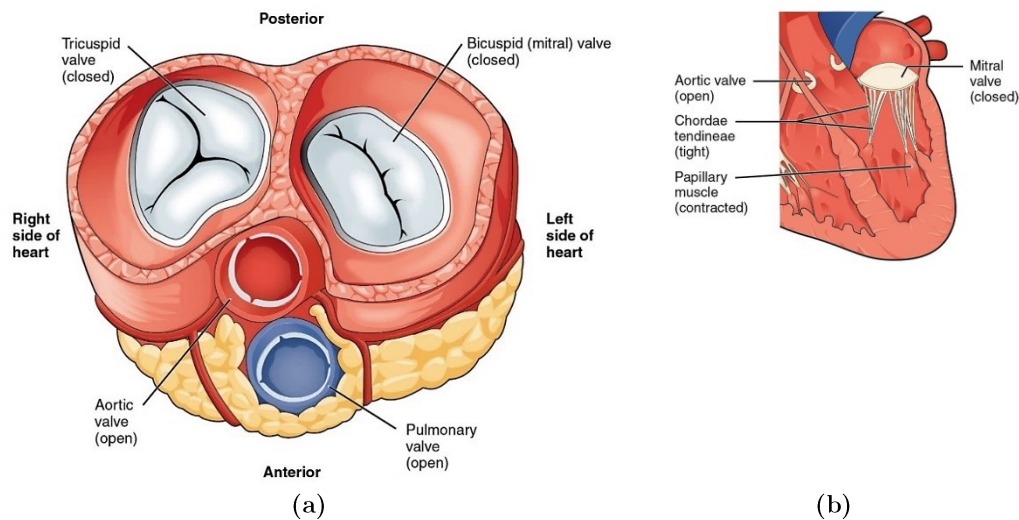


Figure 5. Internal anatomy of the heart: (a) transverse section (the atrioventricular valves are closed, while the semilunar valves are open); (b) frontal section (the aortic valve is open, while the mitral valve is closed to prevent blood backflow into the left atrium) [23].

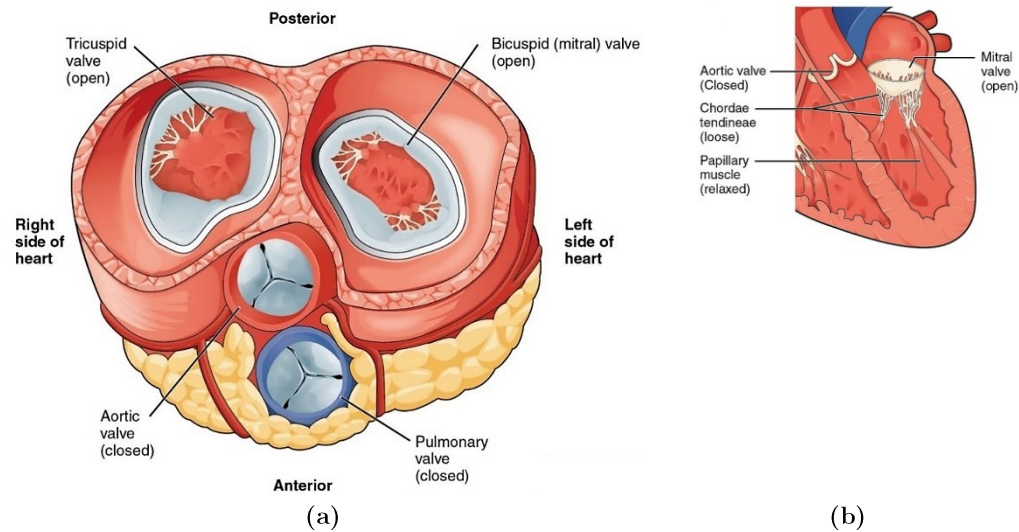


Figure 6. Internal anatomy of the heart: (a) transverse section (the atrioventricular valves are open, while the semilunar valves are closed); (b) frontal section (the aortic valve is closed to prevent blood backflow into the aorta, while the mitral valve is closed) [23].

The atria have superficial ear-shaped projections, known as auricles, that extend anteriorly and contribute to their filling with blood. Along the outer surface of the heart are grooves containing the coronary arteries, which supply blood to whole

cardiac muscle. These are the interatrial sulcus, placed between the atria, the two interventricular sulci that separate the ventricles anteriorly and posteriorly, and the coronary sulcus, placed between the atria and ventricles (see **Figure 7**).

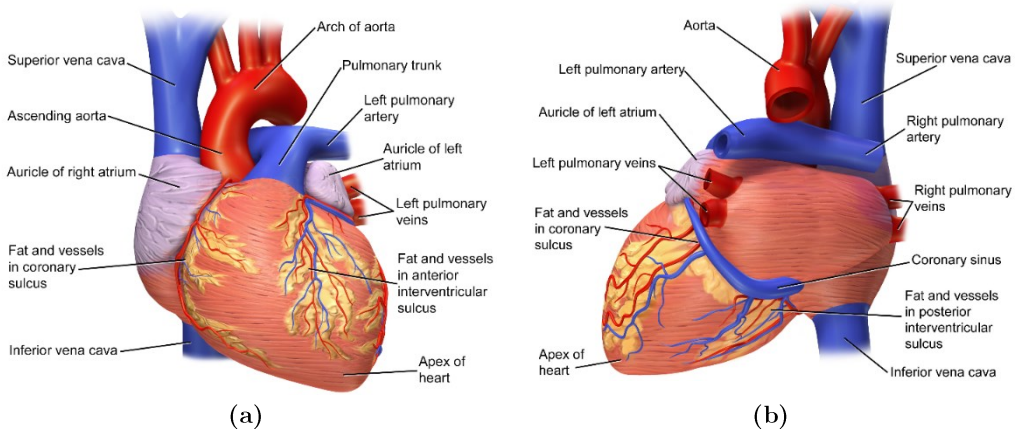


Figure 7. Auricles and coronary circulation of the heart: (a) anterior view [26]; (b) posterior view [27].

The heart wall consists of three continuous layers of varying thickness, that are, from the outside in, the epicardium, the myocardium and the endocardium (see **Figure 8**). As already mentioned, the epicardium protects the heart, while lubricating its external surface. The myocardium is the thickest layer of the heart, and its contraction is responsible for pumping blood. It is mainly composed of cardiac muscle cells, which are organized into bundles of fibers and arranged in spirals that form approximately two 8-shaped configurations, one wrapping around the atria and the other around the ventricles (see **Figure 9a**). The myocardium of the left ventricle is thicker than that of the right ventricle, even though they pump the same amount of blood. Moreover, the left ventricle must overcome a higher pressure to eject blood into the long systemic circulation, unlike the right one which propels blood into the short pulmonary circulation (see **Figure 9b**). The endocardium is made of epithelial tissue, which lines the cardiac chambers and covers the heart valves, and is linked to the myocardium by a thin layer of connective tissue.

2.2 THE HEART

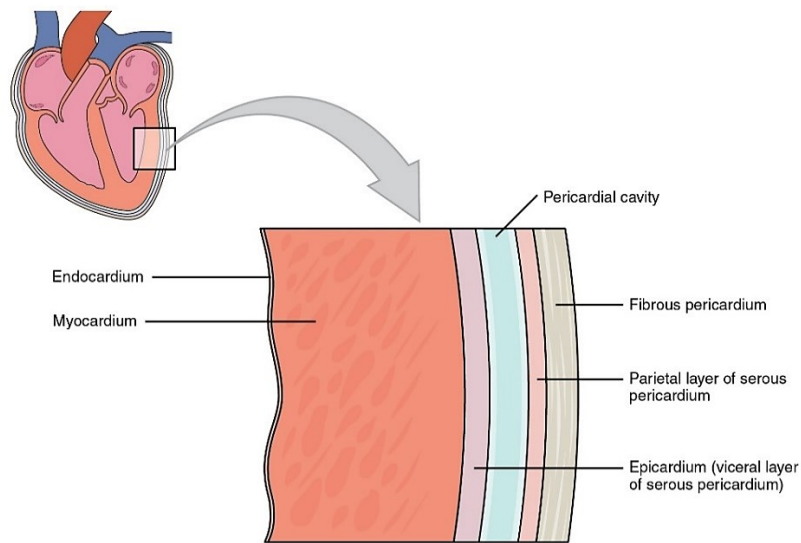
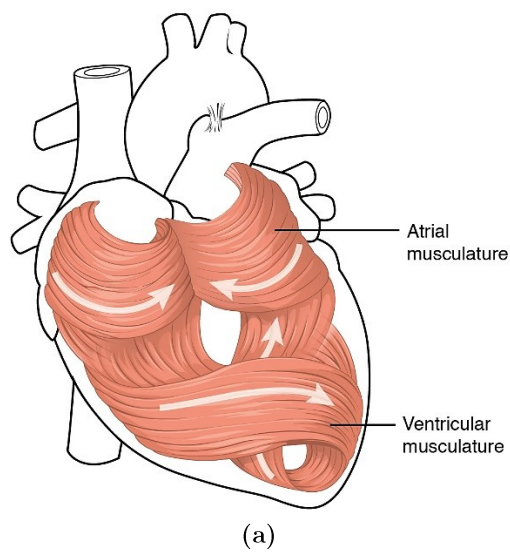


Figure 8. Heart wall. The heart wall consists of the epicardium (outer layer), the myocardium (middle layer) and the endocardium (inner layer) [23].



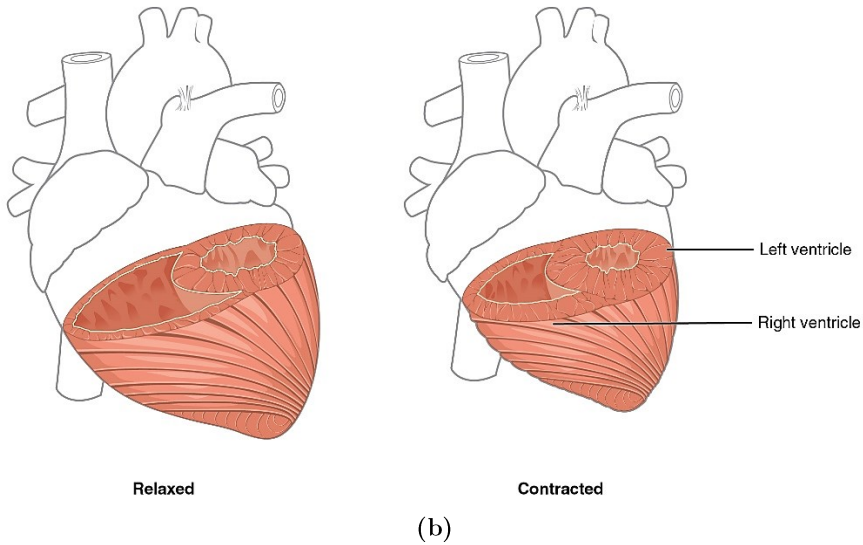


Figure 9. *The myocardium: (a) configuration of cardiac muscle fibers; (b) ventricular muscle thickness [23].*

2.2.3 The conduction system of the heart

Cardiac muscle cells, known as cardiomyocytes, can be grouped into two main types: contractile myocardial cells, which make up the 99% of the myocardium and are responsible for myocardial contraction, and conductive myocardial cells, which represent the remaining 1% of the myocardium and form the conduction system of the heart. Contractile cardiomyocytes undergo twitch-type contractions which mean contractions alternated with long refractory periods followed by short periods of relaxation. Relaxation allows the heart to fill with blood with every cardiac cycle. The long refractory period prevents tetanus, i.e., the involuntary contraction of the myocardium that would arrest the pumping action of the heart.

The conduction system of the heart is made up of specialized muscle cells, the conductive myocardial cells, which have the unique ability to self-excite, thus initiating the action potential, i.e., the depolarization wave that propagates from cell to cell throughout the myocardium triggering its mechanical contraction. This property is known as auto-rhythmicity. The conduction system of the heart consists of the sinoatrial (SA) node, the AV node, the AV bundle, the AV bundle branches, and the Purkinje fibers (see **Figure 10**). The SA node is in the right atrium, near

2.2 THE HEART

the orifice of the superior vena cava. The cells of the SA node spontaneously initiate the depolarizing electrical impulse, namely the sinus rhythm. For this reason, the SA node is often referred to as the natural pacemaker of the heart. The electrical impulse originating from the SA node propagates through all contractile myocardial cells of the atria, which start to contract almost simultaneously as a functional syncytium, until it reaches the AV node. This takes a time interval of about 50 ms. The AV node is located within the AV septum. In particular, the cardiac skeleton prevents the electrical impulse from spreading directly into the ventricles. From the AV node the electrical impulse takes approximately 100 ms to propagate into the AV bundle, also known as bundle of His. This allows the atrial syncytium to complete its contraction, while pumping blood into the ventricles. The AV bundle originates from the AV node, then passing into the upper portion of the interventricular septum where it is divided into right and left bundle branches. The bundle branches proceed downward to the apex. The electrical impulse takes approximately 25 ms to accomplish this path. Here, the bundle branches are connected to the Purkinje fibers, which travel upward along the external walls of the ventricles. The depolarization wave propagates throughout the entire ventricles in about 75 ms, which start to contract from the apex towards their upper portion, while pumping blood into the pulmonary trunk and aorta.

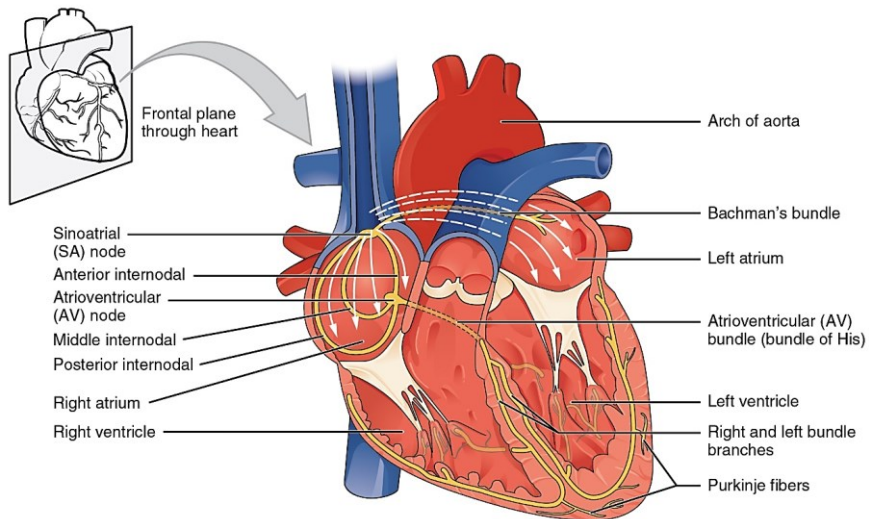


Figure 10. The conduction system of the heart. The conduction system of the heart consists of the SA node, the AV node, the AV bundle, the AV bundle branches, and the Purkinje fibers [23].

Contractile myocardial cells differ from conductive myocardial cells in the mechanism underlying the generation of an action potential.

Conductive myocardial cells own the property of auto-rhythmicity since they can generate an action potential without requiring an external stimulus. This can be explained as follows. The resting potential of a conductive myocardial cell is not stable. The presence of sodium (Na^+) channels allows the slow diffusion of Na^+ towards the intracellular material, which results in a spontaneous depolarization (also known as prepotential depolarization) of the membrane potential that rises from -60 mV to -40 mV. This value represents the threshold for triggering an action potential. At this moment, voltage-gated channels play an essential role. Indeed, calcium (Ca^{2+}) channels open and Ca^{2+} ions enter the cell, causing a further and more rapid depolarization of the membrane potential up to $+5$ mV. Afterwards, the Ca^{2+} channels close, while potassium (K^+) channels open. In this way, K^+ ions leave the cell, thus inducing the repolarization of the membrane potential which drops to the resting value of -60 mV. Next, K^+ channels close, while Na^+ channels open. Hence, a new prepotential depolarization starts (see **Figure 11**).

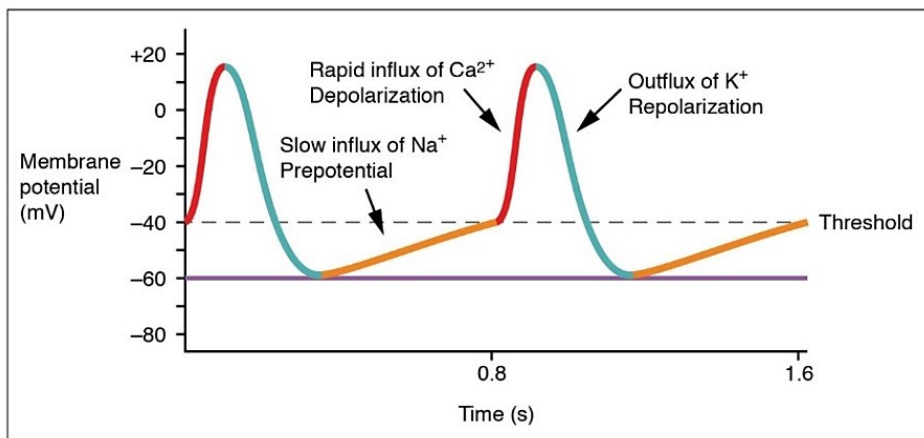


Figure 11. *The action potential of a conductive myocardial cell [23].*

Alternatively, a contractile myocardial cell shows a more stable resting potential of about -90 mV. In this case, the depolarization occurs more rapidly (it takes about 3–5 ms) due to the early opening of the Na^+ voltage-gated channels under the stimulation of an action potential. This results in a more rapid influx of Na^+ until

2.2 THE HEART

the membrane potential reaches +20 mV. At this moment, the Na^+ channels close, while Ca^{2+} channels and only few K^+ channels open. This allows Ca^{2+} to slowly enter the cell, while few K^+ ions exit. Therefore, the rapid depolarization phase is followed by a long refractory period. In particular, the slow diffusion of Ca^{2+} results in a plateau lasting about 175 ms. When the membrane potential reaches approximately 0 mV, Ca^{2+} channels close, while more K^+ channels open. Hence, K^+ ions leave the cell causing the repolarization of the membrane potential which drops until it reaches the resting level of -90 mV (it takes approximately 75 ms). It is worth mentioning that the long refractory period plays an essential role (it extends from the plateau to a portion of the repolarization period and has a duration of about 250 ms) in preventing premature contractions, so that the heart can pump the vital amount of blood (see **Figure 12**).

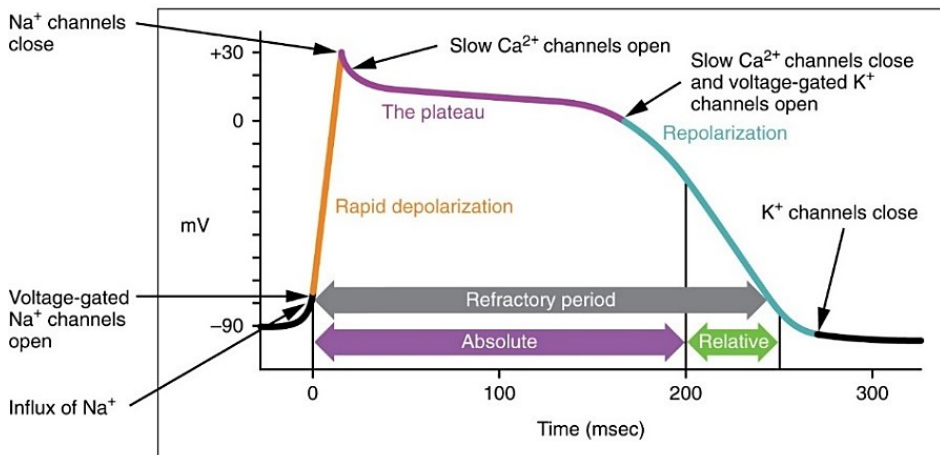


Figure 12. *The action potential of a contractile myocardial cell [23].*

2.2.4 The cardiac cycle

The cardiac cycle is the alternated and coordinated sequence of systoles and diastoles of atria and ventricles (triggered by the electrical activity of cardiomyocytes) that governs the major events of cardiac mechanics. The systole is the contraction of the heart during which it pumps blood, while the diastole is the relaxation of the heart during which it fills with blood. Atria and ventricles do not contract and relax

simultaneously. Indeed, when the atria are contracted, the ventricles are relaxed and vice versa. Therefore, in the cardiac cycle, a distinction can be made between atrial and ventricular systole, as well as between atrial and ventricular diastole. However, these events are closely related. The cardiac cycle is well described by the Wiggers' diagram reported in **Figure 13**, representing blood pressure and blood volume curves. Blood flows according to a pressure gradient, moving from areas of higher pressure to areas of lower pressure.

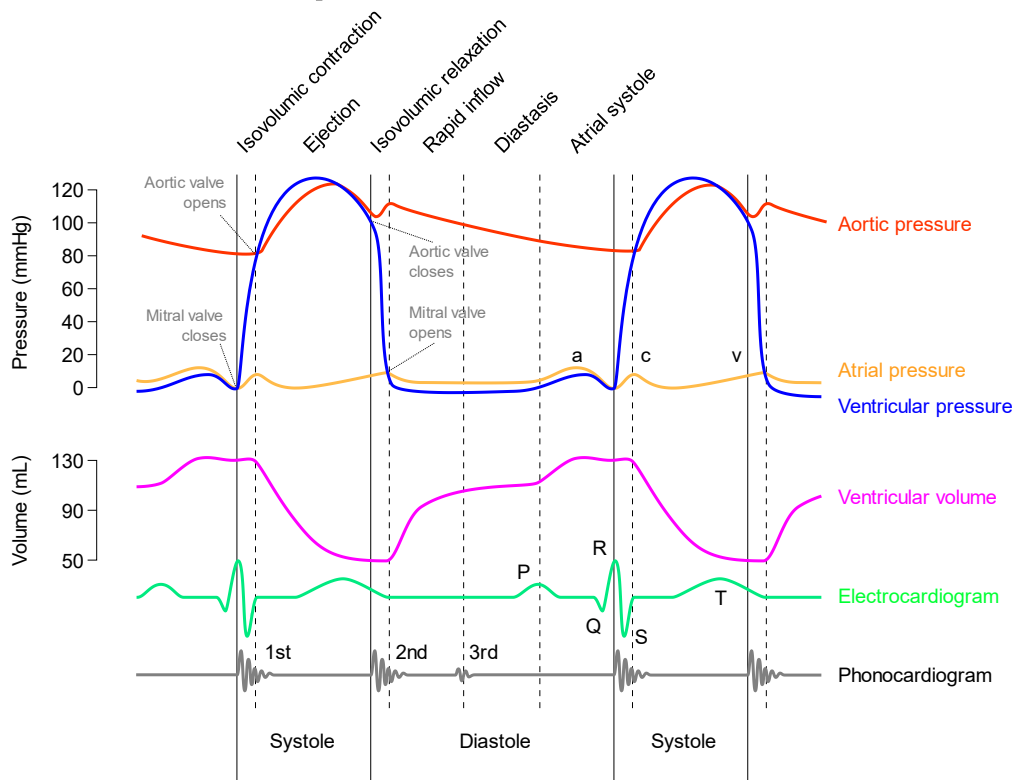


Figure 13. Wiggers' diagram showing blood pressure and blood volume curves along with Electrocardiography and Phonocardiography tracings [28].

At the beginning of the cardiac cycle, both atria and ventricles are relaxed. The AV valves (the tricuspid and mitral valves) and the semilunar valves (the pulmonary and aortic valves) are closed. The right atrium receives deoxygenated blood from the superior vena cava, the inferior vena cava and the coronary sinus, while the left atrium collects oxygenated blood from the pulmonary veins. When the intra-atrial

pressure exceeds the intra-ventricular pressure, the AV valves open, thus allowing blood to passively flow from the atria into the ventricles, while the two semilunar valves are still closed. This prevents regurgitation of blood from the pulmonary trunk and aorta into the ventricles, which are filled with blood to 70–80% of their total volume. This phase is referred to as rapid ventricular filling, during which a decrease in intra-atrial pressure can be observed. Then, both intra-atrial and intra-ventricular pressures rise as the atria and ventricles continue to slowly fill with blood. This phase is known as slow ventricular filling (also called diastasis). Afterwards, the atria start to contract (this event is referred to as atrial kick and marks the onset of atrial systole). As a result, blood is pumped into the ventricles which are completely filled. Blood volume in each ventricle at the end of diastole is known as end-diastolic volume (EDV) or preload. Next, the atria relax, while the ventricles start to contract (this is the onset of ventricular systole). The intra-ventricular pressure overcomes the intra-atrial pressure, and blood backflow causes the closure of AV valves. The ventricular systole is divided into two phases. In the first one, known as isovolumetric or isovolumic contraction, the intra-ventricular pressure is not high enough to induce the opening of the semilunar valves. Hence, the ventricles are closed until the intra-ventricular pressure reaches a certain value, thus inducing the opening of the semilunar valves. At this moment, the ventricles start to pump blood into the pulmonary trunk and aorta. This is the second phase of ventricular systole, namely the ejection phase, and is divided into rapid and slow ejection. The intra-ventricular pressure, as well as the pressure in the pulmonary trunk and aorta increase. When its maximum value is reached, the intra-ventricular pressure starts to decrease until it becomes lower than pressure in the pulmonary trunk and aorta. Blood flows back causing the closure of the semilunar valves (the well-known dicrotic notch can be observed in the pressure curve). Afterwards, the intra-ventricular pressure sharply drops, and the ventricular diastole occurs. Blood volume in each ventricle at the end of the systole is known as end-systolic volume (ESV) or afterload. The ventricular diastole is also divided into two phases. In the first one, namely the isovolumetric or isovolumic relaxation, the AV valves are closed, and the ventricles relax without changing their blood volume. The second phase occurs when the intra-atrial pressure exceeds the intra-ventricular pressure.

Hence, the AV valves open, and a new cycle starts. All phases of the cardiac cycle are represented in **Figure 14**.

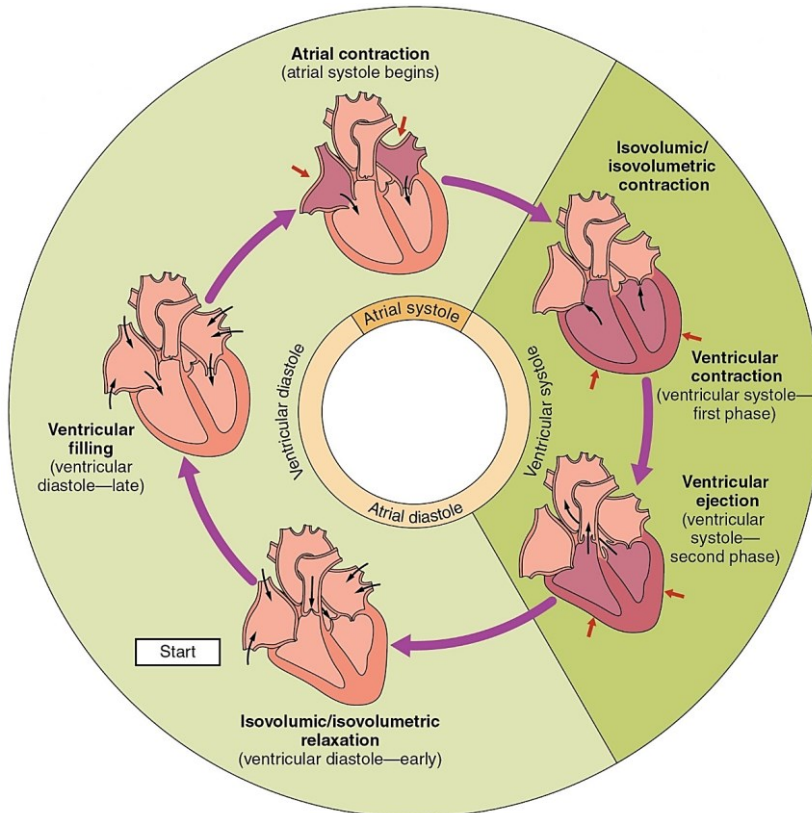


Figure 14. The cardiac cycle. The cardiac cycle is the alternated and coordinated sequence of contractions (systoles) and relaxation (diastoles) of atria and ventricles [23].

During the cardiac cycle, the heart contracts in response to the electrical impulse propagating along its conduction system. The action potential causes the depolarization of myocardial cells. This results in a charge separation and thus an electrical dipole, which induces a current to flow. Hence, the heart can be represented by a net equivalent current dipole (that is the sum of multiple current dipoles), of time-varying magnitude and orientation, due to the charge separation between depolarized and resting regions. Therefore, a potential due to a current flow can be measured. The electrocardiogram (ECG) is the measurement of this potential on the body surface. Generally, the ECG is acquired by measuring the potential

difference between two points along specific directions, called leads. The most common leads are acquired in the frontal plane and are referred to as lead I, II and III. An ECG lead I measures the potential difference between right arm and left arm. An ECG lead II measures the potential difference between right arm and left leg. An ECG lead III measures the potential difference between left arm and left leg. The ECG shows a waveform repeating over time (see **Figure 15**). It consists of characteristic waves related to the events in the cardiac cycle, that are P wave, corresponding to the depolarization of the atria, QRS complex (Q and S waves are negative deflections, while R wave is a positive deflection), corresponding to the depolarization of the ventricles, and T wave, corresponding to the repolarization of the ventricles. Atrial repolarization is masked by the QRS complex since it occurs simultaneously. For this reason, it cannot be identified in the ECG signal. Specifically, the atria start to contract approximately 25 ms after the onset of P wave, which has a normal duration of 80–100 ms. The contraction of the ventricles begins when the QRS complex reaches the peak of the R wave. Normally, the QRS complex lasts 60–100 ms.

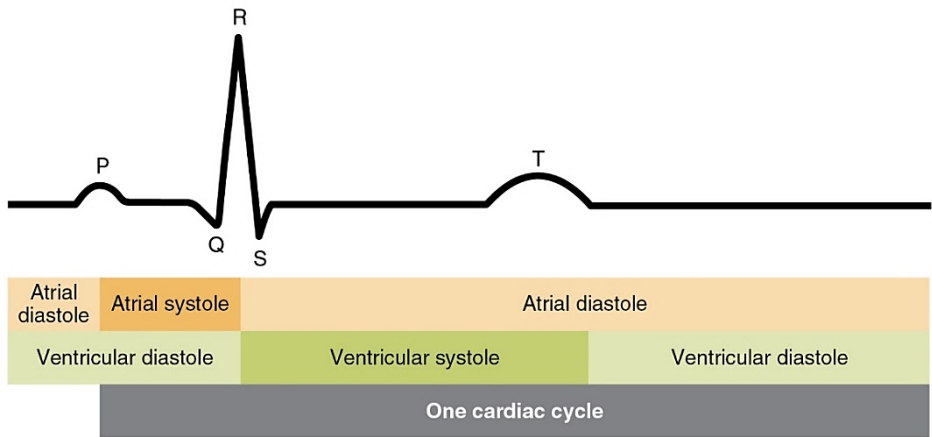


Figure 15. ECG waveform and its relation to the phases in the cardiac cycle [23].

Different intervals and segments of clinical relevance can be identified in the ECG signal, as shown in **Figure 16**. A segment is a portion of the signal between two waves, while an interval is the duration of a portion of the signal that includes a segment and one or more waves. In particular, the PR segment is the portion of the

signal from the end of P wave to the onset of QRS complex. The PR interval is the time interval from P wave to the onset of QRS complex. A normal PR interval is in the range 120–200 ms. The QT interval is the time interval from Q wave to the onset of T wave. Its normal range is 350–440 ms. The ST segment is the portion of the signal from the end of S wave to the beginning of T wave. Finally, due to the prominence of R wave in ECG signal, the R-R interval is commonly used to express the duration of the cardiac cycle (for more details see Section 3.1.1).

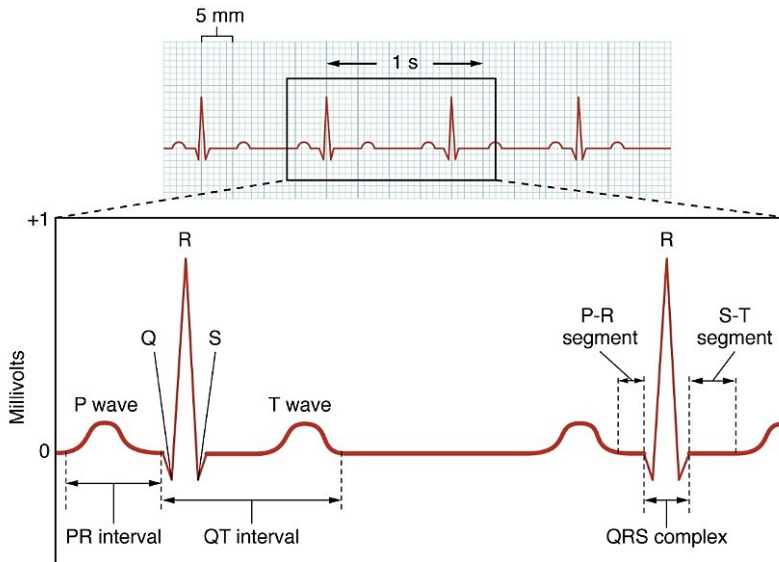


Figure 16. ECG waves, intervals and segments [23].

2.3 Physiological parameters

The following is a brief description of the most relevant cardiac physiological parameters.

2.3.1 Heart rate

Heart rate (HR) is the number of contractions (also known as beats) that the heart accomplishes in 1 minute. It is measured in beats per minute (bpm). Under physiological conditions, the normal resting HR of an adult is in the range 60–100 bpm, with a mean value of approximately 70 bpm. Although the sinus rhythm is

regulated by the pacemaker cells of the SA node, HR is also modulated by the Central Nervous System (CNS). It is influenced by several factors, such as age, gender, exercise, stress, sleep, body temperature, pH, drugs, and any other factor that can affect the Sympathetic or Parasympathetic Nervous System. Indeed, stimulation to the Sympathetic Nervous System (SNS) results in increased permeability of cardiomyocytes to Ca^{2+} , thus causing an increase in the firing rate of SA pacemaker, referred to as positive chronotropic effect. On the contrary, stimulation to the Parasympathetic Nervous System (PNS) results in increased permeability of cardiomyocytes to K^+ , thus causing a decrease in the firing rate of SA pacemaker, referred to as negative chronotropic effect. Moreover, SNS and PNS also regulate the conduction velocity of the action potential along the conduction system of the heart.

2.3.2 Stroke volume

Stroke volume (SV) is the volume of blood pumped by the left ventricle per contraction. Generally, it is obtained as follows:

$$SV = EDV - ESV \quad (1)$$

where EDV is the end-diastolic volume (or preload) and ESV is the end-systolic volume (or afterload). SV is the same for right and left ventricles. However, the left ventricle is assumed as the reference. SV is affected by several factors, such as gender, heart size, systolic time intervals, preload, afterload, exercise. For a healthy 70 kg male, the mean SV is approximately 70 mL (EDV is about 120 mL, while ESV is about 50 mL).

Preload, afterload and contractility are the parameters that primary affect SV. As already mentioned, preload and afterload are alternative ways of indicating EDV and ESV, respectively. Preload refers to the level of stretching of ventricular cardiomyocytes prior to contraction which varies according to ventricular filling. Indeed, shorter filling time results in decreased EDV and preload. Afterload is the tension that the ventricles must overcome to open the semilunar valves and pump blood against the resistance in the vascular system. Furthermore, contractility is the

ability of the myocardium to contract, that is the function responsible for both the force and velocity of contraction. Preload, afterload and contractility are intimately related. The relationship between SV and preload is described by the Frank-Starling law, which states that, under physiological conditions, an increase in preload results in increased SV. This mechanism ensures that the blood volume pumped by the heart is the same of that entering the atria and ventricles. However, an excessive increase in preload does not result in increased SV. Moreover, an increase in afterload reduces the ability of the ventricles to eject blood which results in decreased SV and increased ESV. Furthermore, even an increase in myocardial contractility results in enhanced SV. Hence, a greater amount of blood is ejected, which determines a decrease in ESV. Factors that cause an increase in myocardial contractility are called positive inotropic factors, while those that cause a decrease in myocardial contractility are called negative inotropic factors.

Moreover, SV and EDV are useful for the computation of the left ventricular ejection fraction (LVEF) that is the fraction of blood volume pumped by the left ventricle per contraction. LVEF is expressed as follows:

$$LVEF = \frac{SV}{EDV} \cdot 100 = \frac{EDV - ESV}{EDV} \cdot 100 \quad (2)$$

For a healthy 70 kg male, the mean LVEF is approximately 58%. Its normal range is 55–65%.

2.3.3 Cardiac output

Cardiac output (CO) is the volume of blood pumped by the left ventricle in 1 minute. It is measured in mL per minute (mL/min). CO is related to HR and SV according to the following equation:

$$CO = HR \cdot SV \quad (3)$$

Since it is a function of HR and SV, CO is affected by the same factors that influence these two parameters. Dependence on SV, governed by the Frank-Starling law, guarantees equivalent CO for right and left ventricles. Moreover, under physiological

conditions, when HR increases, SV and CO initially do not change. However, further increase in HR results in shorter filling time and decreased SV and CO.

The normal resting CO of an adult is in the range 4–8 L/min, with a mean value of approximately 5.25 L/min (this value is obtained from the equation (3) by considering a mean HR of 75 bpm and a mean SV of 70 mL). During exercise, CO can increase up to a maximum value. The difference between maximum and resting value of CO is known as cardiac reserve. To account the dependence on body size and weight, CO is often expressed as a cardiac index (CI) according to the following equation:

$$CI = \frac{CO}{BSA} \quad (4)$$

where BSA is the body surface area in m². A normal CI is within 2.5–4.3 L · m²/min.

2.3.4 Blood flow

Blood flow (BF) is the volume of blood that travels through blood vessels in a time unit. It is measured in mL per minute (mL/min). Blood flows according to a pressure gradient, moving from areas of higher pressure to areas of lower pressure. BF in the heart is primarily laminar. Blood is pumped into large arteries originating from the heart. From these, it passes into smaller arteries, then into arterioles until it reaches capillaries of body tissues. Capillaries connect smaller arterioles to smaller veins. Indeed, blood from capillaries is drained into venules, veins and then into large veins returning to the heart (see **Figure 17**).

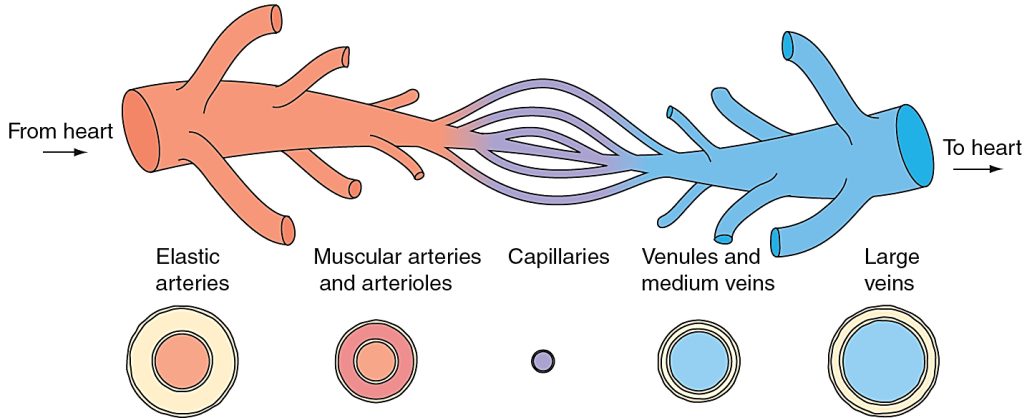


Figure 17. *Blood vessels. Blood from the heart flows through arterics, arterioles and capillaries towards body tissues; blood from body tissues flows through capillaries, venules and veins towards the heart [24].*

Blood vessels are hollow structures that, except for capillaries, share the same features. Their cavity, known as lumen, represents the pathway through which blood flows. As shown in **Figure 18a**, arteries have thicker walls than veins, as well as smaller lumen since they are located closer to the heart, thus transporting blood at higher pressure. Their lumen has round-shaped cross section. On the contrary, veins have a lumen with flattened cross-section and larger diameter. Blood vessels wall consists of three different layers, namely tunics, that are the tunica intima, the tunica media and the tunica externa (see **Figure 18b**). The tunica intima is a thin layer of epithelial and connective tissues. The tunica media is made of smooth muscle cells and connective tissue, and generally is the thickest layer in arteries. Contraction and relaxation of smooth muscle cells, specifically in arteries, result in vasoconstriction (i.e., decrease in lumen diameter) and vasodilation (i.e., increase in lumen diameter), respectively, thus causing an increase or decrease in blood flow. The tunica externa, also known as tunica adventitia, is a protective layer of connective tissue that generally represents the thickest layer in veins.

2.3 PHYSIOLOGICAL PARAMETERS

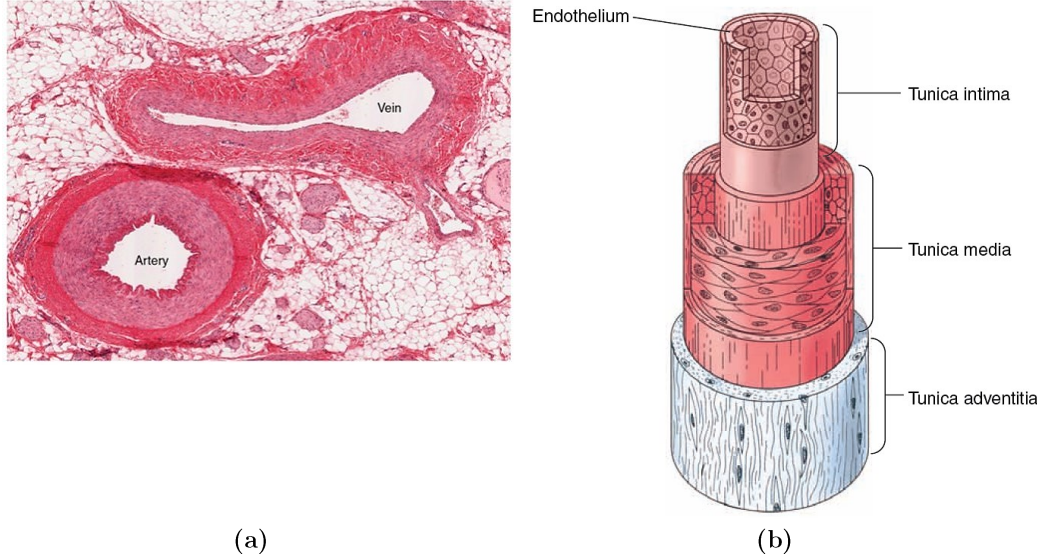


Figure 18. Structure of a blood vessel: (a) comparison between artery and vein lumen [23], (b) the tunics of blood vessel wall [24].

BF can be expressed as follows:

$$BF = \frac{\Delta P}{R} \quad (5)$$

where ΔP is the pressure difference (mmHg) between the inlet and outlet of a blood vessel, and R is the resistance to flow (mmHg \cdot min/L) due to friction between blood and blood vessel wall. Resistance also takes into account blood viscosity.

Blood vessels can be considered approximately as cylinders. Under this assumption, their resistance is described by the Poiseuille law according to the following equation:

$$R = \frac{8L\eta}{\pi r^4} \quad (6)$$

where L is the vessel length, η is the blood viscosity and r is the internal radius of the vessel.

Hence, by combining equation (5) and (6), blood flow can be expressed as follows:

$$BF = \Delta P \frac{\pi r^4}{8L\eta} \quad (7)$$

Therefore, BF is affected by the pressure difference (ΔP), the internal radius of the vessel (r), the length of the vessel (L), and the blood viscosity (η). Of these, L and η cannot be regulated, r varies according to the type of vessel and under vasoconstriction or vasodilation conditions, and ΔP must guarantee that the arterial pressure is greater than the venous pressure so as to allow blood flow.

For a more accurate description, other factors affecting vascular resistance, such as blood vessel compliance, distensibility and stiffness, should be considered.

2.3.5 Blood pressure

Blood pressure (BP) is the force exerted by blood on the inner walls of blood vessels. Generally, if not specified, it refers to pressure in the arteries of systemic circulation (i.e., arterial blood pressure). BP is measured in mmHg. It oscillates between a maximum and a minimum value according to the phases of the cardiac cycle. During the systole, the heart contracts, thus pumping blood into arteries. As a result, BP reaches its highest value, i.e., the systolic blood pressure (SBP). A normal SBP is less than 140 mmHg. On the contrary, during the diastole, the heart relaxes, and BP drops until it reaches its lowest value, i.e., the diastolic blood pressure (DBP). A normal DBP is less than 90 mmHg. For this reason, blood pressure measurements always report two values, the higher corresponding to the SBP and the lower corresponding to the DBP. A typical arterial blood pressure waveform is represented in **Figure 19**. Its positive peak indicates the SBP, while its negative peak refers to the DBP. The upstroke and downstroke of the waveform are related to myocardial contractility and systemic vascular resistance (SVR), respectively. The incisura, known as dicrotic notch, is due to the closure of the aortic valve and its position provides information on SVR. The area under the curve is an estimate of SV.

2.3 PHYSIOLOGICAL PARAMETERS

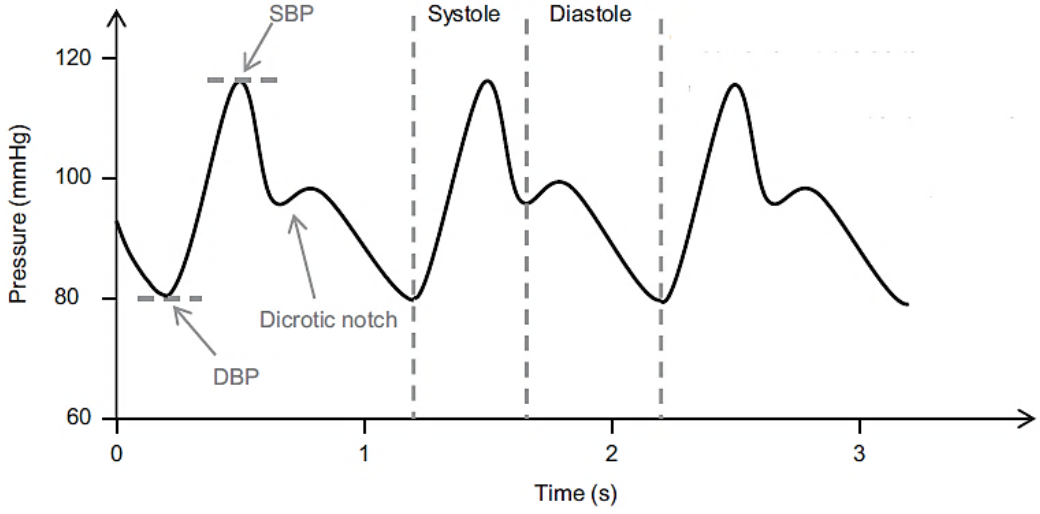


Figure 19. Typical arterial blood pressure waveform [29].

The mean of SBP and DBP during the cardiac cycle is the mean arterial blood pressure (MAP), which represents the time-weighted average arterial blood pressure. It can be computed as follows:

$$MAP = DBP + \frac{SBP - DBP}{3} \quad (8)$$

MAP is considered a good indicator of tissue perfusion. Its normal range is 70–110 mmHg.

Furthermore, BP can be calculated according to the following equation:

$$BP = CO \cdot SVR \quad (9)$$

where CO is the cardiac output and SVR is the systemic vascular resistance, that is the resistance offered by the vasculature to flow.

Furthermore, pulse pressure is the difference between SBP and DBP.

2.3.6 Pulse

Pulse refers to the elastic outward and inward movements of arterial walls, induced by their expansion and recoiling during systoles and diastoles due to an increase in local blood pressure caused by blood surge, which result in a pressure wave that propagates throughout the whole arterial system. These tiny movements can be manually perceived by a practice known as palpation. However, their intensity decreases with distance. Pulse is a good estimator of HR. For this reason, the pulse rate is measured in bpm. Even the pulse strength provides valuable information since it is an estimate of CO. A strong pulse indicates high SBP, while a weak pulse indicates low SBP. The pulse can be palpated by placing the fingertips on the skin above a superficial artery and applying a light pressure. Commonly, it is palpated from the radial artery at the wrist and the carotid artery at the neck. However, there are multiple pulse sites on the human body, as reported in **Figure 20**.

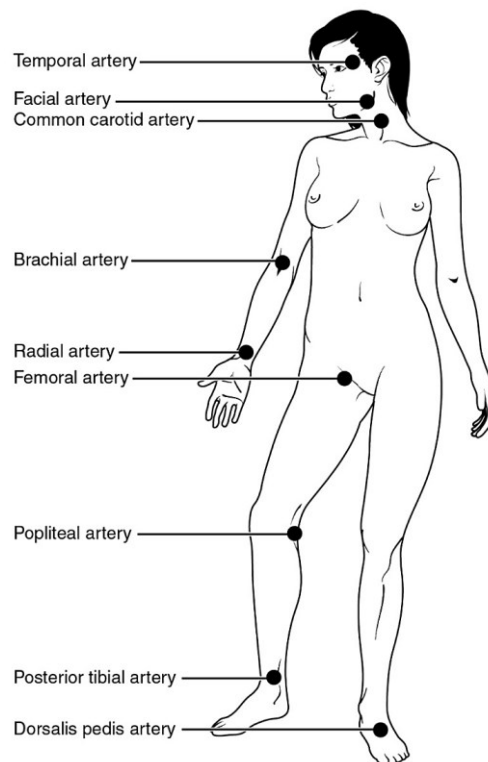


Figure 20. Pulse sites on the human body [23].

2.3.7 Heart sounds

The mechanical activity of the heart produces vibrations audible to the human ear by auscultation, known as heart sounds. Four normal heart sounds can be identified, as represented in **Figure 21**, along with pressure curves.

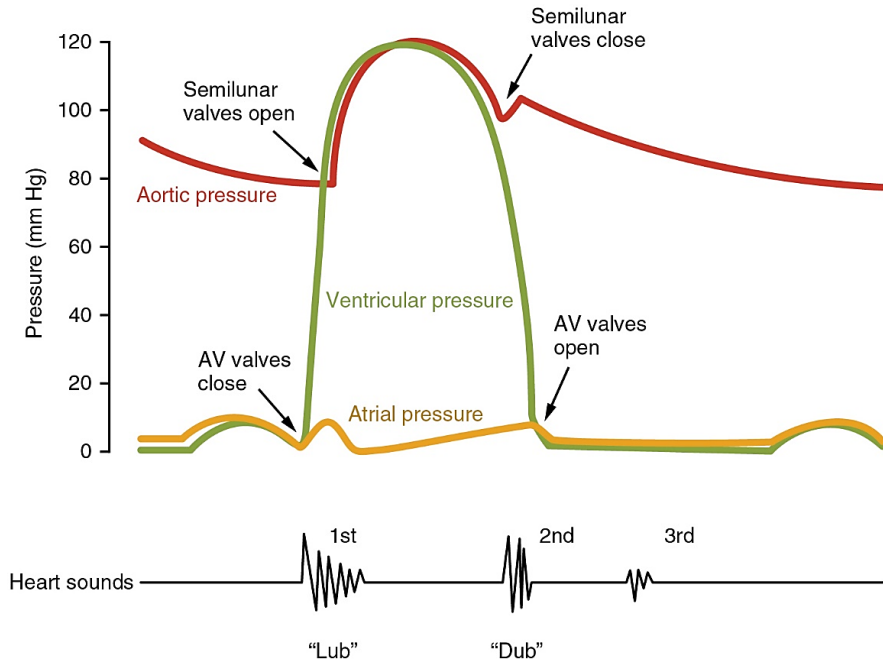


Figure 21. Heart sounds recording along with pressure curves [23].

The first heart sound (S_1) is caused by the closure of the atrioventricular valves during ventricular systole, specifically by the closure of the mitral valve followed by the closure of the tricuspid valve, and can be described by the onomatopoeic “lub”. The second heart sound (S_2) is associated with the closure of the semilunar valves during ventricular systole, particularly it is due to the closure of the aortic valve followed by the closure of the pulmonary valve, and can be described by the onomatopoeic “dub”. The physiological third heart sound (S_3) is a low-pitched sound produced by the rapid ventricular filling and can be heard in children, adolescents and young adults. If heard in people over 30 years of age, it is referred to as “Kentucky gallop” and could be a sign of a cardiovascular disease. The physiological fourth heart sound (S_4) is a soft, low-pitched sound caused by rapid ventricular

filling during atrial systole and is generally heard in infants, young children and people over 50 years of age. A pathological S_4 is referred to as “Tennessee gallop”. Furthermore, murmurs represent abnormal heart sounds caused by turbulent blood flow under pathological conditions. The graphical representation of heart sounds recording is known as phonocardiogram (for more details see Section 3.2.1).

2.3.8 Cardiac time intervals

Cardiac time intervals (CTIs) represent the temporal distance between the major events in the cardiac cycle, such as heart valves opening and closure, ventricular emptying and filling, etc. They provide valuable information for the assessment of cardiac function. CTIs can be divided into systolic and diastolic time intervals.

Systolic time intervals (STIs) are:

- S_1 – S_2 , defined as the time interval between mitral valve closure (i.e., 1st heart sound) and aortic valve closure (i.e., 2nd heart sound);
- total systolic time (TST), defined as the time interval from the Q wave in the ECG to aortic valve closure;
- electromechanical delay (EMD), defined as the time interval from the Q wave in the ECG to mitral valve closure;
- pre-ejection period (PEP), defined as the time interval from the Q wave in the ECG to aortic valve opening;
- left ventricular ejection time (LVET), defined as the time interval between aortic valve opening and closure;
- isovolumetric contraction time (IVCT), defined as the time interval from mitral valve closure to aortic valve opening;

Furthermore, the ratio PEP/LVET is referred to as contractility coefficient.

Diastolic time intervals (DTIs) are:

- left ventricular filling time (LVFT), defined as the time interval between mitral valve opening and closure;
- rapid ventricular filling time (RVFT), defined as the time interval from mitral valve opening to the rapid filling phase;

2.3 PHYSIOLOGICAL PARAMETERS

- isovolumetric relaxation time (IVRT), defined as the time interval from aortic valve closure to mitral valve opening (see **Figure 22**).

Finally, myocardial performance index (MPI) is defined as the ratio $(IVCT + IVRT)/LVET$ [30]-[33].

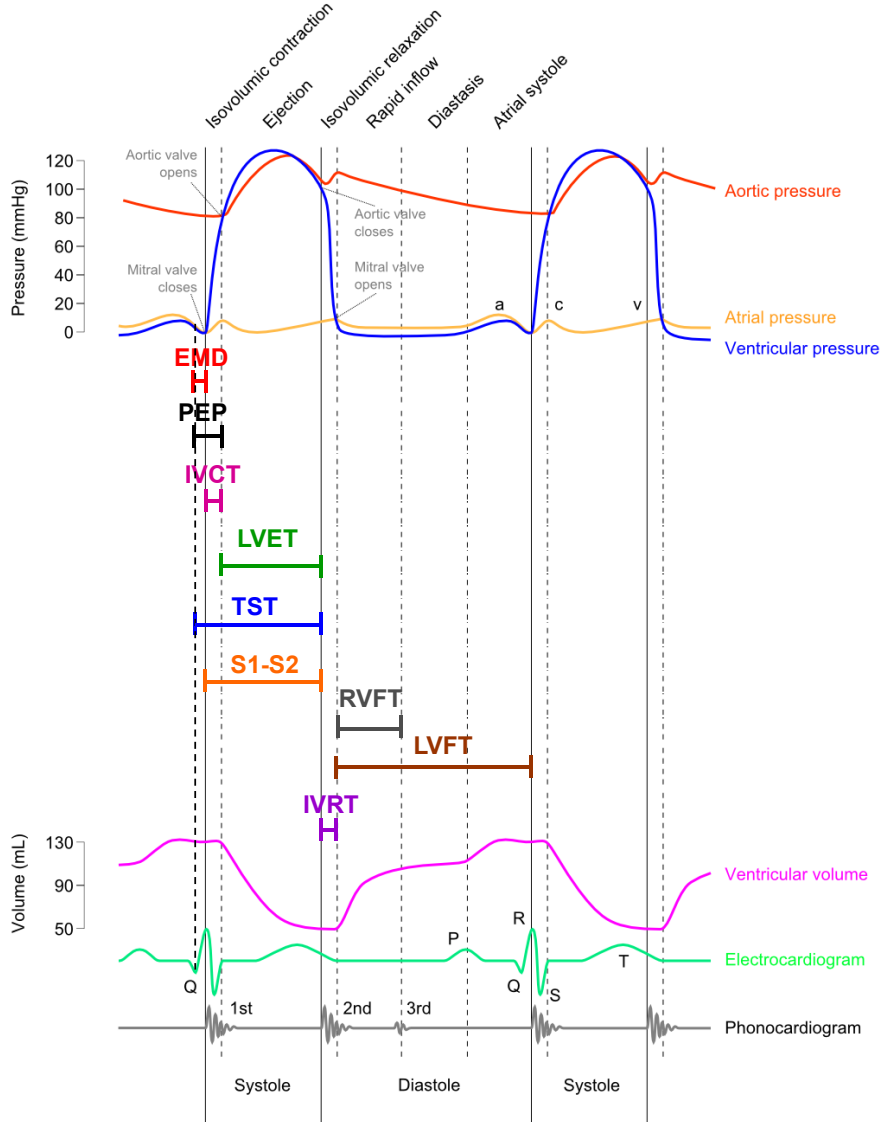


Figure 22. Representation of cardiac time intervals on Wiggers' diagram, along with Electrocardiography and Phonocardiography tracings [28].

2.4 Pathologies of the cardiovascular system

Cardiovascular diseases (CVDs) are the leading cause of death worldwide. According to the World Heart Federation (WHF), 18.6 million people globally die of CVD every year, with a 24 % increase in incidence from 2000 to 2019, accounting for 33 % of all global deaths. Of these, 1 in 3 CVD deaths occur in people under 70 years of age, 85 % of CVD deaths are due to heart attack and stroke, and more than 75 % of CVD deaths occur in low- and middle-income countries [1].

The following is a brief description of the main CVDs.

- Coronary artery disease is a pathological condition caused by the occlusion of a coronary artery due to the presence of an atherosclerotic plaque within the walls of the artery, which results in reduced blood flow to tissues, known as ischemia, and insufficient oxygen supply, known as hypoxia. If not treated, coronary artery disease can lead to myocardial infarction.
- Myocardial infarction or heart attack is the death of cardiac muscle cells due to the occlusion of a coronary artery (i.e., coronary artery disease) or thrombosis (i.e., presence of a blood clot) of atherosclerotic origin.
- Stroke is a brain injury due to arterial occlusion, referred to as ischemic stroke, or hemorrhage, referred to as hemorrhagic stroke. This results in the absence of oxygen supply to the brain region perfused by the blocked artery, with subsequent impairment of its function.
- Heart failure is a chronic condition due to reduced CO, with subsequent diminished circulating blood and thus nutrients supply to body tissues. It can be classified into heart failure with reduced ejection fraction (LVEF is lower than 40 %), also known as systolic heart failure, or heart failure with preserved ejection fraction, also known as diastolic heart failure. The former is primarily caused by a reduction in myocardial contractility, while the latter by a reduction in ventricular compliance.

2.4 PATHOLOGIES OF THE CARDIOVASCULAR SYSTEM

- Cardiomyopathy is a chronic condition characterized by an alteration in the heart anatomy (generally its enlargement, thickening or rigidity), which results in reduced ability to pump blood.
- Heart valve stenosis is a chronic condition due to rigidity or even calcification of a valve, which results in the obstruction of forward blood flow. Its most common causes are congenital factors, trauma or diseases.
- Heart valve regurgitation is a chronic condition due to the failure of a valve in its closure mechanism which results in backward blood flow. Its most common cause is the valve prolapse (probably due to damaged or broken chordae tendineae).
- Arrhythmias are alterations in normal heart rhythm. Among these, bradycardia is characterized by an HR lower than 60 bpm, while tachycardia is characterized by an HR greater than 100 bpm. Some others are characterized not only by alteration in the heart rhythm, but also in the pacemaker site and the conduction pathway, such as atrial fibrillation, atrial flutter, ventricular tachycardia, ventricular fibrillation, AV blocks.



Chapter 3

Cardiac monitoring techniques

This chapter illustrates the main techniques for non-invasive cardio-mechanical monitoring. Before, a brief description of three well-established techniques, namely Electrocardiography, Echocardiography and Impedance cardiography, is provided since they are commonly regarded as references for the characterization of cardio-mechanical signals.

3.1 Reference techniques

Electrocardiography, Echocardiography and Impedance cardiography are three well-established techniques in clinical practice for heart monitoring and diagnosis of CVDs. Electrocardiography measures the electrical activity generated by the heart, which triggers its mechanical contraction. It is generally used as a reference in providing the timings of cardiac cycle events. Echocardiography produces images of the heart; therefore, it enables the visualization of cardiac events (e.g., opening and closure of heart valves) almost in real-time, and the analysis of blood flow through the heart and great vessels, providing useful information for the estimation of hemodynamic parameters. Impedance cardiography measures changes in thoracic electrical impedance due to blood volume variations, thus allowing the estimation of hemodynamic parameters. The following is a brief description of these techniques, even if their discussion is beyond the scope of this thesis.

3.1.1 Electrocardiography

Electrocardiography (ECG) is a non-invasive technique that measures the electrical activity generated by the heart on the body surface. A recording of this electrical activity is known as electrocardiogram. As described in Section 2.2.4, the cardiac electrical activity arises from the depolarization of myocardial conductive cells. Electrical events precede and trigger the mechanical contraction of the myocardium. Therefore, abnormalities in cardiac electrical pattern can reveal signs of heart dysfunction and provide clinical evidence for the diagnosis of CVDs. The heart can be viewed as a net equivalent current dipole due to the presence of charge separation between active (i.e., depolarized) and inactive (i.e., repolarized or resting) regions that induces a current to flow. The current dipole can be represented by a vector of time-varying magnitude and orientation, pointing to the propagation direction of an action potential along the conduction pathway. If two electrodes are placed at two points on the body surface, a potential difference can be measured between them, which represents the projection of the cardiac vector along a specific direction, known as lead. In the early 1900, Einthoven provided a standardization for bipolar electrodes placement by considering three specific directions, namely lead I, between right arm and left arm, lead II, between right arm and left leg, and lead III, between left arm and left leg. These leads form the well-known Einthoven triangle with the heart placed in its center (see **Figure 23**). Moreover, a further electrode is commonly placed on the right leg and used as reference point for the biopotential amplifier to reduce common mode electrical noise. Einthoven is also credited with the nomenclature of the characteristic waves composing a normal ECG tracing. These are the positive P wave, which represents the depolarization of the atria, the QRS complex, which consists of an upward deflection (the R wave) between two downward deflections (the Q and S waves) and is due to the depolarization of the ventricles, and the positive T wave, which represents the repolarization of the ventricles (see **Figure 15** and **Figure 16** in Section 2.2.4) [3],[35]-[36].

ECG is a valuable tool for heart monitoring and diagnosis of many CVDs, such as arrhythmias, myocardial infarction, cardiomyopathies, which result in alterations of normal heart rhythm and typical ECG waveform. As an example, ST segment elevation is associated with myocardial infarction, while ST segment depression

could be a sign of myocardial ischemia [3]. Different ECG applications are well-established in clinical practice, such as: standard 12-lead ECG system, which allows the recording of 12 different ECG leads with 10 electrodes (consisting of the three leads defined by Einthoven, the three unipolar augmented leads due to Goldberger and the six unipolar precordial leads introduced by Wilson [36]), thus providing cardiologists with a representation of the heart electrical activity from different perspectives and supporting diagnosis with a more comprehensive dataset; exercise or stress ECG during which the physical exercise (e.g., via a treadmill) can induce ischemia, not presence at rest, and therefore is very useful for the diagnosis of coronary artery disease; dynamic ECG, also known as Holter, which allows continuous heart monitoring, usually up to 72 h, for the diagnosis of arrhythmias.

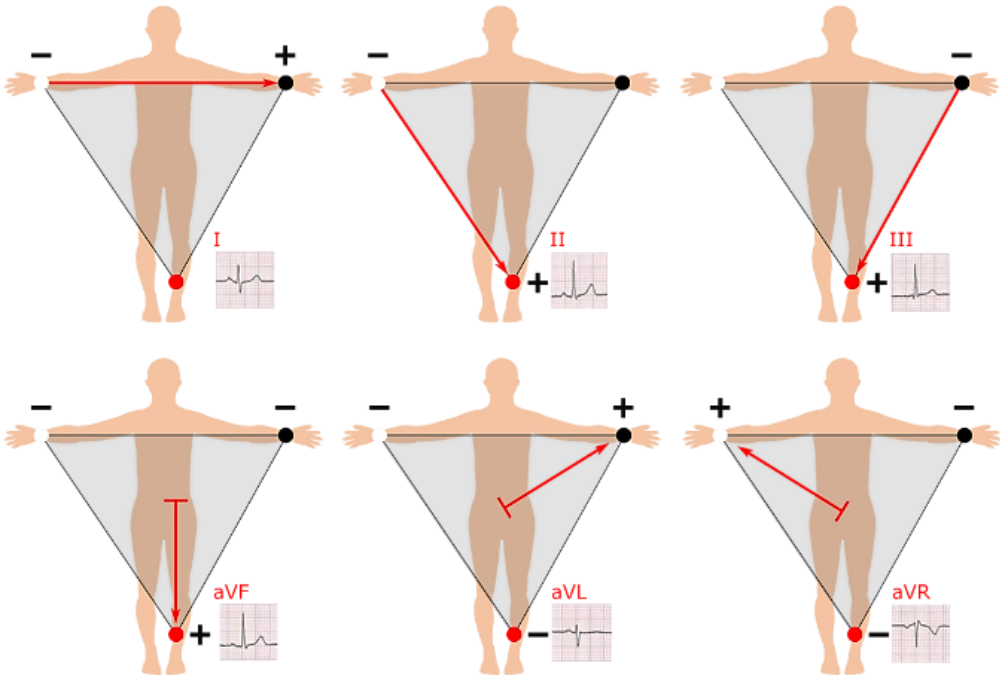


Figure 23. Einthoven's triangle. I, II and III indicate the ECG bipolar leads defined by Einthoven. aVF, aVL and aVR indicate the ECG augmented unipolar leads due to Goldberger [37].

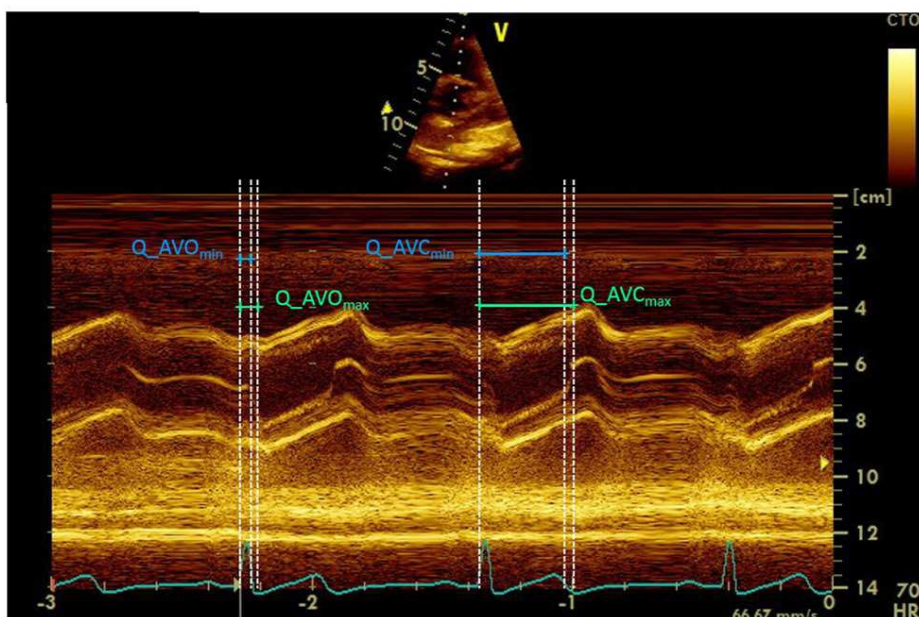
However, ECG is not well suited to long-term monitoring, especially in home environment, and early diagnosis of CVDs since electrical alterations often occur when the pathological condition is in an advance state. Therefore, the ECG examination is often combined with other clinical tests to perform a deeper

investigation and obtain a more complete clinical picture [3]. Moreover, electrical risks must be taken into account [5].

ECG signal is commonly adopted as a reference for the characterization of cardio-mechanical signals. Since electrical events trigger the mechanical contraction of the myocardium, they provide for temporal localization of mechanical events during the cardiac cycle. Moreover, the ECG characteristic waves, especially the Q wave representing the onset of ventricular depolarization, are widely used for the estimation of CTIs.

3.1.2 Echocardiography

Echocardiography (ECHO) is a diagnostic imaging technique that uses sound waves at frequencies above the human hearing threshold (i.e., 20 kHz), known as ultrasound (US), to produce images of the heart. The US probe consists of piezoelectric transducers that emit US waves through the thorax, towards the heart, and detect reflected waves returning to the probe, referred to as echoes. The time a reflected wave takes to return to the probe is proportional to the distance of the reflective structure from the receiver. Reflection is due to discontinuity at the interface between tissues of different density. To obtain high-quality images, a right trade-off between frequency and penetration depth must be found. Frequency is inversely related to wavelength. If frequency increases, wavelength decreases, and therefore spatial resolution (i.e., the minimum distance at which two distinct structures can be recognized as separated) improves. However, as frequency increases, the depth of US penetration into tissues decreases. Hence, it is fundamental to set a proper frequency according to the structure to be investigated. There are several modalities to perform echocardiographic examinations. Among them, M-mode produces a sequence of images over time, along a specific direction, thus enabling the visualization of the movement of cardiac structures (e.g., heart chambers and valves) almost in real-time, while also providing information about their morphology (e.g., shape, size, wall thickness). This supports the diagnosis of CVDs, such as cardiomyopathies, myocardial infarction, heart valve diseases. When combined to ECG, it provides the timings of mechanical events (e.g., opening and closure of heart valves) within the cardiac cycle (see **Figure 24a**). Moreover, EDV



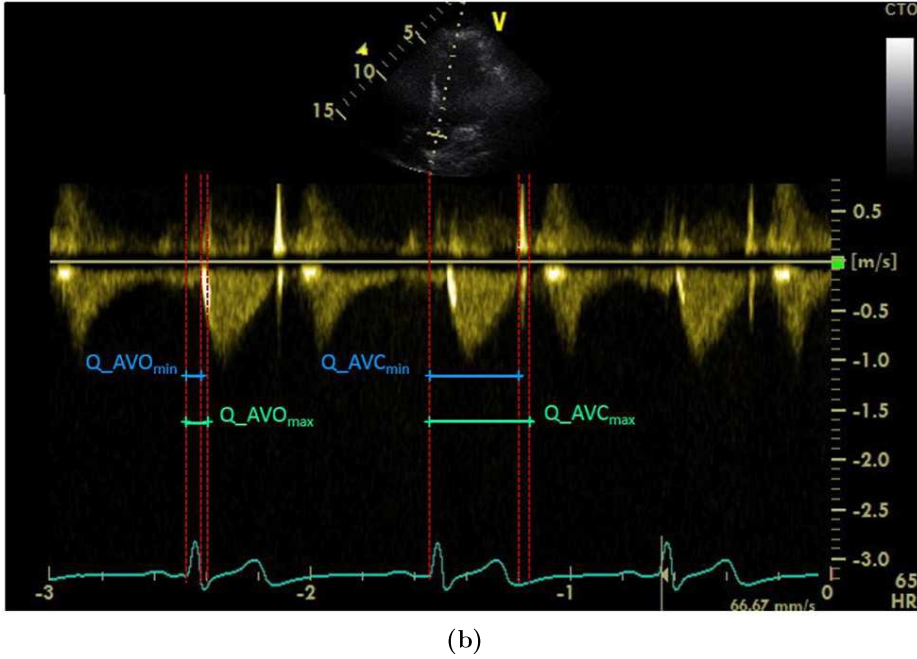


Figure 24. Examples of ECHO images: (a) M-mode; (b) Blood flow from ECHO Doppler. AVO and AVC indicate aortic valve opening and closure events, while MVO and MVC indicate mitral valve opening and closure events. Max and min subscripts represent the start and the end points of ECHO ranges for these events [38].

3.1.3 Impedance cardiography

Impedance cardiography (ICG) is a non-invasive technique that measures changes in thoracic electrical impedance due to blood volume variations during the cardiac cycle. As represented in **Figure 25**, ICG systems are typically based on 4 band electrodes, divided into 2 current or input electrodes and 2 voltage or output electrodes, which are placed around the neck (the current electrode is mounted above the voltage electrode) and the upper abdomen (the current electrode is fixed below the voltage electrode). An alternating current of low intensity (e.g., 4 mA) and high frequency (e.g., 100 kHz) is impressed to flow through the current electrodes and a time-varying voltage is measured by the voltage electrodes.

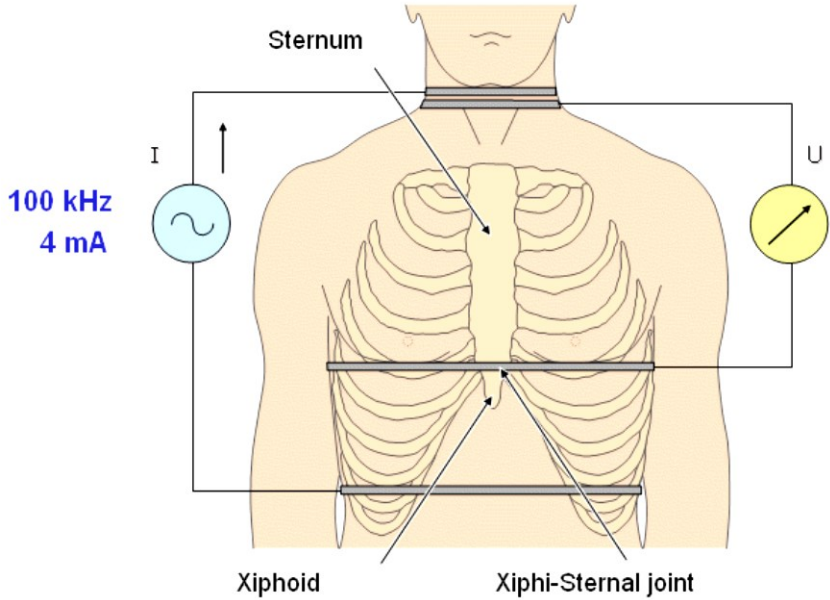


Figure 25. ICG acquisition configuration: electrodes placement [40].

Since the current is held at a constant level, voltage amplitude variations are directly related to changes in the thoracic electrical impedance, indicated as $\Delta Z(t)$. The thoracic electrical impedance essentially consists of a relevant resistive real part and a negligible imaginary part. The thoracic resistance is equal to the sum of the resistances offered by each component within the thorax (e.g., the lungs, bones, vessels, skeletal muscles, the heart, adipose tissue, air, etc.). Specifically, the thoracic electrical impedance changes according to the amount of fluid in the body. In particular, the ejection of blood during systole results in decreased thoracic impedance which, on the contrary, increases during diastole. The thoracic electrical impedance is also affected by respiration. In fact, it varies according to air volume in the lungs. Changes in thoracic impedance associated with breathing activity are usually filtered out electronically. In this way, only those related to blood volume variations during the cardiac cycle are considered of interest. By convention, a positive deflection in the normal ICG signal indicates lower electrical impedance. ICG signals are usually acquired simultaneously with ECG and PCG recordings. The first derivative of $\Delta Z(t)$, representing blood velocity curve and indicated as $dZ(t)/dt$, is the most used ICG waveform in clinical practice. Indeed, some reference

points that primarily correspond to cardiac cycle events (e.g., B-point that marks the onset of left ventricular ejection, X-point that indicates the closure of the aortic valve, $(dZ(t)/dt)_{\max}$ that is the peak of aortic blood flow velocity) are localized on $dZ(t)/dt$ signal. Therefore, various parameters of cardiac function can be directly extracted or derived from this curve, such as HR, PEP, LVET, SV, CO, CI, contractility index, etc. (see **Figure 26**), which provide valuable information for the diagnosis of CVDs [4],[39]-[41]. However, it has the same drawbacks as ECG.

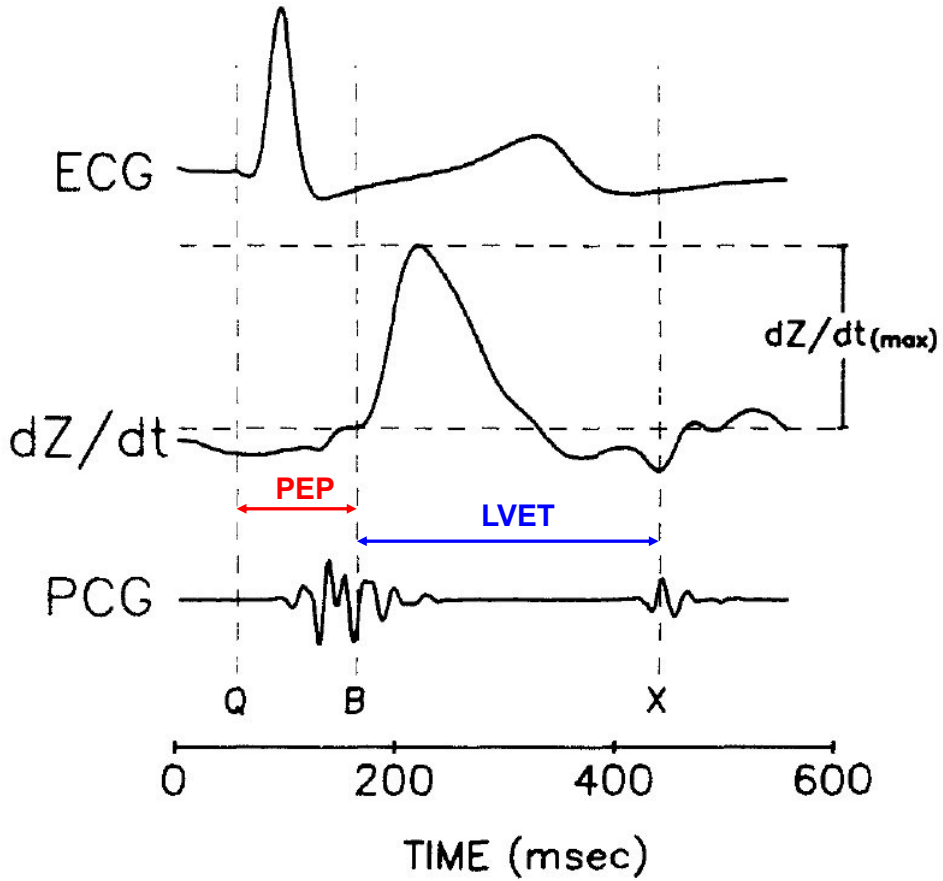


Figure 26. First derivative of thoracic electrical impedance, $dZ(t)/dt$, along with simultaneous ECG and PCG recordings. Q refers to the Q-wave in the ECG signal; B marks the onset of left ventricular ejection on $dZ(t)/dt$; X indicates the closure of the aortic valve on $dZ(t)/dt$. PEP is the time interval from the Q wave to the B-point. LVET is the time interval from the B-point to the X-point [41].

3.2 Cardio-mechanical monitoring techniques

The mechanical activity of the heart generates vibrations that propagate to the surrounding tissues, eventually reaching the surface. These waves provide relevant information about the mechanical behaviour of the heart and can be grouped into two classes: precordial vibrations and whole-body vibrations. Precordial vibrations are local pulses caused by the mechanical activity of the beating heart that induce small movements of the chest wall, which can be perceived via sensors placed on it; whole-body vibrations, instead, are produced by variations in the body's center of mass due to blood flowing towards the feet.

Precordial vibrations can be further divided into infrasonic and sonic components. Moreover, they can also be categorized according to their frequency band into low-frequency precordial vibrations (i.e., in the 0 – 30 Hz frequency range also including infrasound), which are caused by the motion of the heart and its morphological changes during the cardiac cycle, and high-frequency precordial vibrations (i.e., in the 20 – 2000 Hz frequency range), which are produced by the opening and closure of heart valves, blood ejection and turbulences [42][41].

Heart motion and its changes in shape during the cardiac cycle are reported in literature. Due to the recoil effect that causes the stretch of elastic tissues, the heart contracts and propels itself towards the apex during systole, whereas it relaxes and springs back towards the base during diastole [43]. Specifically, the heart has been observed to undergo a counterclockwise twisting motion during contraction (facing to the subject), along its long axis, thus inducing the left ventricle to move towards the chest. As described in Section 2.2, the heart is a hollow, cone-shaped muscular organ. At the end of diastole, it reaches its maximum volume or radius. On the contrary, during the isovolumic contraction phase, an increase in its external circumference and anterior-posterior diameter, as well as a shortening along the base-to-apex direction, occurs. As a result, the heart assumes a more spherical shape. The intraventricular pressure rises and induces an increase in ventricular walls tension; in particular, the tautness of the left ventricle reaches a peak just before the opening of the aortic valve. At the onset of ejection, the left ventricle is propelled against the chest, but its walls tension starts to drop, and the overall size of the heart becomes smaller. In the late systole, a further decline in ventricular walls

tension occurs as the intraventricular pressure decreases and the heart starts to relax, while moving backward because of an inward depression. Chest wall movements are induced by precordial pulsations; among them is to consider the apical impulse, which is attributed to the motion of the anterior wall of the left ventricle. During the early systole, the left ventricle experiences an outward movement, towards the chest wall; on the contrary, it moves backward, away from the chest wall, during the mid-late systole. However, the apical impulse is not due to ventricular contraction, but is produced by the recoil effect that occurs when blood is ejected into the aorta. Indeed, during the isovolumic contraction phase, an equally distributed pressure is exerted on the walls of the left ventricle and no movement can be appreciated. As the aortic valve opens, the ejection of blood into the aorta induces the heart to move downward, since the force applied against the apex is no longer balanced by an equal reaction. During blood ejection, the aortic arch straightens under the recoil effect that causes the left ventricle to move upward and forward towards the chest wall. In this way, the apical impulse is generated (see **Figure 27**) [44]-[46].

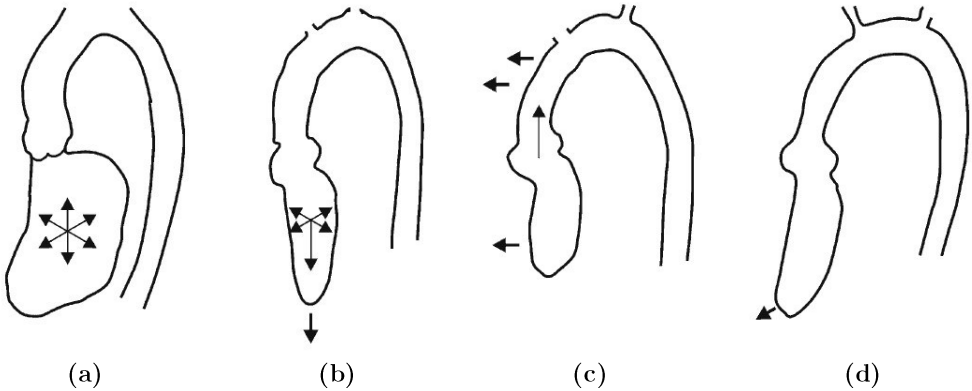


Figure 27. Heart motion during the cardiac cycle. (a) During the isovolumic contraction phase, an equally distributed pressure is exerted on the walls of the left ventricle and no movement can be appreciated; (b) when the aortic valve opens, the ejection of blood into the aorta induces the heart to move downward, since the force applied against the apex is no longer balanced by an equal reaction; (c) during blood ejection, the aortic arch straightens under the recoil effect that causes the left ventricle to move upward and forward towards the chest wall; (d) the upward and downward movement of the left ventricle generates the apical impulse [44].

For this reason, even if the left ventricle becomes smaller during its contraction, the apex moves towards the chest wall. The apical impulse is then transmitted through

the surrounding tissues until it reaches the chest surface. Therefore, obesity, chest wall deformities or rigidity can affect its transmission. Furthermore, the force of the apical impulse is influenced by the velocity of blood ejection, which depends on myocardial contractility, while the amount of the aortic recoil that contributes to heart momentum is determined by SV [44]-[46].

Heart motion also depends on the mechanical coupling to adjacent structures [47]. Because of its housing within the thoracic cavity, which is also occupied by the lungs, the heart is often referred to as “*a pressure chamber within a pressure chamber*” [48]-[50]. In such a natural anatomic arrangement, the heart and lungs are forced to mechanically interact, by applying variable pressures on each other, both via direct physical contact and through the blood vessels they are connected with [48]-[51]. The resulting cardio-respiratory interactions are known to affect various physiological parameters of cardiac function, such as HR, CTIs and SV [52]-[56], and turned out to be impaired by many cardio-pulmonary diseases [57]-[60]. Hence, heart motion is affected by respiration. Specifically, respiration is characterized by two motion components: thoracic, due to the movement of the rib cage, and abdominal, due to the displacement of the diaphragm [61]. Indeed, during inspiration, the rib cage expands, while the diaphragm moves downward. On the contrary, during expiration, the rib cage releases, while the diaphragm moves upward. Since the heart sits on the diaphragm and is in contact with the lungs, it moves with them during breathing acts. It is well known from the literature that the heart movement during respiration essentially occurs along the superior-inferior direction, is linearly related to the displacement of the diaphragm, and can be considered approximately as a global longitudinal translation [62].

3.2.1 Phonocardiography

The mechanical activity of the heart generates vibrations that can be perceived by the human ear at the chest surface by auscultation, known as heart sounds. These mechanical waves are produced by the closure of heart valves, contraction of the ventricles, pressure variations in heart cavities and blood flow through great vessels [6]. Auscultation was originally performed via acoustic stethoscopes that acted as closed air compartments between the chest wall and the human ear.

Phonocardiography (PCG) is the method for recording the sonic components of precordial vibrations via modern stethoscopes equipped with microphones. PCG recordings are commonly synchronized with ECG tracings to identify the temporal relationship between heart sounds and cardiac cycle events. The spectral components of heart sounds extend in a wide frequency band (typically 20 – 1000 Hz) [63]. However, PCG transducers are also sensitive to further mechanical vibrations that come from the human body caused by respiration, gross movement of the beating heart and its mechanical coupling to adjacent structures, emptying and filling of the ventricles [64], peristalsis of the stomach and intestine, as well as to environmental noises [63] and even vibrations due to friction of the pickup with the skin [6]. Moreover, increased distance between the source and the detector, as in the case of obese subjects, prevents accurate recordings and results in heart sounds of weak intensities. In the last decades, these factors, along with the outbreak of ECHO technique, have led to a loss of clinical interest in PCG, although recently it has been renovated by the introduction of electronic stethoscopes [63],[65].

Low-frequency PCG recordings present four normal heart sounds, namely S_1 , S_2 , S_3 and S_4 . S_3 and S_4 disappear in high-frequency PCG, while time-shifted components of S_1 and S_2 can be recognized. This effect is known as splitting. An example of PCG signal is shown in **Figure 28**.

S_1 can be split into four components. The first component is a low-frequency vibration due to an increase in ventricular tension as a consequence of increased intra-ventricular pressure; the second and third components are high-frequency and high-amplitude sounds caused by the closure of mitral and tricuspid valves during the isovolumic contraction period, and the opening of the semilunar valves at the beginning of ejection, respectively; the fourth component is a low-frequency vibration due to blood flow through large arteries at the time of maximal ejection. S_1 has a normal duration of about 0.1 – 0.16 s [6]. Many CVDs can affect the timing and intensity of these components. Right bundle branch block, tricuspid stenosis, and atrial septal defect result in delayed tricuspid component, while left bundle branch block causes the merge of mitral and tricuspid components. Lower intensity of S_1 is found in cases of myocardial infarction, cardiomyopathy, heart failure, left bundle branch block, mitral regurgitation and aortic stenosis. On the contrary, higher intensity of S_1 is found in mitral stenosis and atrial septal defect [63].

Four components can be recognized also in S_2 . The first component is a low-frequency vibration due to ventricular relaxation; the second component is a high-frequency and high-amplitude sound caused by the closure of semilunar valves; the third component has lower amplitude and is due to blood flow through arteries; the fourth component is a low-frequency vibration produced by the opening of mitral and tricuspid valves. S_2 has a normal duration of about 0.08 – 0.14 s [6]. Physiological S_2 splitting into aortic and pulmonary components can be observed during inspiration because of increased venous return into right ventricle which delays the closure of the pulmonary valve [7], while they can be appreciated as a unique sound at the end of expiration [65]. Indeed, an increase in right ventricular filling during inspiration, and therefore a decrease in left ventricular filling, results in different time duration of left and right ventricular systole [65]. Pathological S_2 splitting could be a sign of many CVDs. Right bundle branch block, pulmonary stenosis, congenital heart disease, pulmonary hypertension, atrial septal defect result in delayed pulmonary component, while left bundle branch block, aortic stenosis and arteriosclerotic heart disease cause a delay in aortic component. Moreover, while early pulmonary closure is due to tricuspid regurgitation and premature right ventricular activation, early aortic closure is caused by mitral regurgitation and ventricular septal defect. In addition, these components cannot be appreciated in severe pulmonary or aortic valve stenosis [6],[63].

The physiological S_3 is a weak, low-frequency sound produced by vibrations of ventricles' walls during their rapid filling [63], that is delayed about 0.16 – 0.24 from S_2 [6] and can be heard in children, adolescents and young adults. If heard in people over 30 years of age, it is referred to as “Kentucky gallop” and could be a sign of CVDs, such as mitral regurgitation, aortic stenosis, ischemic heart disease [22]-[23], ventricular or atrial septal defect [7].

The physiological S_4 is a soft, low-frequency sound caused by rapid ventricular filling during atrial systole and is generally heard in infants, young children and people over 50 years of age. A pathological S_4 is referred to as “Tennessee gallop” and can be found in mitral regurgitation, aortic stenosis, and ischemic heart disease [22]-[23], right or left ventricular hypertension, pulmonary hypertension, AV block [7].

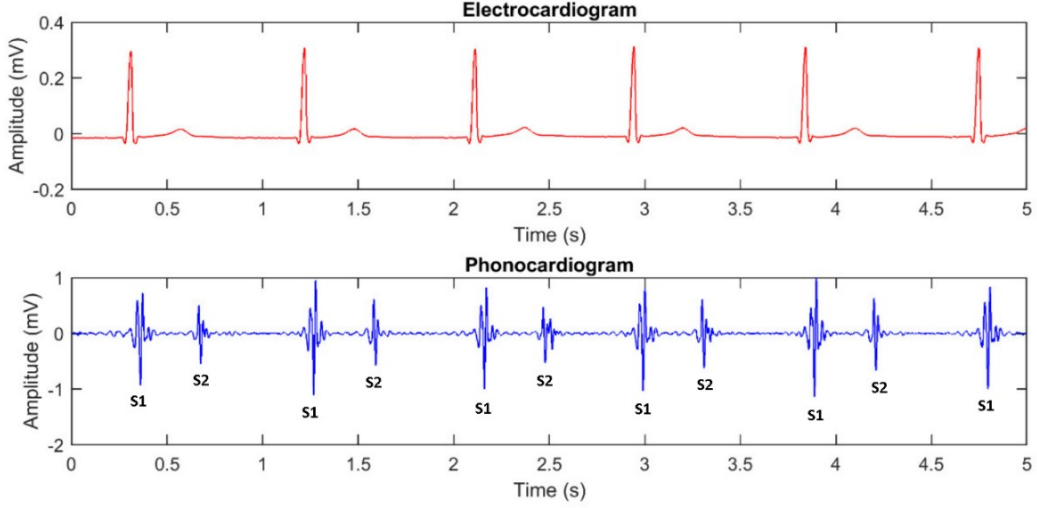


Figure 28. Example of PCG signal (blue line) along with a simultaneous electrocardiogram (red line) [65].

Finally, murmurs are abnormal heart sounds of low intensity and high frequency [6] caused by turbulences in blood flow, which result in vibrations of blood vessels walls, under pathological conditions, such as valvular stenosis or leakage [63].

3.2.2 Apexcardiography

Apexcardiography (ACG) records the infrasonic vibrations of the precordium (typically in 0.1 – 20 Hz frequency range) over the apex of the heart. As shown in **Figure 29**, the subject lies in left lateral decubitus position, with the left arm raised and the right arm relaxed along the body. The pickup (the funnel or bell of a microphone) is placed at the point of maximal impulse (PMI), which is identified by palpation, and firmly held at this location. A rubber tube connects the pickup to a piezoelectric crystal. The chest wall experiences upward and downward movements due to the apical impulses of the beating heart. These tiny movements are sensed by the pickup as changes in air pressure and transmitted through the tube to the piezoelectric transducer, which converts them into voltage variations that are amplified and displayed on the screen of an oscilloscope [8],[66].

A normal apexcardiogram is recorded at the mid-expiration and is composed of waves corresponding to cardiac mechanical events, namely a wave, systolic wave, rapid filling wave and slow filling wave (see **Figure 30**).



Figure 29. *Measurement setup for apexcardiogram recording [66].*

The a wave is produced by ventricular filling during atrial contraction and is coincident with S_4 or the atrial component of S_1 . It is characterized by a rapid rise reaching a peak at the closure of AV valves. The a wave occurs $0.08 - 0.12$ s after the onset of the P wave in the ECG and is followed by the systolic wave. The time interval from the end of the a wave to the peak of the systolic wave, named as E-point, is an estimate of isometric contraction duration (0.04 s on average). The E-point follows the QRS complex in the ECG by approximately 0.07 s.

The systolic wave is due to ventricular contraction and has a typical tent shape starting from the E-point. It is followed by a depression (that indicates the maximal ventricular ejection) which reaches a plateau (coincident with slow ventricular ejection) and finally a sharp and rapid drop. This drop ends at the O-point which indicates the opening of AV valves (referred to as opening snap) and the onset of ventricular diastolic filling. The time interval from the O-point to S_2 provides the

duration of isometric relaxation (0.06 s on average), while the interval from the E-point to S_2 is an estimate of ventricular ejection time.

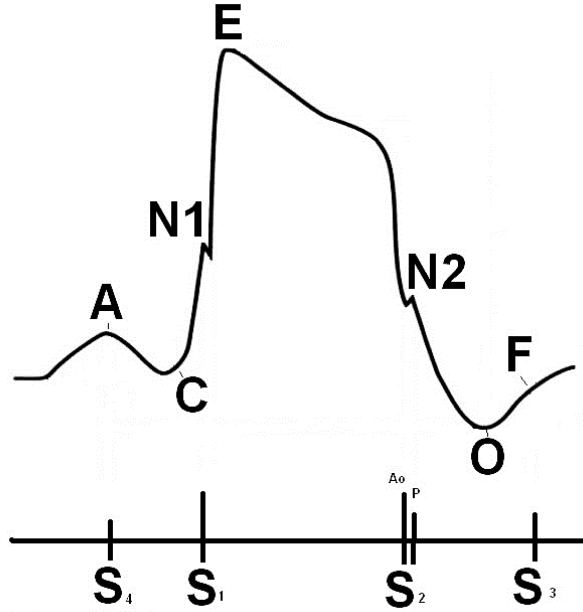


Figure 30. ACG waveform along with schematic PCG signal. The typical ACG waveform is represented on the top. A = a wave that reflects ventricular filling due to atrial contraction; C = systolic wave due to ventricular contraction; E-point = peak of the systolic wave; O-point = onset of the rapid filling wave (AV valves opening); F = onset of slow filling wave (diastasis). A schematic PCG signal is depicted on the bottom. A_o = aortic valve closure; P = pulmonary valve closure [67].

The diastolic filling is divided into rapid filling wave and slow filling wave. The former is a sharp rise (it lasts approximately 0.04 – 0.12 s) from the O-point to a peak corresponding to S_3 (its height is 10% to 30% of the total amplitude), which occurs after the T wave in the ECG. The latter is a slow rise and ends at the beginning of the following a wave [66],[68]-[69].

ACG recordings were carried out on healthy subjects and ischemic patients before and after exercise. The a wave did not show an increase in its amplitude after exercise, nor systolic and diastolic waves did change their amplitude or morphology. On the contrary, in patients with ischemic heart disease, the a wave had greater amplitude and longer duration (thus longer a-E interval) than that of healthy subjects. This was caused by abnormal high ventricular resistance to atrial systole.

A further increase in a wave amplitude was noticed in ischemic patients after exercise [9]. Furthermore, a wave of greater amplitude was observed in patients with aortic stenosis, subaortic obstructive disease, hypertensive cardiovascular disease and cardiomyopathies [70]. Larger a wave and longer a-E interval were also monitored in patients with arteriosclerotic heart disease, and higher relevance of these alterations was reported after exercise [71].

The ACG also allows the identification of murmurs, some types of arrhythmias and AV conduction effects, all inducing alterations in the normal ACG waveform.

Generally, the right ventricular apexcardiogram is not recorded in normal subjects, but it has been shown to roughly present the same morphology of the left ventricular apexcardiogram [69]. In [72], right and left ACG recordings were compared. The a wave in the right ACG showed greater amplitude than that in the left ACG; in addition, a systolic wave of gothic shape was observed in the right ACG. Moreover, patients with reactive pulmonary hypertension showed abnormal right ACG. In particular, the E-point in the right ACG was synchronous to the same point in the left ACG in case of pulmonary hypertension around systemic level, whereas the E-point in the right ACG occurred before the E-point in the left ACG in case of pulmonary hypertension lower than systemic; the duration of isometric relaxation was longer than that in the normal ACG; the a wave in the right ACG had greater amplitude than normal.

Furthermore, ACG recordings are impractical in patients with increased heart distance from the pickup, as in the case of pulmonary emphysema, marked chest deformity and obesity [66],[69].

Rios et al. showed that ACG is a valuable tool for the diagnosis of left ventricular disease. They stated that the configuration of the systolic complex depends on the spatial relationship between the pickup and the apex, while its amplitude depends on SV; on the contrary, the diastolic complex is affected by volume variations, as well as diastolic pressure, in the left ventricle. Indeed, patients with left ventricular disease showed reduced SV. This should have resulted in smaller diastolic displacement. However, increased left ventricular diastolic pressure caused a greater diastolic displacement in patients with left ventricular disease, due to an increase in left ventricular tension or firmness that was perceived as a displacement [73].

Finally, CTIs estimates were obtained from ACG recordings of patients with myocardial infarction. ACG waveforms showed a wave of greater amplitude and longer duration, flat systolic plateau and systolic bulges, and shorter CTIs, except for EMD and IVRT, were estimated [74].

Despite its diagnostic value, ACG is no longer practiced because of the cumbersome instrumentation required and the clear diagnostic superiority of ultrasound imaging techniques.

3.2.3 Applications of PCG and ACG in the estimation of CTIs

Since the 1960s, there have been many studies on CTIs measurement by simultaneous recordings of ECG, carotid pulse tracing, PCG and even ACG.

In [75], the relationships between LVET, HR and SV were investigated both in healthy and pathological subjects in supine or 45° head-up tilted position. First, CO was measured via indicator-dilution method or the direct-oxygen Fick technique. Then, SV was derived from CO and HR. The LVET was computed from carotid pulse tracing as the time interval between the upstroke and the trough of the incisural notch. The ratio SV/LVET was used as an indicator of mean rate of left ventricular ejection. An inverse linear relationship was found between HR and LVET. Indeed, as HR increases, the LVET decreases. On the other hand, a direct linear relationship was found between SV and LVET. Furthermore, also the mean rate of left ventricular ejection showed a linear relationship with SV. It was concluded that both SV and HR affect the LVET. These relationships were also investigated in patients with heart diseases (e.g., myocardial failure, aortic valvular disease, mitral valvular disease, hypertension, pericardial disease and pulsus paradoxus). No significant differences were observed for LVET in patients with myocardial failure, mitral valvular disease and hypertension. On the contrary, patients with aortic insufficiency and aortic stenosis, as well as patients with associated mitral stenosis and aortic insufficiency, showed longer LVET relative to SV. Moreover, patients with pericardial disease showed a shortening of LVET at the onset of inspiration reaching a minimum just before the end of inspiration.

In a study by Harris et al. [76], the PEP was estimated as the difference between TST and LVET. The TST was computed as the time interval between the beginning

of the QRS complex in the ECG and the first high frequency vibration of S_2 , whereas the LVET was obtained as the time interval between the upstroke and the trough of the incisura in the pulse tracing. These CTIs were estimated from subjects in supine position. The PEP was found in the range 105 ± 2 ms for normal subjects. The PEP includes the time required for ventricular depolarization, electrical-mechanical coupling, and the rise of left ventricular pressure from ventricular end-diastolic to aortic-diastolic levels. It was observed that the PEP is not directly related to HR. Indeed, it was not affected by changes in HR induced by the administration of atropine or by right atrial electrical pacing.

Weissler et al. performed simultaneous recordings of ECG, carotid pulse tracing and PCG on 221 normal subjects (121 males and 90 females) and 27 patients with heart failure in supine position. TST, LVET and S_1 - S_2 were directly estimated from the recordings, while PEP, EMD and IVCT were derived from them. Regression equations relating HR and STIs were obtained. It was observed that TST, LVET and PEP are inversely and linearly related to HR (however, only a slight decrease in PEP was observed with increasing HR), while IVCT does not change with HR; LVET and TST are longer in females than in males, unlike PEP, EMD and IVCT that are not affected by gender. Furthermore, longer PEP, shorter LVET and normal TST were estimated in patients with heart failure. Changes in PEP and LVET due to HR variations were correlated with hemodynamic parameters. Indeed, PEP is not only inversely related to blood flow but also to arterial pressure. On the contrary, changes in LVET do not depend on arterial pressure. Moreover, longer PEP and shorter LVET are well correlated with reduced levels of SV and CO [30]. Changes in STIs induced by exercise were reported in a study by Cardus et al. [31], during which measurements of TST, EMD, IVCT and LVET were obtained from 30 healthy subjects while performing bicycle ergometer test. ECG, carotid pulse tracing and PCG were simultaneously acquired from the subjects at rest supine, at rest sitting on the bicycle, every minute during exercise and every minute for 5 min following exercise. No correlation and low correlation were found between EMD and inter-beat intervals, obtained as differences between R-peaks locations in the ECG signal (RR), at rest and during exercise followed by recovery, respectively. EMD during exercise is shorter than at rest and is not affected by arterial blood pressure and the intensity of physical work. A moderate correlation was found between IVCT

and RR at rest, during exercise and recovery. It is not affected by arterial blood pressure and workload. High correlation was found between LVET and RR at rest, during exercise and recovery. Moreover, for LVET, the regression coefficients vary with subject's posture. Indeed, they decrease in going from supine to sitting position and even with exercise. It is affected by age at rest but not during exercise and is not influenced by workload. High correlation was also found between TST and RR at rest, during exercise and recovery. Again, the regression coefficients increase in going from supine to sitting position. Furthermore, during the recovery phase, HR decreases, while EMD, IVCT and LVET return to their resting values. However, for certain values of HR, LVET and TST are shorter than during exercise. Finally, during isometric exercise, HR, IVCT and PEP increase, while LVET does not change.

In a further study, CTIs estimates were obtained from healthy and pathological subjects, divided into four groups: 1) 11 healthy men; 2) 9 patients with angina; 3) 11 hypertensive patients; 4) 10 patients with healed myocardial infarction. ECG, ACG, PCG and carotid pulse tracing were simultaneously acquired from all subjects in lateral decubitus position at the PMI during mid expiration. TST, LVET, IVRT and RVFT were directly measured from the recordings, while PEP was obtained as the difference between TST and LVET. A slight longer PEP was observed in group 4; no differences were obtained for LVET; higher PEP/LVET ratio was found in patients with angina and hypertension; longer IVRT was measured in group 2 [32]. In Cokkinos et al. [77], ECG, PCG and carotid pulse tracing were acquired from 26 supine subjects before and after the production of tachycardia (via the administration of atropine or right atrial electrical pacing) and STIs were estimated. It was observed that TST and LVET decrease with increasing HR. On the other hand, PEP is minimally affected by HR (it substantially does not change with HR) but is well correlated with $(dP/dt)_{\max}$ and ejection fraction. Moreover, the ratio PEP/LVET increases with increasing HR.

Again, in [78], LVET and TST were directly measured from simultaneous ECG, carotid pulse tracing and PCG recordings, whereas PEP was obtained as the difference between TST and LVET and HR was derived from RR intervals. Weissler's regression equations are largely adopted to express the relationships between STIs and HR. In clinical practice, for a rapid comparison with normal

values, deviations from normal regressions are obtained in two ways: 1) by subtracting the actual value from the predicted value for a given HR; 2) by computing STI indices (these indices are the offsets of Weissler's regression equations multiplied by 103 and correspond to normal values at zero HR). STIs are influenced by various factors. PEP lengthens in case of left ventricular muscle failure, left bundle branch block, reduced preload and negative inotropic agents, whereas it shortens in case of aortic valve disease, reduced left ventricular isovolumic pressure and positive inotropic agents. LVET increases in case of aortic valve disease, while it decreases with left ventricular muscle failure, reduced preload, positive inotropic agents, and negative inotropic agents. TST increases in case of left bundle branch block and aortic valve disease, while it decreases with positive inotropic agents.

Furthermore, simultaneous recordings of ECG and PCG, combined with carotid pulse tracing (in supine position) or ACG (in left lateral decubitus position), were performed on three groups (healthy subjects, hypertensive patients and infarct patients). TST, EMD, LVET, PEP (obtained as the difference between TST and LVET), IVCT (obtained as the difference between PEP and EMD), PEP/LVET ratio, ICT/LVET ratio, the time interval from S_2 to the downstroke of ACG (corresponding to a 90% reduction of total height), and the time interval from S_2 to the O-point of ACG were considered. Abnormal values of these time intervals were set by considering the second highest or lowest value in the reference group. EMD was longer in the infarct group than in the reference group and the percentage of infarct patients with EMD longer than 40 ms (that is the abnormal value) was higher than in the reference group. No significant differences were found for IVCT and PEP between the groups. A negative correlation to HR was found for IVCT in the infarct group but not in the reference group, and for PEP in the hypertensive group but not in the infarct and reference groups. LVET was negatively correlated to HR, but no significant differences were found between groups. Moreover, no significant differences were found for ICT/LVET and PEP/LVET between groups. The time interval from the S_2 to the O-point on the ACG was longer in the infarct and hypertensive groups than in the reference group, and it was negatively correlated to HR in the infarct and hypertensive groups, but not in the reference group [79].

In a study by Ferro et al. [80], the relationships between STIs and HR during tachycardia (induced by atrial or ventricular pacing) were investigated. The study was performed in 21 healthy subjects (12 subjects were studied during atrial pacing, while 9 subjects were studied during ventricular pacing). Simultaneous recordings of ECG, PCG and carotid pulse tracing were acquired from the subjects in supine position. LVET, TST, PEP, IVCT, EMD and PEP/LVET ratio were computed for each subject at rest and during tachycardia (HR was gradually increased until it reached 150 bpm). STIs were measured 2 min after each increment of HR. An inverse relationship with HR was found for LVET, both during atrial and ventricular pacing. No relationships with HR were found for PEP, IVCT and EMD during both types of electrostimulations. However, while no significant changes were found between rest and atrial pacing conditions, an increase was observed for PEP and EMD at the beginning of ventricular pacing, then settled at constant values with further increment of HR. IVCT was not influenced by ventricular pacing. The PEP/LVET ratio showed a direct correlation with HR both during atrial and ventricular stimulation.

STIs were also obtained from 23 healthy subjects at rest, during atrial pacing and dynamic exercise. ECG, PCG and carotid pulse tracing were simultaneously recorded. TST, LVET, PEP and PEP/LVET ratio were obtained for each subject. Two protocols were used: 1) rest + atrial pacing (from 80 to 160 bpm) + rest + dynamic exercise (bicycle exercise in the supine position); 2) rest + dynamic exercise. During atrial pacing, TST and LVET showed an inverse linear relationship with HR, PEP was not affected by changes in HR, PEP/LEVET ratio increased with HR (a 40% increase). During dynamic exercise after atrial pacing, TST and LVET shortened (the shortening of TST was greater with dynamic exercise than with atrial pacing, while the shortening of LVET was greater with atrial pacing than with dynamic exercise), while PEP did not change during atrial pacing, but it shortened with dynamic exercise (it experienced a 50% reduction). Finally, PEP/LVET ratio decreased with dynamic exercise (a 31% reduction). During dynamic exercise alone, PEP and LVET showed an inverse linear relationship with HR. It should be underlined that, in addition to HR, PEP could be affected by several factors: conduction velocity, left ventricular end-diastolic pressure, left ventricular end-diastolic volume, afterload, and the inotropic state of the myocardium. Since the

diastolic blood pressure did not change during atrial pacing and dynamic exercise, it is reasonable to assume that the different behaviour of PEP with pacing and exercise is controlled by the inotropic state of the left ventricle. Moreover, an increase in CO, SV and left ventricular $(dP/dt)_{\max}$ was observed with dynamic exercise, but not during atrial pacing. Therefore, an increase in SV during dynamic exercise could explain the smaller shortening of LVET with respect to the atrial pacing. For this reason, the shortening of PEP during exercise is the result of changes in left ventricle contractility and is not primarily correlated to HR alone [81].

In [82], HR, TST, LVET and PEP were computed from 30 healthy male volunteers in supine position, both at rest and after four different stress tests (handgrip test, orthostatic test, Valsalva maneuver and cold pressor test). During the handgrip test, LVET and TST shortened, while PEP and PEP/LVET ratio did not change. During the orthostatic test and the Valsalva maneuver tests, LVET and TST shortened, while PEP and PEP/LVET ratio increased. During the cold pressor test, LVET, TST and PEP shortened (the PEP significantly shortened in the first quarter of immersion), while PEP/LVET ratio increased.

Moreover, CTIs were obtained from simultaneous recordings of ECG, PCG, carotid pulse tracing, M-mode ECHO of the mitral valve and respiratory curve on 25 healthy subjects (20 men and 5 women) in sitting position. LVET, IVCT, PEP, TST were considered as STIs, while IVRT and LVFT as DTIs. CTIs appear as modulated by respiration. It was found that STIs have stronger dependency on respiration than DTIs. While LVET experienced a decrease during inspiration, PEP and IVCT increased. In particular, PEP and IVCT were longest at the transition from inspiration to expiration and shortest at mid-expiration. IVRT did not vary as much as other intervals. Finally, LVFT reached the maximum value at the beginning of inspiration and the minimum in the second half of inspiration, but in all other conditions it showed little variations [52].

Finally, CTIs are affected by subject's posture. This was investigated in 20 healthy subjects (18 men and 2 women) by simultaneous recordings of ECG, PCG, carotid pulse tracing and M-mode ECHO of the mitral valve. Systolic (i.e., PEP, LVET, EMD, IVRT) and diastolic (IVRT and LVFT) time intervals were obtained from subjects both in sitting and supine positions. PEP, EMD, IVCT and IVRT were

longer in sitting position than in supine position; on the contrary, LVET and LVFT, together with RR interval, were longer in supine position than in sitting position. Furthermore, the relationship between LVET or LVFT and HR did not change with position. These changes in CTIs can be understood as a depression of cardiac function in the sitting position due to the pooling of blood in the lower extremities; indeed, reduced filling leads to a diminished contractile and relaxation response due to shortened myocardial fibers [83].

3.2.4 Ballistocardiography

Ballistocardiography (BCG) records the whole-body vibrations induced by displacements of the body's center of mass due to blood flowing towards the feet. The BCG is based on the physical principle of Newton's third law of motion, which states that for each action there is an equal and opposite reaction. Indeed, when the heart contracts, a column of blood is first propelled towards the head through the ascending aorta and pulmonary arteries, therefore the recoil effect causes a displacement of the body in the opposite direction, towards the feet. Then, when blood flows downward through the descending aorta, the body experiences upward movement in order to maintain the center of mass of the whole system in place. As an example, *"if 100 g of blood were moved 7 cm toward the head, the remainder of the body of a man weighing 70100 g would be moved 0.01 cm toward the feet"*. A BCG signal is the recording of these recoil movements in response to changes in blood distribution during the cardiac cycle [84].

In 1877 Gordon observed that a bed suspended from the ceiling by ropes moved synchronously with the heartbeat of a subject placed on it [85]. Later, in 1905, Henderson replicated Gordon's experiment by using a suspended bed, similar to an antique four-poster bed, and a swinging table hanging from the bed frame by wires, while a subject was lying on it. The table was limited to move in the longitudinal direction and was connected at one end to a recording lever which allowed to amplify table movements 100 times and write them on a paper. The subjects were asked to stop breathing since it was observed that respiration involved displacements of many millimeters, unlike recoil effect that caused displacements of at most a tenth of a millimeter [84].

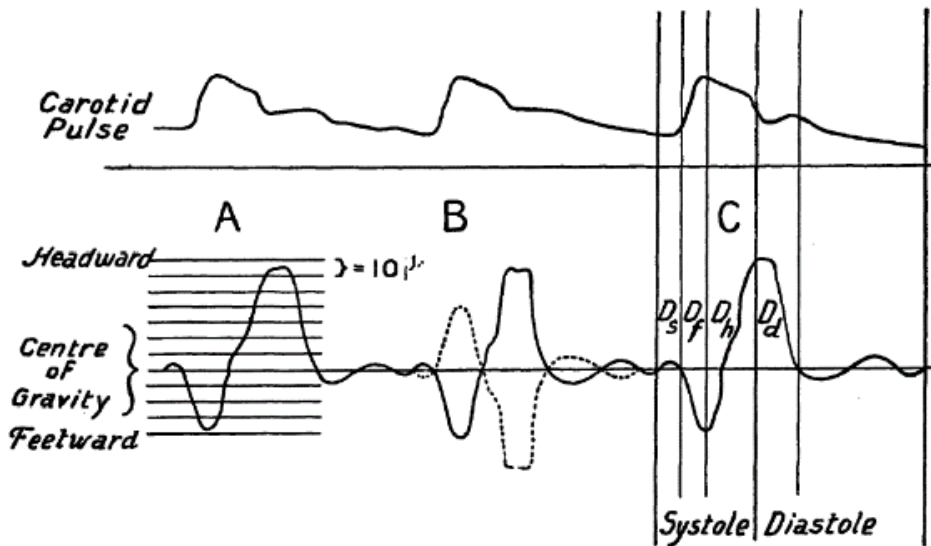


Figure 31. BCG signal obtained from Henderson's apparatus, along with carotid pulse tracing. Four waves can be recognized: D_s , which is a slight upward movement at the onset of systole; D_f , which is a rapid and considerable downward movement due to blood ejection; D_h , which is a large upward movement caused by blood flowing toward the feet; and D_d , which is a large downward movement during diastole, followed by an upward wave of slight amplitude [84].

As depicted in **Figure 31**, from simultaneous recordings to carotid pulse tracings, Henderson identified four different waves in the recoil curve, namely D_s , which is a slight upward movement due to blood flow through the heart and heart gross motion at the onset of systole; D_f , which is a rapid and considerable downward movement due to blood ejection into the aorta and pulmonary arteries; D_h , which is a large upward movement caused by blood flowing toward the feet through the descending aorta; and D_d , which is a large downward movement during diastole, probably due to a rapid reflux of blood into the aorta, followed by an upward wave of slight amplitude. According to Henderson, the obtained curve was the result of the algebraic sum of recoil movements due to mass displacements of blood flowing simultaneously in both headward and footward directions [84].

In 1939, Starr and colleagues introduced the term Ballistocardiography and contributed to the development of the modern BCG. In their system, a steel spring opposed the longitudinal movement of the swinging table in order to overcome the problem of Gordon and Henderson's apparatuses which had frequencies comparable

to respiratory rate [86]. However, high-frequency BCG are affected by a strong coupling between the subject and the surroundings. Moreover, the recoil forces are first transmitted to the arterial system, then to the body surface through the surrounding tissues and finally to the platform the subject is lying on. Hence, the subject and the platform do not act as a rigid whole, but they produce oscillations toward each other [87]. In addition, the heart and the circulatory system are mechanically coupled to the rigid skeleton via various elastic tissues. When a force is applied to the body, it moves and oscillates back before coming to rest. This results in the typical frequency response of a highly damped system. The forces generated by the heart could be subjected to distortion along their pathway, through the surrounding tissues and the skeleton, before reaching the surface where they are sensed [88]. In 1945, Nickerson et al. devised a critically damped apparatus with a natural frequency between that of Gordon and Henderson's systems and that of Starr's undamped table [89]. In 1949, Dock and Taubman paved the way for BCG recordings directly acquired from the body [90]. Starr observed that the amplitude of normal BCG signal is related to SV, cardiac work and cardiac forces, even if it could be affected by body size, body habitus, blood pressure, arteriosclerosis and technical errors [91]. Later, he also reported that acceleration BCG provides information on cardiac function since it is able to identify early evidence of cardiac weaknesses, unlike displacement BCG which can detect heart problems only when they have already occurred [92].

BCG systems were classified by the American Heart Association's Committee of Ballistocardiographic Terminology into:

- ultra-low-frequency and aperiodic BCG (Gordon, Henderson et al);
- low-frequency BCG (Nickerson et al);
- high-frequency BCG (Starr et al.);
- direct-body BCG (Dock et al.).

This classification was obtained by comparing the natural frequency of BCG systems with a normal heart rate of 1 Hz. Hence, ultra-low-frequency BCG systems have a natural frequency lower than 1 Hz; low-frequency BCG systems have a natural frequency of approximately 1 Hz; high-frequency BCG systems have a natural frequency in the range 10 – 15 Hz. Finally, direct-body BCG systems pertain to the category of high-frequency BCG systems [87].

Studies by Noordegraf et al. based on the prediction of ballistocardiograms via mathematical equations and the comparison of predicted waveforms with experimental data have significantly contributed to the comprehension of the genesis of BCG signal [93]-[96]. A normal high-frequency BCG signal is composed of pre-systolic (i.e., F, G), systolic (i.e., H, I, J, K) and diastolic (i.e., L, M, N) waves and is usually recorded along the longitudinal (i.e., head to foot) direction (see **Figure 32**), while not all these waves can be appreciated in low-frequency BCG signals. The F wave is a headward deflection, not always visible, and is followed by the G wave, which is a small footward deflection associated with atrial systole. The H wave is a headward deflection; its onset is close to the peak of R wave in the ECG, while its peak is near the beginning of ventricular ejection. The I wave is a footward deflection arising early in systole and preceding the J wave, which is the largest headward deflection occurring late in systole. The K wave is a footward deflection before the end of systole. Finally, L and N waves are two smaller headward deflections, while M wave is a footward deflection between them [96].

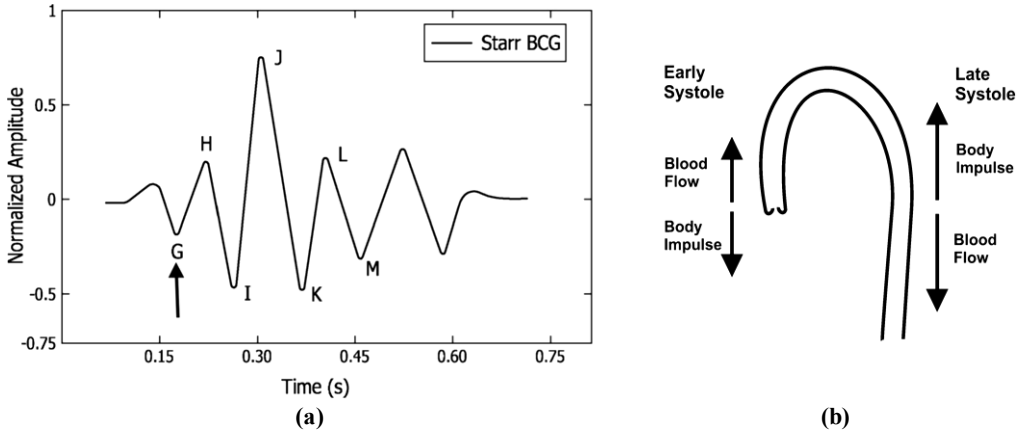


Figure 32. (a) Example of a typical BCG signal with its characteristic waves. The arrow indicates the timing of the QRS complex onset in the electrocardiogram; (b) Aortic arch and force vectors coming from blood ejection by the left ventricle [97].

BCG signal morphology shows inter and intra subjects' variability depending on the measurement device as well as the subject's posture (i.e., supine or sitting) [97]. Furthermore, it is affected by respiration. Indeed, the I-J tract has greater amplitude during inspiration than during expiration due to changes in intrathoracic pressure [88]. HR can be estimated by evaluating J-J time intervals [11]. However, because

of the cumbersome instrumentation required and the advent of ECHO and magnetic resonance imaging (MRI) techniques, BCG lost its appeal. The need for cardiovascular monitoring in home settings opened the way to a new research trend on BCG. This research activity has led to the development of wearable systems, systems embedded in a bed or chair and systems using weighing scales. Wearable systems are simple, unobtrusive, and well suited to continuous monitoring. However, changes in signal morphology depending on the sensor placement site and motion artifacts are their major drawbacks. Bed-based systems are very useful in sleep studies or vital signs monitoring in bedridden patients. Alternatively, chair-based systems can be used for patients that cannot stand on their own. Bed and chair-based systems have the advantages of being less prone to motion artifacts, comfortable and suitable to home settings, but signals are influenced by subject's posture, cannot be recorded simultaneously to other physiological parameters without affecting systems unobtrusiveness and, in case of chair-based systems, have reduced amplitude. Weighing scale-based systems are characterized by day-to-day measurements repeatability and suitability to home environment, but motion artifacts, posture-induced changes in signals morphology and limited duration are their inconveniences [10]-[11].

3.2.5 Seismocardiography

Seismocardiography (SCG) records the cardiac-induced precordial vibrations via accelerometers placed on the chest wall. To date, SCG is widely considered as the mechanical equivalent of ECG and regarded as a reference for cardio-mechanical monitoring. Indeed, SCG signals feature peaks and valleys that are well correlated to cardiac mechanical events (e.g., opening and closure of heart valves, isovolumic contraction, rapid ventricular ejection and filling). Their amplitude is usually expressed in units of milli-g (mg) [11],[13],[33],[98].

The origins of SCG date back to the second half of the 20th century. In 1957, Mounsey was the first to measure precordial accelerations via an accelerometer that consisted of a glass capillary tube, containing alternated layers of metallic mercury and sulfuric acid. The sensor was fixed on a light wooden bar and attached to the subjects' chest (over the apex, the upper sternal area at the level of the second

intercostal space or the lower sternal area at the level of the fourth intercostal space) by using two rubber bands. The subjects were seated with their backs approximately 45° tilted. Movements of the tube along its longitudinal axis, perpendicular to the chest surface, caused variations at the metal-electrolyte interface and thus changes in the electrical potential measured and then amplified. Mounsey named this type of recording precordial ballistocardiogram and identified different phases in the waveform related to the cardiac cycle (see **Figure 33**), by means of simultaneous ECG and PCG acquisitions (i.e., atrial systole, ventricular proto-systole, ventricular isometric contraction, maximum ventricular ejection, ventricular reduced ejection, isometric relaxation, diastolic rapid inflow and diastasis) [99].

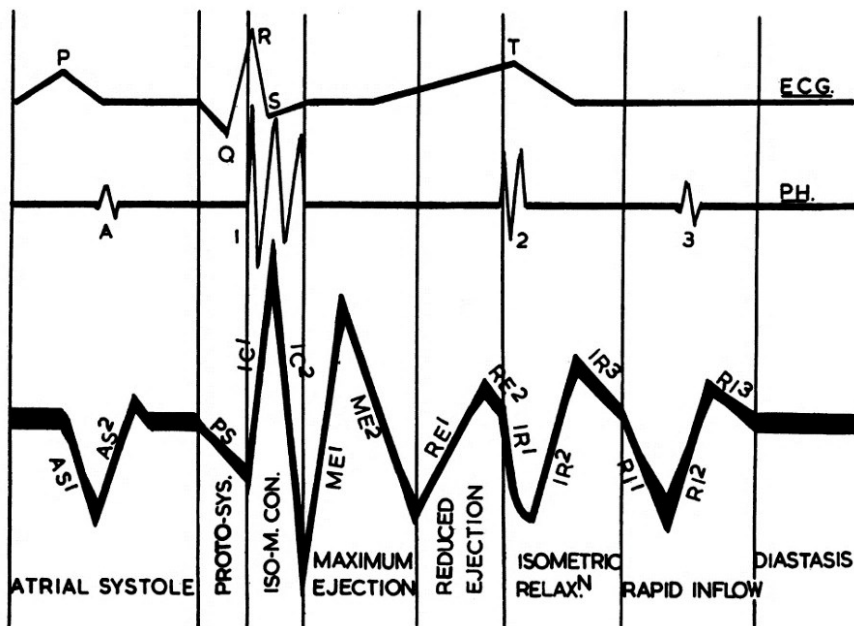


Figure 33. Mounsey's precordial ballistocardiogram, along with simultaneous ECG and PCG signals [99].

A few years later, two research groups, led by Bozhenko and Baevski, introduced the term Seismocardiography by taking inspiration from seismography. In fact, they compared precordial accelerations acquired from healthy and pathological subjects in order to predict cardiac abnormalities, as in the case of earthquakes [11]. In 1990, the SCG was applied for the first time to clinical practice by Zanetti and Salerno, who described it as “a non-invasive technique for recording and analyzing vibrations

induced by the heart during its movement and transmitted to the chest wall”, claiming that SCG signals reflect the compression waves due to acceleration and deceleration of the chest wall produced by heart walls motion and blood flow. SCG signals were acquired by means of ultra-low frequency, piezoelectric accelerometers placed on the xiphoid process (i.e., at the lower end of the sternum) of subjects lying in a supine position and oriented along the dorso-ventral (i.e., posterior-to-anterior) axis. Simultaneous acquisitions of ECG, M-Mode and pulsed-wave Doppler ECHO were carried out in order to correlate peaks and valleys on SCG signals with cardiac mechanical events and provide their timings within the cardiac cycle, as well as estimates of CTIs [12],[100]. Zanetti and Salerno also analysed changes in the morphology of SCG signals from patients with CVDs (e.g., left bundle branch block, myocardial infarction, cardiomyopathy, myocardial ischemia) [101], while Wilson et al. showed that the combination of exercise SCG and ECG allows more accurate diagnosis of coronary artery disease [102]. In 1994, Crow et al. investigated the relationship between SCG and ECHO, by measuring the lag between the temporal locations of SCG fiducial points and the timings of the cardiac events (e.g., opening and closure of heart valves) captured by the US images, combined to simultaneous ECG recordings. Nine fiducial points were identified by Crow et al., as reported below and shown in **Figure 34**:

- peak of atrial systole (AS), which is “*the 2nd positive peak occurring after the ECG P wave*”;
- mitral valve closure (MO), which is “*the beginning of the sharp downslope on the SCG following QRS onset*”;
- isovolumic movement (IM), which is “*the nadir of the MC downslope and has not been related to a specific ECHO point*”;
- aortic valve opening (AO), which is “*the peak of the upsloping segment starting at IM*”;
- isovolumic contraction (IC), which is “*the nadir of the downsloping segment beginning at the AO point and has not been correlated with an ECHO event*”;

- peak of rapid systolic ejection (RE), which is “*the peak of the rounded positive wave following IC*”;
- aortic valve closure (AC), which is “*a sharp slope change (down going) near the end of the ECG T wave*”;
- mitral valve opening (MO), which is “*the 2nd nadir on the downslope following AC*”;
- peak of rapid systolic filling (RF), which is “*the 2nd rounded peak of the SCG following the MO point*” [103].

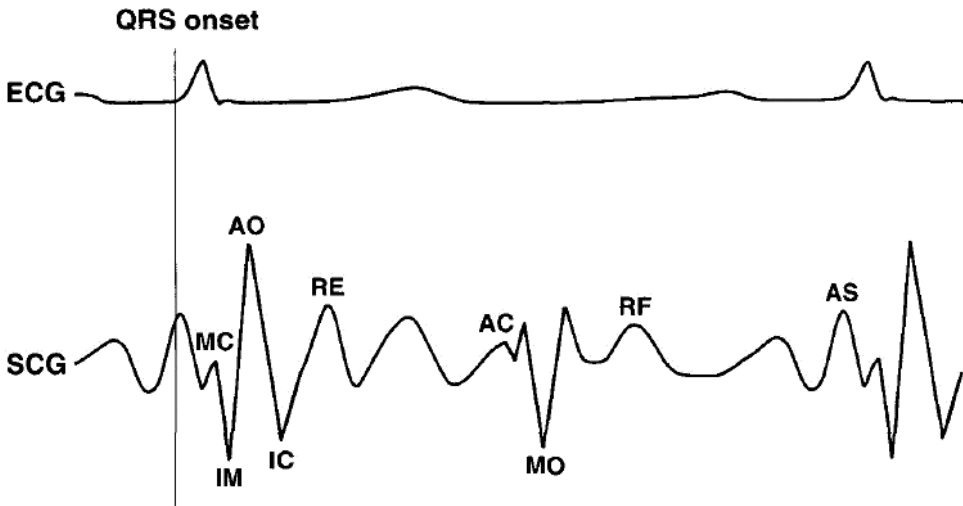


Figure 34. SCG signal annotation by Crow, along with a simultaneous electrocardiogram [103].

Originally, the SCG involved the use of bulky, heavy and uncomfortable accelerometers. For this reason, despite its potentiality, during the 1900s, it was eclipsed by the emergence of imaging techniques (e.g., MRI and ECHO). Later, the development of lightweight, low-noise, miniaturized accelerometers, manufactured via micro-electromechanical systems (MEMS) technology, opened new perspectives, thus renewing clinical interest in SCG. In fact, SCG sensors have gained particular attention in the field of wearable applications for continuous, long-term monitoring of cardiac function in daily life environments with the aim of supporting early diagnosis of CVDs, improving patients’ management and, at the same time, reducing healthcare costs. MEMS accelerometers are electromechanical devices that

essentially consist of a transduction element (e.g., capacitive, piezoresistive, piezoelectric) which converts mechanical signals into electrical ones, ranging in size from less than one micrometer to several millimeters. Triaxial accelerometers are also available, which allow to acquire SCG signals along the horizontal (or right-to-left), vertical (or head-to-foot) and dorso-ventral (or anterior-to-posterior) directions. However, the dorso-ventral component of SCG signal is the most studied. SCG signals are usually recorded at different anatomical locations, such as the sternum (at the xiphoid process), the left and right clavicles, the manubrium, and various intercostal spaces [11],[13],[33],[98]. Recently, changes in SCG signals morphology recorded at the auscultation sites of the heart valves have been reported and new fiducial points have been identified (e.g., left-ventricular lateral wall contraction peak velocity, septal wall contraction peak velocity, trans-aortic valve peak flow, transpulmonary peak flow, trans-mitral ventricular relaxation peak flow, and trans-mitral atrial contraction peak flow) from multi-point SCG recordings [104]. The genesis of the characteristic waves in the SCG signal, which are considered as the result of myocardial contraction, opening and closure of heart valves, blood flow turbulences and changes in momentum, is not yet fully understood. The localization of fiducial points on these waves (see **Figure 35**) and the estimation of HR and CTIs provide relevant information about cardiac function both in physiological and pathological conditions, thus supporting diagnosis of many CVDs (e.g., arrhythmias, heart valves diseases, heart failure, myocardial infarction, myocardial ischemia, coronary artery disease, etc.) [13],[33],[38], [98],[105]-[122].

In particular, the PEP has been the subject of numerous studies because of its key role in determining the health status of patients with heart failure [123]-[126]. However, the localization of SCG fiducial points is not an easy task because of morphological alterations, motion artifacts and noise. Therefore, it is usually addressed by first detecting individual heartbeats, with or without the use of ECG recordings, and then searching for the various markers [109],[117],[122]. Existing approaches for heartbeats localization usually require several processing steps, and most of them rely on the knowledge of ECG R-peaks locations. Moreover, although the study by Crow et al. is widely adopted as a reference for the annotation of the SCG fiducial points, a universally accepted standard is still missing. In addition, SCG signals acquired at the xiphoid process and the carotid can also be used for the

estimation of the pulse transmit time (PTT) and therefore the monitoring of arterial blood pressure [13],[33],[98].

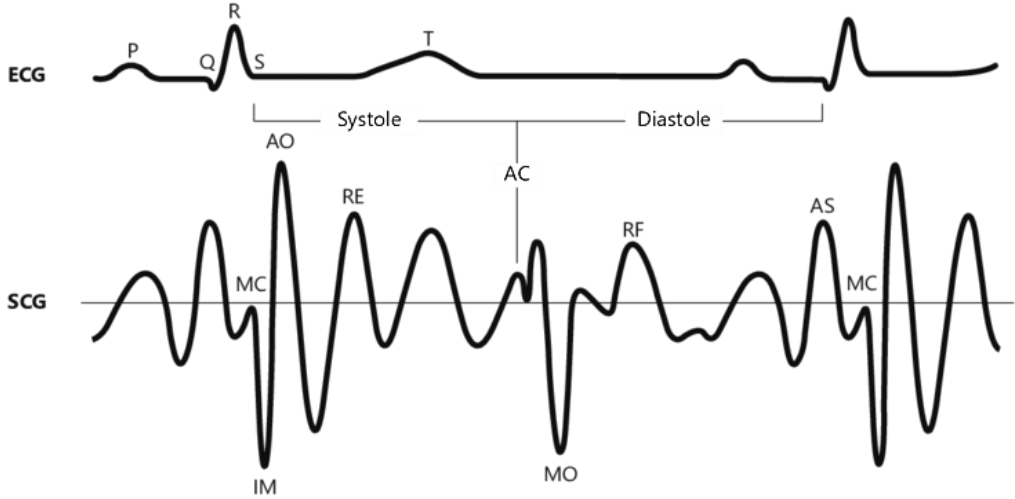


Figure 35. SCG signal along with a simultaneous electrocardiogram. MC = mitral valve closure; IM = isovolumic movement; AO = aortic valve opening; RE = rapid ejection; AC = aortic valve closure; MO = mitral valve opening; RF = rapid filling; AS = atrial systole [102].

In [127], a 3D electromechanical model of heart ventricles, developed from MRI images of canine hearts, was used to investigate the mechanisms underlying the generation of SCG signals. The model included a representation of the sternum and surrounding organs, both in case of elastic and viscous behaviour, and was also coupled with a circulatory model in order to simulate the phases of the cardiac cycle. Particular attention was paid to the orientation of the ribs with respect to the ventricles during respiration in order to assess its effect on SCG signals morphology. For this reason, the ribs were 15° tilted towards the ventricular longitudinal axis during expiration. Simulated SCG signals were compared to those acquired from healthy and pathological subjects. In addition, US measurements were carried out to assess blood flow velocity. Results obtained from simulated SCG signals showed that the negative and global positive peaks of the SCG signals mark the onset of the isovolumic contraction phase and the opening of aortic valve, respectively; signals amplitude during ejection is characterized by a rapid drop followed by a slow increase; the maximum velocity (in the elastic case) or acceleration (in the viscous case) of blood during ejection corresponds to the negative peak on the SCG signal;

local positive and negative peaks can be identified during the isovolumic relaxation and ventricular filling. These results were confirmed by experimental data (see **Figure 36**).

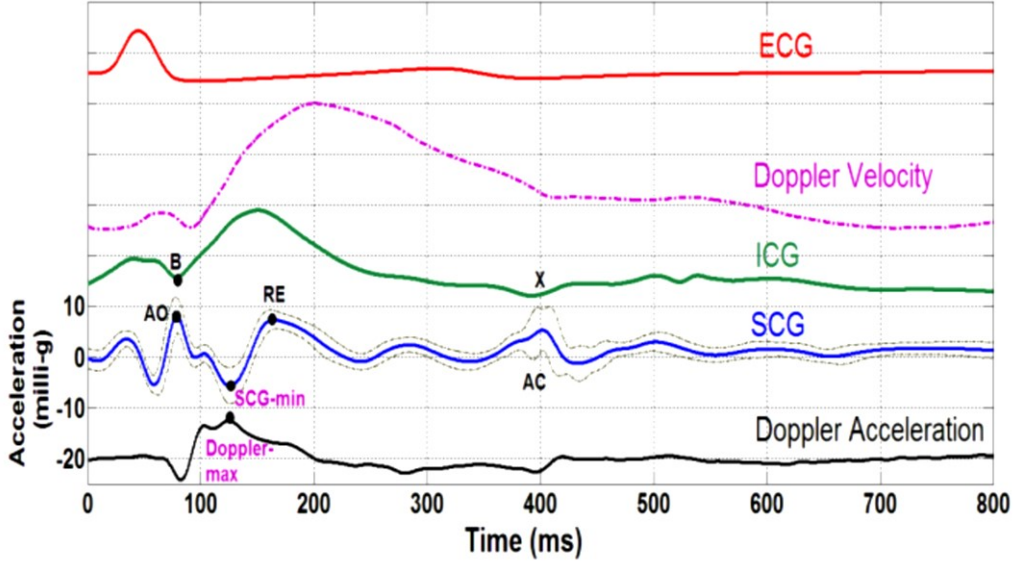


Figure 36. Example of experimental SCG signal. From bottom to top: the acceleration of aortic blood derived from Doppler ultrasound, SCG and its 95% higher and lower confidence intervals, ICG, Doppler velocity ultrasound, and ECG. AO: aortic valve opening, AC: aortic valve closure, RE: rapid ejection, SCG-min: global minimum of SCG, Doppler-max: global maximum of the Doppler blood acceleration signal [127].

Moreover, a decrease in the longitudinal diameter of the ventricles was observed during contraction. This was reported to influence SCG signals morphology, unlike the orientation of the ribs during respiration that has only a minor effect.

As documented in literature, several factors have been recognized to affect SCG signals morphology, such as sensor location, myocardial contractility, heart rhythm, health condition, subject's age, gender and posture, digestion [13],[33],[98], and also respiration [110],[128]-[133]. Many studies addressed the respiratory-induced variations of heartbeat morphology in SCG, aiming either to improve the performance of ensemble averaging by applying it separately to groups of similar heartbeats, or to extract respiratory signals to be used for the monitoring of breathing activity.

Pandia et al. investigated the effects of respiration on SCG signals acquired via a MEMS accelerometer both on the midsternal line and the left midclavicular line [130], with the aim of extracting useful signals for respiratory monitoring. To this end, the authors identified three time-domain parameters that are affected by respiration, namely the S1-S1 interval, the S1-S2 interval and the S1-S2 intensity ratio, with S1 and S2 corresponding to the systolic and diastolic complexes of the SCG, in analogy with the heart sounds terminology [130]. The S1-S1 interval is a measure of the inter-beat interval (as much as the R-R interval in the ECG), so the respiratory-induced modulation of the S1-S1 interval simply reflects the physiological respiratory sinus arrhythmia [134], which is not specific to the SCG signal, but confirms its strong relationship with the cardiac cycle and its modulation due to cardio-respiratory interplay. The S1-S2 interval is an estimate of the LVET [135], which is known to be modulated by respiration [52]. Indeed, respiratory-induced changes in intrathoracic pressure result in alterations of both left and right ventricular preload, afterload, and contractility, which in turn affect the pressure gradients across the heart valves [136]-[137], and, eventually, the onset, duration, and force of ventricular contractions [52]. However, the authors reported that, due to beat-to-beat changes in SCG morphology, accurate localization of S1 and S2 complexes to obtain S1-S2 interval estimates was too difficult and unreliable, so they rather directly estimated the variation of S1-S2 interval ($\Delta S1S2$) by finding the time-warped version of each SCG heartbeat that exhibited the highest correlation with the previous beat, and considering the related amount of time warping as an estimate of $\Delta S1S2$. Finally, the authors suggested that the three respiratory-modulated parameters should be used together to provide a robust extraction of respiratory activity from SCG recordings, as an alternative to relying on the near-DC components of measured acceleration (the variable fraction of the gravitational acceleration due to variable chest inclination during breathing) which could be easily fooled by postural changes.

Azad et al. investigated the performance of 6 different respiratory signals, comprising triaxial SCG, against respiratory volume signals extracted from respiratory air flow measurements [131]. The respiratory signals extracted from SCG were the baseline wander (information about chest inclination), the amplitude modulation, and the frequency modulation (respiratory sinus arrhythmia). Among

the SCG-derived respiratory signals, the baseline wandering turned out to be the most reliable.

Taebi and Mansy addressed the effects of respiration on SCG morphology with the aim of improving the results of ensemble averaging by grouping the most similar SCG heartbeats based on the current respiratory phase or lung volume, and then computing the ensemble averages separately on different groups [132]. In fact, by averaging all SCG heartbeats over several respiratory cycles, various time-varying details are filtered out of the resulting ensemble average, thus jeopardizing the effort made to separate the true underlying waveform from the noise. Taebi and Mansy proposed two grouping criteria, one based on the respiratory phase (inspiration/expiration) extracted from respiratory airflow measurements, and one based on the lung volume (low/high) obtained by integrating the respiratory airflow signals. The goodness of grouping was assessed by comparing the differences between a group of heartbeats and their ensemble average versus the differences with the ensemble average of the other group. It turned out that grouping based on lung volume yielded a higher goodness, thus suggesting that lung volume is the main cause of respiratory-induced changes in SCG morphology. However, the methodology proposed by Taebi and Mansy allows distinguishing only two underlying waveforms for SCG, thus neglecting transitions between them.

Zakeri et al. developed a machine learning model based on support vector machines that was able to recognize the respiratory phase (inhalation or exhalation) by analyzing features extracted from single SCG heartbeats [133]. The time averages of 512 intervals (4 ms length) within each heartbeat were considered as time-domain features, while the first 512 Fourier coefficients of each heartbeat (corresponding to the 0 – 500 Hz frequency band) were considered as frequency-domain features. The proposed approach yielded a recognition accuracy of about 88% in leave-one-subject-out validation, and about 95% in single-subject validation. The rationale behind this study was to improve the performance of ensemble averaging by grouping similar SCG heartbeats, in order to filter out noises and disturbances, while maintaining vital differences between SCG waveforms that would have been deleted by ensemble averaging SCG heartbeats with different underlying morphologies.

Moreover, inter and intra subjects' variability of SCG signals is still unclear [13],[33],[98].

3.2.6 Gyrocardiography

Gyrocardiography (GCG) records the rotational components of infrasonic precordial vibrations (i.e., in the 0.1 – 20 Hz frequency range) via gyroscopes placed onto the chest wall. Specifically, it measures the three-dimensional (3D) angular velocity and displacement of the thorax induced by the activity of the beating heart (i.e., twisting and untwisting motion of the myocardium, valves opening and closure, blood flow etc.). This technique was first proposed in 2015 by Meriheinä et al. and originally referred to as angular BCG. In 2016, Tadi et al. introduced the term Gyrocardiography. To date, the most widely used GCG sensors are triaxial gyroscopes manufactured via MEMS technology due to their low cost and power consumption, small size, and high accuracy. It is well-known that the motion of an object has 6 degrees of freedom: 3 translations, which can be measured via accelerometers, and 3 rotations, which can be measured via gyroscopes. Hence, GCG and SCG are complementary techniques, thus recording mutually orthogonal signals. Moreover, GCG, BCG and SCG are all included in the more general Mechanocardiography or Vibrational Cardiography.

GCG signals have amplitude of a few degrees per second (dps). Their x, y and z components are recorded along the horizontal (or transversal), vertical (or longitudinal) and dorso-ventral (or sagittal) axis, respectively. Of these, the y component provides the highest signal-to-noise ratio (SNR). Peaks and valleys on GCG signals have clear correlation with cardiac mechanical events. However, there is a lack of standardization in GCG signal annotation. Some methods adopt a reference signal, such as BCG or SCG, while others provide labels that are the combination of the axis and the point number.

Generally, four fiducial points can be detected in the y-GCG signal, as shown in **Figure 37**, referred to as g_I , g_J , g_K and g_L . In detail, g_I is identified as a negative peak around the R wave in the ECG, g_J is the highest positive peak after the R wave, g_K is a negative peak roughly after the T wave in the ECG, and g_L is a second negative peak after g_K . Moreover, by taking advantage of a simultaneous SCG recording, g_I , g_J , g_K and g_L are recognized as markers of mitral valve closure, aortic valve opening, aortic valve closure and mitral valve opening events, respectively (see **Figure 38**).

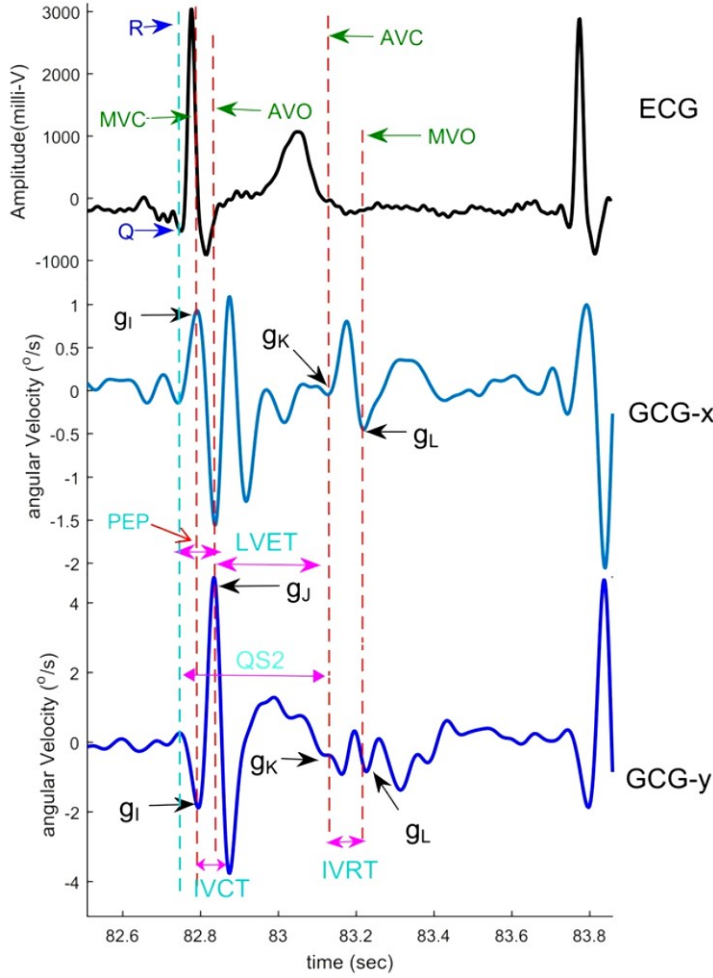


Figure 37. GCG signal annotation, along with a simultaneous electrocardiogram [138].

GCG also provides velocity measurements. Systolic and diastolic peak velocities in GCG signal have been shown to be highly correlated with systolic myocardial velocity and early diastolic velocity obtained from Tissue Doppler Imaging (TDI), which are measures of longitudinal systolic and diastolic function.

Intra and inter subjects' variability of GCG signal is not yet fully understood. Alterations in GCG signal morphology or amplitude reduction can be used for the diagnosis of many CVDs. GCG signal is affected by sensor placement, body mass index (BMI), age, gender, health status, respiration. However, it is less affected by subject's posture than SCG, but peaks on GCG signal have lower temporal accuracy

than those on SCG. GCG is suitable for wearable systems, especially for home monitoring. GCG technique has a wide range of applications such as: estimation of HR, CTIs (in particular, changes in the EMD are referred to as myocardial mechanical dispersion) and SV; analysis of heart rate variability (HRV); diagnosis of CVDs (e.g., atrial fibrillation and other cardiac arrhythmias, myocardial infarction, coronary artery disease, heart failure, aortic stenosis); measurement of PPT when combined to Photoplethysmography (PPG); heartbeat detection; automatic annotation of SCG; motion artifacts removal; measurement of respiratory activity; sleep monitoring; fetal heart rate (FHR) monitoring; identification of heart sounds; assessment of myocardial contractility [15]-[16],[138].

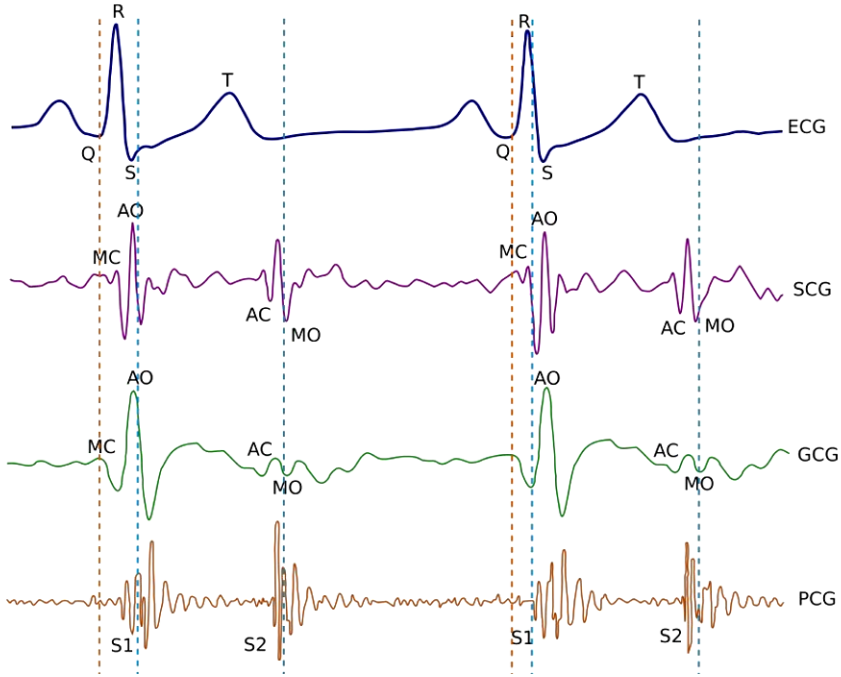


Figure 38. Simultaneous recordings of ECG, SCG (z-axis), GCG (y-axis), and PCG signals captured in the supine position. MC = mitral valve closure; AO = aortic valve opening; AC = aortic valve closure; MO = mitral valve opening [16].

GCG signals are often acquired via small inertial measurement units (IMUs) that contain both accelerometers and gyroscopes. This has led to the investigation on the joint use of GCG and SCG [17],[139]. Moreover, these techniques have also been combined with BCG in the recent Kinocardiography (KCG) [19],[140].

Finally, all cardio-mechanical monitoring techniques described in this chapter are summarized in **Figure 39**.

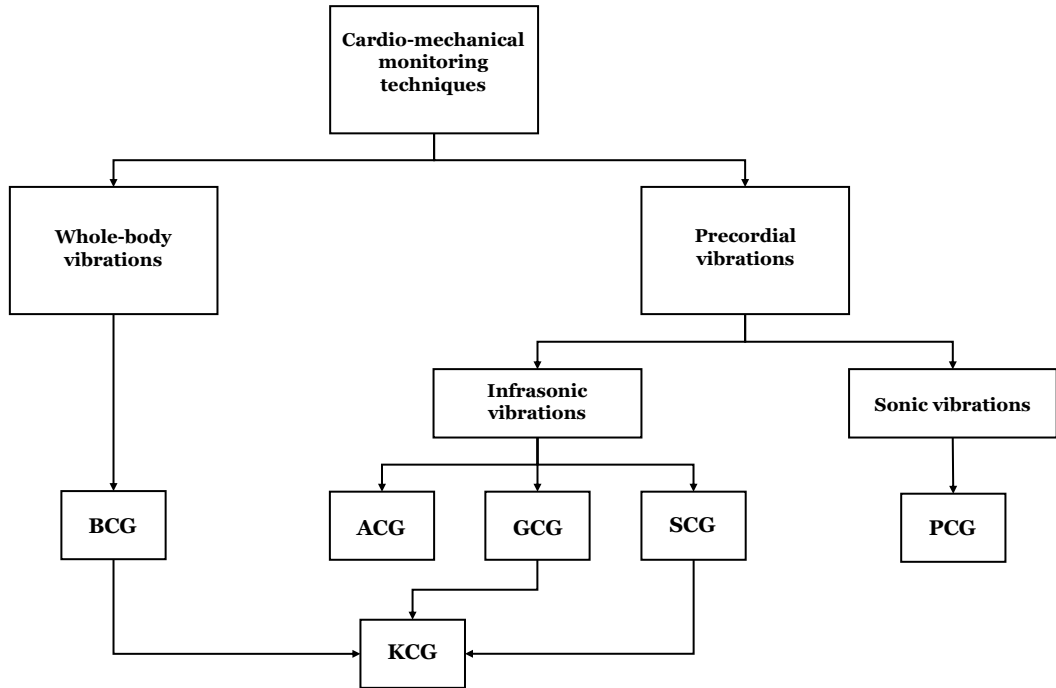


Figure 39. Main cardio-mechanical monitoring techniques.

Chapter 4

Forcecardiography

In this chapter, a novel technique, namely Forcecardiography (FCG), is presented, which has been recently introduced as a promising tool for continuous, non-invasive, mechanical assessment of cardiovascular function [20]-[21] and will be the focus of this thesis. FCG records the local forces induced onto the chest wall by the mechanical activity of the beating heart via broadband force sensors based on the piezoresistive [20] or the piezoelectric effect [21]. FCG sensors are able to acquire infrasonic cardiac vibrations and heart sounds, simultaneously from a single contact point on the chest.

4.1 The FCG signal

The raw signal provided by the FCG sensor consists of two infrasonic components, namely low-frequency FCG (LF-FCG) and high-frequency FCG (HF-FCG), and a sonic component that captures heart sounds, referred to as HS-FCG (see **Figure 40**). These components can be extracted from the raw FCG sensor signal by means of very simple filtering operations in different frequency ranges. The LF-FCG signal is characterized by large, negative peaks occurring approximately at the end of the T waves in the ECG signal, which correspond to forces directed inward. The HF-FCG signal features much smaller, high-frequency oscillations. Finally, the HS-FCG signal has spectral components in the audible range. Hence, the FCG sensor allows

capturing a signal with a rich information content, thus providing valuable information about multiple aspects of the mechanical behaviour of the heart (e.g., heart walls motion, opening and closure of heart valves, blood flow and turbulences, etc).

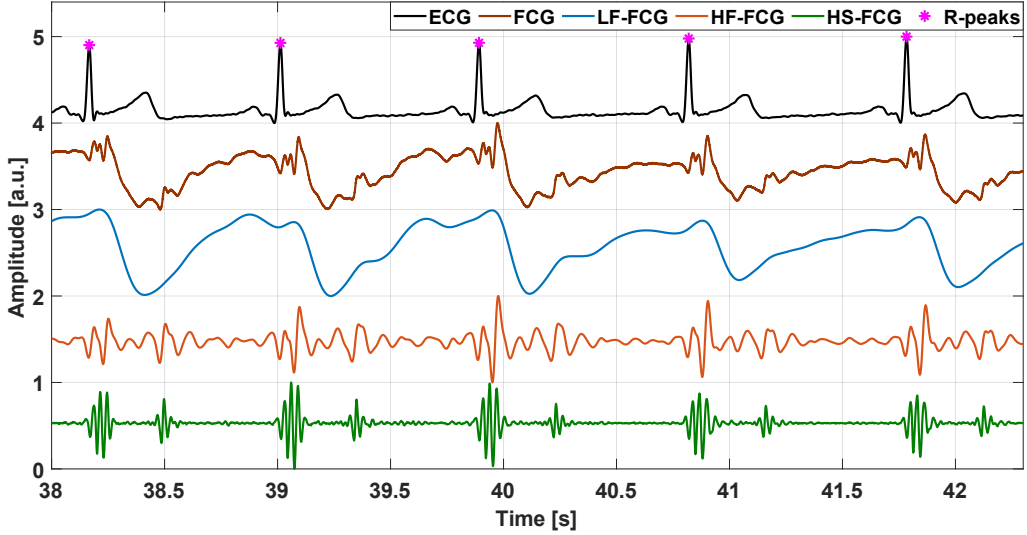


Figure 40. An excerpt of ECG signal (black line) and FCG signal (brown line), along with LF-FCG (blue line), HF-FCG (orange line) and HS-FCG (green line) components. The pink asterisks mark R-peaks locations.

In the studies that first introduced FCG [20]-[21], a morphological comparison between FCG and SCG signals was carried out. To this end, FCG recordings obtained from both a piezoresistive and a piezoelectric FCG sensor were acquired simultaneously with accelerometric SCG signals from the same contact point on the chest, on a standard SCG location (i.e., the xiphoid process) or on the PMI, in order to reliably compare the measurements. Simultaneous ECG signals were also recorded and considered as the benchmark for heartbeats detection; indeed, heartbeats were marked by the locations of R-peaks on the ECG signals. An excerpt of FCG (blue line) and SCG (red line) signals, along with the simultaneous ECG signal (green line), is depicted in **Figure 41**.

The low-frequency and high-frequency components of both FCG and SCG signals were extracted via the same band-pass filtering operations. It has been reported that the slow oscillations observed in the LF-FCG signals seem to be associated with ventricular emptying and filling events, thus potentially carrying information on SV

variations, and cannot be directly appreciated in the corresponding SCG recordings, as shown in **Figure 42**. On the contrary, the HF-FCG components have been shown to share very high similarity with the corresponding SCG signals (see **Figure 43**).

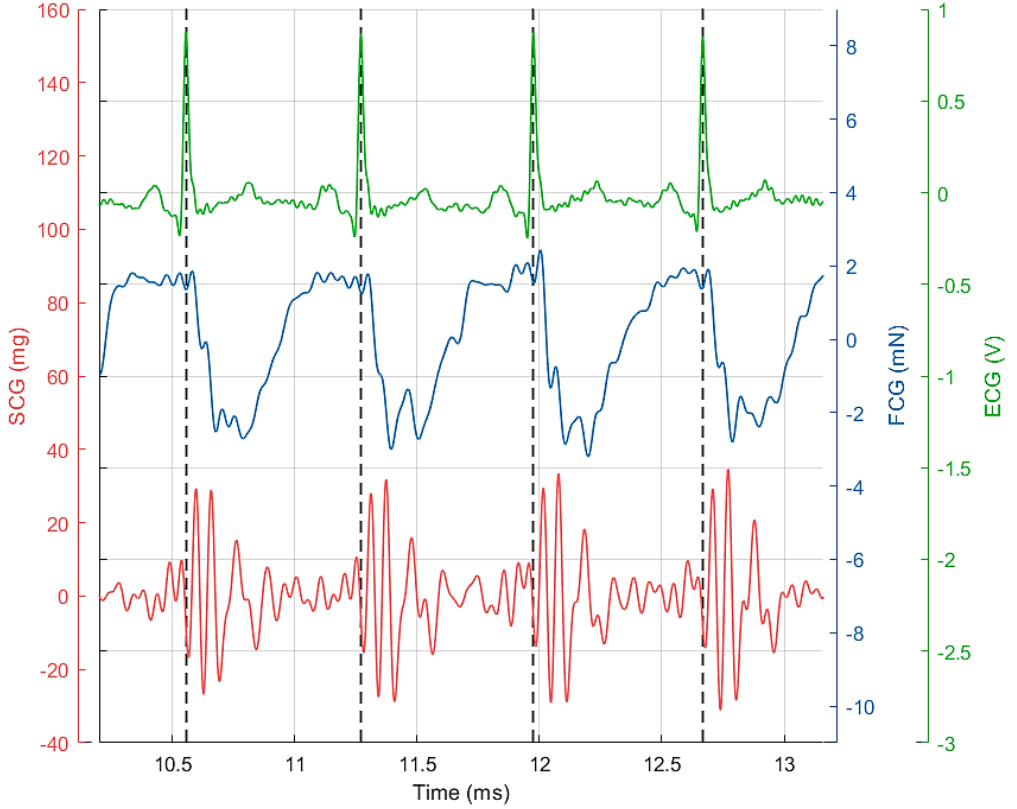


Figure 41. An excerpt of FCG (blue line) and SCG (red line) signals, along with the simultaneous ECG signal (green line). The dashed vertical lines indicate R-peaks locations [20].

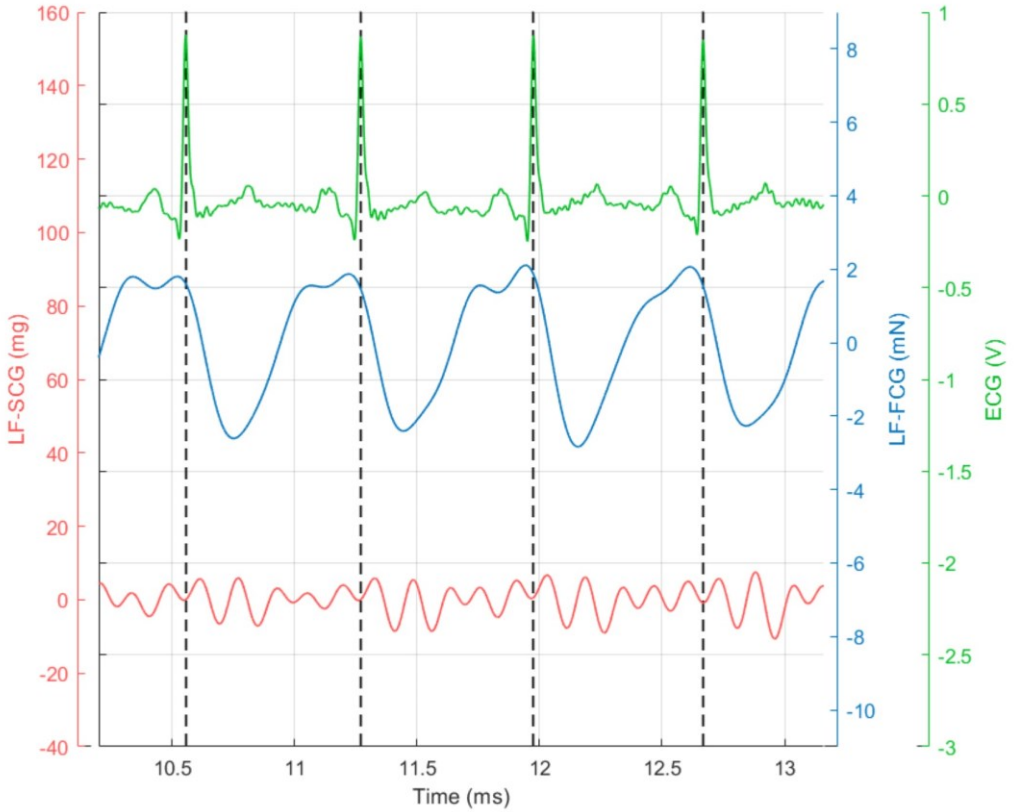
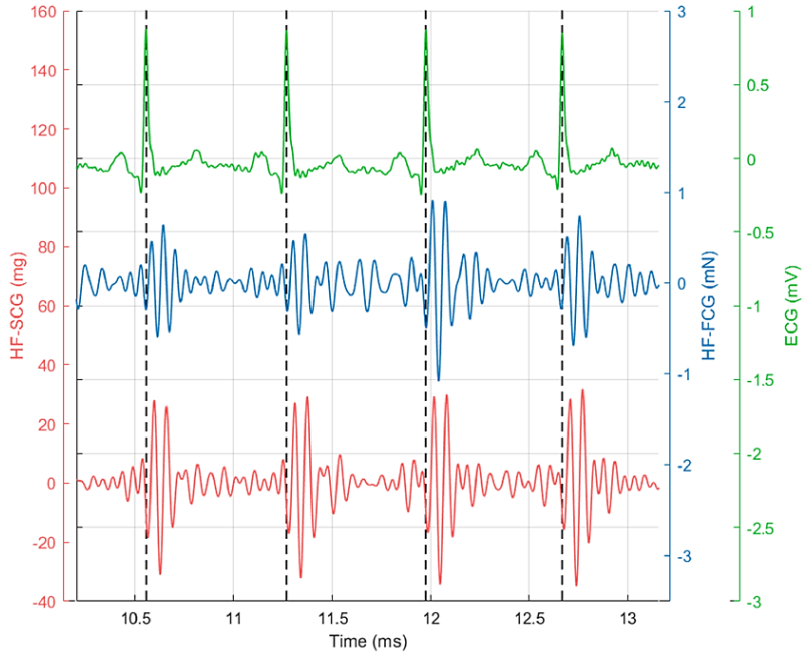
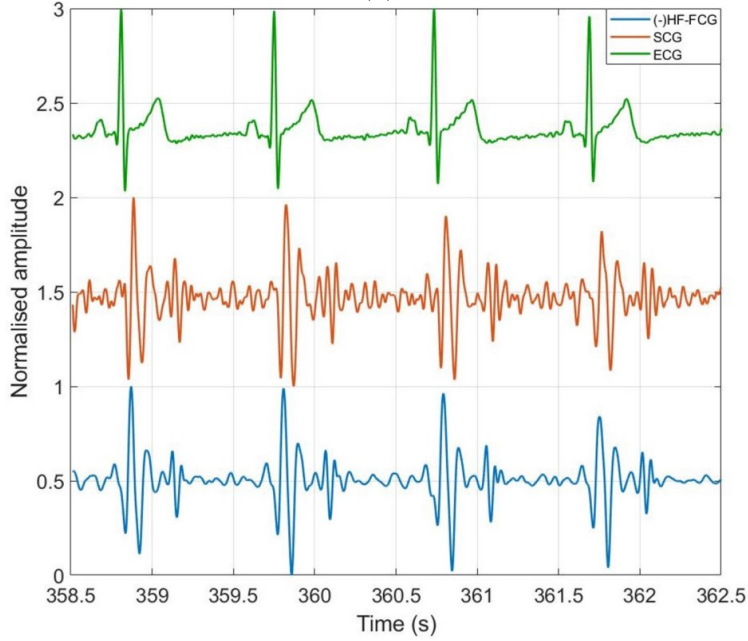


Figure 42. An excerpt of LF-FCG (blue line) and LF-SCG (red line) signals, along with the simultaneous ECG signal (green line). The dashed vertical lines indicate R-peaks locations [20].

4.1 THE FCG SIGNAL



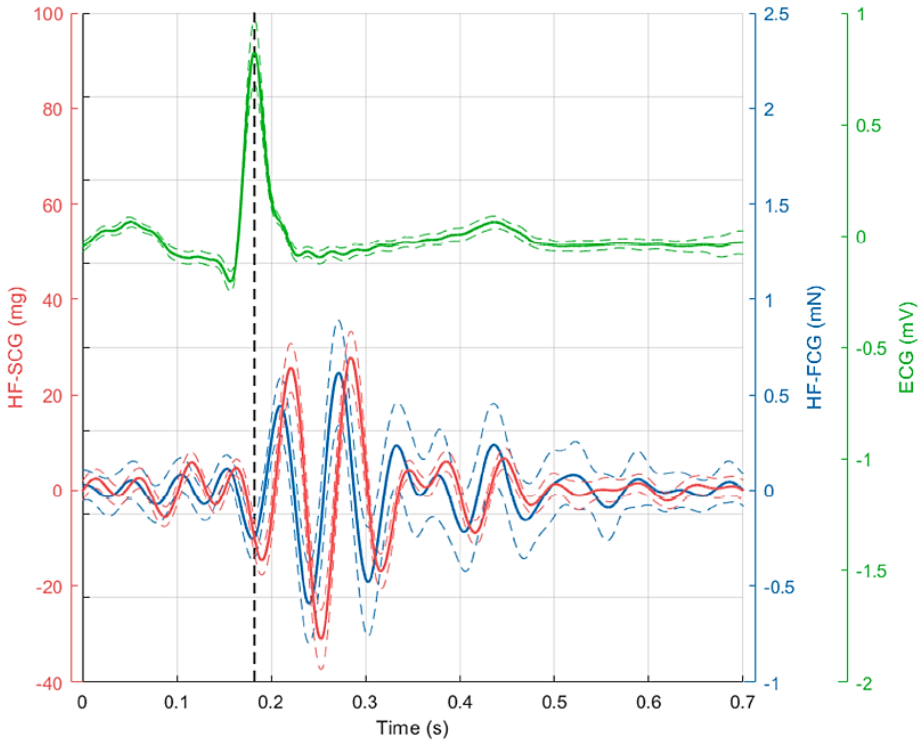
(a)



(b)

Figure 43. Some excerpts of ECG (green line), HF-SCG (red/orange line) and HF-FCG (blue line) signals [20]-[21]. The dashed vertical lines in panel (a) indicate R-peaks locations.

Indeed, the ECG-triggered ensemble averages of the high-frequency components of FCG and SCG signals, synchronized with the R-peaks, turned out be very similar (high Pearson's correlation coefficients), although lagged of about tens of milliseconds (see **Figure 44**).



(a)

4.1 THE FCG SIGNAL

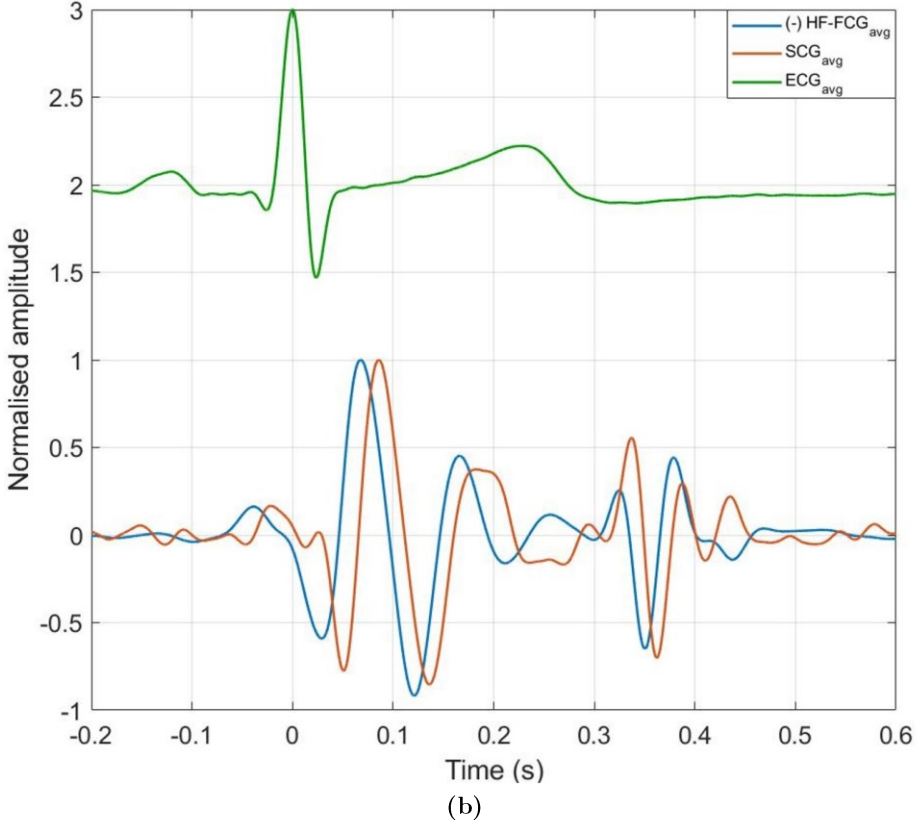


Figure 44. Some examples of ECG-triggered ensemble averages of ECG (green line), HF-SCG (red line) and HF-FCG (blue line), synchronized with the R-peaks [20]-[21]. The dashed lines in panel (a) indicate standard deviation (SD) intervals.

Furthermore, a beat-by-beat comparison with the reference ECG signals was also performed to assess the performances of FCG for cardiac monitoring. Therefore, inter-beat intervals were computed from both LF-FCG and HF-FCG components and compared to the corresponding intervals provided by the ECG signals. In detail, the first largest negative peaks of LF-FCG signals and the first positive peaks of HF-FCG signals, after each R wave in the simultaneous ECG recordings, were considered as heartbeats fiducial points (see **Figure 45**), and then used for the estimation of inter-beat intervals.

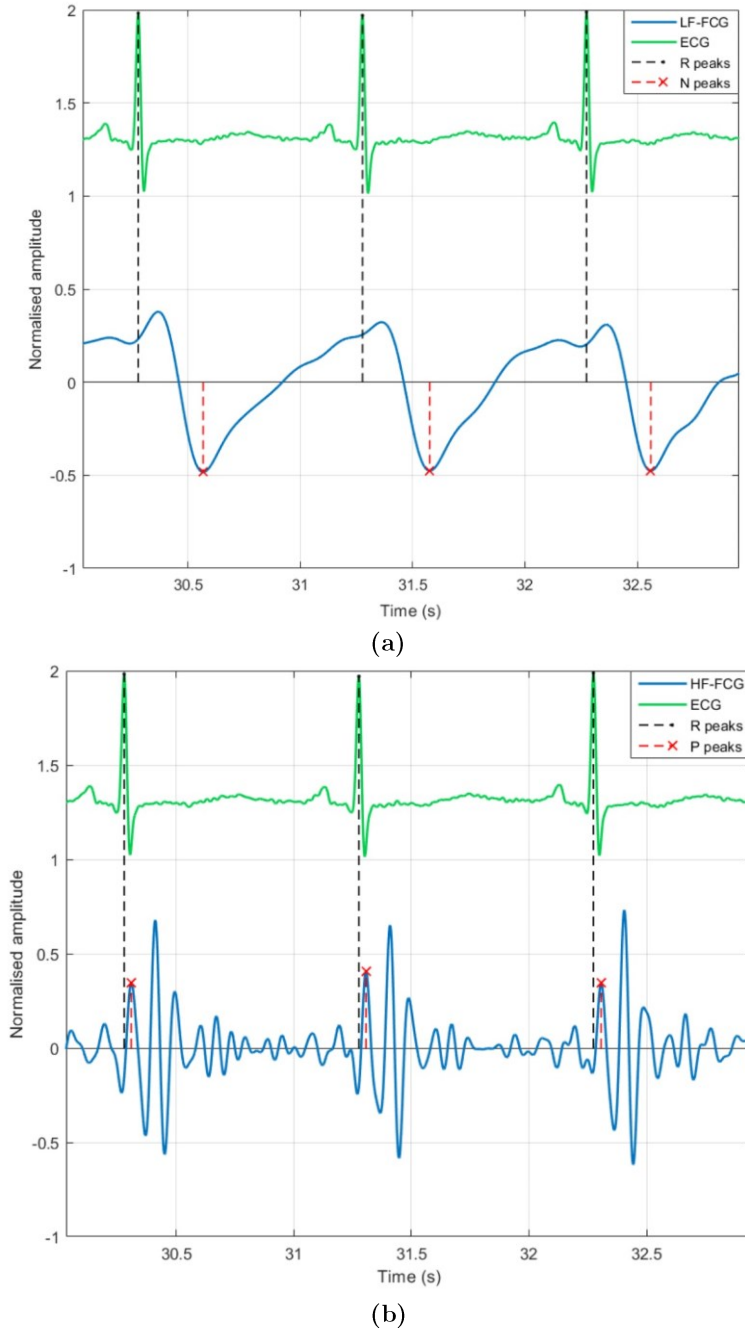
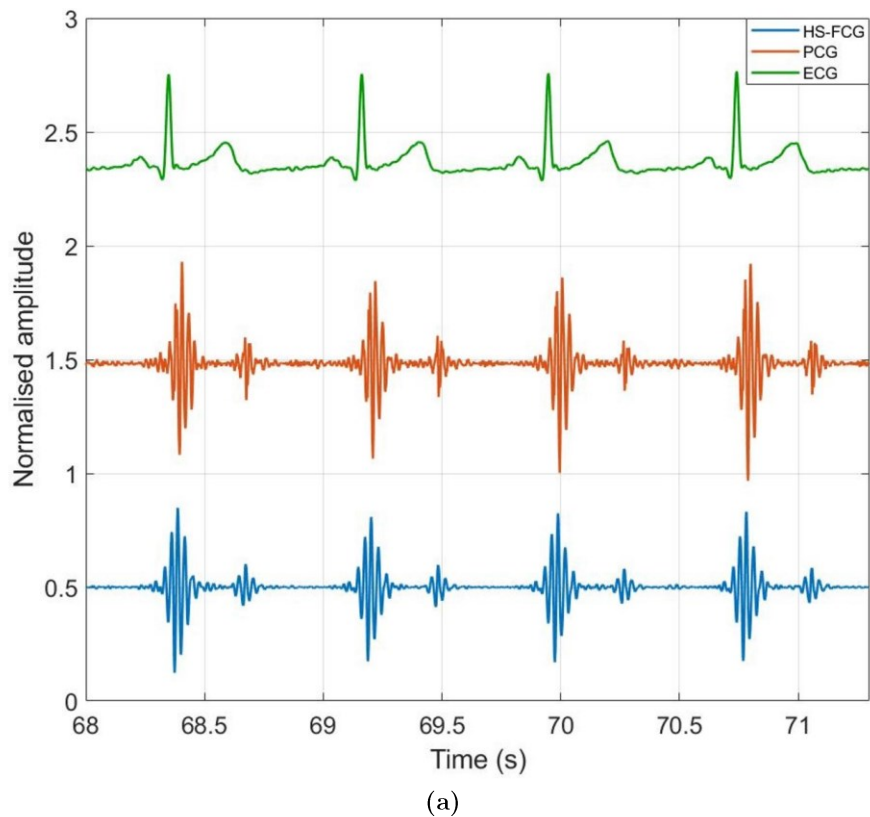


Figure 45. Some excerpts of ECG signal (green line), (a) LF-FCG signal (blue line) with its largest negative peak (red cross) marked as heartbeat fiducial point and (b) HF-FCG signal (blue line) with its positive peak (red cross) marked as heartbeat fiducial point. The dashed vertical lines indicate R-peaks locations [20].

4.1 THE FCG SIGNAL

The results of this beat-by-beat comparison demonstrated that both infrasonic components of FCG signal are strongly related to the cardiac cycle. In addition, also the correlation between HS-FCG signals and simultaneous PCG recordings was assessed (see **Figure 46a**). To this aim, the ECG-triggered ensemble averages of both HS-FCG and PCG signals, synchronized with the R-peaks, were computed in order to evaluate their similarity (see **Figure 46b**).



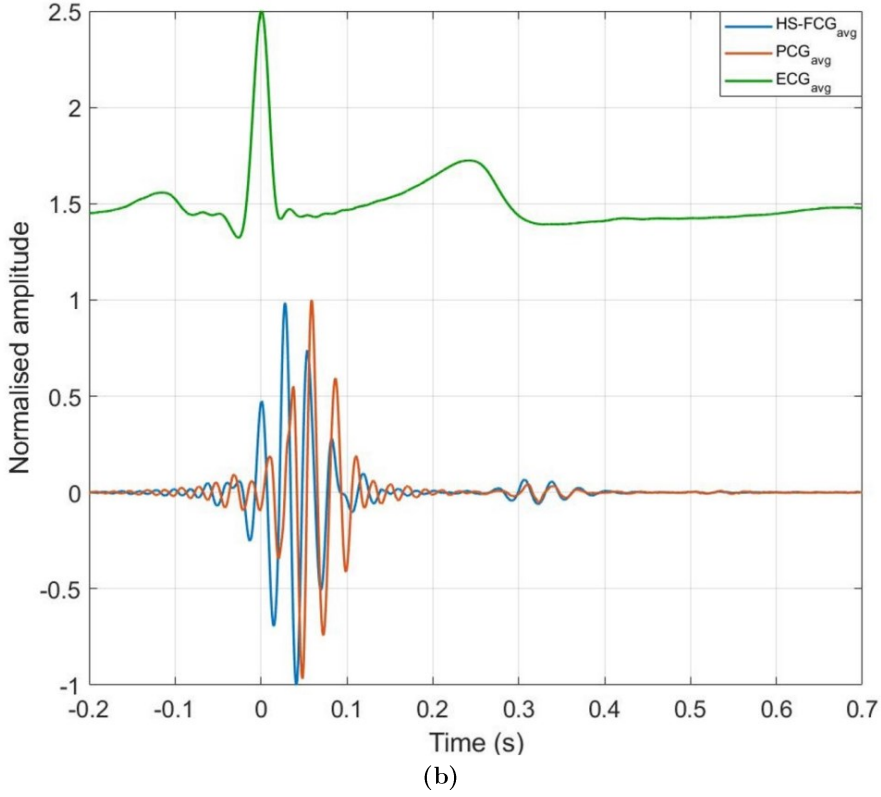


Figure 46. HS-FCG (blue line), PCG (orange line) and ECG (green line) signals: (a) an excerpt; (b) an example of ECG-triggered ensemble averages [21].

A very high similarity was obtained between the HS-FCG and PCG signals, both in terms of morphology and acoustic impression. Moreover, it is worth noting that this sonic component is difficult to acquire by using accelerometers because of low SNRs of SCG signals, which therefore cannot capture heart sounds.

The effect of respiration on FCG signals

This chapter describes the materials and methodologies adopted for the experimental tests aimed at investigating the effect of breathing activity on FCG signals and reports the results obtained from these studies.

5.1 Respiration monitoring via FCG sensors

This study aims to demonstrate the suitability of an FCG sensor [20] for accurate, continuous and unobtrusive monitoring of respiration. FCG sensors are characterized by a wide bandwidth. Therefore, they reasonably appear to be suitable for the measurement of tissues motion originating from many kinds of physiological mechanical events. For this reason, this study investigates their potential application in respiration monitoring. Indeed, if properly coupled with a subject's chest, an FCG sensor can measure the force exerted by the ribcage expansions and consequent releases that occur during the breathing acts, thus offering the possibility to simultaneously record a respiration-related component in addition to the cardiac activity captured by the FCG signal.

5.1.1 The piezoresistive FCG sensor

The FCG sensor used in this study is depicted in **Figure 47**. It consists of a force-sensing resistor (FSR) (FSR03CE, Ohmite Mfg Co, Warrenville, IL, USA), equipped with a rigid dome-shaped mechanical coupler of plastic material, which ensures a good transduction of the force to the sensor's active area. The sensor has an external diameter of 30.50 mm [20].



Figure 47. *The piezoresistive FCG sensor used in the experimental tests.*

The FSR responds to a force applied on its active area by changing its electrical resistance, which must be conveniently transduced into a voltage signal by means of the conditioning circuit depicted in **Figure 48** [141]-[142]. Since the FSR shows a linear response to the impressed force in terms of electrical conductance, a conditioning circuit based on a transimpedance amplifier was used [143]-[144]. This circuit ensures linearity over a wide range of the applied force and minimizes sensor drift by keeping the voltage across the FSR at a constant value [141]-[143]. The

FCG sensor was calibrated before measurements in order to obtain the transduction coefficient from voltage to force [143]-[144].

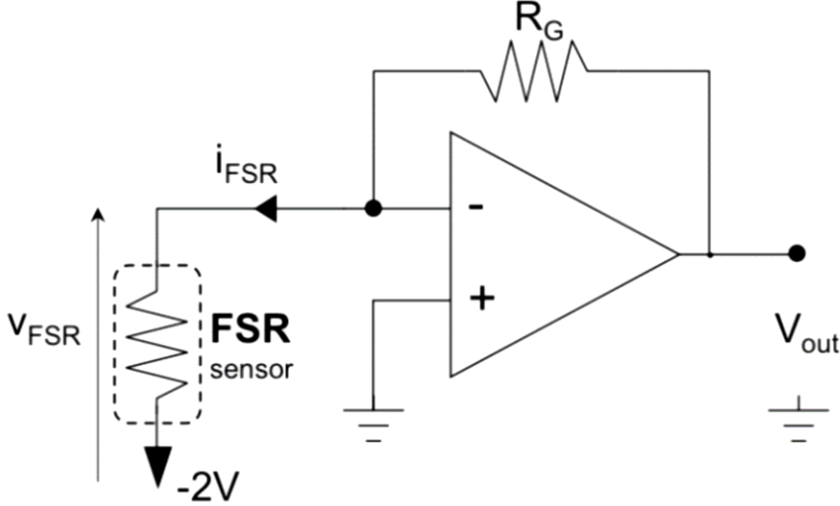


Figure 48. Conditioning circuit for the FSR-based sensor [143].

5.1.2 Electro-resistive band for respiration monitoring

The assessment of FCG sensor performances in respiration monitoring required the comparison with a reference method. To this end, the respiration monitoring method presented in [145], which is based on the use of an electro-resistive (ERB) band applied on the chest of the subject, was adopted as a benchmark. An ERB consists of a stretchable stripe or cord, made of conductive rubber, that increases its electrical resistance when stretched. Hence, it can be used to monitor the increases and decreases in chest circumference that occur during the inhalation and exhalation phases of the respiratory acts. The ERB used in the experimental tests is based on carbon-black-impregnated polymer in a U-shaped configuration and is shown in **Figure 49**.



Figure 49. *The electro-resistive band used in the experimental tests.*

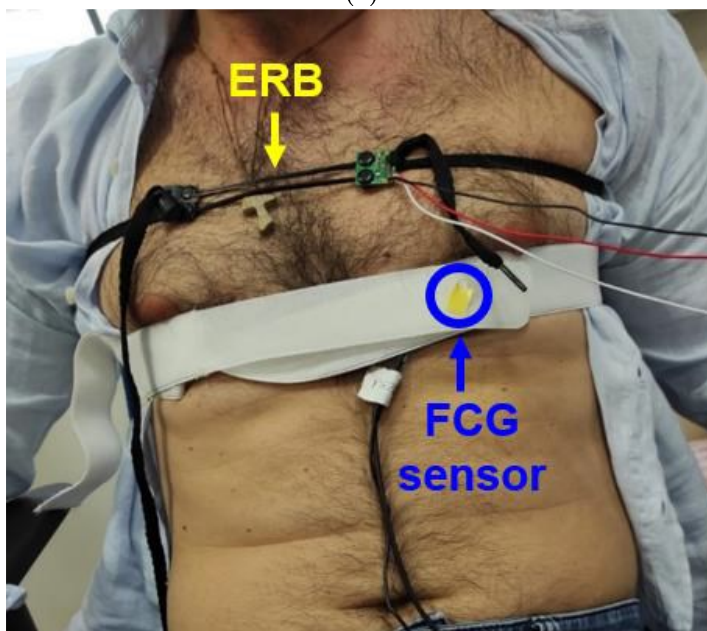
5.1.3 Sensor placement and measurement setup

The FCG sensor was placed on the subjects' chest via a medical adhesive tape, by first locating the PMI (i.e., the point, around the fifth intercostal space on the mid-clavicular line, corresponding to the maximum signal amplitude), and then fastened with a belt around the thorax. The ERB for respiration monitoring was mounted on the upper chest of the subjects so as not to interfere with the FCG sensor. An ECG lead II was also acquired by means of a WelchAllyn Propaq® Encore monitor (Welch Allyn Inc., New York, NY, USA). **Figure 50** shows the placement of the FCG sensor and the ERB on subject #7. The signals provided by the ERB, the FCG sensor and the ECG monitor were simultaneously acquired via a National Instrument NI-USB6009 DAQ board (National Instruments Corp., 11500 N Mopac Expwy, Austin, TX 78759-3504, USA), with 13-bit precision and 5 kHz sampling frequency.

5.1 RESPIRATION MONITORING VIA FCG SENSORS



(a)



(b)

Figure 50. Example of ERB and FCG sensor placement on the chest of subject #7: (a) FCG sensor mounted on patient's chest by means of medical adhesive tape; (b) FCG secured on the chest via a belt fastened around the thorax, and the ERB mounted on the upper chest, so as not to interfere with the FCG sensor.

The experimental tests were carried out on 7 healthy volunteers (5 males and 2 females, age 33.7 ± 11.5 years), who signed the informed consent. The subjects were comfortably seated in a chair, leaning against the seatback while keeping their back straight. Different acquisitions were performed, during which each subject was first asked to breathe in a natural way, then to slightly increase the breathing rate and finally to slow down the respiratory rhythm, so as to obtain measurements of a wide range of breathing rates.

5.1.4 Signal processing and analysis

The raw signals acquired from the FCG sensor, the ERB and the ECG monitor were first pre-processed to extract the respiration signals. In detail, both the FCG and ERB signals were low-pass filtered at 0.6 Hz, to maintain the low-frequency components that provide information on the respiratory activity and filter out the spectral components at higher frequencies, which are mainly related to the cardiac activity and the electronic noise. The rationale for the choice of the cut-off frequency is that the average number of breaths per minute in adult healthy subjects ranges between 12 and 18 [146], corresponding to the 0.2 – 0.3 Hz frequency range, and thus the cut-off frequency was set by considering a doubled rate (i.e., 0.6 Hz) as a reasonable upper limit, able to filter out the cardiac components. The respiration signal extracted from the raw FCG signal was originally referred to as R-FCG to avoid confusion with the whole FCG, which also contains information on the cardiac activity. The ECG-derived respiration (EDR) signal [147]-[148] was extracted from the raw ECG signal by means of the “BioSigKit” MATLAB® toolbox [149] and was reversed in amplitude to obtain positive peaks corresponding to inspiratory acts, as for the R-FCG and ERB respiration signals. Then, in each of the three respiration signals thus obtained, the positive peaks were located via the MATLAB® function “findpeaks”, and the inter-breath intervals were computed as differences between adjacent inspiratory peaks. All processing operations were performed in MATLAB® 2017b (MathWorks, Inc., 1 Apple Hill Drive, Natick, MA, USA).

Figure 51a shows an excerpt of the raw FCG, ERB and ECG signals acquired during this study. In the raw FCG signal, the typical FCG components related to the cardiac activity [20] appear as superimposed to a much larger and slower

component, which is related to the respiration. Indeed, **Figure 51b** shows the respiratory and the cardiac components extracted from the same FCG signal depicted in **Figure 51a**. Examples of ERB, R-FCG and EDR signals are shown in **Figure 52**. In particular, an excerpt from signals acquired on subject #3 during quiet breathing is depicted in panel (a), while excerpts from signals corresponding to forced breathing at higher and lower respiratory rates are shown in panels (b) and (c), respectively. In all three panels, it can be observed that the R-FCG signals featured very similar peaks as compared to the reference ERB signals. The EDR signals, instead, exhibited a much higher variability, which is particularly noticeable in the signals related to the forced slower breathing. Indeed, the EDR clearly presented peaks that turned out to be inconsistently lagged with respect to ERB ones, as well as a number of double peaks corresponding to single ERB peaks, which resulted in a conspicuous number of spurious peak detections.

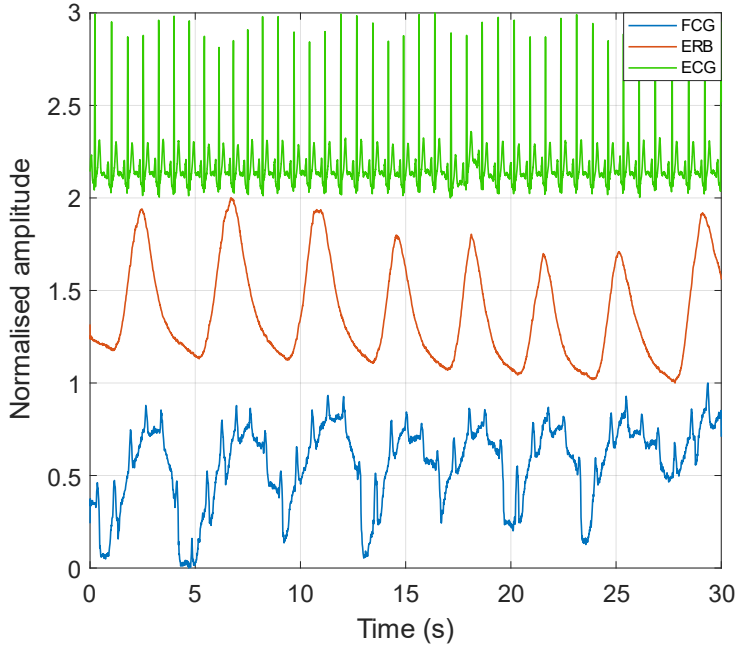
The inspiratory peaks detected in the R-FCG and EDR signals were compared with those detected in the ERB signals to annotate the number of missed and spurious peaks. **Table 1** outlines the number of respiratory acts detected per subject in the ERB, R-FCG and EDR signals, along with the number of missed and spurious acts in the R-FCG and EDR signals. Hence, the performance of respiratory acts detection was assessed by computing sensitivity and positive predictive value (PPV) according to the following mathematical expressions:

$$Sensitivity = \frac{TP}{TP + FN} \cdot 100 \quad (10)$$

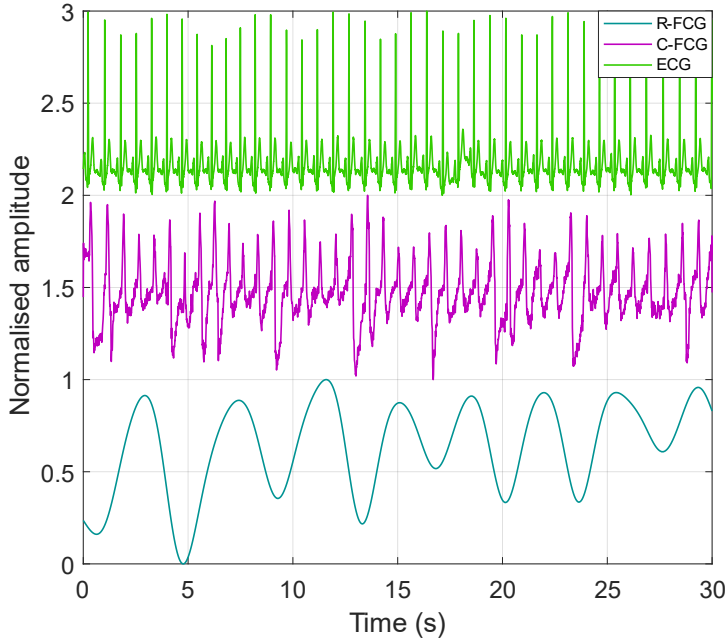
$$PPV = \frac{TP}{TP + FP} \cdot 100 \quad (11)$$

where TP is the number of true positives, FN is the number of false negatives and FP is the number of false positives.

In detail, the respiratory acts detected in the ERB signals and in the R-FCG and EDR signals of all subjects were considered as TP, while the number of missed and spurious acts, detected in the R-FCG and EDR signals with respect to the reference ERB signals, were considered as FN and FP, respectively.

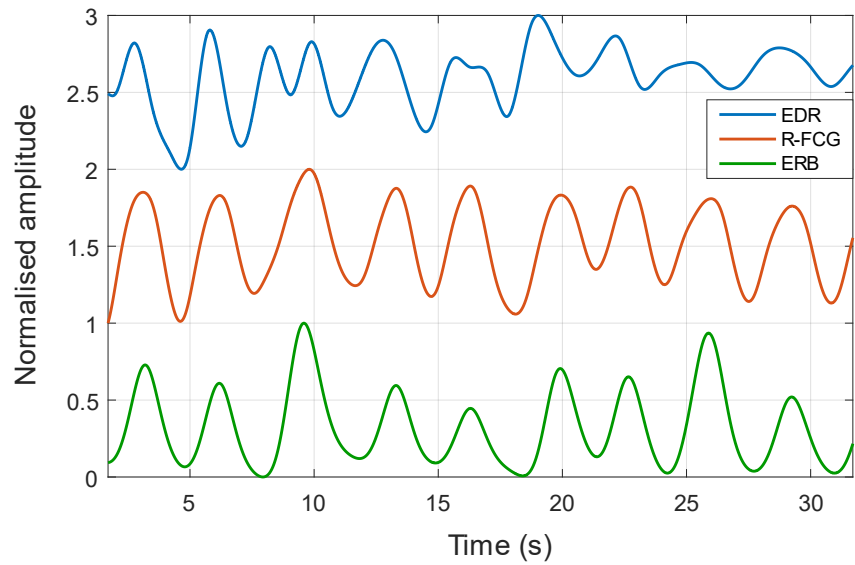


(a)

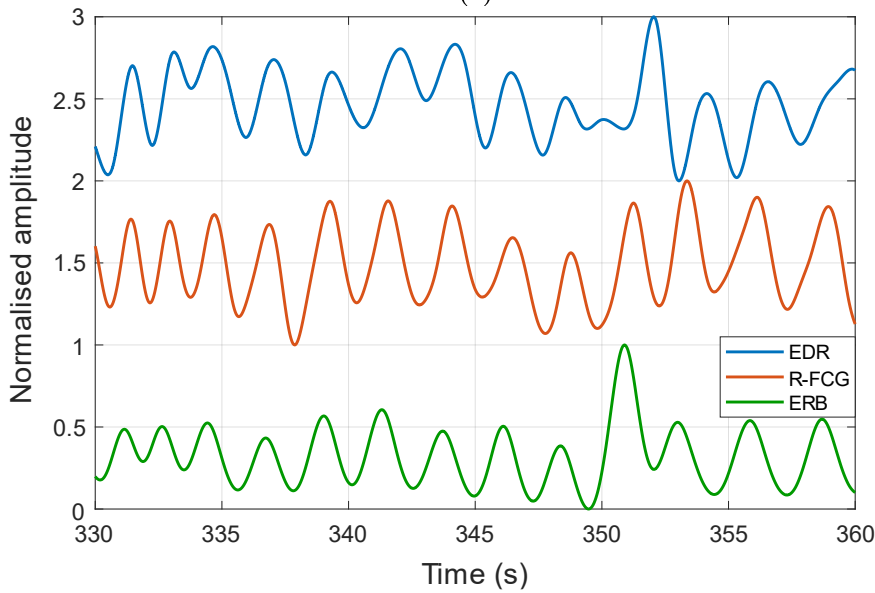


(b)

Figure 51. (a) An excerpt of raw FCG, ERB and ECG signals acquired from subject #7; (b) respiratory (R-FCG) and cardiac (C-FCG) components extracted from FCG signal depicted in panel (a).



(a)



(b)

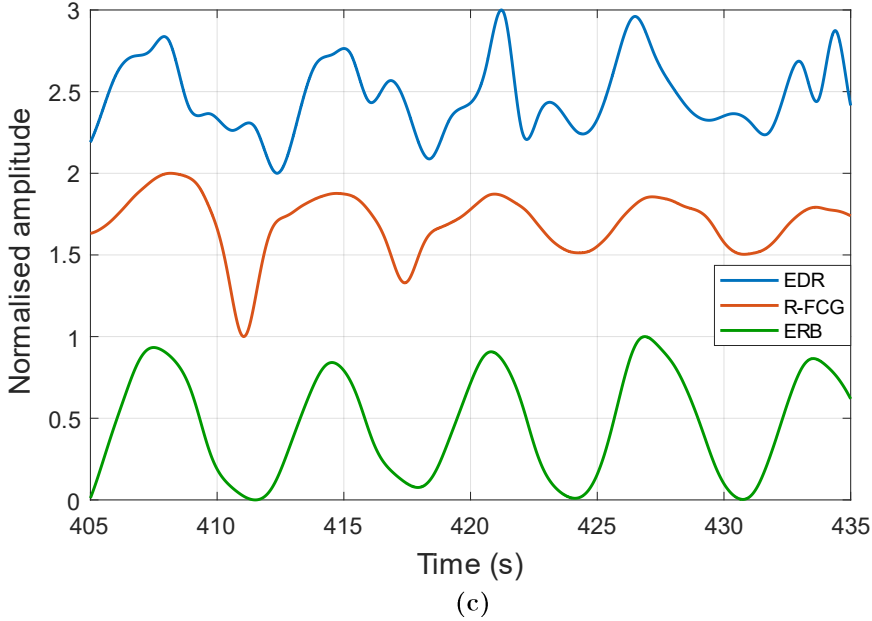


Figure 52. Examples of ERB, R-FCG and EDR signals extracted from data acquired on subject #3: (a) quiet breathing; (b) forced breathing at higher rate; (c) forced breathing at lower rate.

Table 1. Respiratory acts detected in the ERB, R-FCG and EDR signals. The missed and spurious acts are reported for the R-FCG and EDR signals with reference to the acts detected in the ERB signal.

Subject #	Respiratory acts			Missed acts		Spurious acts	
	ERB	R-FCG	EDR	R-FCG	EDR	R-FCG	EDR
1	90	93	95	0	0	3	5
2	110	111	107	0	7	1	4
3	177	180	178	0	6	3	7
4	74	74	75	0	3	0	4
5	86	87	95	0	3	1	12
6	76	76	88	0	12	0	24
7	130	130	132	0	0	0	2
Total	743	751	770	0	31	8	58

A total of 743 respiratory acts were detected in the reference ERB signals. No missed respiratory acts were found in the R-FCG signal, i.e., all actual inspiratory peaks were correctly detected, and only 8 spurious peaks were misclassified as actual

respiratory acts. Hence, the R-FCG scored a sensitivity of 100% and a PPV of 98.9%. As opposed to the R-FCG signal, a total of 31 missed respiratory acts were found in the EDR signal, along with 58 spurious respiratory acts, resulting in an overall sensitivity and a PPV of 95.8% and 92.5%, respectively. Sensitivity and PPV of respiratory acts detection in the R-FCG and EDR signals are also reported in **Table 2**.

Table 2. *Sensitivity and PPV of respiratory acts detection in the R-FCG and EDR signals.*

	Sensitivity (%)	PPV (%)
R-FCG	100	98.9
EDR	95.8	92.5

The accuracy and reliability of the FCG sensor in respiration monitoring were assessed by comparing the inter-breath interval measures obtained from the R-FCG signals with those provided by the ERB. To this end, correlation and Bland–Altman [150]–[151] analyses were carried out via the MATLAB® function “bland-altman-and-correlation-plot” [152]. The same analyses were repeated for the inter-breath intervals obtained from the EDR. Finally, the FCG sensor and EDR performances obtained from these analyses were compared. In detail, the intervals related to the missed and spurious respiratory acts were discarded from both the particular signal under test and the reference ERB signal, so as to carry out the analyses only on reliable measurements. The statistical analyses were performed on 743 and 689 inter-breath intervals for the R-FCG and EDR signals, respectively, and the results are depicted in **Figure 53** and **Figure 54**. The correlation analysis reported for the R-FCG a slope and intercept of 0.99 and 0.026 s, with a coefficient of determination (R^2) of 0.98, and for the EDR a slope and intercept of 0.98 and 0.11 s, with an R^2 value of 0.88. The Bland–Altman analysis reported a null bias (p-value = 0.87) with limits of agreement (LoA) of ± 0.61 s for the R-FCG and a bias of 0.040 s (not statistically significant as p-value = 0.11) with LoA of (−1.4; +1.5) s for the EDR. The results of regression, correlation and Bland–Altman analyses are also summarized in **Table 3**.

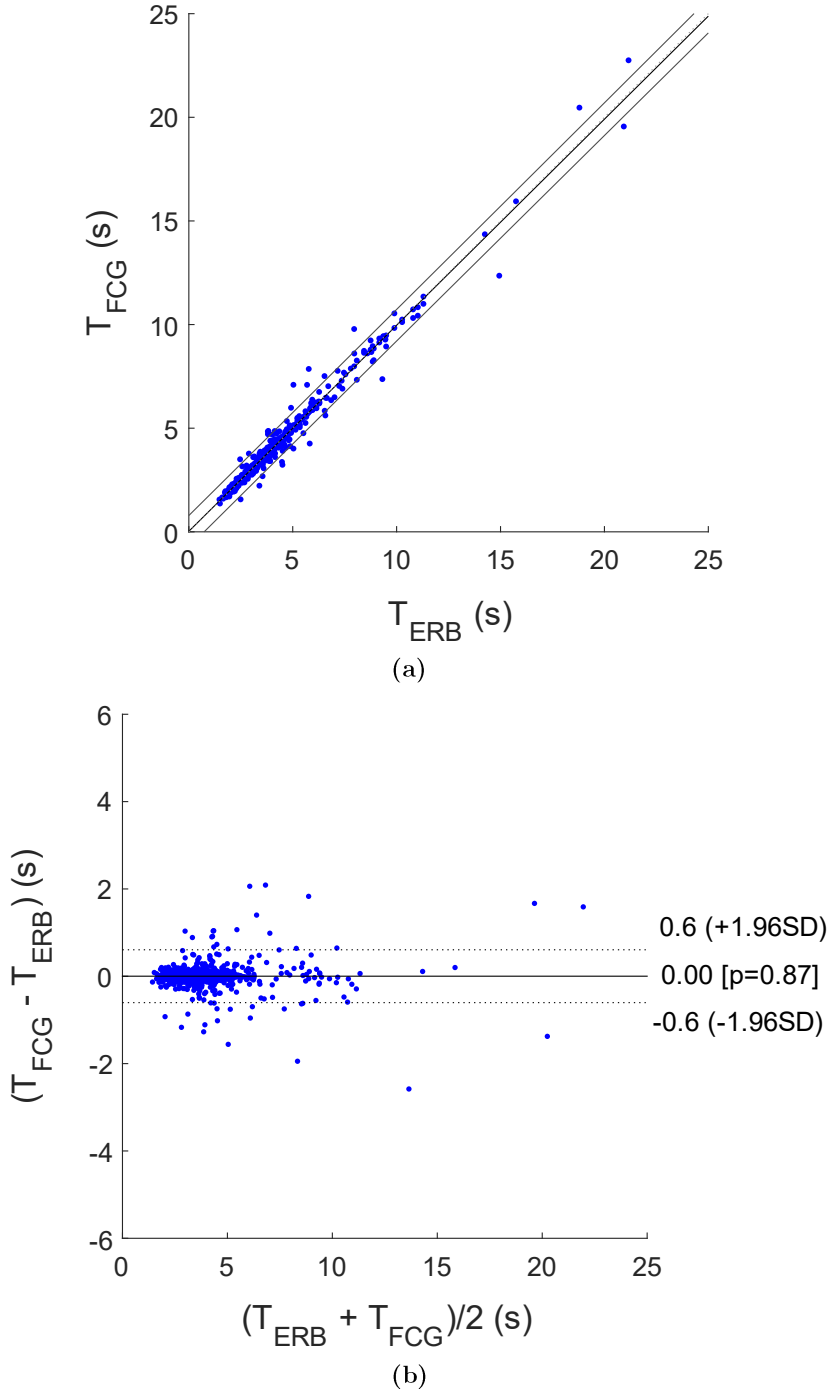


Figure 53. Statistical analyses on inter-breath intervals estimated from EDR and ERB: (a) results of correlation analysis; (b) results of Bland–Altman analysis.

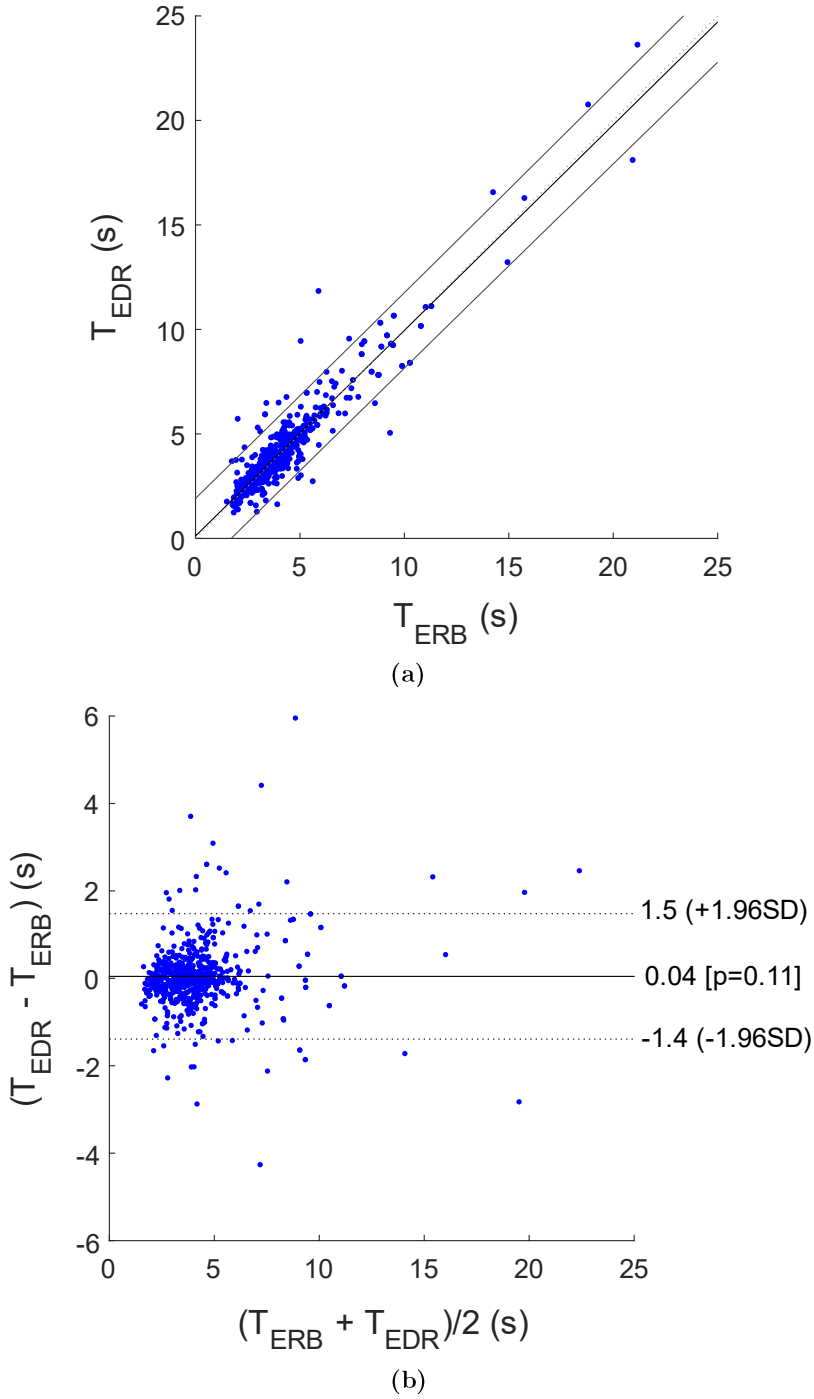


Figure 54. Statistical analyses on inter-breath intervals estimated from FCG and ERB: (a) results of correlation analysis; (b) results of Bland-Altman analysis.

Table 3. Results of regression, correlation and Bland–Altman analyses for R-FCG and EDR signals. Non-significant bias is indicated as “NS”.

	Slope	Intercept (s)	R ²	Bias	p-value	LoA (s)
R-FCG	0.99	0.026	0.98	0.0	0.87	± 0.61
EDR	0.98	0.11	0.88	NS	0.11	(-1.4; +1.5)

5.1.5 Discussion

The results of this study demonstrated the feasibility of FCG sensors for respiration monitoring, which provides accurate detection and measurements of respiratory cycles in subjects at rest. Although no particular problems arose with the two female subjects involved in this study, some issues may possibly arise due to the particular morphology of the breasts. In principle, large breast tissue could cause attenuation of the precordial vibrations, as well as motion artifacts. This hypothetical drawback deserves deeper investigation in larger female cohorts. The possibility of monitoring the respiration and FCG signals simultaneously by means of a single, local, small, unobtrusive, cheap sensor extends the scope of FCG to monitoring multiple vital signs, as well as to the analysis of cardiorespiratory interactions, also paving the way for applications that support the pervasive, continuous, long-term monitoring of cardio-respiratory functions in patients with heart and pulmonary diseases. Moreover, future studies should focus on assessing the viability of FCG-based monitoring in physical activities, such as walking or running, performing heavy work or engaging in sport activities. This would require extensive testing to verify the robustness of FCG regarding motion artifacts, as already observed in accelerometers-based SCG studies [153]-[156].

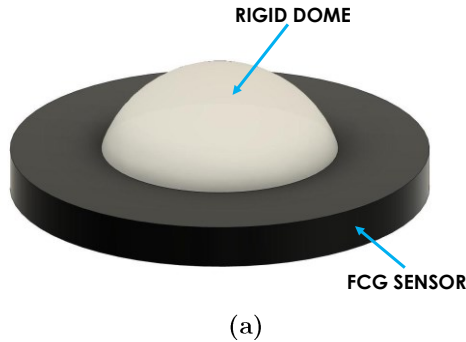
5.2 Respiratory-induced amplitude modulation of FCG signals

The sonic and infrasonic components of the FCG signal reflect mechanical waves that propagate from the heart to the chest surface, where they are sensed by FCG sensors placed in fixed sites of the chest wall. Since the heart experiences upward

and downward motions during respiration, these mechanical waves turn out to be generated by a moving source and propagate along paths of varying length and physical properties. Depending on the position of the measurement site over the chest, the varying distance from the source is reasonably to cause a likewise variable attenuation of the amplitude of the mechanical waves, thus resulting in amplitude modulation of the FCG signal components. This study investigates the effect of respiration on FCG signals, by focusing on the respiratory-related amplitude modulation of LF-FCG and HF-FCG signals sensed from a specific site over the chest.

5.2.1 The piezoelectric FCG sensor

A retrospective analysis of the signals acquired in [21] was carried out in this study. The FCG sensor used in [21] consists of a lead-zirconate-titanate (PZT) piezoelectric disk enclosed in a plastic cylindric protective shell (see **Figure 55a**). The PZT sensor has an electrical capacitance of 22 nF (measured via a GWINSTEK LCR-816 LCR meter at 2 kHz) and an external diameter of 30.50 mm. The sensor was loaded with a very large resistance and amplified via a voltage amplifier, which is depicted in **Figure 55b**. This conditioning circuit allows obtaining a good response at very low frequencies, thus providing a cut-off frequency lower than 0.005 Hz. Furthermore, the sensor was equipped with the same dome-shaped mechanical coupler used for the FSR-based sensor, as in [20]-[21], which ensures good mechanical transduction from the subject's skin.



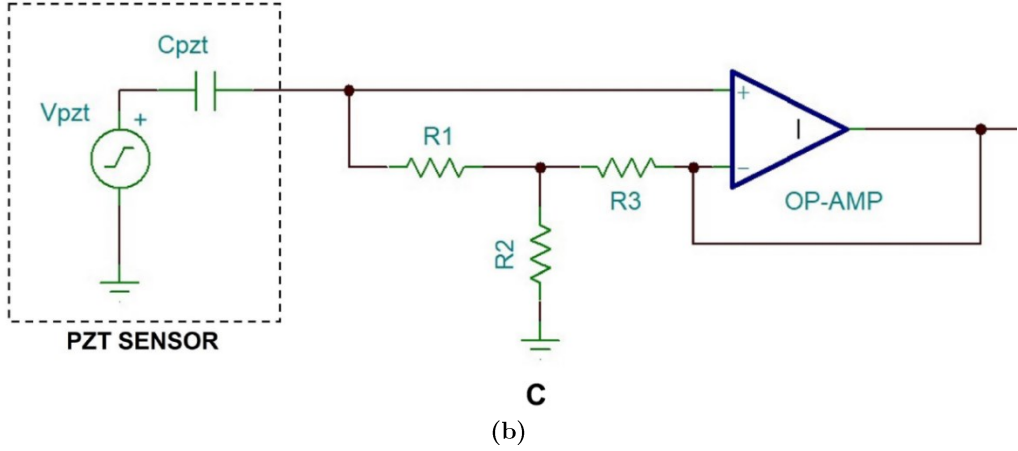


Figure 55. The piezoelectric FCG sensor used in the experimental tests: (a) schematic representation; (b) conditioning circuit for the PZT sensor [21].

5.2.2 Sensor placement and measurement setup

The FCG sensor was placed on the subjects' chest via a medical adhesive tape, by roughly locating the PMI, as shown in **Figure 56**, and then fastened with a belt around the thorax.

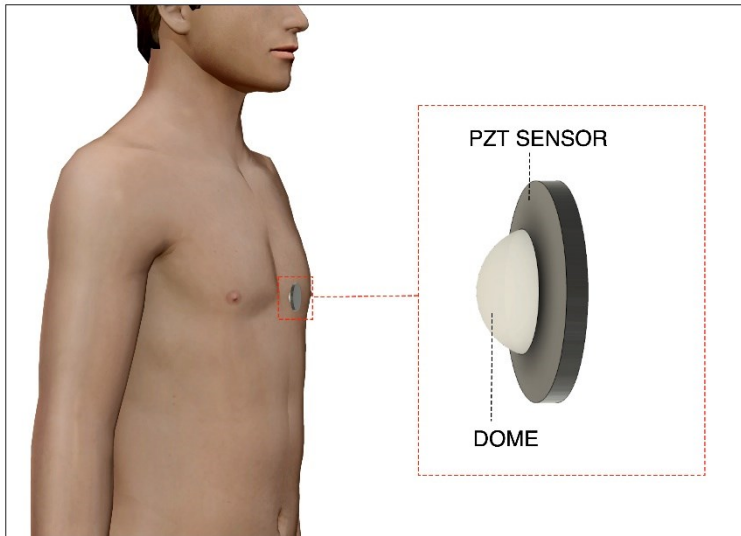


Figure 56. Piezoelectric FCG sensor placement.

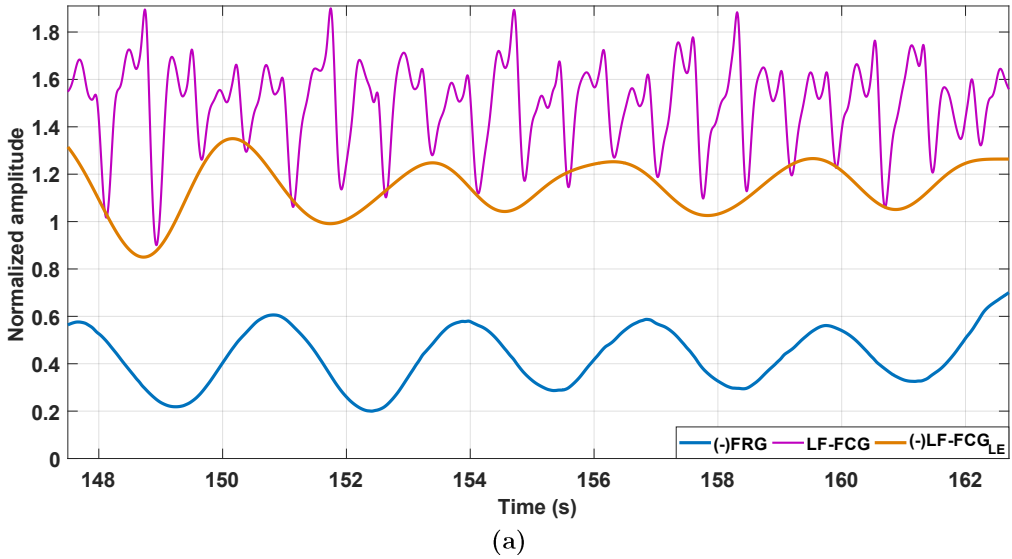
Six subjects (4 males and 2 females, age 36.6 ± 11.0 years) were enrolled for this study, who were comfortably seated in a chair, leaning against the seatback, while keeping their back straight. FCG acquisitions were performed via a National Instrument NI-USB4431 DAQ board (National Instruments Corp., 11,500 N Mopac Expwy, Austin, TX 78759-3504, USA), with 24-bit precision and 10 kHz sampling frequency. FCG recordings were acquired during quiet breathing.

5.2.3 Signal processing and analysis

As demonstrated in the previous study (see Section 5), the raw FCG sensor signal is composed by a large, very low-frequency component related to the breathing activity, referred to as the Forcerespirogram (FRG), which was originally named R-FCG, and a much smaller, superimposed component related to the cardiac activity, which represents the actual Forcecardiogram. Such components must be separately analysed, so an efficient separation strategy is required. To this aim, the FRG component was first extracted, and then subtracted from the raw FCG signal in order to isolate the actual FCG. The FRG was extracted via a 3rd order Savitzki–Golay filter [157], with a frame length corresponding to an approximate interval of 1.5 s. As opposed to common filters, the Savitzki–Golay filter fits signal portions of a given length with polynomials of a given order. This makes it well suited to separate a large signal from a much smaller oscillating signal, which is the case of the superimposed large respiratory component and the much smaller cardiac components of the raw FCG sensor signal. The actual FCG signal obtained by subtracting the FRG consists of two infrasonic components, namely LF-FCG and HF-FCG, and an audible component, corresponding to the heart sounds (HS-FCG). The analyses carried out during this study focused on the two infrasonic components, which were extracted from the FCG signal via band-pass filtering. In particular, 4th order zero-lag Butterworth band-pass filters with 0.6–5 Hz and 7–30 Hz frequency bands were used to extract the LF-FCG and HF-FCG components, respectively. In order to obtain information on the amplitude modulation of the LF-FCG and HF-FCG signals, their linear envelopes were extracted by performing rectification (i.e., absolute value), followed by a low-pass filtering via a 4th order zero-lag Butterworth filter with a cut-off frequency of 0.5 Hz. The linear envelopes

were further filtered via the same 3rd order Savitzki–Golay filter used to extract the FRG signal. For all the subjects considered in this study, the heart rate was always more than two times the respiratory rate. This ensured the correct extraction of amplitude modulation, since the Nyquist–Shannon criterion was always met.

Figure 57 depicts some excerpts of the FRG signals, LF-FCG signals and their linear envelopes from subjects #4 and #5. It could be noted by visual inspection that the amplitude of the LF-FCG signals (violet lines) appeared to be modulated by the respiration; indeed, their linear envelopes (orange lines) reflected the morphology of the FRG signals (blue lines) very well. The good similarity between the FRG signals and the linear envelopes of LF-FCG signals is highlighted by **Figure 58**, which shows some excerpts of these signals from subjects #4 and #5.



5.2 RESPIRATORY-INDUCED AMPLITUDE MODULATION OF FCG SIGNALS

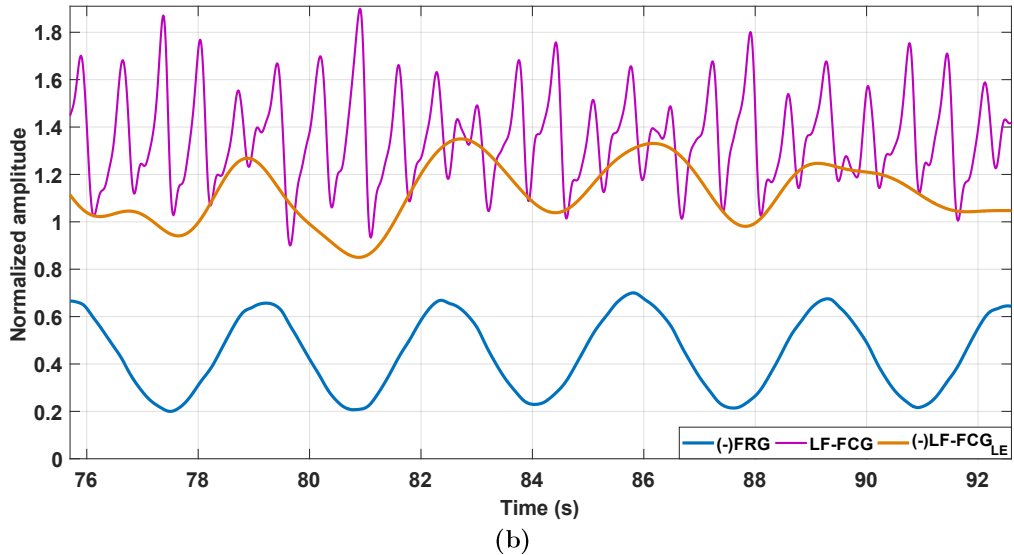
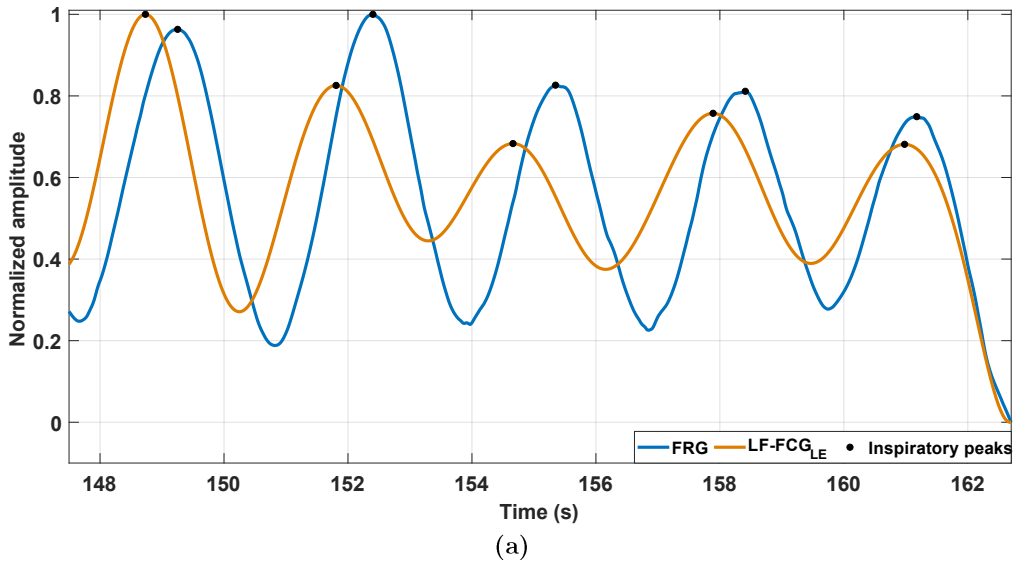


Figure 57. Some excerpts of FRG signal (blue line), LF-FCG signal (violet line) and its linear envelope (orange line) from: (a) subject #4; (b) subject #5.



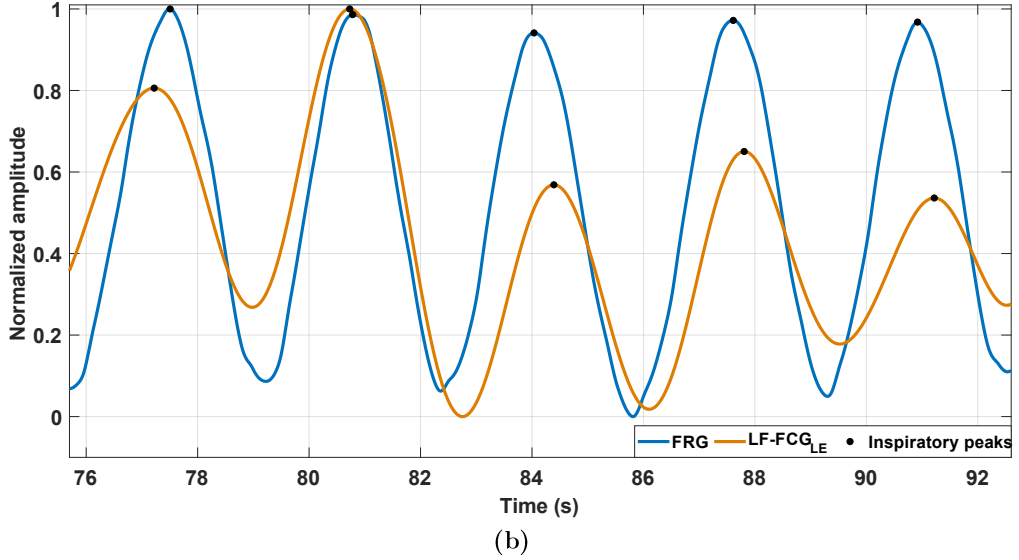


Figure 58. Some excerpts of FRG signal (blue line) and the linear envelope of LF-FCG signal (orange line) from: (a) subject #4; (b) subject #5.

Figure 59, instead, depicts some excerpts of the FRG signals, HF-FCG signals and their linear envelopes from the same subjects #4 and #5. It could be observed that also the amplitude of the HF-FCG signals (red lines) was modulated by the respiration and their linear envelopes (green lines) reflected the morphology of the FRG signals (blue lines) very well. The high similarity between the FRG signals and the linear envelopes of HF-FCG signals is highlighted by **Figure 60**, which shows some excerpts of these signals from subjects #4 and #5.

5.2 RESPIRATORY-INDUCED AMPLITUDE MODULATION OF FCG SIGNALS

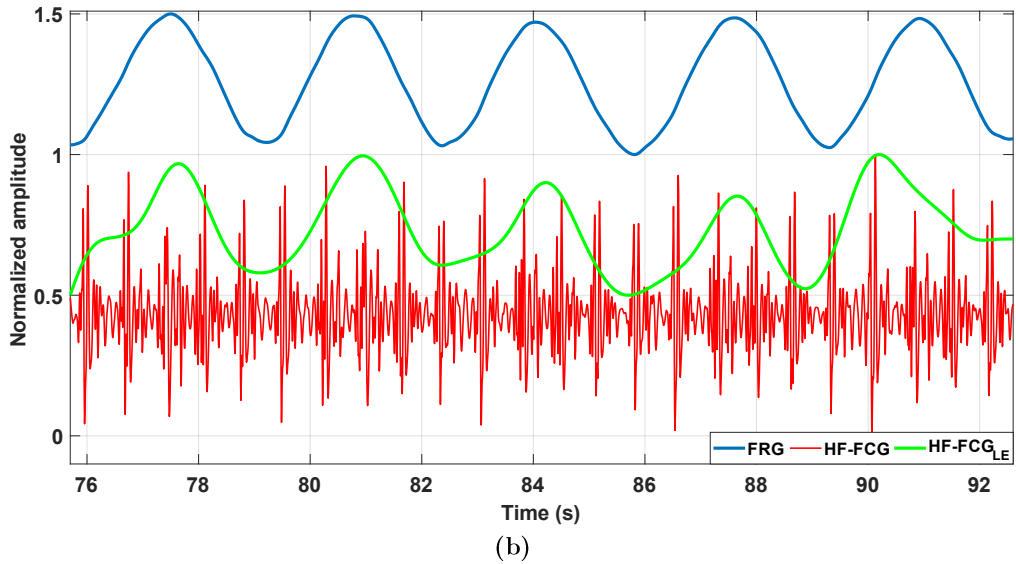
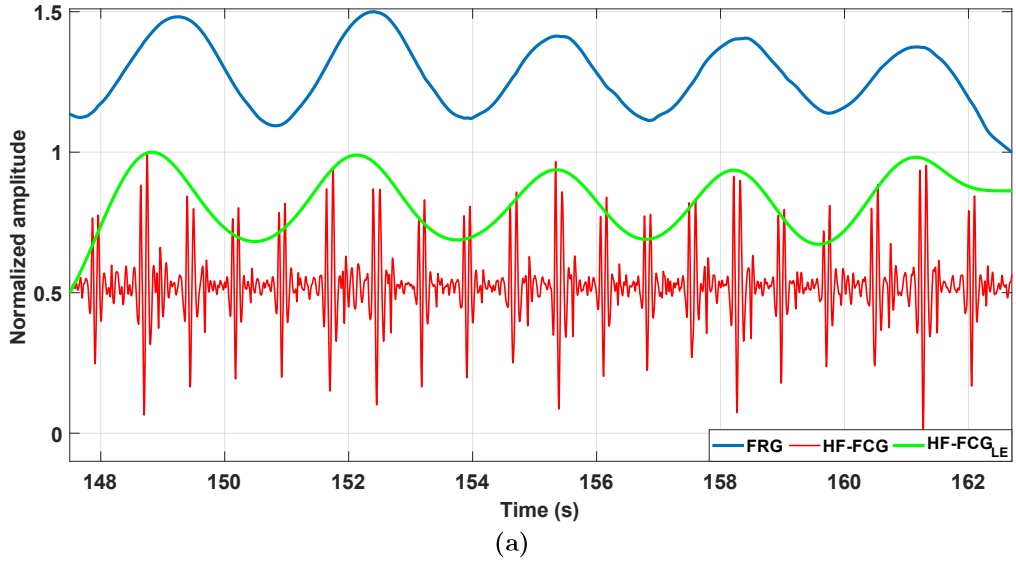


Figure 59. Some excerpts of FRG signal (blue line), HF-FCG signal (red line) and its linear envelope (green line) from: (a) subject #4; (b) subject #5.

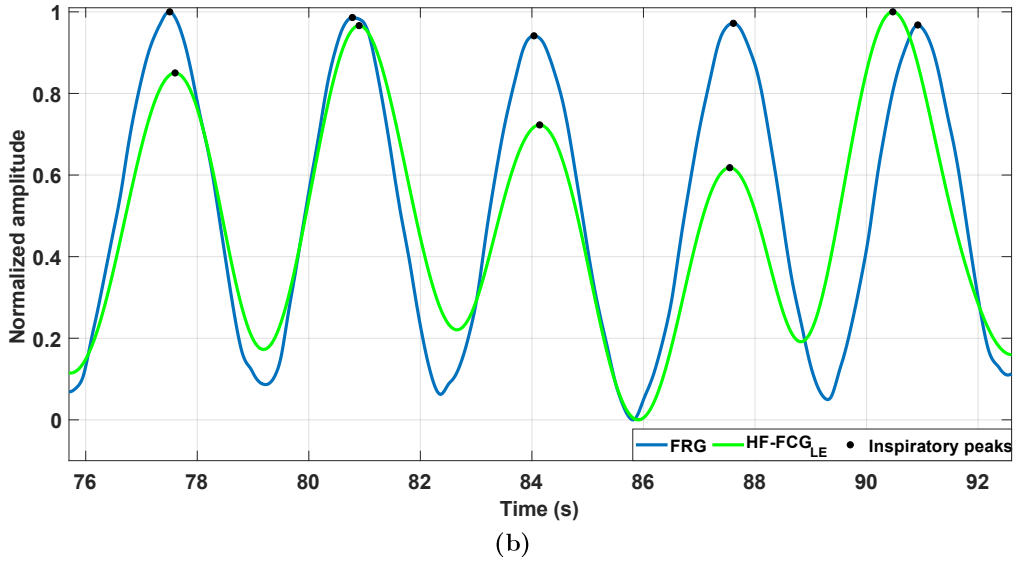
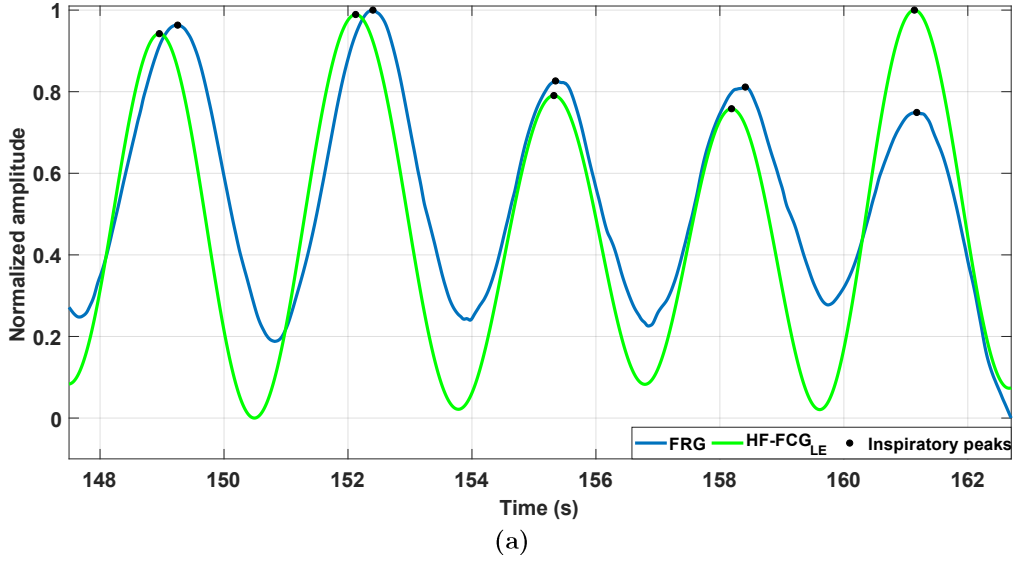


Figure 60. Some excerpts of FRG signal (blue line) and the linear envelope of HF-FCG signal (green line) from: (a) subject #4; (b) subject #5.

Figure 61 depicts the same excerpts of the FRG signals (blue lines), the linear envelopes of the LF-FCG signals (orange lines) and the linear envelopes of the HF-FCG signals (green lines) from subjects #4 and #5.

5.2 RESPIRATORY-INDUCED AMPLITUDE MODULATION OF FCG SIGNALS

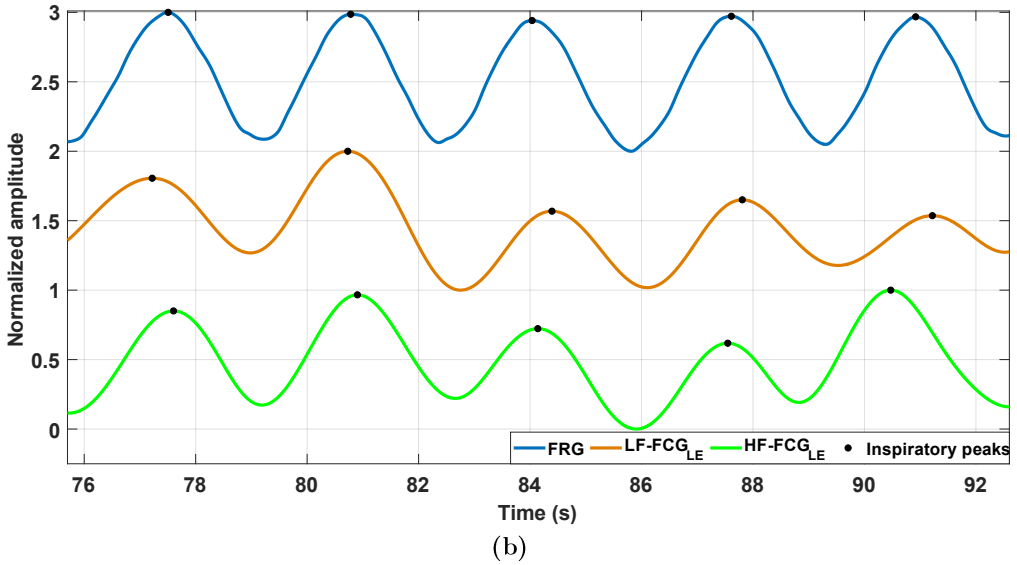
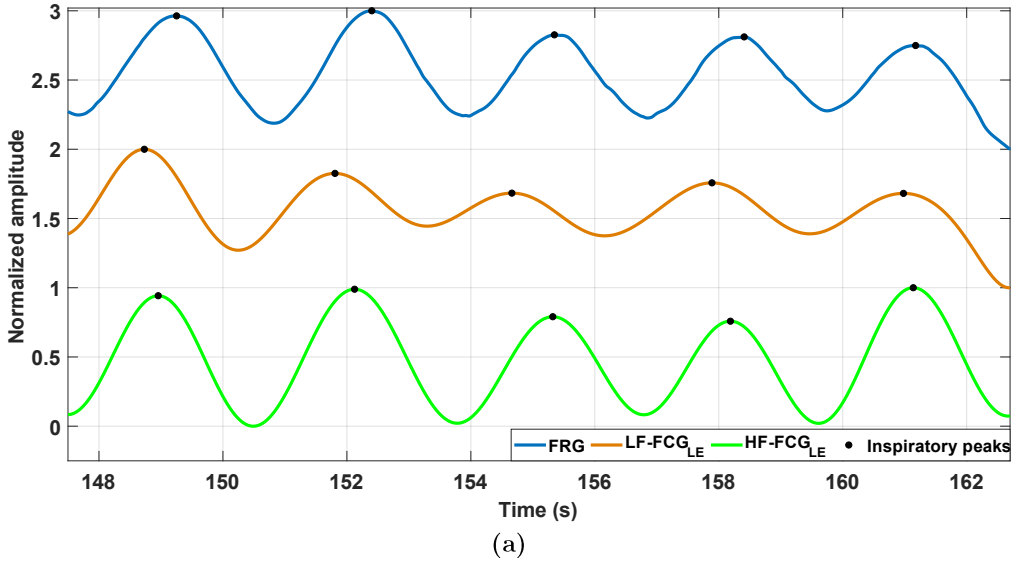


Figure 61. Some excerpts of FRG signal (blue line), the linear envelope of LF-FCG signal (orange line) and the linear envelope of HF-FCG (green line) from: (a) subject #4; (b) subject #5.

Finally, the positive peaks related to inspiratory acts were located on both the FRG signals and the linear envelopes of the LF-FCG and HF-FCG signals to estimate the inter-breath intervals. Furthermore, respiratory acts in the FRG signal corrupted by motion artifacts and the corresponding acts in the linear envelopes of

LF-FCG and HF-FCG signals were excluded from the analysis. All processing operations were performed in MATLAB® R2018b (MathWorks, Inc., 1 Apple Hill Drive, Natick, MA, USA).

Table 4 outlines the number of respiratory acts detected per subject in the FRG signal and in the linear envelopes of the LF-FCG and HF-FCG signals. The table also reports the number of missed and spurious respiratory acts identified in the linear envelopes of the LF-FCG and HF-FCG signals by assuming the FRG signal as the reference. In detail, a total of 272 respiratory acts were detected in the FRG signals, while 263 respiratory acts, 9 missed acts and 21 spurious acts were found in the linear envelopes of LF-FCG signals, and 270 respiratory acts, 2 missed acts and 1 spurious act were found in the linear envelopes of HF-FCG signals.

Table 4. *Respiratory acts detected in the FRG signal and the linear envelopes of LF-FCG and HF-FCG signals per subject. The missed and spurious acts are reported for the linear envelopes of LF-FCG and HF-FCG signals with reference to the acts detected in the FRG signal.*

Subject #	Respiratory acts			Missed acts		Spurious acts	
	FRG	LF-FCG	HF-FCG	LF-FCG	HF-FCG	LF-FCG	HF-FCG
1	57	58	57	4	0	5	0
2	21	28	21	3	0	10	0
3	83	86	83	0	1	3	1
4	52	53	52	2	0	3	0
5	18	18	18	0	0	0	0
6	41	41	40	0	1	0	0
Total	272	284	271	9	2	21	1

Respiratory acts detected in the linear envelopes of both LF-FCG and HF-FCG signals were considered as TP, while missed and spurious acts were considered as FN and FP, respectively. Hence, respiratory acts detection in the linear envelopes of LF-FCG and HF-FCG signals was evaluated by computing sensitivity and PPV according to the equations (10)-(11) provided in Section 5.1.4. The LF-FCG scored a sensitivity of 96.7% and a PPV of 92.6%, while the HF-FCG scored a sensitivity of 99.3% and a PPV of 99.6%. Sensitivity and PPV of respiratory acts detection in the linear envelopes of LF-FCG and HF-FCG signals are also reported in **Table 5**.

Table 5. *Sensitivity and PPV of respiratory acts detection in the linear envelopes of LF-FCG and HF-FCG signals.*

	Sensitivity (%)	PPV (%)
LF-FCG	96.7	92.6
HF-FCG	99.3	99.6

Moreover, to assess the consistency of the amplitude modulation of LF-FCG and HF-FCG signals within the respiratory cycle, regression, correlation, and Bland–Altman [150]–[151] analyses were carried out on the inter-breath intervals obtained from FRG and the linear envelopes of LF-FCG and HF-FCG, by means of the MATLAB® function “bland-altman-and-correlation-plot” [152]. To this end, the intervals related to the missed and spurious respiratory acts in the linear envelopes of the LF-FCG and HF-FCG and the corresponding intervals in the FRG signals were excluded from the analysis. The statistical analyses were performed on 241 inter-breath intervals and the results are depicted in **Figure 62** for LF-FCG and **Figure 63** for HF-FCG. The regression and correlation analyses reported a slope and intercept of 1.05 and -0.147 s, with an R^2 value of 0.86 for LF-FCG, while a slope and intercept of 0.991 and 0.0350 s, with an R^2 value of 0.95 for HF-FCG. The Bland–Altman analysis reported a non-significant bias (p-value = 0.65) with LoA of ± 1.34 s for LF-FCG, while a non-significant bias (p-value = 0.91) with LoA of ± 0.710 s for HF-FCG. The results of regression, correlation and Bland–Altman analyses are also summarized in **Table 6**.

Table 6. *Results of regression, correlation and Bland–Altman analyses for LF-FCG and HF-FCG signals. Non-significant bias is indicated as “NS”.*

	Slope	Intercept (s)	R^2	Bias	p-value	LoA (s)
LF-FCG	1.05	-0.147	0.86	NS	0.65	± 1.34
HF-FCG	0.991	0.0350	0.95	NS	0.91	± 0.710

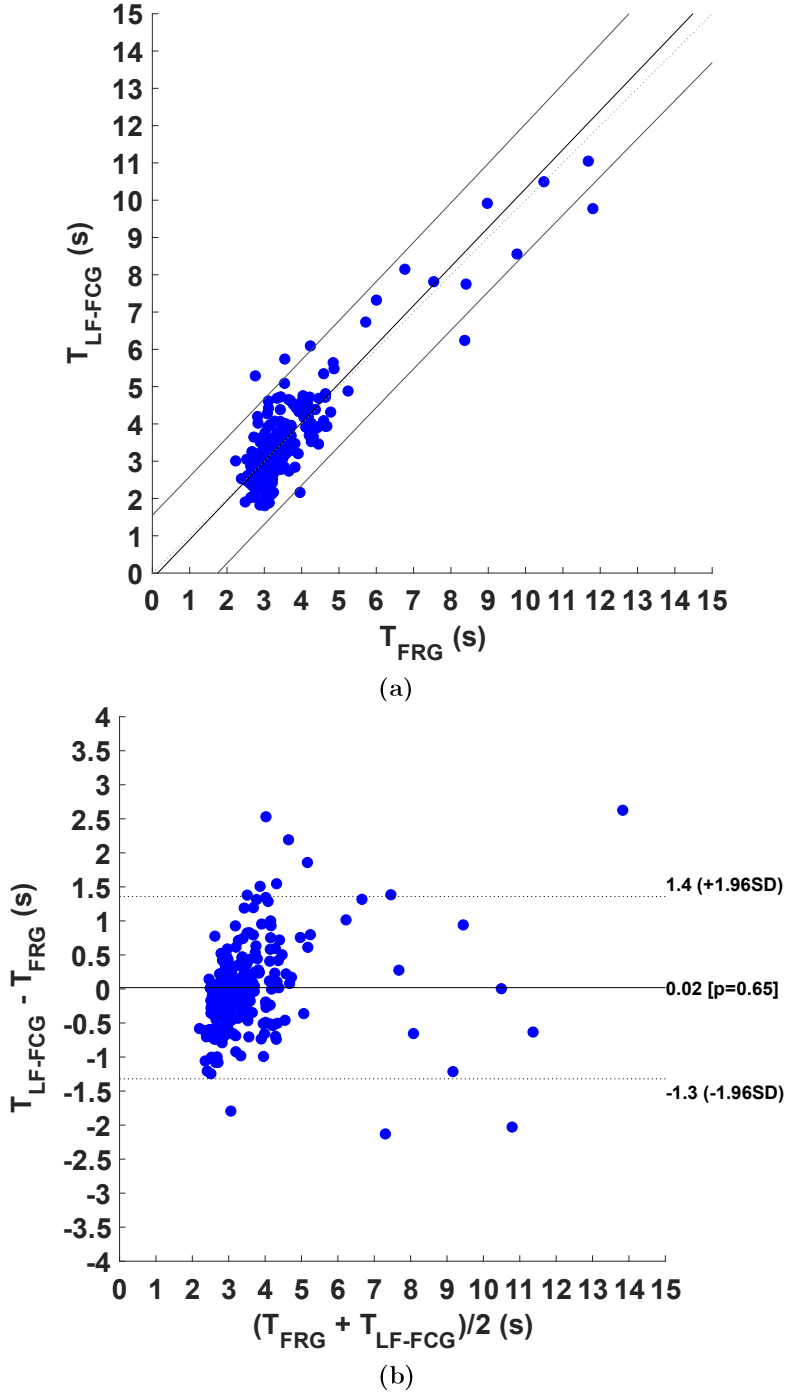


Figure 62. Statistical analyses of inter-breath intervals: (a) results of regression and correlation analyses; (b) results of Bland–Altman analysis for LF-FCG signals.

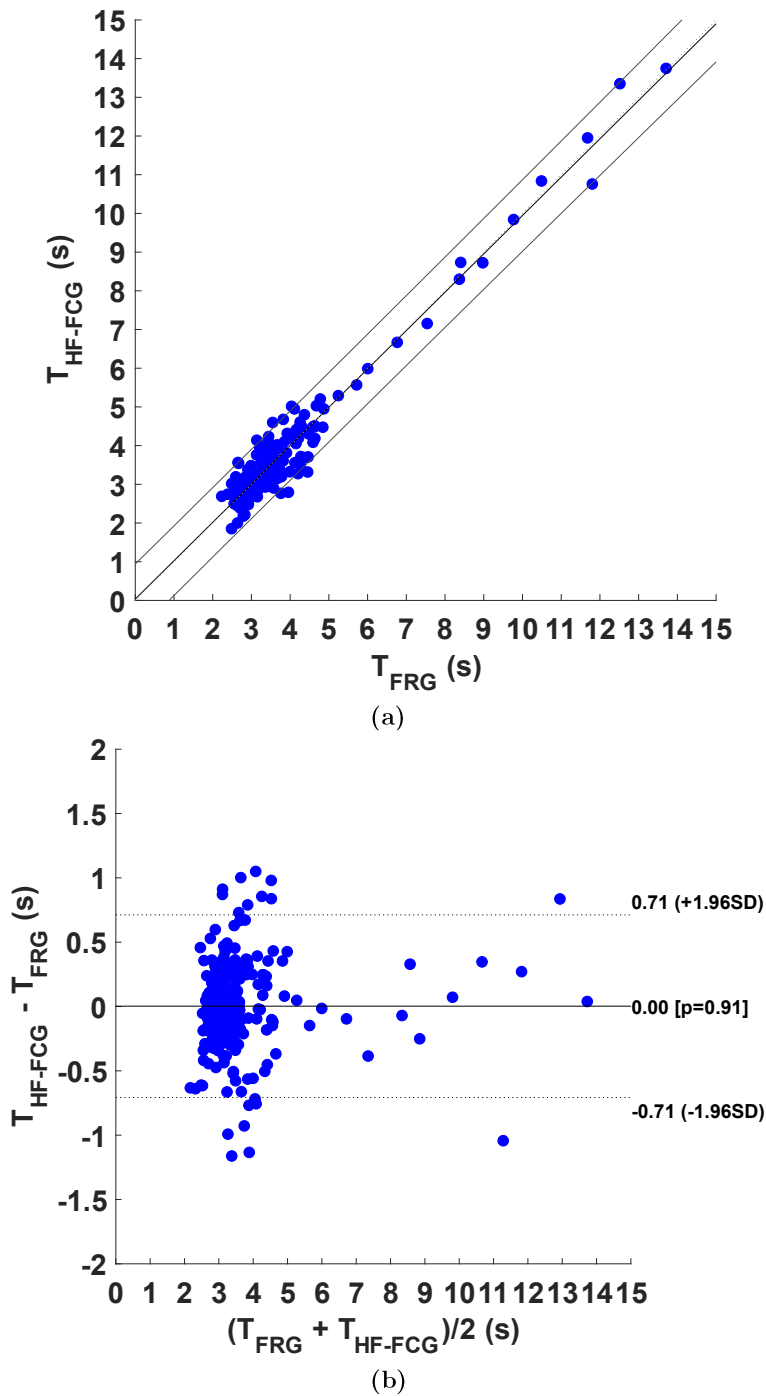


Figure 63. Statistical analyses of inter-breath intervals: (a) results of regression and correlation analyses; (b) results of Bland–Altman analysis for HF-FCG signals.

5.2.4 Discussion

These preliminary results suggest that the amplitude modulation of both LF-FCG and HF-FCG signals has good consistency within the respiratory cycle. These findings are in line with the results of previous studies on SCG [11],[13],[130],[158]-[159] and heart sounds [160]-[163], thus providing further support to the hypothesis that the amplitudes of cardiac vibrations are modulated by respiration. Indeed, the heart, which is attached via the pericardium to the diaphragm, moves up and down during the respiratory cycle, so the mutual distance between the heart and the sensors placed on the chest wall varies in accordance with the respiratory phases. As a result, the mechanical waves produced by the heart propagate through portions of tissues with different orientation and mechanical properties, along paths of variable length, thus being subject to variable amplitude attenuation. It is worth noticing that the amplitude modulation of LF-FCG exhibited a lower consistency than that of HF-FCG, because the LF-FCG scored a lower R^2 value and almost doubled LoA.

However, only a few subjects were involved in this investigation. Therefore, the preliminary results obtained from this study need to be assessed on a larger cohort of subjects. In addition, future studies could focus on amplitude modulation and possible morphological changes in other FCG components (e.g., HS-FCG), also investigating potential differences between FCG signals recorded from different sites on the chest. These analyses could also be extended to different experimental conditions, such as subjects in standing or supine positions, while performing voluntary tachypnea or bradypnea, during or after physical exertion, and also by using different FCG sensor numbers and placement sites. Understanding the relationship between breathing activity and the morphological changes in FCG signals in healthy subjects could pave the way for the identification of potential alterations in this relationship in pathological subjects, which could eventually be used for diagnostic purposes.

5.3 Changes in FCG heartbeat morphology induced by cardio-respiratory interactions

This study presents a more in-depth investigation on the effects of respiration on FCG signals, which focused on respiratory-induced changes in the morphology of dHF-FCG heartbeats. The investigation was carried out as a retrospective analysis on the signals acquired in [21], also used for the previous study (see Section 5.2.1 for details on the FCG sensor and Section 5.2.2 for information on measurement setup and protocol). In particular, the beat-by-beat variation of the LVET estimated from dHF-FCG signals was considered as a first respiratory-modulated parameter. In addition, the variation of an index of morphological similarity (MSi) between single heartbeats was considered as a second respiratory-modulated parameter. The consistency of the time trends of these parameters within the respiratory cycle was assessed by the comparison with the time trends of a reference respiration signal.

5.3.1 Signal pre-processing

The FRG component was first extracted from the raw FCG sensor signal via a 3rd order Savitzki–Golay filter, with a frame length of approximately 1.5 s time interval [157]. Then, the FRG was subtracted from the raw FCG sensor signal in order to isolate the actual Forcecardiogram. Subsequently, the HF-FCG component was extracted from the actual Forcecardiogram resulting from the respiratory signal removal via a 4th order zero-lag Butterworth band-pass filter with cut-off frequencies of 7 and 30 Hz. Afterwards, the first derivative of the HF-FCG signal, namely dHF-FCG, was computed (as finite forward difference), since its morphology has the highest similarity to the SCG signal (this will be demonstrated in Chapter 0). Finally, the ECG signal was filtered via a 4th order zero-lag Butterworth band-pass filter in 0.5 – 40 Hz frequency band. **Figure 64** shows an example of FRG, dHF-FCG, and ECG signals. All processing operations were performed in MATLAB® R2018b (MathWorks, Inc., 1 Apple Hill Drive, Natick, MA, USA).

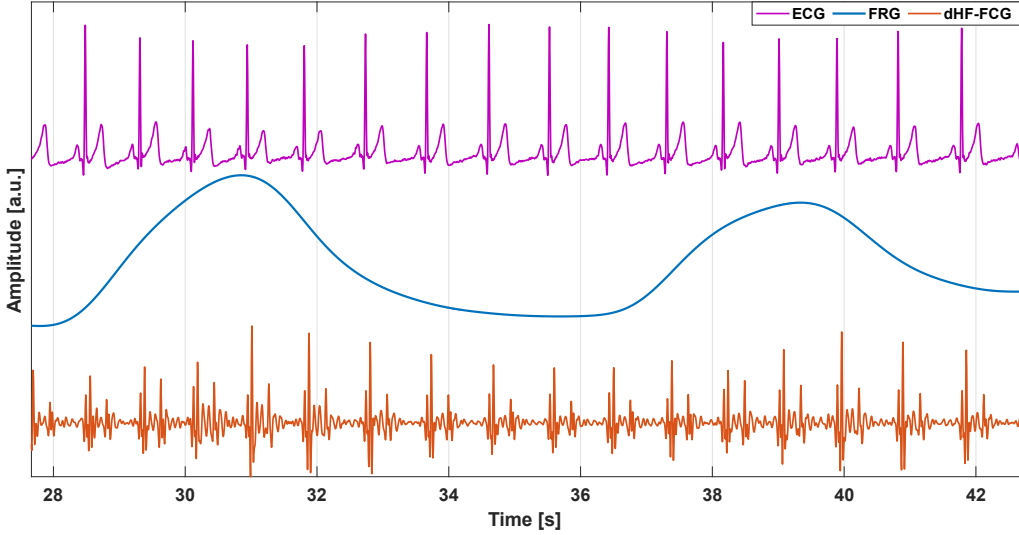


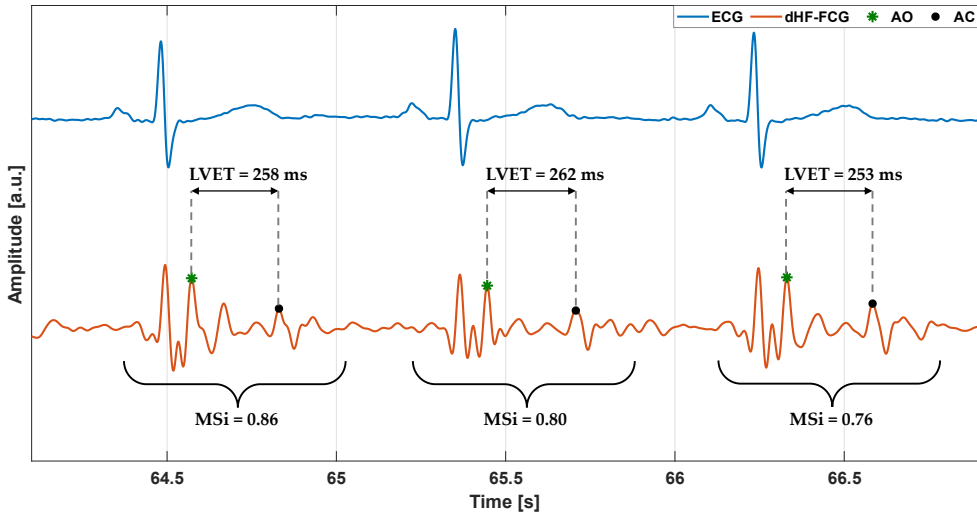
Figure 64. Example of FRG (blue line), dHF-FCG (orange line) and ECG (purple line) signals. The FRG signal captures the expansion and relaxation of the thorax during breathing and allows accurate monitoring of respiration. The dHF-FCG is a high-frequency component of the FCG signal, which is very similar to the seismocardiogram and provides information about the heart mechanical function. The ECG is a well-established signal that provides information about the heart electrical function.

5.3.2 Extraction of the LVET and MSi trends

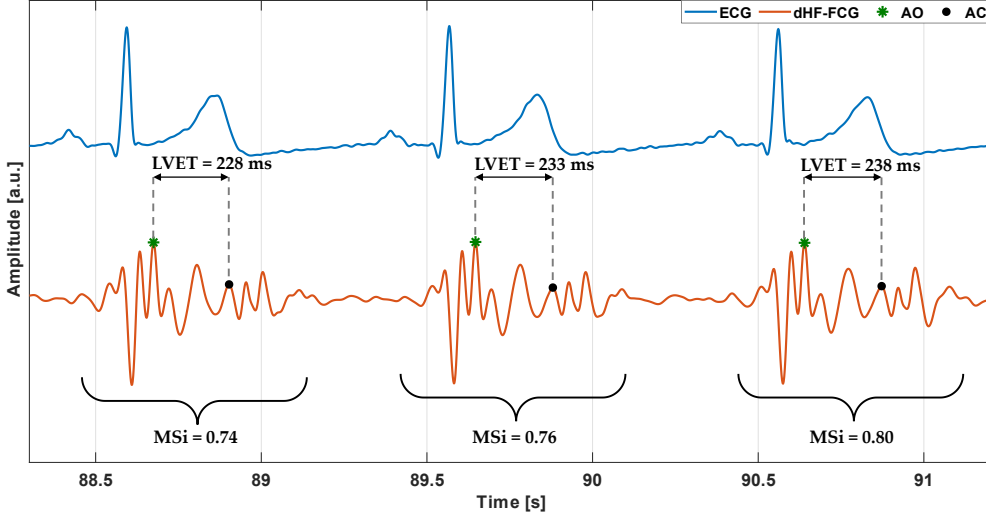
As reported in Section 2.3.8, the LVET is defined as the time interval between aortic valve opening (AO) and closure (AC) events. According to [103], the AO and AC markers were located on dHF-FCG signal by taking advantage of the simultaneous ECG recording. Spurious AO and/or AC peaks due to portions of the signal corrupted by motion artifacts were excluded from the analysis. Then, the LVET was estimated for each heartbeat. Finally, a continuous LVET trend was obtained via spline interpolation by using the MATLAB® function “interp1”. **Figure 65** shows an example of AO and AC markers localization and estimation of the related LVET for each heartbeat in some excerpts of dHF-FCG signals from subjects #2 and #4. The ECG signals simultaneously acquired are also reported to provide a time reference for the cardiac cycle.

The MSi was defined with the aim of quantifying the changes in heartbeat morphology in dHF-FCG signals. To this end, the main idea was to evaluate the similarity between one heartbeat, assumed as a morphological reference, and each

single heartbeat in the dHF-FCG signal. The normalized cross-correlation (NCC) was considered as the similarity index [20]-[21]. In detail, after the reference heartbeat had been selected, the R-peaks were located in the ECG signal via the Pan and Thompkins algorithm implemented in the “BioSigKit” MATLAB® toolbox [149]; then, the NCC function was computed between the reference heartbeat and the dHF-FCG signal, by considering only the lags belonging to windows of 100 ms after the locations of the R-peaks; finally the absolute maxima of NCC function in each window were located, thus providing both the location of each heartbeat in the dHF-FCG signal and a measure of its morphological similarity with the reference heartbeat. The points thus identified in the NCC function represented the actual values of the MSi, which were further interpolated to obtain a continuous time trend, as previously done for the LVET. **Figure 65** shows an example of MSi estimation for each heartbeat in some excerpts of dHF-FCG signals from subjects #2 and #4. It is worth underlying that the heart rate was more than two times the respiratory rate in all the signals analysed, which ensured that the Nyquist-Shannon criterion was always met in the estimation of time trends of LVET and MSi.



(a)



(b)

Figure 65. Example of LVET and MSi estimation in dHF-FCG signals (orange lines) from: (a) subject #2; (b) subject #4. ECG signals (blue lines) are also reported as a time reference for the cardiac cycle.

5.3.3 Analysis of consistency within the respiratory cycle

Both the LVET and MSi trends, previously extracted, were filtered via a 2nd order zero-lag Butterworth low-pass filter with a cut-off frequency of 0.5 Hz in order to filter out very small, superimposed oscillations of higher frequencies. Then, the temporal locations of respiratory acts were identified on both the reference signal, i.e., the FRG, and the LVET and MSi trends by considering the positive inspiratory peaks as fiducial points. Moreover, inspiratory peaks detected on portions of the reference signal affected by motion artifacts and the corresponding peaks on the LVET and MSi trends were not considered for the analysis.

Figure 66 depicts some excerpts of the FRG signals (blue lines) and LVET trends (orange lines) from subjects #2 and #4. The comparison showed that the LVET was modulated by respiration. Indeed, the same number of respiratory acts could be detected on the two signals.

Some excerpts of the FRG signals (blue lines) and MSi trends (green lines) from the same subjects #2 and #4 are depicted in **Figure 67**. It was observed that also the MSi trend appeared as modulated by respiration, therefore corresponding respiratory

acts could be identified on the two signals. Moreover, its morphology exhibited higher similarity to the respiratory signal.

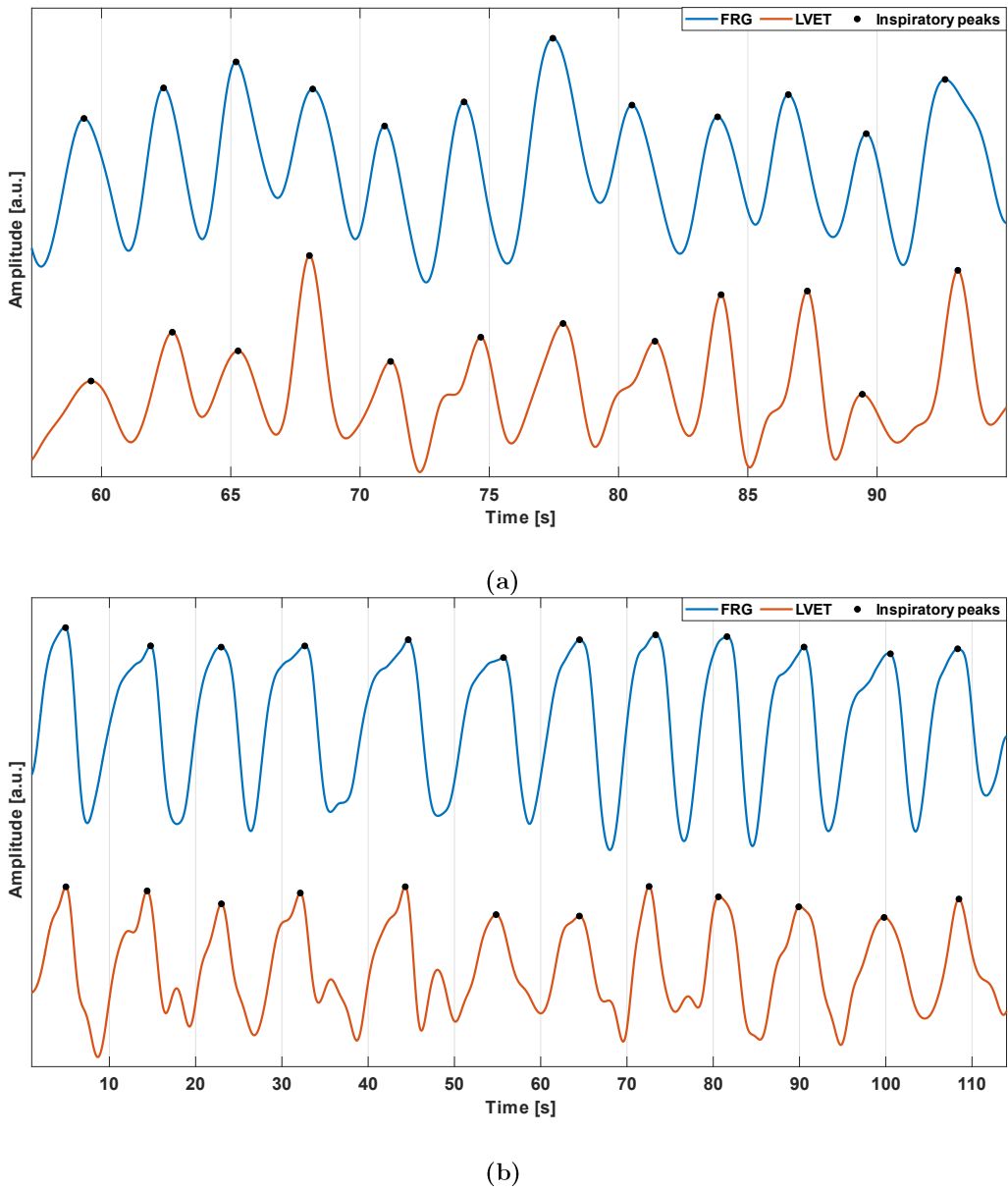


Figure 66. Some excerpts of FRG signal (blue line) and LVET trend (orange line) from: (a) subject #2; (b) subject #4.

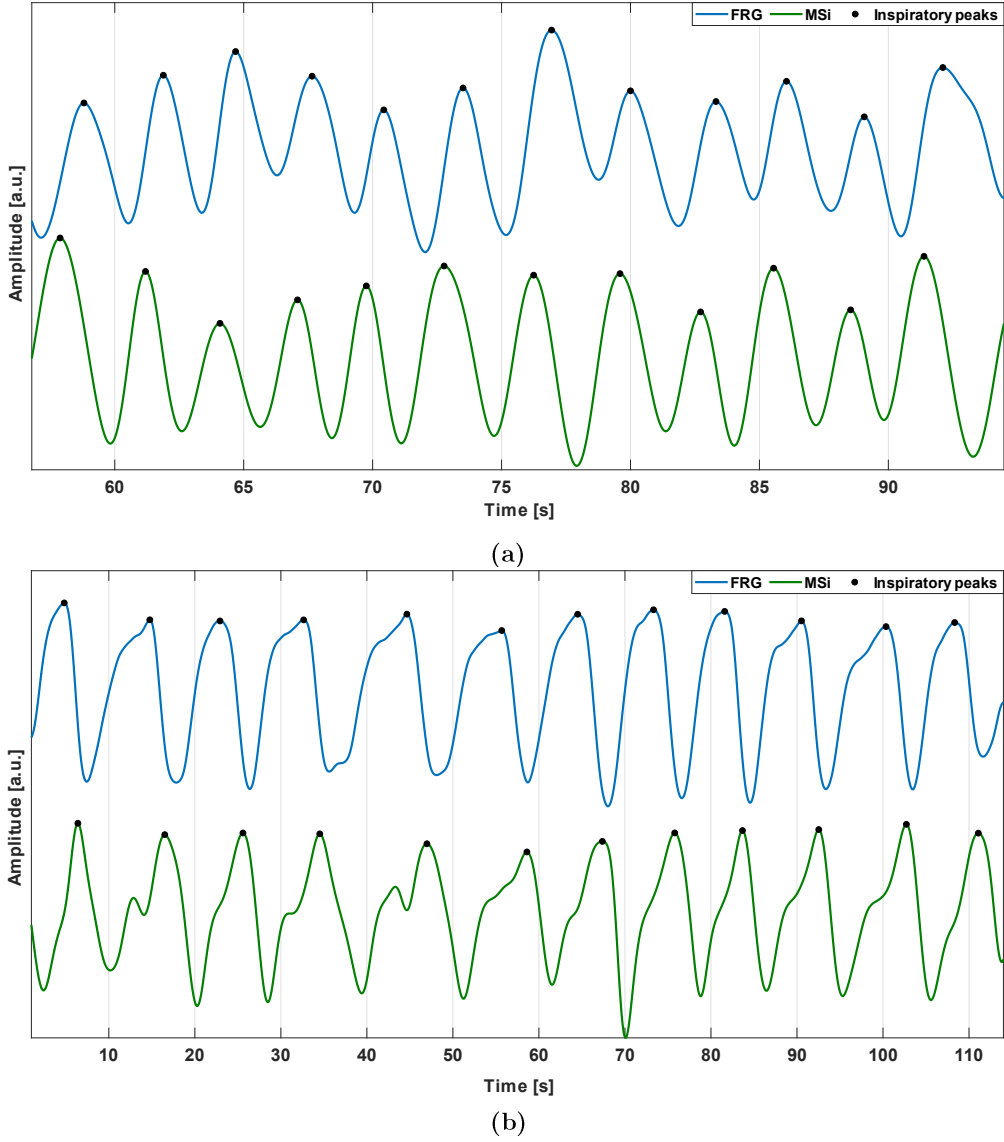


Figure 67. Some excerpts of FRG signal (blue line) and MSi trend (green line) from: (a) subject #2; (b) subject #4.

Table 7 outlines the number of respiratory acts detected per subject in the FRG signal and in the LVET and MSi trends. The table also reports the number of missed

and spurious respiratory acts identified in the LVET and MSi trends by considering the FRG signal as the reference.

Table 7. *Respiratory acts detected in the FRG signal and the LVET and MSi trends per subject. The missed and spurious acts are reported for the LVET and MSi trends with reference to the acts detected in the FRG signal.*

Subject #	Respiratory acts			Missed acts		Spurious acts	
	FRG	LVET	MSi	LVET	MSi	LVET	MSi
1	112	109	112	6	0	3	0
2	38	39	37	0	1	1	0
3	60	51	60	9	0	0	0
4	16	18	19	0	0	2	3
5	21	24	33	0	0	3	12
6	58	61	57	1	1	4	0
Total	305	302	318	16	2	13	15

A total of 305 respiratory acts were detected in the FRG signals, while 289 respiratory acts, 16 missed acts and 13 spurious acts were found in the LVET trends, and 303 respiratory acts, 2 missed acts and 15 spurious acts were found in the MSi trends. The respiratory acts detected in the FRG signals and in the LVET and MSi trends of all subjects were considered as TP, while the number of missed and spurious acts, which were identified in the LVET and MSi trends with respect to the reference FRG signals, were considered as FN and FP, respectively. Hence, sensitivity and PPV of respiratory acts detection in the LVET and MSi trends were computed according to the equations (10)-(11) provided in Section 5.1.4. The LVET trend scored a sensitivity of 94.7 % and a PPV of 95.7 %, while the MSi trend scored a sensitivity of 99.3 % and a PPV of 95.3 %. Sensitivity and PPV values obtained for respiratory acts detection in the LVET and MSi trends are also reported in **Table 8**.

Table 8. *Sensitivity and PPV of respiratory acts detection in the LVET and MSi trends.*

	Sensitivity (%)	PPV (%)
LVET	94.7	95.7
MSi	99.3	95.3

Finally, to assess the consistency of the LVET and MSi trends within the respiratory cycle, inter-breath intervals estimates obtained from these two signals were compared with those computed from the FRG signal via regression, correlation, and Bland–Altman [150]–[151] analyses, by means of the MATLAB® function “bland-altman-and-correlation-plot” [152]. In detail, the inter-breath interval estimates were obtained from the three signals as difference between the time locations of consecutive inspiratory peaks. Then, those related to the missed and spurious respiratory acts in the LVET and MSi trends and the corresponding intervals in the FRG signals were excluded. The statistical analyses were performed on 267 inter-breath intervals for the LVET trend, while on 294 inter-breath intervals for the MSi trend, and the results are depicted in **Figure 68** and **Figure 69**, respectively. As reported in **Table 9**, a slope and intercept of 0.99 and 0.067 s, with an R^2 value of 0.86 were obtained for LVET trend as results of regression and correlation analyses, while a slope and intercept of 1.02 and -0.063 s, with an R^2 value of 0.97 resulted for MSi trend. Moreover, the Bland–Altman analysis reported a non-significant bias for both LVET (p-value = 0.39) and MSi (p-value = 0.54) with LoA of ± 1.68 s and ± 0.771 s, respectively. The differences between the measures provided by LVET and MSi and those provided by the FRG did not exhibit clear dependences on the inter-breath intervals.

Table 9. Results of regression, correlation and Bland-Altman analyses for LVET and MSi trends. Non-significant bias is indicated as “NS”.

	Slope	Intercept (s)	R^2	Bias	P- value	LoA (s)
LVET	0.99	0.067	0.86	NS	0.39	± 1.68
MSi	1.02	-0.063	0.97	NS	0.54	± 0.771

5.3 CHANGES IN FCG HEARTBEAT MORPHOLOGY INDUCED BY CARDIO-RESPIRATORY INTERACTIONS

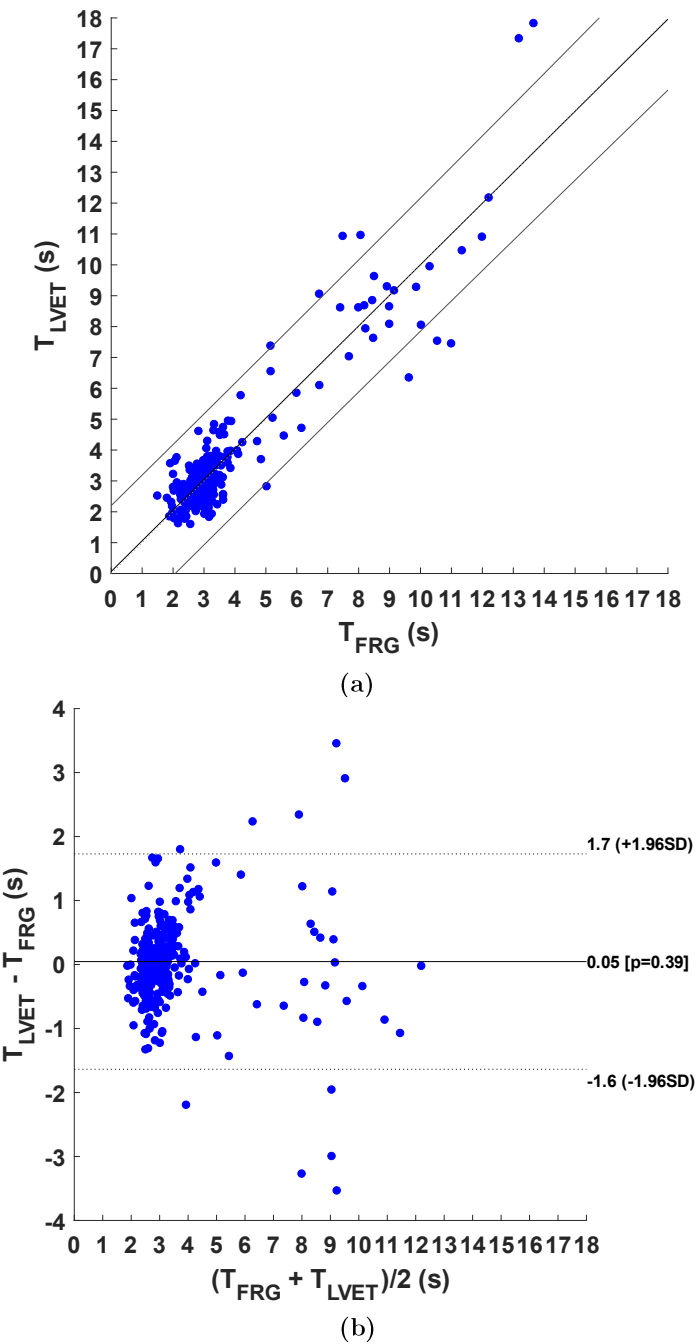


Figure 68. Statistical analyses on inter-breath intervals extracted from FRG and LVET time trend: (a) results of linear regression; (b) results of Bland-Altman analysis.

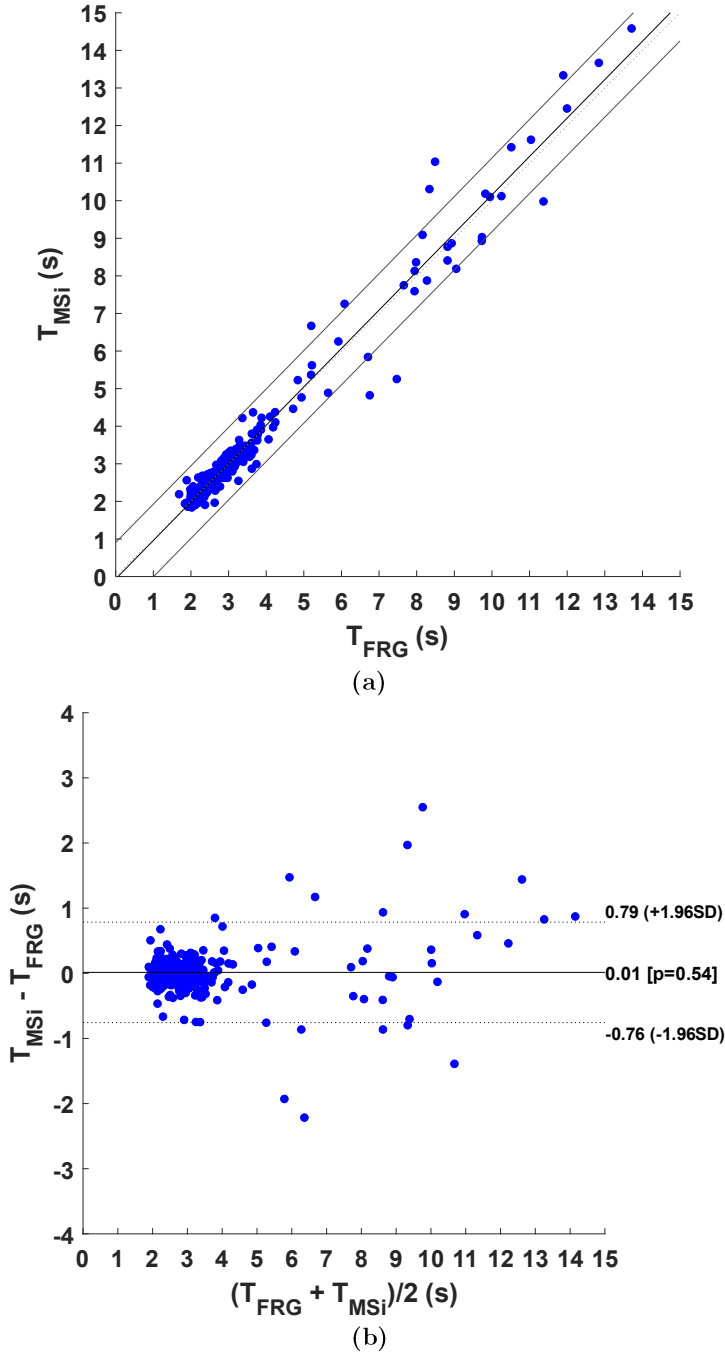


Figure 69. Statistical analyses on inter-breath intervals extracted from FRG and MSi time trend: (a) results of linear regression; (b) results of Bland-Altman analysis.

5.3.4 Discussion

The preliminary results of this study clearly showed a tight relationship between the respiratory activity, as captured by the FRG, and two respiratory-modulated parameters. In particular, the results obtained for the LVET time trends extracted from dHF-FCG signals are very similar to those obtained by Pandia et al. in [130] for the variations in the S1-S2 interval extracted from SCG signals. Nonetheless, they did not directly measure the S1-S2 interval, i.e., by locating specific markers on the SCG signals, because the beat-by-beat changes in morphology made the marker localization unreliable. In this study, instead, the LVET was estimated directly, by locating the time markers corresponding to the AO and AC points. This was possible thanks to the high SNR of the dHF-FCG, which obviates the need for ensemble averaging to obtain reliable data [21]. The time trends of the MSi provided a global measure of the beat-by-beat changes in the heartbeat morphology. The findings of this study provide a strong suggestion that such changes are tightly linked to the respiratory activity. A similar result was presented by Taebi and Mansy in [132]. However, by dividing SCG heartbeats into only two groups (either based on the corresponding respiratory phase or lung volume), they intrinsically considered only two possible underlying morphologies for SCG, thus neglecting a sort of continuum in the underlying heartbeat morphologies, which was captured, for the first time, in this study of dHF-FCG signals by analysing the time trends of an index of the morphological similarity between heartbeats. The analysis of changes in heartbeats morphology via the MSi could be investigated in future also for SCG signals. In summary, the results obtained from the morphological changes of heartbeats in the dHF-FCG signals, both in terms of the LVET and MSi, are substantially in line with previous findings on SCG signals, which adds to the evidence that dHF-FCG and SCG signals share the same information content. This preliminary investigation on the respiratory-induced changes of heartbeat morphology in dHF-FCG signals has some limitations. Indeed, the physiological signals analysed in this study were acquired only from a small cohort of healthy subjects, during quiet respiration at rest and in a sitting position. Therefore, the preliminary yet interesting findings of this study must be confirmed by further

investigations on larger cohorts of healthy subjects and with different experimental conditions, for example, by considering different postures (e.g., supine or standing), different levels of physical activity, and a wider range of respiratory frequencies (e.g., forced respiration at very low and very high paces).

Moreover, the analyses presented in this study could be extended to other components of FCG signals, e.g., the heart sounds captured in the HS-FCG, which are known to be affected by respiration [136]-[137], and the LF-FCG, which potentially carries information on stroke volume variations, which are also affected by respiration [48]-[56]. Considering that the morphology of cardio-mechanical signals is highly dependent on the specific sensor location over the chest [18],[164], the analyses presented in this study could also be extended to multi-channel measurements to be acquired by means of FCG sensor matrices.

Localization of cardiac cycle events in FCG signals

This chapter describes the materials and methodologies of the experimental tests that were performed during this thesis focused on the localization of cardiac cycle events in FCG signals and reports the results obtained from these studies.

6.1 Detection of aortic valve opening and estimation of PEP in FCG signals

FCG has not yet been demonstrated to provide the timings of well-established SCG markers with reasonable accuracy, and this currently limits the possibility to obtain the same valuable information provided by SCG. For this reason, this study addresses the detection of the AO marker in FCG signals and the performance comparison with simultaneous SCG signals.

6.1.1 Measurement setup and protocol

The piezoelectric FCG sensor presented in [21], also described in Section 5.2.1, was used in this study. The FCG sensor and a Freescale MMA7361 triaxial accelerometer (Freescale Semiconductor – NXP Semiconductors, Eindhoven, the Netherlands)

were rigidly fixed to each other to simultaneously acquire FCG and SCG signals from the same contact point on the chest (see **Figure 70**). Moreover, a WelchAllyn Propaq® Encore monitor (Welch Allyn Inc., New York, NY, USA) was used to acquire ECG recordings.

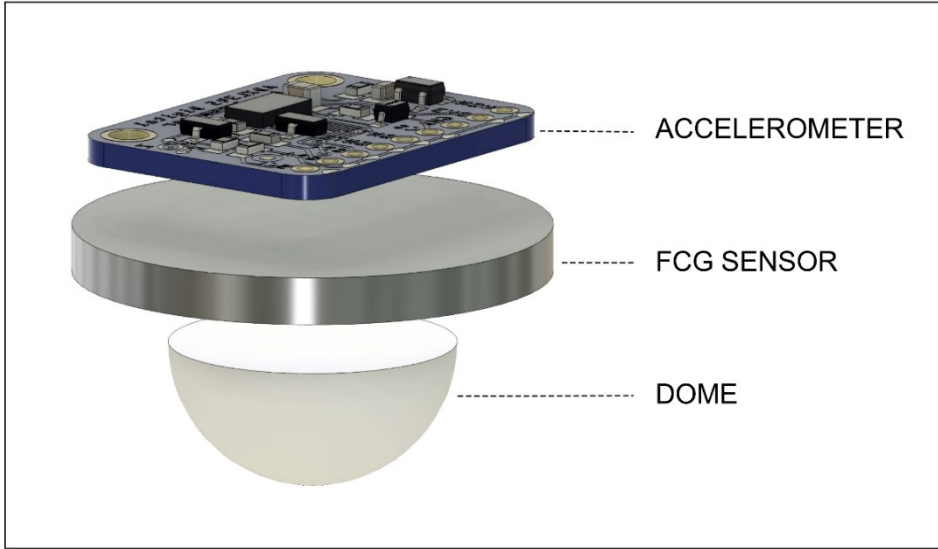
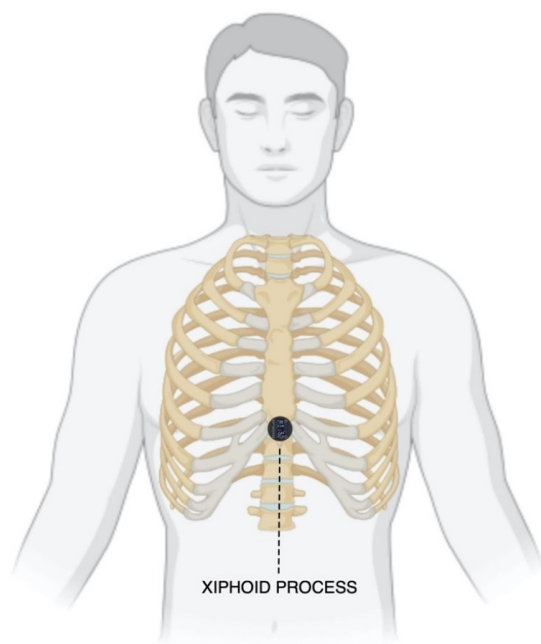


Figure 70. Sensors assembly: piezoelectric FCG sensor with a dome and MMA7361 accelerometer.

Three healthy volunteers (2 males and 1 female, age 29.7 ± 2.52 years), who signed the informed consent, were asked to comfortably sit in a chair, leaning against the seatback while keeping their back straight. The FCG and SCG sensors assembly was placed onto the xiphoid process of each subject via a medical adhesive tape and then fastened with a belt around the thorax. **Figure 71** shows frontal and lateral views of a subject equipped with the FCG/SCG sensors assembly. Simultaneous acquisitions of FCG and dorso-ventral SCG signals, together with an ECG lead I, were carried out via a National Instrument NIUSB4431 DAQ board (National Instruments Corp., 11,500 N Mopac Expwy, Austin, TX 78759-3504, USA), with 24-bit precision and 10 kHz sampling frequency. Multiple acquisitions were performed for each subject, both during quiet breathing and apnea.



(a)



(b)

Figure 71. Sensors assembly placement on a subject: (a) frontal view; (b) lateral view.

6.1.2 Signal processing

The FRG signal was first extracted via a 3rd order Savitzki–Golay filter [157], with a frame length corresponding to about 1.5 s time interval, and then subtracted from the raw FCG sensor signal acquired during quiet breathing in order to isolate the actual FCG signal. Afterwards, the actual FCG signal resulting from the respiration signal removal was band-pass filtered in the 7 – 30 Hz frequency band via a 2nd order zero-lag Butterworth filter to extract the HF-FCG component. The raw FCG sensor signal acquired during apnea was directly band-pass filtered to obtain the HF-FCG component. The first derivative of the HF-FCG signal thus obtained was finally computed and referred to as dHF-FCG (the derivative was computed as finite forward difference). The dorso-ventral SCG signal was obtained from the raw z-axis acceleration signal via the same 2nd order zero-lag Butterworth filter used to extract the HF-FCG component from the FCG signal. All processing operations were performed in MATLAB® R2018b (MathWorks, Inc., 1 Apple Hill Drive, Natick, MA, USA).

Some excerpts of HF-FCG, dHF-FCG, SCG and ECG signals from subjects #1 and #3 are depicted in **Figure 72**. It could be noted by visual inspection that the HF-FCG was lagged with respect to the SCG, and their peaks and valleys did not match very well. Indeed, the peaks and valleys of SCG appeared as corresponding to the points of maximum slope of the HF-FCG. The dHF-FCG, on the other hand, was practically synchronous with the SCG and featured peaks and valleys that matched those of SCG remarkably well.

6.1 DETECTION OF AORTIC VALVE OPENING AND ESTIMATION OF PEP IN FCG SIGNALS

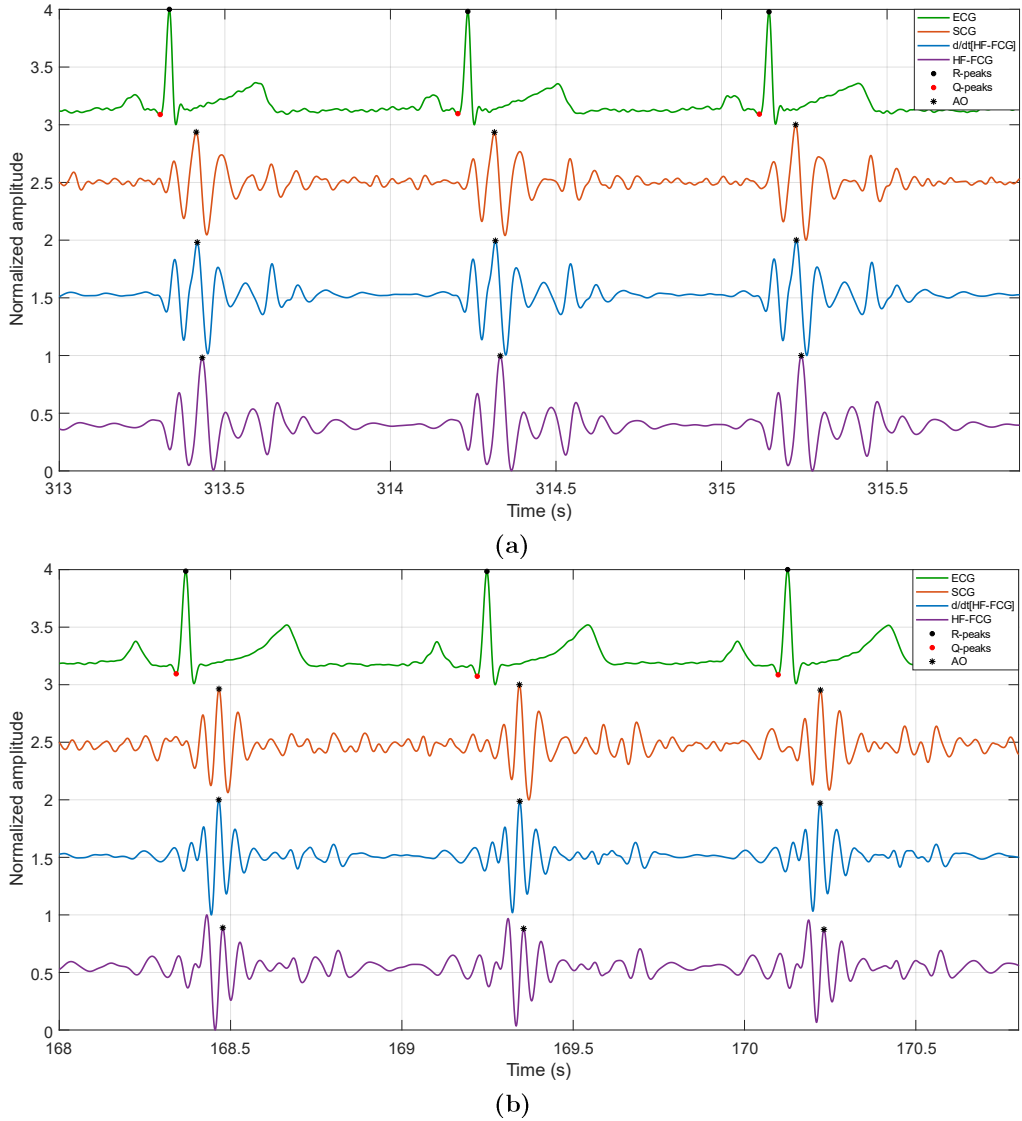


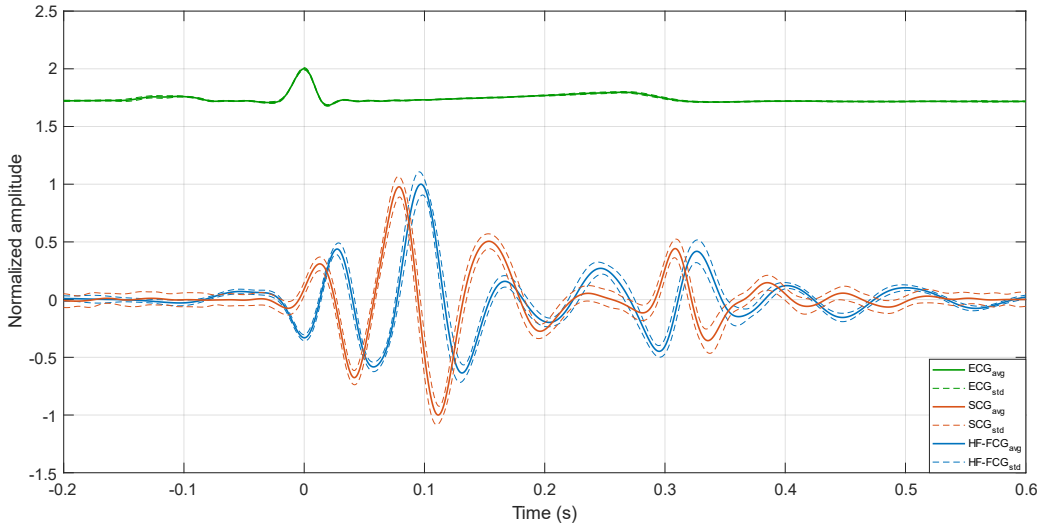
Figure 72. Examples of HF-FCG (violet line), dHF-FCG (blue line), SCG (orange line) and ECG (green line) signals from: (a) subject #1; (b) subject #3.

6.1.3 Morphological comparison between FCG and SCG signals

The ECG-triggered ensemble averages, synchronized with R-peaks, of ECG, SCG, HF-FCG and dHF-FCG signals acquired in apnea conditions were computed. To this aim, the R-peaks were first located in the ECG signal via the “BioSigKit”

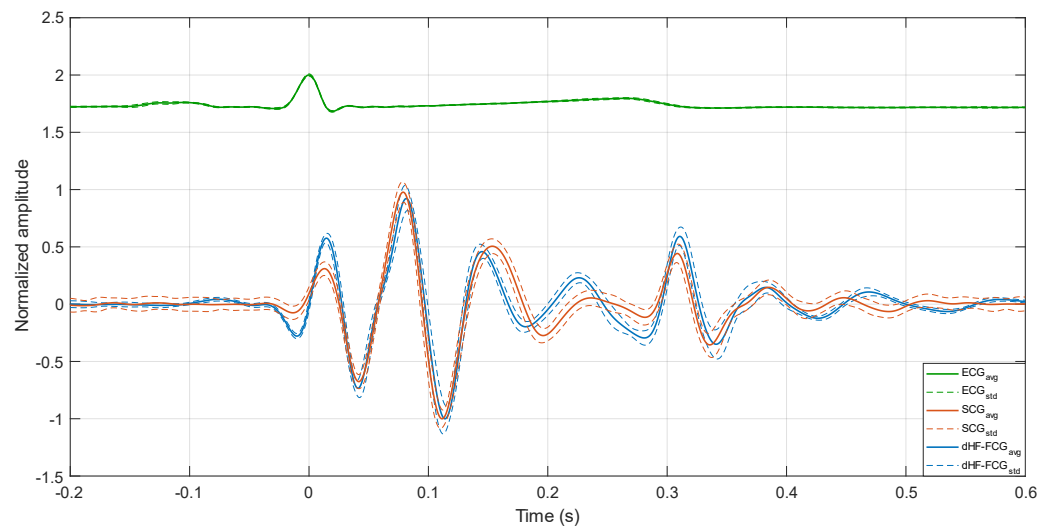
MATLAB® toolbox, which implements the well-known Pan and Thompkins algorithm [149]. Then, NCC indices and the time lags of the ensemble averages of HF-FCG vs. SCG and dHF-FCG vs. SCG were evaluated for each subject. In detail, the dHF-FCG and SCG signals scored both a higher NCC index and a lower time lag; therefore, the dHF-FCG signals were actually used for the estimation of PEP from FCG recordings.

Figure 73a,b depict, respectively, the ensemble averages of HF-FCG, SCG and ECG and of dHF-FCG, SCG and ECG for subject #1, while **Figure 73c,d** depict the same signals for subject #3. **Table 10** reports the NCC indices and the time lags for each subject. As a reconfirmation of what has been observed in **Figure 72**, it can be noticed in **Figure 73** that the ensemble averages of dHF-FCG and SCG showed up with almost the same peaks and valleys. Moreover, dHF-FCG and SCG scored, at the same time, higher NCC indices and lower time lags with respect to HF-FCG and SCG (on average, 0.80 vs. 0.87, 14.7 ms vs. -0.7 ms). These results, which are consistent across the subjects involved in the study, suggest that the first derivative of the HF-FCG signal captures the salient features of the SCG signal better than the HF-FCG signal itself. For this reason, the dHF-FCG was used to locate the AO events and obtain the PEP estimates to be compared with the SCG ones.

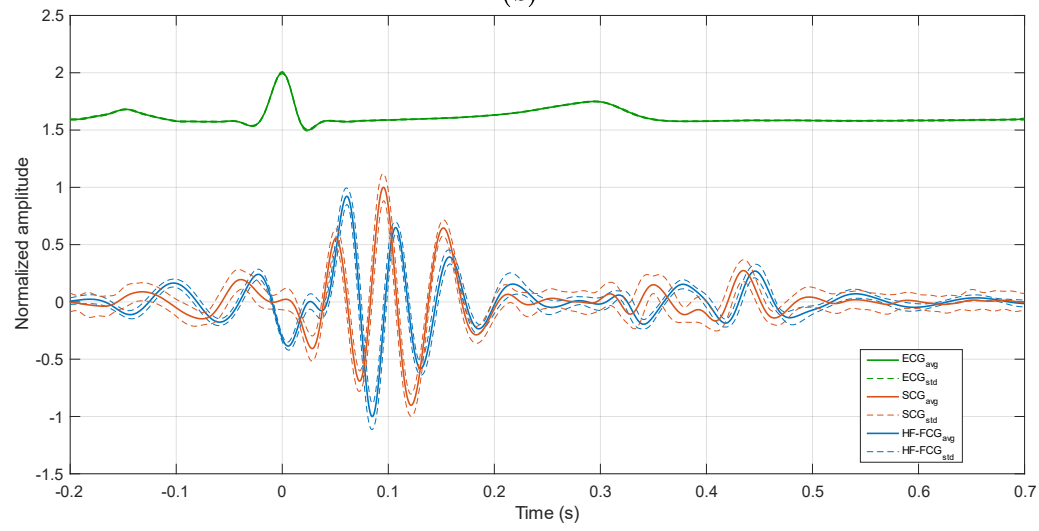


(a)

6.1 DETECTION OF AORTIC VALVE OPENING AND ESTIMATION OF PEP IN FCG SIGNALS



(b)



(c)

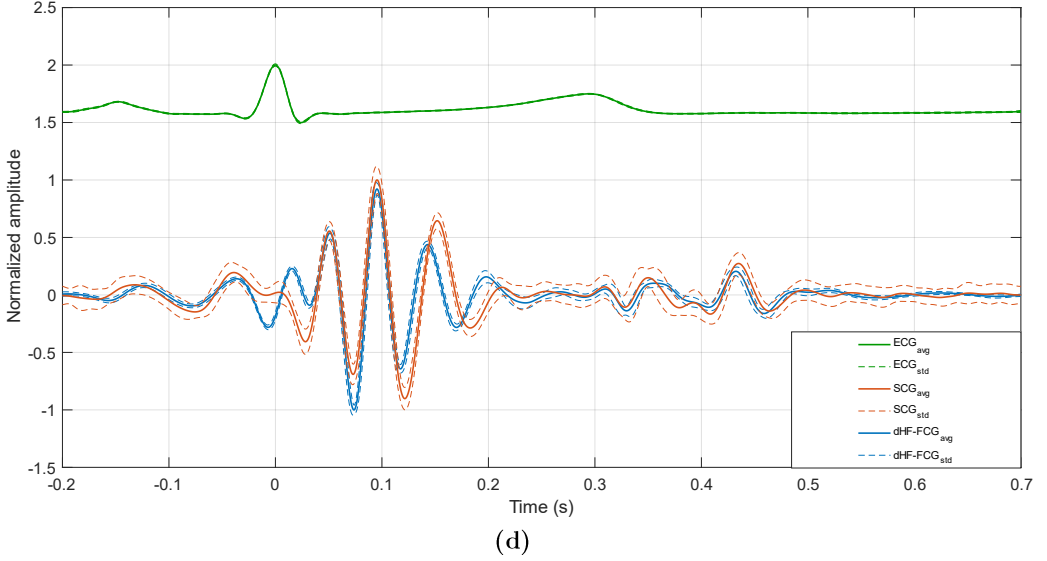


Figure 73. Ensemble averages of: (a) HF-FCG, SCG and ECG of subject #1; (b) dHF-FCG, SCG and ECG of subject #1; (c) HF-FCG, SCG and ECG of subject #3; (d) dHF-FCG, SCG and ECG of subject #3. The ensemble averages are depicted as solid lines, while the limits of the \pm SD ranges are depicted as dashed lines.

Table 10. NCC indices and time lags between the ensemble averages of HF-FCG vs. SCG and dHF-FCG vs. SCG for each subject. Positive time lags corresponded to FCG signals delayed with respect to SCG.

Subject #	HF-FCG vs SCG		dHF-FCG vs SCG	
	NCC	Lag (ms)	NCC	Lag (ms)
1	0.8333	18.6	0.9107	1.2
2	0.7764	14.7	0.8988	-2.2
3	0.7773	10.7	0.7998	-1.2

6.1.4 Statistical analyses on PEP estimates

The PEPs were estimated as the intervals between the ECG Q waves, provided by “BioSigKit”, and the related AO markers located on both SCG and dHF-FCG signals. The AO markers corresponding to each heartbeat were located by taking advantage of the a priori knowledge of the R-peaks locations on the ECG signals [21]. Both missed and spurious AO events were annotated for each subject. Regression, correlation and Bland–Altman analyses [150]–[151] of the PEP estimates

obtained from SCG and dH-FFCG signals were carried out via the MATLAB® function “bland-altman-and-correlation-plot” [152].

In **Table 11** and **Table 12**, the number of heartbeats detected in ECG, as well as the number of missed and spurious AO events detected in SCG and dHF-FCG, both in quiet breathing and apnea tests, are reported for each subject. Hence, sensitivity and PPV of AO events detection were computed according to the equations (10)-(11) provided in Section 5.1.4. In detail, a total of 227 and 424 heartbeats were found in the ECG signals acquired during apnea and quiet breathing, respectively. 227 AO events were detected in both SCG and dHF-FCG signals recorded during apnea conditions; therefore, no missed and spurious AO events were identified. On the other hand, 423 AO events were obtained for both SCG and dHF-FCG signals acquired in quiet breathing; hence, 1 missed AO event was found in both signals, which, instead, had no spurious AO events. According to these results, the SCG and dHF-FCG scored a sensitivity of 100% and 99.8 % in apnea and quiet breathing conditions, respectively, which are also reported in **Table 13**.

Table 11. *Number of heartbeats in ECG and of missed AO events in SCG and in dHF-FCG for each subject in apnea conditions.*

Apnea							
Subject #	Heartbeats	AO events		Missed AO events		Spurious AO events	
	ECG	SCG	dHF-FCG	SCG	dHF-FCG	SCG	dHF-FCG
1	112	112	112	0	0	0	0
2	54	54	54	0	0	0	0
3	61	61	61	0	0	0	0
Total	227	227	227	0	0	0	0

Table 12. Number of heartbeats in ECG and of missed AO events in SCG and in dHF-FCG for each subject in quiet breathing conditions.

Quiet breathing							
Subject #	Heartbeats	AO events		Missed AO events		Spurious AO events	
	ECG	SCG	dHF-FCG	SCG	dHF-FCG	SCG	dHF-FCG
1	200	200	200	0	0	0	0
2	118	118	118	0	0	0	0
3	106	60	60	1	1	0	0
Total	424	423	423	1	1	0	0

Table 13. Sensitivity and PPV of AO events detection in SCG and dHF-FCG signals.

	Sensitivity (%)	PPV (%)
SCG	100	99.8
dHF-FCG	100	99.8

Figure 74 shows the results of the regression, correlation and Bland–Altman analyses that were performed on a total of 227 PEP estimates obtained from SCG and dHF-FCG signals acquired during apnea tests. The statistical analyses reported a slope and intercept of 0.964 and 5.4 ms ($R^2 = 0.92$) and a bias of 1.2 ms (p-value < 0.0001) with LoA of $(-2.9; 5.4)$ ms. In **Figure 75**, the results of statistical analyses of PEP estimates obtained from signals acquired during quiet breathing are depicted. The analyses were performed on a total of 423 PEP estimates and reported a slope and intercept of 0.919 and 9.8 ms ($R^2 = 0.92$), as well as a bias of 1.4 ms (p-value < 0.0001), with LoA of $(-3.2; 6.0)$ ms. The results of regression, correlation and Bland–Altman analyses are also summarized in **Table 14**.

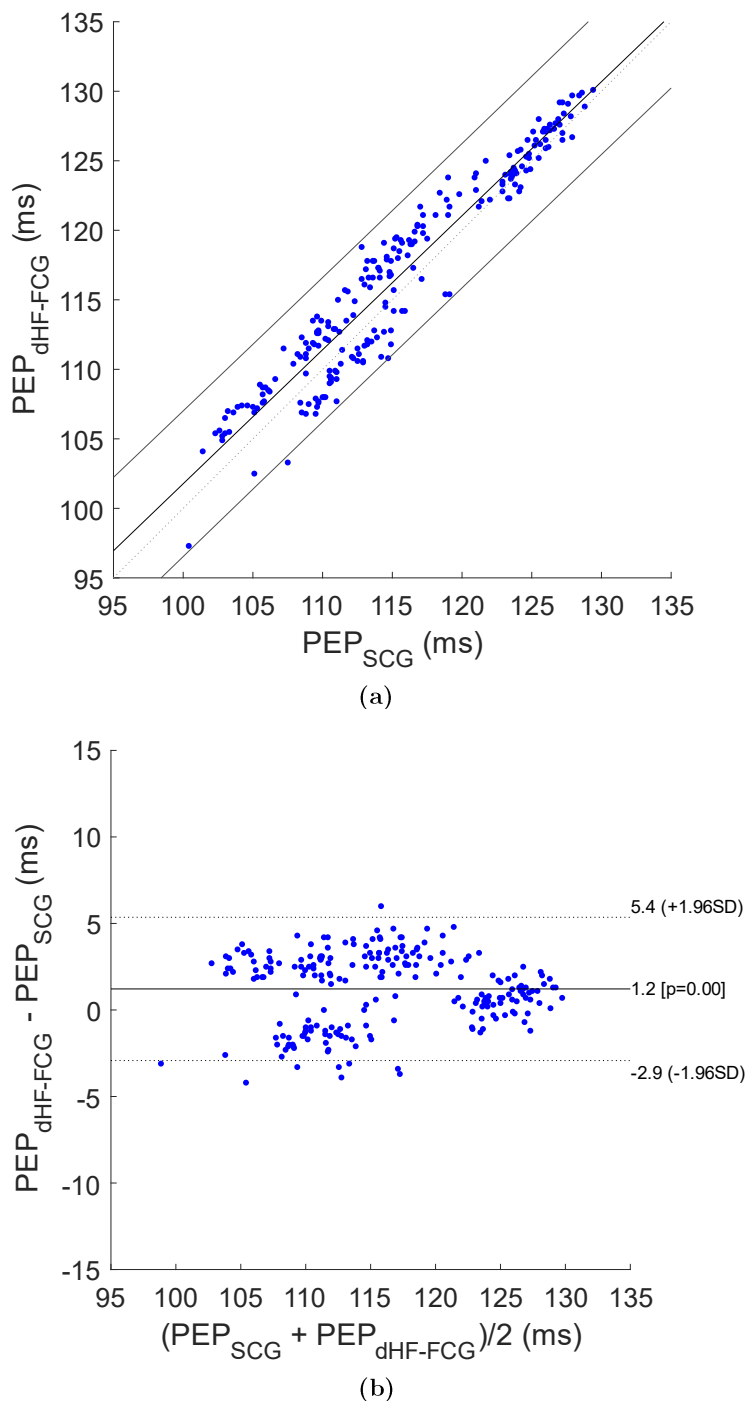


Figure 74. Statistical analyses on PEP estimates related to signals acquired during apneas: (a) results of regression and correlation analyses; (b) results of Bland–Altman analysis.

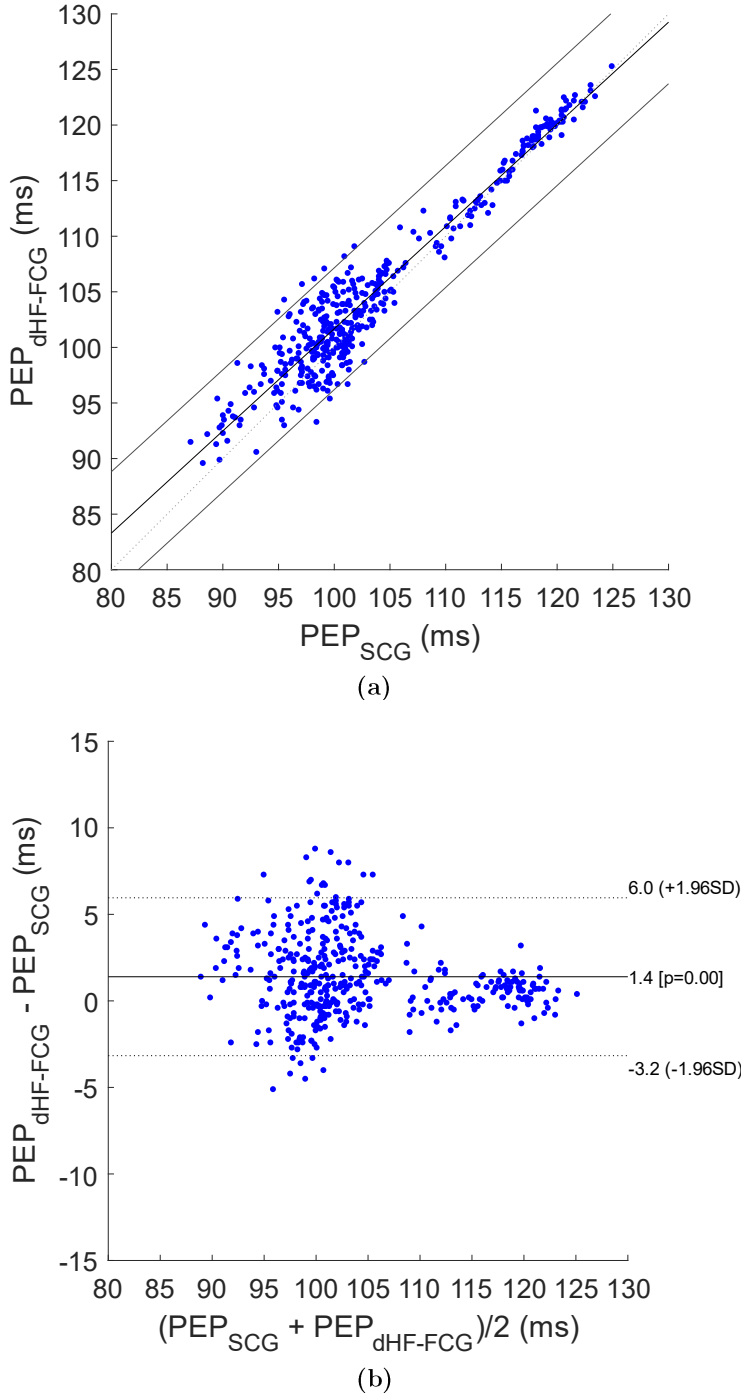


Figure 75. Statistical analyses on PEP estimates related to signals acquired during quiet breathing: (a) results of regression and correlation analyses; (b) results of Bland–Altman analysis.

Table 14. *Results of regression, correlation and Bland–Altman analyses for dHF-FCG vs SCG signals acquired during apnea and quiet breathing conditions.*

	Slope	Intercept (ms)	R ²	Bias	p-value	LoA (ms)
Apnea	0.964	5.4	0.92	1.2	< 0.0001	(-2.9; 5.4)
Quiet breathing	0.919	9.8	0.92	1.4	< 0.0001	(-3.2; 6.0)

6.1.5 Discussion

The results of this study suggest the existence of a derivative relationship between SCG and HF-FCG signals, which could explain the higher time lags observed between them, as well as the higher similarity between SCG and the first derivative of HF-FCG. The reason behind this derivative relationship is currently not clear and may lie in the dynamic response of the piezoelectric sensor; this phenomenon undoubtedly deserves an in-depth investigation, which is out of the scope of this research and will be addressed in future studies. Based on these results, the dHF-FCG was actually used to locate the AO events in the FCG recordings and then to obtain the PEP estimates to be compared with those extracted from SCG. These preliminary results, as compared to the results of other studies that analysed the performances of different techniques for PEP estimation [38],[165]-[166], suggest that FCG can provide accurate measurements of PEP in subjects at rest. Indeed, Dehkordi et al. [38] reported that 95% of the differences between PEP estimates obtained via SCG and ECHO were distributed within ± 25 ms around biases of about 2 ms, and, based on these results, they concluded that SCG provides acceptable accuracy and precision in estimating cardiac timings. Su et al. [165] found similar results concerning the 95% interval of the differences between PEP measurements obtained from an ankle-brachial device as compared to ECHO, although with a significantly higher bias of about 30 ms and correlations lower than 0.7, and they concluded that the device under test turned out to be a good alternative to ECHO in the evaluation of left ventricular systolic dysfunctions based on the estimation of PEP and other STIs.

This study has some limitations. The data analysed were acquired only on three healthy subjects at rest. Therefore, the results should be considered as preliminary and need to be confirmed on a larger cohort of subjects, including subjects performing different activities (e.g., walking, speaking, doing sports). Furthermore, FCG was compared with SCG due to its wide use for PEP monitoring in wearable applications, but SCG is not yet regarded as a gold standard for PEP estimation, so only the agreement between the two techniques could be evaluated. Hence, a comparison of FCG with echocardiographic measurement is envisioned in future studies to assess the performances of FCG in AO detection and PEP estimation against an actual gold standard.

6.2 Heartbeats localization in FCG signals via template matching

This study presents a preliminary investigation on the performances of a novel template matching approach for heartbeats localization in dHF-FCG signals, which is based on a very simple processing.

6.2.1 Measurement setup and protocol

Five healthy subjects were enrolled for this study. The piezoelectric FCG sensor described in [21] was used to acquire FCG signals from the subjects involved, who were asked to comfortably sit in a chair, leaning against the seatback with their back straight, and breathing at a natural pace. The FCG sensor was placed on the apical area of subjects' chest by roughly locating the PMI (see **Figure 76**). An ECG lead I was acquired simultaneously by means of a WelchAllyn Propaq® Encore monitor (Welch Allyn Inc., New York, NY, USA) to provide the ground truth for heartbeats locations and inter-beat intervals estimation. FCG and ECG signals were sampled via a National Instruments NI-USB4431 DAQ board (National Instruments Corp., 11,500 N Mopac Expwy, Austin, TX 78759-3504, USA), with 24-bit precision and 10 kHz sampling frequency.

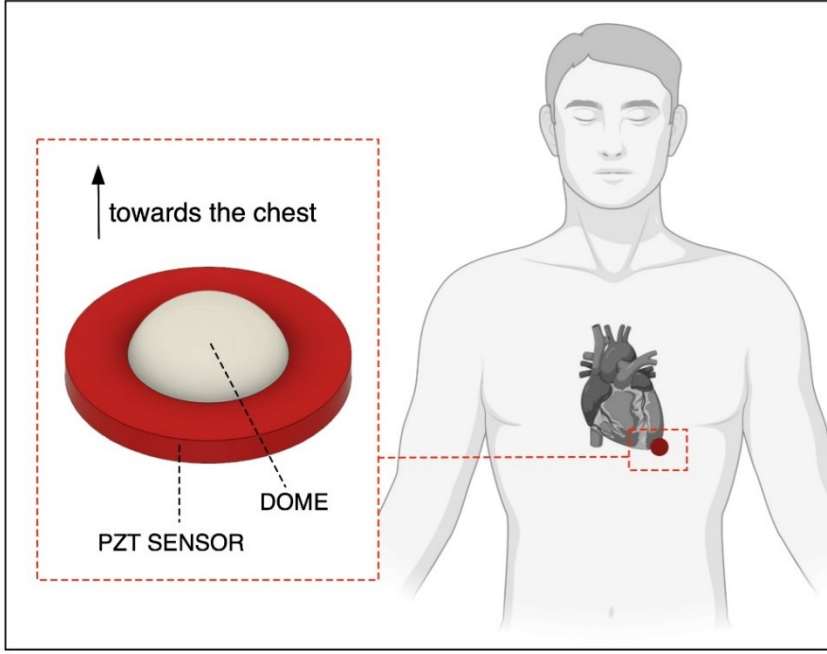


Figure 76. Piezoelectric FCG sensor applied on a subject's chest.

6.2.2 Signal pre-processing

A first pre-processing of the raw FCG sensor signals was performed to separate the actual Forcecardiogram from the respiratory component, i.e., the FRG signal. To this aim, a 3rd order Savitzki-Golay smoothing filter [157] with a frame length corresponding to about 1.5 s time interval was applied to extract the FRG, which was then subtracted from the raw FCG sensor signal to isolate the actual FCG signal. The FCG signal thus obtained was processed via a 4th order zero-lag Butterworth band-pass filter with cut-off frequencies of 7 and 30 Hz to extract the HF-FCG component, which provides information similar to the SCG. Finally, the first derivative of the HF-FCG signal (i.e., dHF-FCG) was computed, since the dHF-FCG exhibits the highest similarity to the SCG signal, also allowing accurate detection of AO events, as demonstrated in the previous study. The ECG signal was band-pass filtered in the 0.5 – 40 Hz band via a 4th order zero-lag Butterworth filter. Then, the R-peaks were located via the well-known Pan and Thompkins algorithm, implemented in the “BioSigKit” MATLAB® toolbox [149]. All processing operations

were performed in MATLAB® R2018b (MathWorks, Inc., 1 Apple Hill Drive, Natick, MA, USA).

6.2.3 Heartbeats localization via template matching

This study investigated the performance of a novel algorithm for heartbeats localization based on template matching. The first step of the proposed approach is the selection of the template, which should comprise both the systolic and diastolic complexes that appear in each cardiac cycle of the dHF-FCG signal. **Figure 77** shows an example of a template. After template selection, the NCC function is computed between the dHF-FCG signal to be analysed and the template, which slides along the entire signal. The NCC is defined as:

$$NCC[k] = \frac{\sum_n (s[n] - \mu_{s_k}) \cdot (t[n - k] - \mu_t)}{\sqrt{\sum_n (s[n] - \mu_{s_k})^2 \cdot \sum_n (t[n] - \mu_t)^2}} \quad (12)$$

where s is the signal, t is the template, μ_t is the mean of the template, and μ_{s_k} is the mean of the signal over the shifted template interval. NCC is a measure of similarity, conceptually corresponding to the cosine of the angle between two vectors in the Euclidean space and is independent from the amplitude of the two signals.

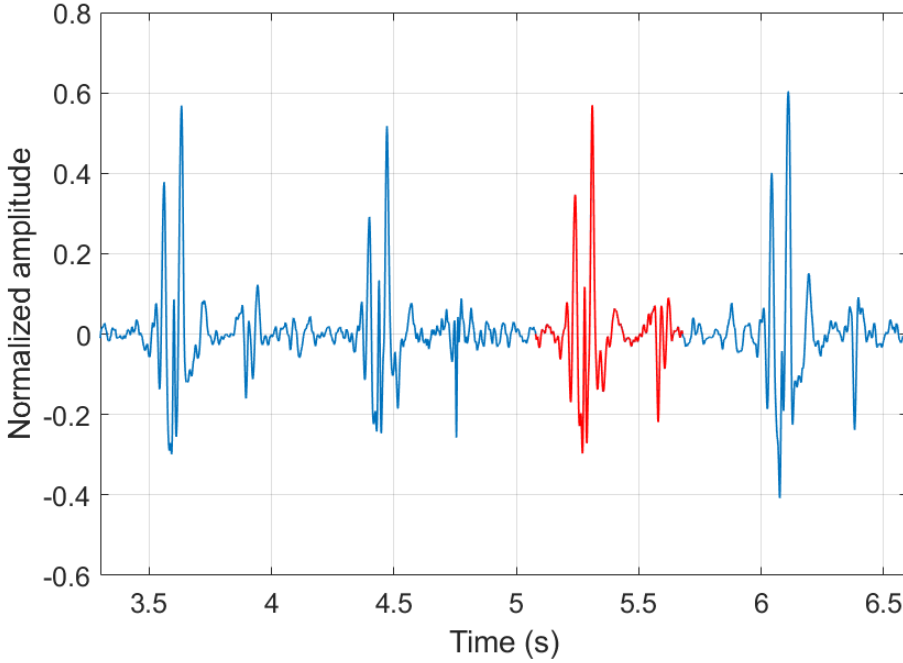


Figure 77. Example of a template (red line) selected within a dHF-FCG signal (blue line).

The dHF-FCG is a quasi-periodic signal and can be roughly represented as the repetition of a heartbeat pattern (selected as a template) with a period corresponding to the inter-beat interval. It follows that the NCC function computed between the dHF-FCG and the template is quasi-periodic as well, presenting peaks at the heartbeats. The highest peaks (i.e., the highest NCC values) mark the locations of dHF-FCG signal chunks that exhibit the highest similarity with the template, corresponding to each single heartbeat. In the proposed approach, these peaks are located via the Matlab® function “findpeaks”, by specifying a minimum peak prominence of 0.35 and a minimum peak distance of 500 ms (see **Figure 78**). Finally, the inter-beat intervals are obtained as differences between the locations of adjacent peaks.

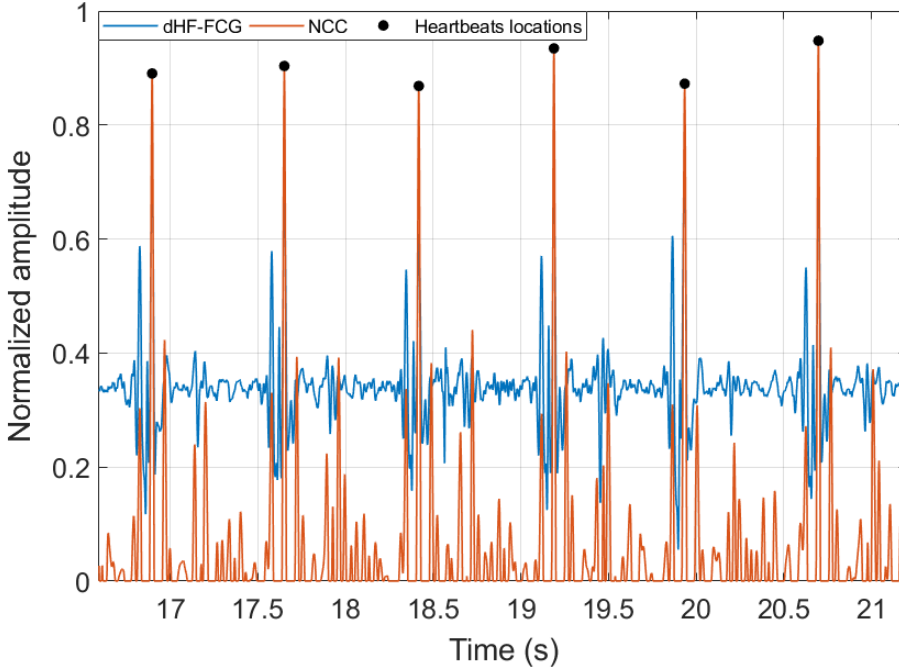


Figure 78. dHF-FCG signal (blue line) with the NCC (red line) obtained via the template depicted in Figure 77, and the heartbeat markers (black dots) located in the NCC.

6.2.4 Statistical analyses on inter-beat intervals

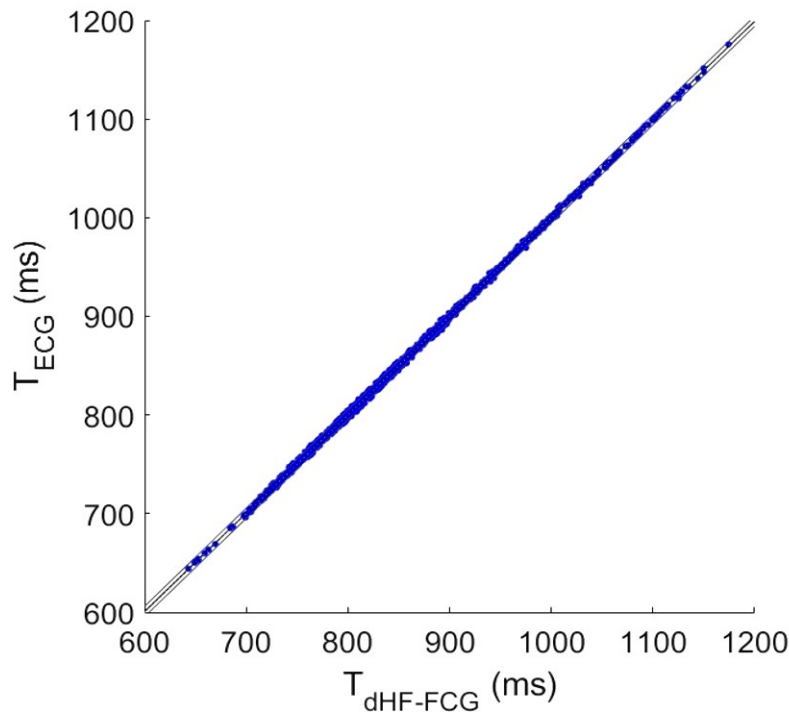
Sensitivity and PPV were assessed as performance metrics for heartbeats detection, according to the equations (10)-(11) provided in Section 5.1.4. The proposed approach allowed detecting all the heartbeats without false detections, thus scoring both sensitivity and PPV of 100 % on a total of 1214 heartbeats.

The accuracy of the temporal localization of heartbeats was evaluated by comparing the inter-beat interval estimates obtained from dHF-FCG and ECG via statistical analyses. To this aim, linear regression and Bland-Altman [150]-[151] analyses were carried out, by means of the MATLAB® function “bland-altman-and-correlation-plot” [152]. In detail, the statistical analyses were performed on a total of 1213 inter-beat intervals estimated from the recordings of all the subjects involved. Very accurate inter-beat intervals estimates were obtained via the proposed approach. Indeed, the linear regression analysis reported a slope of 0.9972 and an intercept of 2.383 ms, with an R^2 value of 0.9995 (see **Figure 79**). The Bland-Altman analysis

reported a non-significant bias (p-value = 0.8198) and LoA of ± 4.2 ms, i.e., the 95% of the differences between the measurements obtained with ECG and FCG turned out to be confined within the 0.5% of the average of all measurements. No specific trends were observed in the measurements’ differences, which appeared to be distributed around zero (see **Figure 79**). The results of regression, correlation and Bland–Altman analyses are also summarized in **Table 15**.

Table 15. Results of regression, correlation and Bland–Altman analyses for dHF-FCG signals. Non-significant bias is indicated as “NS”.

	Slope	Intercept (ms)	R ²	Bias	p-value	LoA (ms)
dHF-FCG	0.9972	2.383	0.9995	NS	0.8198	± 4.2



(a)

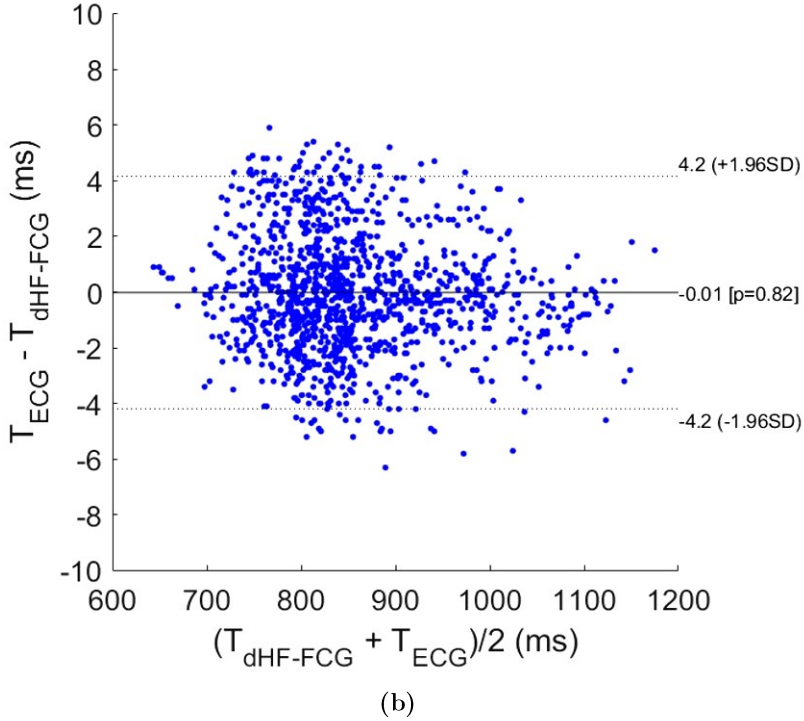


Figure 79. Statistical analyses on inter-beat interval estimates: (a) results of regression and correlation analyses; (b) results of Bland–Altman analysis.

6.2.5 Discussion

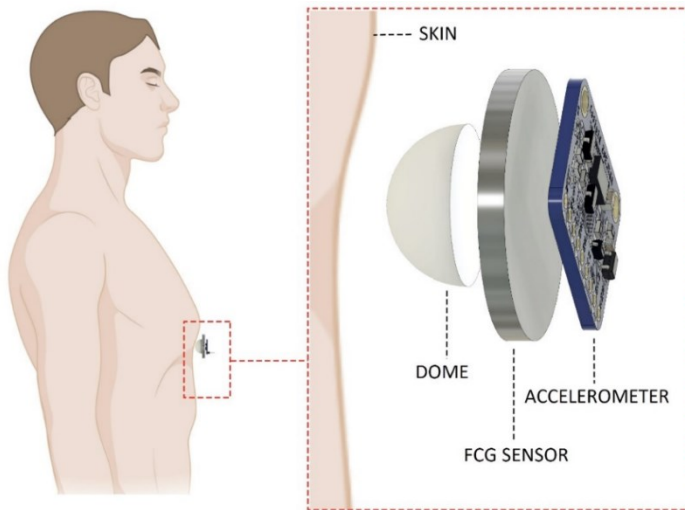
The preliminary results of this proof-of-concept study are very promising, as a surprisingly high sensitivity and PPV were achieved for heartbeats detection at the cost of few processing operations, also with a very accurate estimation of inter-beat intervals, as compared to the gold standard (i.e., the ECG). However, such a performance was assessed on a very limited cohort of subjects in resting conditions. Therefore, further performance assessment on a much larger cohort, possibly including also subjects performing physical activities, is needed to confirm the promising results observed in this study. It is worth highlighting that the proposed method does not rely on ECG data, thus being also suitable for strictly cardio-mechanical monitoring, which is particularly appealing for continuous, long-term wearable monitoring applications.

Comparison between LF-FCG signal and double integration of seismocardiogram

As already reported in Chapter 4, the LF-FCG component seems to be related to ventricular emptying and filling events, which cannot be appreciated directly in SCG recordings, nor extracted by simple low-pass filtering [20]. The reason could lie in the inherent poor sensitivity that accelerometers exhibit to slow movements. Undoubtedly, the low-frequency displacements associated with the ventricular volume variations usually result in extremely smaller accelerations as compared to those produced by heart valves snaps, thus making their observation in SCG recordings impractical. No successful approaches have been proposed yet in literature to recover information on ventricular emptying and filling from SCG. In this chapter, a method to extract this information from SCG is presented, which is based on numerical double integration of accelerometric SCG signals.

7.1 Measurement setup and protocol

This study presents a retrospective analysis of signals acquired in [21]. In detail, the FCG signals were acquired via the piezoelectric FCG sensor presented in [21], also described in Section 5.2.1, equipped with a dome-shaped mechanical coupler. The dorso-ventral SCG signals were simultaneously acquired by recording the z-axis acceleration signals of a Freescale MMA7361 accelerometer (Freescale Semiconductor – NXP Semiconductors, Eindhoven, the Netherlands), which was fixed onto the FCG sensor, as shown in **Figure 80a**. The FCG and SCG sensors assembly was placed onto the chest of each subject via a medical adhesive tape, by roughly locating the PMI, and then fastened with a belt around the thorax (see **Figure 80b**). Simultaneous acquisitions of FCG and SCG signals, together with an ECG lead I provided by a WelchAllyn Propaq® Encore monitor (Welch Allyn Inc., New York, NY, USA), were carried out via a National Instrument NI-USB4431 DAQ board (National Instruments Corp., 11500 N Mopac Expwy, Austin, TX 78759-3504, USA), with 24-bit precision and 10 kHz sampling frequency. Five healthy volunteers (3 males and 2 females, age 36.6 ± 11.0 years), who signed the informed consent, were asked to comfortably sit in a chair, leaning against the seatback while keeping their back straight. Multiple acquisitions were performed for each subject in two respiratory conditions, i.e., quiet breathing and apnea.



(a)

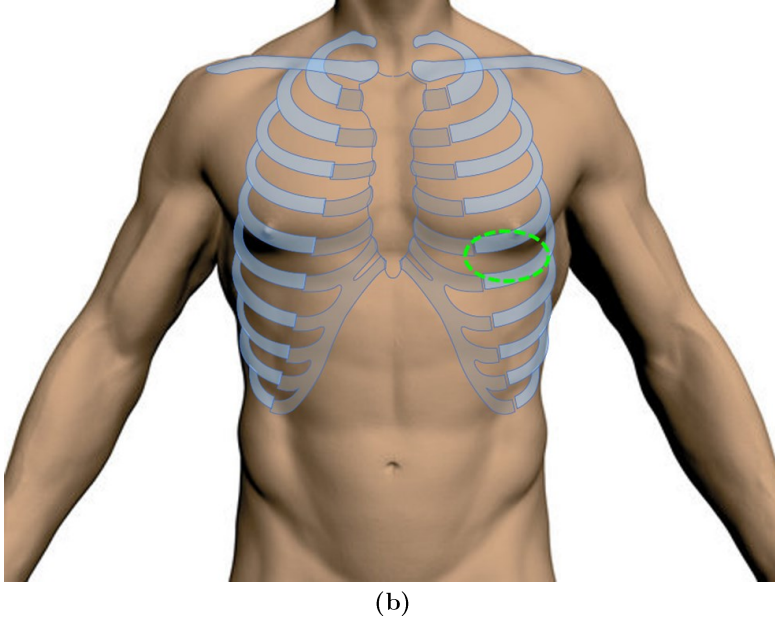


Figure 80. (a) Lateral view of sensors assembly applied on the chest of a subject; (b) frontal view of sensors positioning area on the chest (green dashed line).

7.2 Signals processing

The signals acquired during quiet breathing and apneas were processed and analysed separately. All processing and analyses were carried out in MATLAB® R2017b (The MathWorks, Inc., 1 Apple Hill Drive, Natick, MA 01760, USA).

7.2.1 FCG signals processing

In signals acquired during quiet breathing, the FRG component was first extracted via a 3rd order Savitzki-Golay filter [157], with a frame length corresponding to about a 1.5 s interval. Then, the FRG thus obtained was subtracted from the raw FCG sensor signal to isolate the actual FCG signal, which was further processed via a 2nd order Butterworth band-pass filter with cut-off frequencies set at 0.5 and 5 Hz, to eventually obtain the LF-FCG signal. In signals acquired during apneas, the FRG subtraction step was not carried out since no respiratory activity had been captured,

so the raw FCG sensor signal was directly band-pass filtered in the 0.5 – 5 Hz frequency band to extract the LF-FCG signal.

7.2.2 SCG signals processing

Numerical double integration of SCG signals was performed via the following procedure. Before the integration, DC removal was performed on accelerometric signal by subtracting its time average. The actual numerical integrations were then performed via the MATLAB® function “cumtrapz”, which computes an approximation of the cumulative integral of a signal via the trapezoidal method. After each integration step, the resulting signal was iteratively processed via a 4th order zero-lag Butterworth high-pass filter with 0.6 Hz cut-off frequency for 40 times. This strong high-pass filtering is a fundamental step, since it allows filtering out spurious low-frequency components produced by the numerical integration, which show up with extremely higher amplitudes as compared to the signals of interest. Finally, the double-integrated signal, referred to as “Displacement SCG” (DSCG), was processed via the same band-pass filter used to extract the LF-FCG, so as to obtain the low-frequency component of the DSCG, referred to as LF-DSCG.

7.3 Morphological comparison between LF-FCG and LF-DSCG signals

The morphologies of LF-FCG and LF-DSCG signals were compared by evaluating the following NCC indices: (a) between the whole signals; (b) between single corresponding heart beats extracted from the two signals; (c) between the ECG-triggered ensemble averages (synchronized with R-peaks) of the two signals. This analysis was carried out separately for signals acquired during quiet breathing and during apneas.

7.3.1 LF-FCG vs LF-DSCG during apneas

Figure 81 shows a comparison of the LF-FCG and LF-DSCG signals acquired during apneas from subject #2, along with the ECG signal acquired concurrently. In **Table 16** the NCC indices of the LF-FCG and LF-DSCG signals acquired during

apneas are reported for each subject. For the indices related to the whole signals (NCC_W) and to the ECG-triggered ensemble averages (NCC_E), a single value was reported, while for the indices related to single heartbeats, the mean and the SD of the indices scored for all heartbeats were reported for each subject, and referred to as NCC_{MEAN} and NCC_{SD} , respectively. The ECG-triggered ensemble averages scored NCC_E of 0.93 ± 0.054 , which turned out to be in excess of 0.94 for all but one subject (#5). On single heartbeats, LF-FCG and LF-DSCG scored NCC_{MEAN} of 0.88 ± 0.083 , which turned out to be in excess of 0.9 for 3 out of 5 subjects and reduced by less than 5% with respect to NCC_E in all but one subject (#1), and NCC_{SD} of 0.063 ± 0.057 , which turned out to be lower than 0.1 for all but one subject (#1). The whole LF-FCG and LF-DSCG signals scored NCC_W of 0.82 ± 0.15 and turned out to be reduced by less than 15% with respect to the related NCC_{MEAN} and NCC_E in all but one subject (#1).

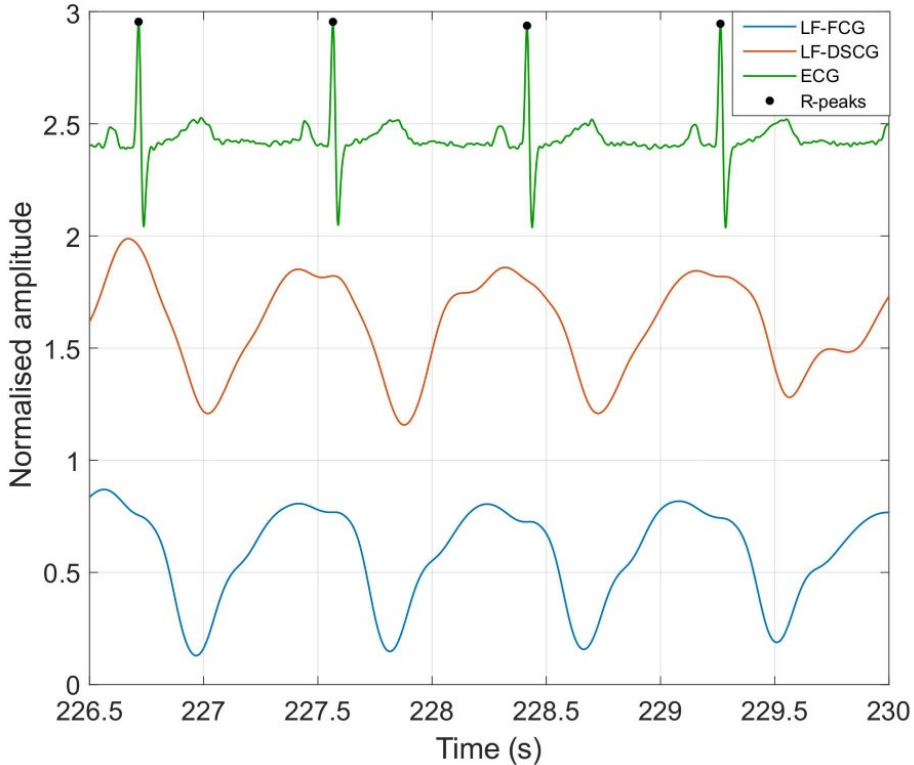


Figure 81. LF-FCG, LF-DSCG and ECG signals acquired during apneas from subject #2. Black points indicate R-peaks locations.

Table 16. *NCC indices of the LF-FCG and LF-DSCG signals acquired during apneas. The correlation indices were computed between the whole signals, between single corresponding heartbeats (mean and SD of correlation indices are reported) and between the ECG-triggered ensemble averages.*

Subject #	Whole signals	Single heartbeats		Ensemble averages
		Mean	SD	
1	0.6003	0.7782	0.1574	0.9647
2	0.8961	0.9132	0.04177	0.9470
3	0.9315	0.9423	0.02863	0.9507
4	0.9473	0.9496	0.01551	0.9556
5	0.7300	0.7932	0.07253	0.8341

7.3.2 LF-FCG vs LF-DSCG during quiet breathing

Figure 82 shows a comparison of the LF-FCG and LF-DSCG signals acquired during quiet breathing from subject #2, along with the ECG signal acquired simultaneously and the FRG signal extracted from the raw FCG sensor signal. In **Table 17** the NCC indices of the LF-FCG and LF-DSCG signals acquired during quiet breathing are reported for each subject. The ECG-triggered ensemble averages scored NCC of 0.90 ± 0.027 , which turned out to be in excess of 0.90 for 3 out of 5 subjects. On single heartbeats, LF-FCG and LF-DSCG scored NCC_{MEAN} of 0.81 ± 0.022 , which turned out to be in excess of 0.8 for 3 out of 5 subjects and reduced by about 10% with respect to the related NCC_E for all subjects, and NCC_{SD} of 0.12 ± 0.011 , which turned out to be lower than 0.15 for all subjects. The whole LF-FCG and LF-DSCG signals scored NCC of 0.72 ± 0.12 and turned out to be reduced by less than 10% with respect to the related NCC_{MEAN} and less than 20% with respect to the related NCC of the ensemble averages, in all but one subject (#5).

7.3 MORPHOLOGICAL COMPARISON BETWEEN LF-FCG AND LF-DSCG SIGNALS

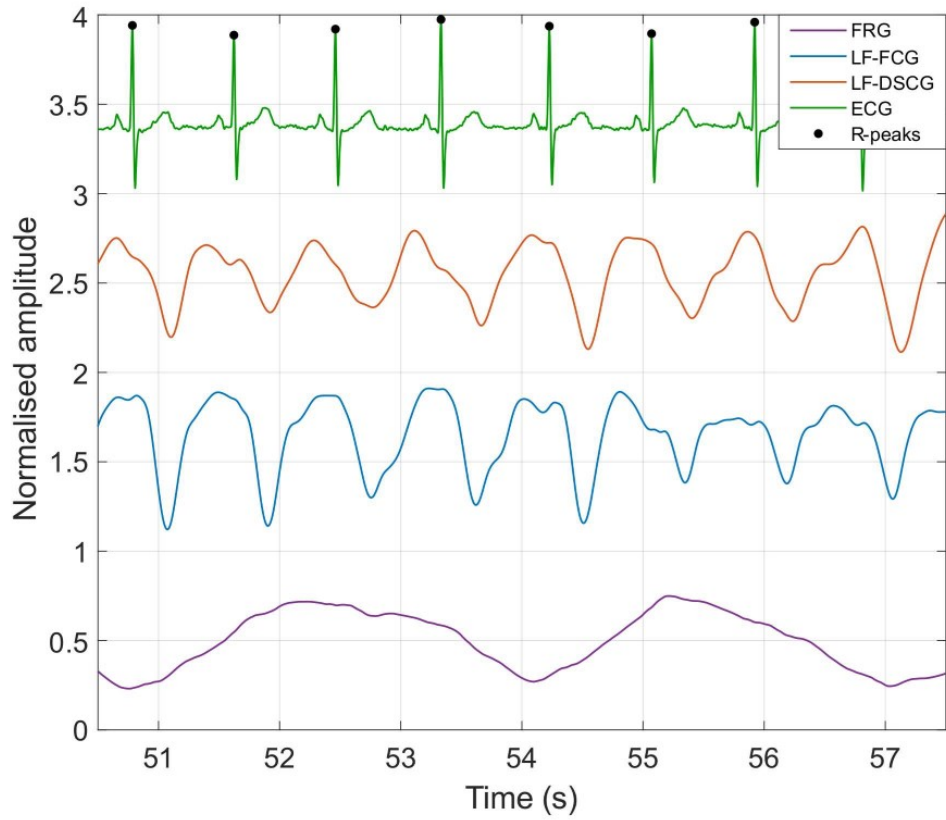


Figure 82. FRG, LF-FCG, LF-DSCG and ECG signals acquired during quiet breathing from subject #2. Black points indicate R-peaks locations.

Table 17. NCC indices of the LF-FCG and LF-DSCG signals acquired during quiet breathing. The correlation indices were computed between the whole signals, between single corresponding heartbeats (mean and SD of correlation indices are reported) and between the ECG-triggered ensemble averages.

Subject #	Whole signals	Single heartbeats		Ensemble averages
		Mean	SD	
1	0.7125	0.7919	0.1232	0.8728
2	0.7840	0.8248	0.1085	0.9262
3	0.8060	0.8244	0.1195	0.9251
4	0.7649	0.8145	0.1040	0.9012
5	0.5166	0.7739	0.1306	0.8728

7.4 Statistical analyses on inter-beat intervals

The consistency of the LF-DSCG signal within the cardiac cycle was assessed by evaluating its ability to detect the heartbeats, as well as the accuracy and precision of the derived HR measurements. These performances were assessed by assuming the ECG signal as the reference and were further compared with those achieved by the LF-FCG signal. To this aim, the R-peaks were first located in the ECG signal via the “BioSigKit” MATLAB® toolbox, which implements the well-known Pan and Thompkins algorithm [149]. Then, the heartbeats were detected both in the LF-FCG and LF-DSCG signals by considering the negative peaks of the first derivatives of the signals as fiducial markers, which were located by taking advantage of the a priori knowledge of R-peaks locations [20]-[21]. The annotation of the missed heartbeats in the LF-FCG and LF-DSCG signals was carried out by comparison with the ECG. Finally, the inter-beat intervals computed from the fiducial markers of the LF-FCG and LF-DSCG signals were compared with those obtained from the ECG R-peaks via regression, correlation and Bland-Altman [150]-[151] analyses, which were carried out by using the MATLAB® function “bland-altman-and-correlation-plot” [152]. The intervals related to the missed heartbeats were excluded from these statistical analyses.

7.4.1 Inter-beat intervals from LF-FCG and LF-DSCG signals acquired during apneas

In the signals acquired from all subjects during apneas, 4 and 63 missed heartbeats were found, respectively, in LF-FCG and LF-DSCG, out of a total of 698 heartbeats detected in the simultaneously acquired ECG signals. Consequently, LF-FCG and LF-DSCG scored a sensitivity of 99.4% and 91.0% respectively. **Figure 83** and **Figure 84** show the results of the regression, correlation and Bland-Altman analyses that were performed on the inter-beat intervals extracted from LF-FCG and LF-DSCG, respectively, as compared to those extracted from ECG. The inter-beat intervals related to the missed heartbeats were discarded from the analyses, which were performed on a total of 670 intervals for LF-FCG and 581 intervals for LF-DSCG. The statistical analyses reported, for LF-FCG, a slope and intercept of 1.003

and -2.8 ms ($R^2 = 0.995$) and a non-significant bias (p-value = 0.96) with LoA of ± 12.6 ms; for LF-DSCG, a slope and intercept of 0.983 and 14.1 ms ($R^2 = 0.603$) and a non-significant bias (p-value = 0.89) with LoA of ± 134.4 ms. The results of regression, correlation and Bland–Altman analyses are also summarized in **Table 18**.

Table 18. Results of regression, correlation and Bland–Altman analyses for LF-FCG vs LF-DSCG signals acquired during apneas. Non-significant bias is indicated as “NS”.

	Slope	Intercept (ms)	R^2	Bias	p-value	LoA (ms)
LF-FCG	1.003	-2.8	0.995	NS	0.96	± 12.6
LF-DSCG	0.983	14.1	0.603	NS	0.89	± 134.4

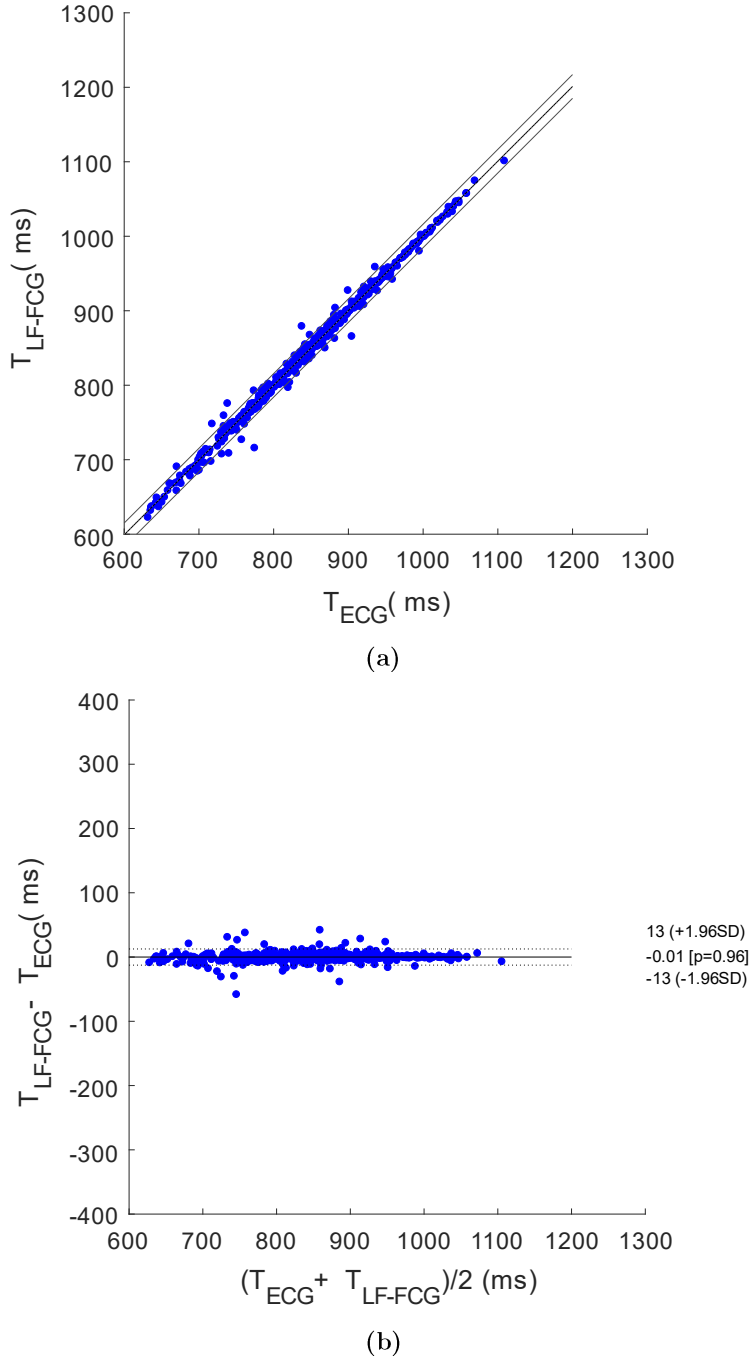


Figure 83. Statistical analyses on inter-beat intervals extracted from LF-FCG signals during apneas. (a) Results of regression and correlation analyses; (b) results of Bland-Altman analysis.

7.4 STATISTICAL ANALYSES ON INTER-BEAT INTERVALS

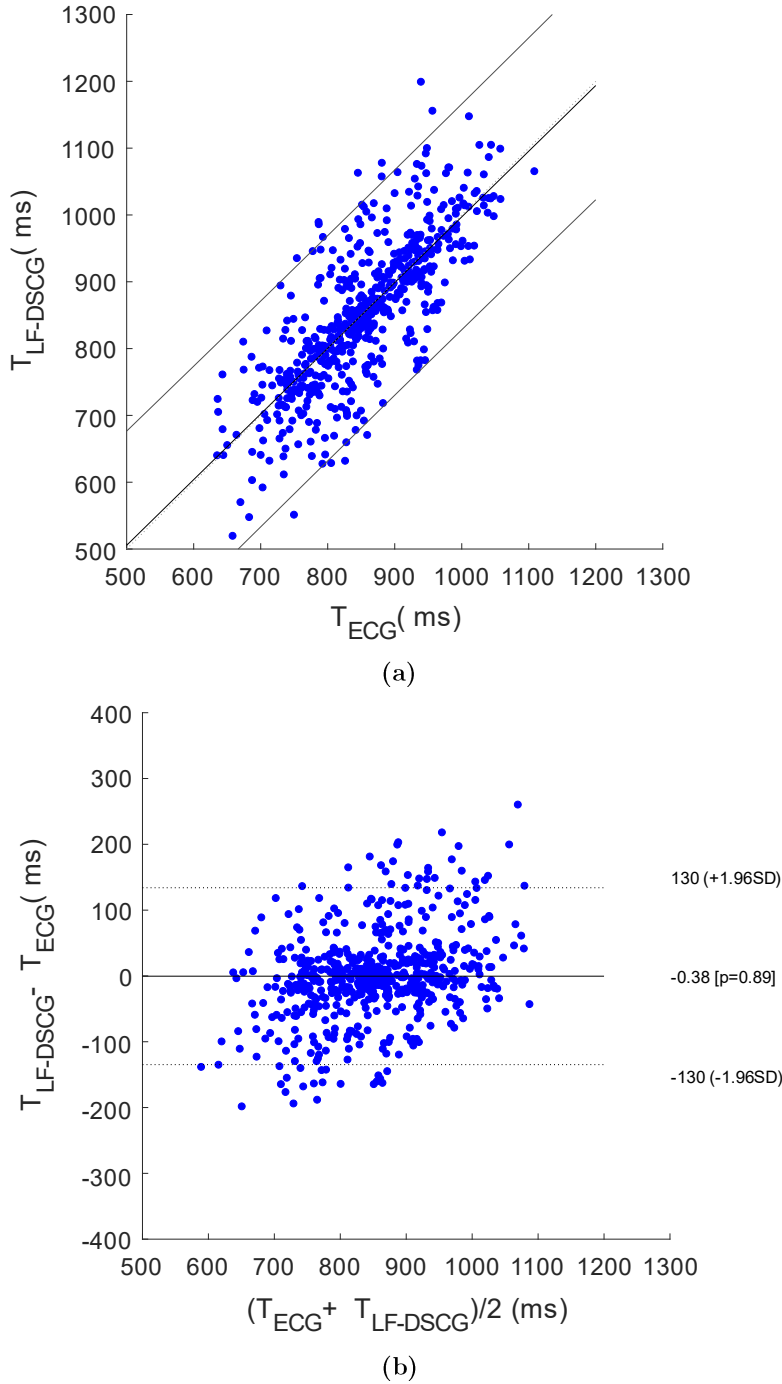


Figure 84. Statistical analyses on inter-beat intervals extracted from LF-DSCG signals during apneas. (a) Results of regression and correlation analyses; (b) results of Bland-Altman analysis.

7.4.2 Inter-beat intervals from LF-FCG and LF-DSCG signals acquired during quiet breathing

A total of 1026 heartbeats were detected in the ECG signals acquired from all subjects during quiet breathing. In the related LF-FCG signals a total of 11 missed heartbeats were found, while 125 missed heartbeats were found in the LF-DSCG signals. Consequently, LF-FCG and LF-DSCG scored a sensitivity of 98.9% and 87.8%, respectively. **Figure 85** and **Figure 86** show the results of the statistical analyses that were performed on the inter-beat intervals extracted from the signals acquired during quiet respiration. The inter-beat intervals related to the missed heartbeats were discarded from the analyses, which were performed on a total of 1000 intervals for LF-FCG and 819 intervals for LF-DSCG. Slope and intercept of 0.9985 and 1.4 ms ($R^2 = 0.993$) were found for LF-FCG, as well as a non-significant bias (p-value = 0.91) with LoA of ± 16.2 ms, while for LF-DSCG, a slope and intercept of 0.997 and 1.3 ms ($R^2 = 0.631$) and a non-significant bias (p-value = 0.51) with LoA of ± 139.9 ms were found. The results of regression, correlation and Bland–Altman analyses are also summarized in **Table 19**.

Table 19. Results of regression, correlation and Bland–Altman analyses for LF-FCG vs LF-DSCG signals acquired during quiet breathing. Non-significant bias is indicated as “NS”.

	Slope	Intercept (ms)	R^2	Bias	p-value	LoA (ms)
LF-FCG	0.9985	1.4	0.993	NS	0.91	± 16.2
LF-DSCG	0.997	1.3	0.631	NS	0.51	± 139.9

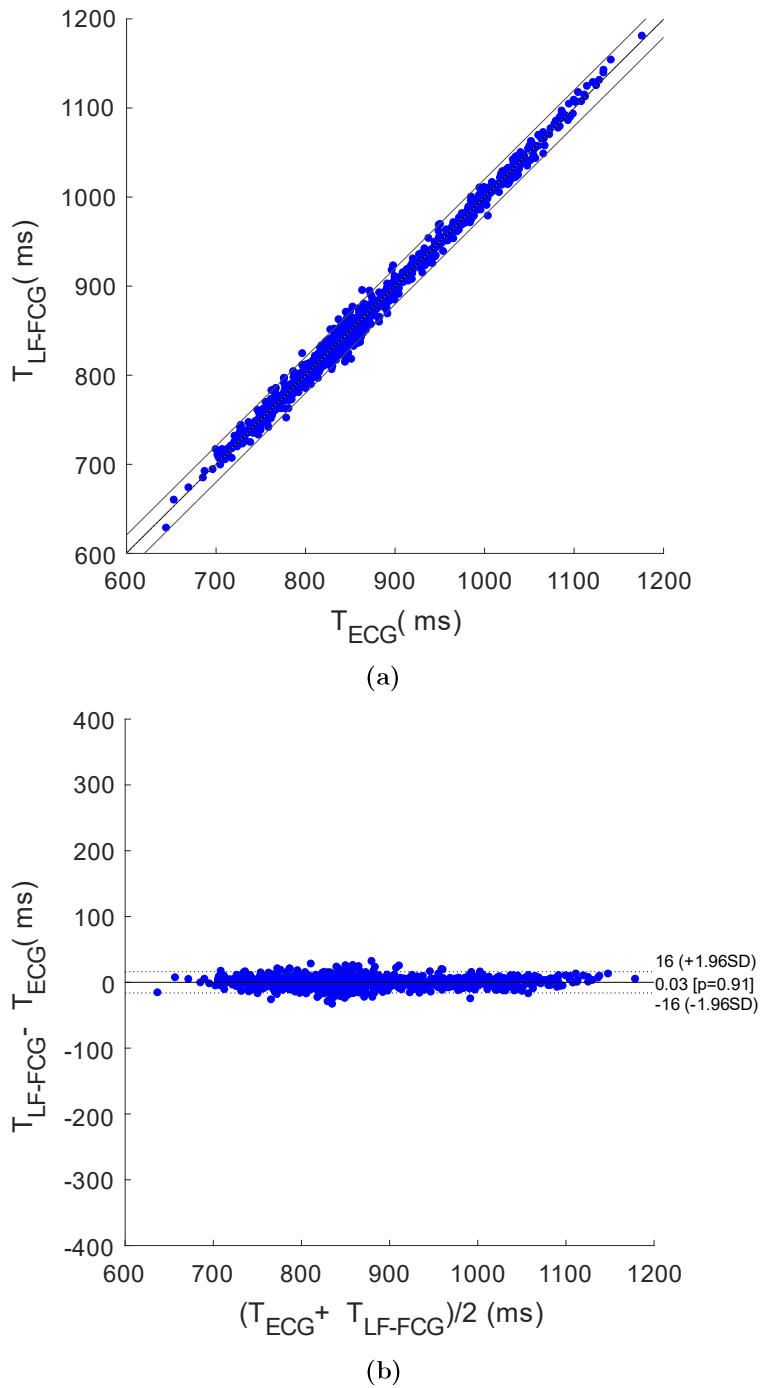


Figure 85. Statistical analyses on inter-beat intervals extracted from LF-FCG signals during respiration. (a) Results of regression and correlation analyses; (b) results of Bland-Altman analysis.

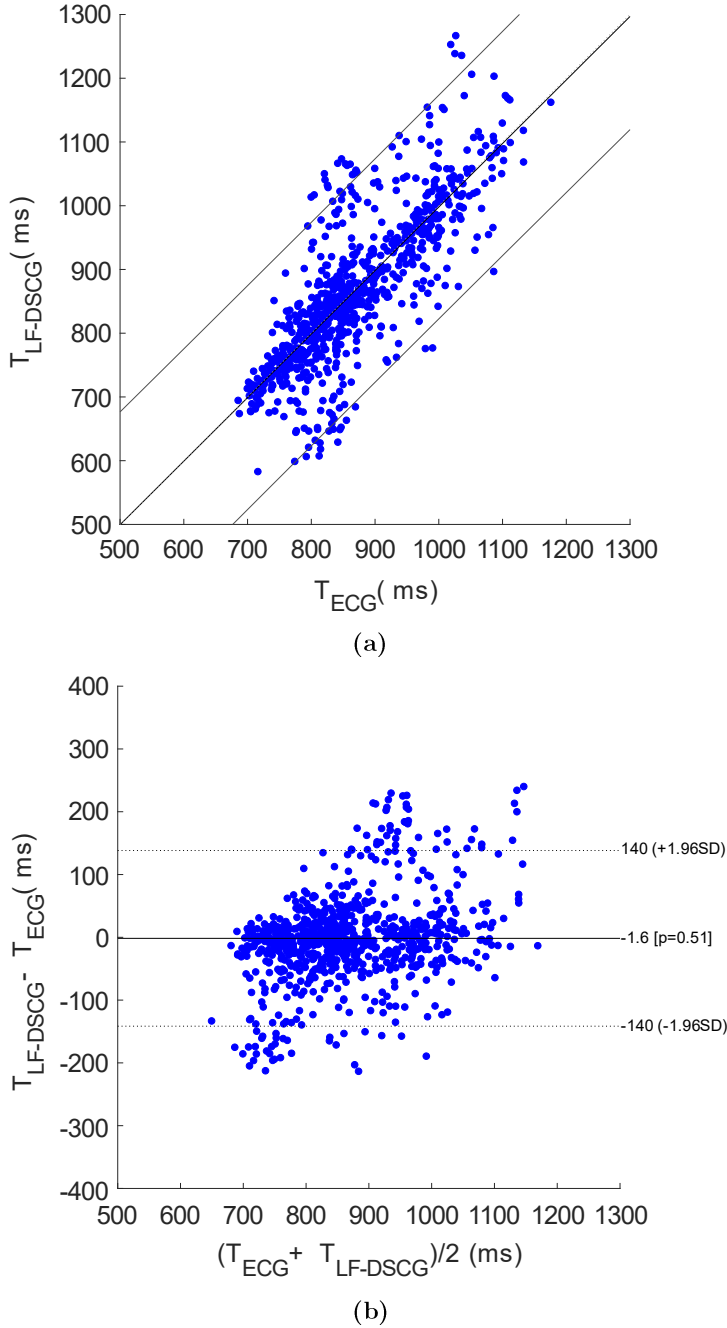


Figure 86. Statistical analyses on inter-beat intervals extracted from LF-DSCG signals during respiration. (a) Results of regression and correlation analyses; (b) results of Bland-Altman analysis.

7.5 Discussion

The results of this study demonstrated that the proposed method yields a new displacement signal (i.e., DSCG), which is not directly visible in SCG recordings, nor can be extracted by simple filtering operations, also overcoming the well-known problems associated with numerical double integration (usually prone to large errors). The DSCG signal features a low-frequency component (i.e., LF-DSCG) that captures ACG-like information on heart walls displacements related to ventricular volume variations. This component also shows high similarity to the LF-FCG signal. Mean NCC indices in excess of 0.9, both during apnea and quiet breathing, scored by the ECG-triggered ensemble averages of LF-FCG and LF-DSCG show that the proposed approach based on numerical double integration of SCG signals successfully recovered the essential features of the LF-FCG morphology, i.e., those that got through the ensemble averaging operation. The morphological comparison of single heartbeats (without ensemble averaging) reported slightly lower correlations (on average $0.8 < \text{NCC}_{\text{MEAN}} < 0.9$), which turned out to be reduced by less than 5% in all but one subject during apneas, and by about 10% in all subjects during quiet breathing. These findings suggest that the LF-DSCG could be able to monitor morphological variations in different heartbeats. However, the higher NCC_{SD} obtained in quiet breathing with respect to apneas suggest that the interference of the respiratory activity may impair the quality of LF-DSCG signals. Concerning the results obtained for the whole signals, while during apneas the average NCC_{W} turned out to be still higher than 0.8, during quiet breathing it reduced to about 0.7, which is by more than 10% with respect to NCC_{MEAN} and more than 20% with respect to NCC_{E} . This result implies that LF-DSCG, as obtained via the proposed approach, is not able to track the beat-by-beat changes in morphology and amplitude of LF-FCG with reasonable accuracy. Moreover, the results of the statistical analyses show that LF-DSCG achieved fair sensitivity in heartbeats detection (about 90%) but exhibited moderate consistency within the cardiac cycle, which led to LoA with ECG higher than 130 milliseconds for inter-beat interval estimation.

In conclusion, when properly processed with a specific numerical procedure, the SCG signal could provide information on heart walls displacements, as the FCG. This

information was first captured by ACG, which has been shown to give important insights into the mechanical behaviour of the beating heart, both under physiological and pathological conditions [68],[73],[167]-[172]. As already reported in Section 3.2.2, this technique has lost its appeal due to the cumbersome instrumentation required and the clear superiority of ECHO as a diagnostic tool in clinical settings. Nonetheless, FCG and DSCG stand as promising ways of recovering the wide knowledge acquired on ACG, both in normal and pathological conditions, and transfer it to wearable monitoring applications. The results of this study show that LF-FCG exhibits higher consistency within the cardiac cycle with respect to LF-DSCG. This suggests that FCG currently outperforms the double integration of SCG. However, further experiments with high-performance accelerometers and advanced processing methods could improve the accuracy and reliability of DSCG [173]. Finally, a deeper investigation through the comparison with ECHO is envisioned in the future to assess the relationship of FCG and DSCG with actual heart walls displacements. To this aim, the application of the proposed double integration procedure to 3D SCG signals will also be investigated, as it has been shown that 3D accelerations may bring more comprehensive information about cardiac-induced vibrations of the chest wall [174].

Multimodal finger pulse wave sensing: comparison of FCG and PPG sensors

In this chapter, a true multimodal pulse wave (PW) sensor is presented, which was obtained by integrating a piezoelectric FCG sensor [21] and a PPG sensor, thus enabling simultaneous mechanical-optical measurements of PWs from the same site on the body.

8.1 Photoplethysmography

Photoplethysmography (PPG) is one of the most widely used techniques for PWs sensing, owing to its ability to measure blood oxygen saturation when both red and infrared light sources are used simultaneously. PPG is commonly used both in clinical and non-clinical settings, and it has been integrated in a variety of consumer electronics products to enable wearable, unobtrusive monitoring of HR and arrhythmias [175]-[177]. PPG monitors blood volume variations in a microvascular bed of the skin non-invasively, by measuring the related changes in the optical absorption, scattering, and transmission properties of human tissues under a specific

light wavelength [178]. In particular, PPG records the amount of light transmitted or reflected by tissues, which varies over time according to pulsation, as it causes changes in the optical path and in the amount of light absorbed by the monitored body part. To this end, PPG sensors irradiate light at specific wavelengths into the skin, which passes through various skin structures (tissues, veins, arteries) and is finally measured by a photodetector [175]-[177]. The measured light intensity depends upon several factors, such as the blood volume at the measurement site, skin pigmentation and composition, the arterial diameter, and the concentration and direction of oxygenated and deoxygenated haemoglobin [179]-[181]. Light sources with various wavelengths can be used, with the depth of penetration usually increasing with the wavelength [182]-[183]. As an example, by increasing the wavelength from 470 nm (which allows it to reach the epidermis with capillaries) to 570 or 660 nm, the irradiated light can penetrate to the dermis with arterioles, and down to arteries in subcutaneous tissues, respectively [184]-[185]. As major blood vessels with solid pulsations are mainly located in the dermis or subcutaneous tissues, light sources with red (640–660 nm) and infrared (880–940 nm) wavelengths are commonly used in PPG sensors [175],[186].

PPG sensors usually feature one or more light-emitting diodes and wavelength-matched photodetectors. According to the positioning of light sources and detectors on the monitored body part, PPG sensors can be divided into the transmissive type and reflective type. Transmissive PPG sensors have the source and detector placed at opposite sides of the monitored body part and measure the intensity of the transmitted light, while reflective PPG sensors have the source and detector placed next to each other on the same side of the monitored body part and measure the intensity of the reflected light [175]. Reflective PPG sensors show less stable performance than transmissive ones [175],[187]. On the other hand, reflective PPG sensors are not restricted to distal, thinner body parts, but can also monitor blood volume changes in other body districts where light transmission is difficult [175]. Indeed, PPG is usually acquired for peripheral body districts, especially extremities such as the fingers, toes, and earlobes, because their shallow vascular beds ensure high-quality measurements of blood volume changes [188]-[190]. This is particularly true for transmissive PPG sensors, as body districts with small widths ensure

reasonable transmitted light intensities, while thicker body districts absorb too much light, thus resulting in unsuitable signal-to-noise ratios. However, reflective PPG sensors can also be applied on the forehead, face, nose, and oesophagus [191]-[194], as well as on shallow arteries of thicker body parts, such as carotid arteries in the neck, radial and ulnar arteries in the wrist, brachial arteries in the arms, and femoral arteries in the thighs [195]-[197].

The low cost and unobtrusiveness of PPG sensors has promoted their use in a broad spectrum of applications, the most popular ones undoubtedly being pulse oximetry, i.e., measurement of saturation of peripheral oxygen (SpO_2) with the combined use of red and infrared wavelengths and HR monitoring [175]-[177]. Other clinical applications of PPG sensors include: BP estimation [198]-[207]; the assessment of vascular aging [208]-[213] and peripheral vascular disease [214]-[217]; the monitoring of respiratory-induced changes in peripheral blood flow and the correlation between intrathoracic pressure and cardiac function in patients with heart failure or respiratory distress [218]-[219]; sleep monitoring for the detection of apnea and hypopnea conditions [220]-[223]; the estimation of SV and CO [224]-[227]; and the detection of atrial fibrillation [228].

The typical pulse waveform recorded via PPG sensors is obtained by inverting the light intensity signal acquired by the photodetector and is commonly divided into pulsatile and non-pulsatile components [175],[177],[229]. The pulsatile component is correlated with the cardiac cycle and influenced by vasodilation, vasomotor, and vascular tones, as well as respiration and autonomic nervous system activity [230]-[238]. The non-pulsatile component is influenced by ambient light [239], biological characteristics such as tissue composition and basic blood volume of the measurement site, and various physiological phenomena such as respiration, vasomotor activity, and thermoregulation [240]-[243]. Skin color, blood vessel distribution, vascular stiffness, oxygen-carrying capacity, bone size, and cardiac output are also known to affect the amplitude of PPG signals [244]-[245]. For these reasons, the analysis of PPG waveforms is still an important subject of scientific research. In addition, the physiological relevance of first and second derivatives of PPG signals (also known as velocity and acceleration PPG, respectively) has been recognized since the 1970s [175]. As an example, it has been shown that indices extracted from peaks and valleys of the second derivative of a PPG signal have

significant correlations with aging [213]. In addition, PPG derivative signals support the robust recognition of specific fiducial markers (e.g., peaks and valleys, inflection points, and points of maximal slope), which can be difficult to locate in the original PPG waveform [175].

8.2 Multimodal PW sensor

The multimodal PW sensor was realized by integrating a PPG and a piezoelectric FCG sensor. In particular, the FCG sensor described in [21], also presented in Section 5.2.1, and a PPG sensor board equipped with a MAX30102 chip (Maxim Integrated Products, INC., 160 Rio Robles, San Jose, CA 95134, USA, 408-601-1000) were firmly attached together, in order to make them integral. FCG sensors are usually equipped with dome-shaped mechanical couplers, as they ensure optimal transduction of force from tissues to the sensor. However, in this case, the PPG sensor had to be in direct contact with the finger, so the FCG sensor could not be directly interfaced with the skin via a dome-shaped coupler. To this end, a small, flat cylinder with a diameter of 5 mm was firmly attached both to the back of the PPG sensor board and to the active area of the FCG sensor. In fact, the overall PPG sensor and flat cylinder compound acted as a mechanical coupler for the FCG sensor, thus ensuring a reasonable transduction of force from the finger to the sensor. **Figure 87** depicts the structure of the proposed multimodal PW sensor.

The multimodal PW sensor thus realized was applied on subjects' fingers by means of medical adhesive tape. Since static contact force is known to affect the performance of PW sensors [175],[177], and piezoelectric sensors cannot be used for static force measurement, an additional FSR (FSR 402 short, Interlink Electronics, Inc., 1 Jenner Suite 200, Irvine, CA 92618) was attached onto the active area of the piezoelectric FCG sensor, beneath the flat cylinder, to monitor the actual contact force applied by the multimodal PW sensor when mounted on subjects' fingers. The FSR had an active area with a diameter of 12.7 mm; therefore, a flat cylinder diameter of 5 mm was appropriate. Static calibration of the FSR was performed as in [20]-[21] to obtain actual force measurements from the FSR sensor readings.

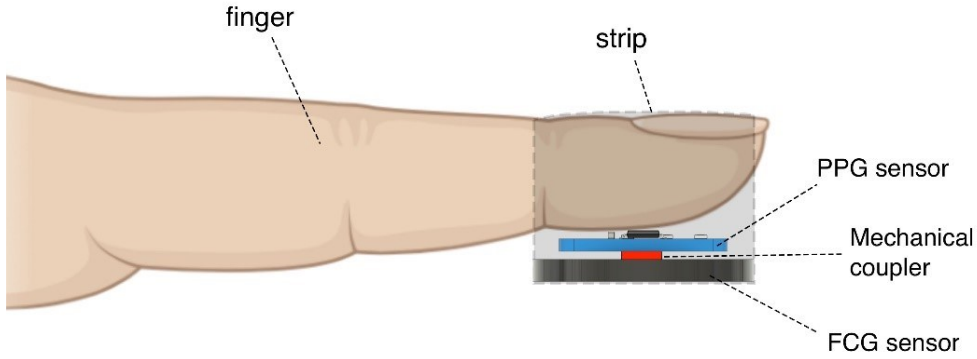


Figure 87. Schematic representation showing the components of the multimodal PW sensor placed on a subject's finger, namely MAX30102 PPG sensor, piezoelectric FCG sensor, and a flat cylinder acting as a mechanical coupler to ensure reasonable force transduction from the PPG sensor to the FCG sensor.

8.3 Measurement setup and protocol

Simultaneous recordings of finger PWs and ECG lead I were obtained, respectively, from the multimodal PW sensor and an ECG board (SparkFun Electronics, Inc., 6333 Dry Creek Parkway, Niwot, Colorado 80503) based on the AD8232 single-lead heart rate monitor front end (Analog Devices, Inc., 1 Analog Way, Wilmington, MA 01887, USA).

Five healthy subjects (4 males and 1 female; age: 26 ± 2.5 years; height: 177 ± 5.87 cm; weight: 86.0 ± 27.2 kg; BMI: 27.3 ± 7.60) were enrolled for the experiments. Information on the subjects' gender, age, height, weight, and BMI are reported in **Table 20**. The subjects were required to comfortably lie on a medical couch in a supine position. The multimodal PW sensor was mounted on the index finger of the right hand with a reasonable contact force, so as to ensure good contact with the finger tissues, without providing excessive stress. Indeed, as reported in the literature [177], if contact force is either too low or too high, the quality of PW signals is substantially impaired. Afterwards, ECG electrodes were placed on subjects' limbs to acquire an ECG lead I. Non-invasive blood pressure (NIBP) measurements were also acquired to ensure that the subjects were not in an altered state. To this end, an NIBP cuff was firmly placed around the left arm and NIBP measurements were

acquired via a multiparameter patient monitor (Dynascope DS-7000, Fukuda Denshi, Co., Ltd., 2-35-8 Hongo, Bunkyo-ku, Tokyo, 113-8420, Japan).

Table 20. *Subjects' demographics.*

Subject #	Gender	Age (years)	Height (cm)	Weight (kg)	BMI
1	Male	23	181	75	22.89
2	Female	27	175	63	20.57
3	Male	30	168	82	29.05
4	Male	26	183	133	39.71
5	Male	26	178	77	24.30

Signals from the multimodal PW sensor and the ECG lead were simultaneously acquired at 200 Hz via an STM32F401RE microcontroller board (STMicroelectronics, Inc., 39 Chemin du Champ des Filles Plan-Les-Ouates, 1228, Switzerland). To this end, the sampling frequency of the MAX30102 digital PPG sensor was set at 200 Hz and the FCG and ECG sensors readings performed by the analog-to-digital converter of the microcontroller (12 bits) were synchronized with the interrupt signal provided by the PPG sensor. This approach did not ensure a perfectly synchronous sampling of all signals (maximum delay lower than 0.5 ms); however, this was not strictly required for this study. An alternative solution to multichannel synchronous sampling is described in [246].

8.4 Signal processing and analysis

All processing and analyses were carried out in MATLAB® R2017b (MathWorks, Inc., 1 Apple Hill Drive, Natick, MA 01760, USA).

8.4.1 Pre-processing

PW signals provided by the piezoelectric FCG sensor, the PPG sensor, i.e., red (PPG-R) and infrared (PPG-IR) signals, as well as the ECG lead I, were first resampled at 1 kHz, and then, pre-processed to remove high-frequency noise and

baseline oscillations. All PW signals were first low-pass filtered via an 8th order zero-lag Butterworth filter (4th order filter applied sequentially in forward and backward directions) with the cut-off frequency set at 20 Hz. Then, a 3rd order Savitzky–Golay filter [157], with a frame length corresponding to about a 1.5 s interval, was applied to extract baseline oscillations, which were then removed from the signals that had previously been obtained after low-pass filtering. The PW signals provided by the PPG sensor were reversed in amplitude to obtain positive systolic peaks. Finally, the ECG signal was band-pass filtered in the 0.5 – 40 Hz frequency band via an 8th order zero-lag Butterworth filter.

8.4.2 Detection of fiducial points

R-peaks were first located in the ECG signal via the well-known Pan and Thompkins algorithm, implemented in the “BioSigKit” MATLAB® toolbox [149]. Then, the following well-established fiducial points [177] were located in the PW signals provided by the PPG and FCG sensors (see also **Figure 88**):

- the foot of the systolic rise (referred to as “foot”);
- systolic peak;
- dicrotic notch;
- diastolic peak.

Since the assessment of robustness to motion artifacts was out of the scope of this preliminary study, all signal segments containing motion artifacts in at least one of the PW signals provided by the multimodal PW sensor were excluded from the analyses.

8.4.3 Extraction of PW morphological parameters

After the PW fiducial markers had been located, the following parameters were computed, which are commonly used to characterize the morphology of PW signals [177]:

- t_{up} : time distance between the foot and the systolic peak;
- t_i : time distance between the foot and the dicrotic notch;
- T : time distance between two consecutive feet;

- t_{up}/T : ratio of foot time distances from the systolic peak and from subsequent foot;
- h_1 : systolic peak height with respect to the foot;
- h_2 : diastolic notch height with respect to the foot;
- h_3 : diastolic peak height with respect to the foot;
- h_2/h_1 : ratio of the diastolic notch to the systolic peak heights;
- h_3/h_1 : ratio of the diastolic to systolic peaks heights.

h_1 , h_2 , and h_3 related to PPG and FCG sensors signals were not compared, because they are related to different physical quantities. Instead, the h_2/h_1 and h_3/h_1 ratios are dimensionless quantities that actually characterize the morphology of PW signals, and were considered for the comparison, along with t_{up} , t_i , T , and t_{up}/T .

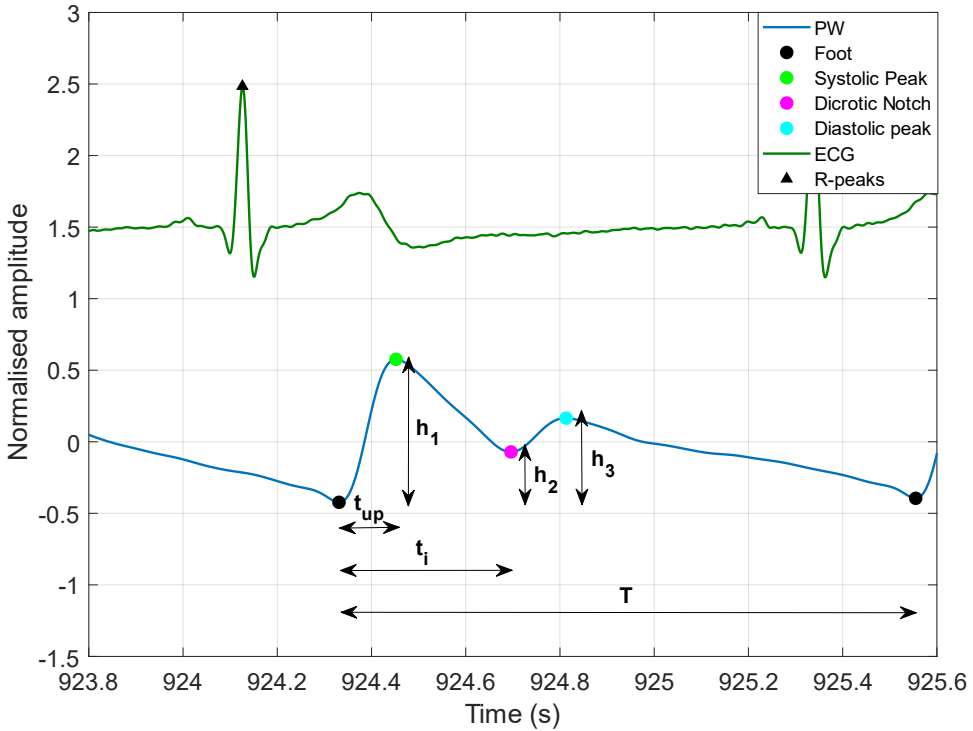


Figure 88. Graphical example of PW fiducial points and morphological parameters.

Figure 89 shows an example of ECG and PW signals acquired from subjects #1 and #3. **Figure 89a,b** show 30-second segments where it can be clearly observed that piezoelectric PWs (blue line) and optical PWs (red and black lines) are very

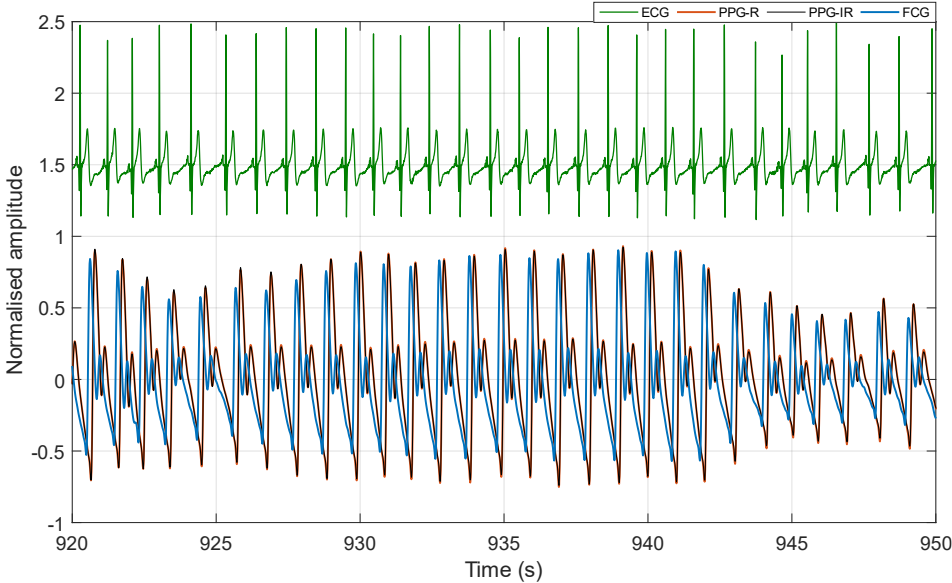
similar, the latter being consistently delayed with respect to the former. A detail on PW morphology is depicted in **Figure 89c,d**, which show 5-second PW signal segments, along with localized fiducial markers. A delay between corresponding markers can also be observed.

The pulse arrival time (PAT), considered as the time interval between PW systolic peaks and ECG R-peaks, across all subjects was 483 ± 20.2 ms for PPG-R (red light), 485 ± 19.4 ms for PPG-IR (infrared light), and 315 ± 22.0 ms for the piezoelectric FCG sensor. The average PATs of the PPG signals were found to be in agreement with those reported in [247], while the PATs of the piezoelectric PW signals turned out to be consistently lower, which further highlights the existence of a time delay between optical and piezoelectric PW signals. This delay was estimated by considering the time intervals between corresponding fiducial markers of piezoelectric and PPG signals, which are outlined in **Table 21**.

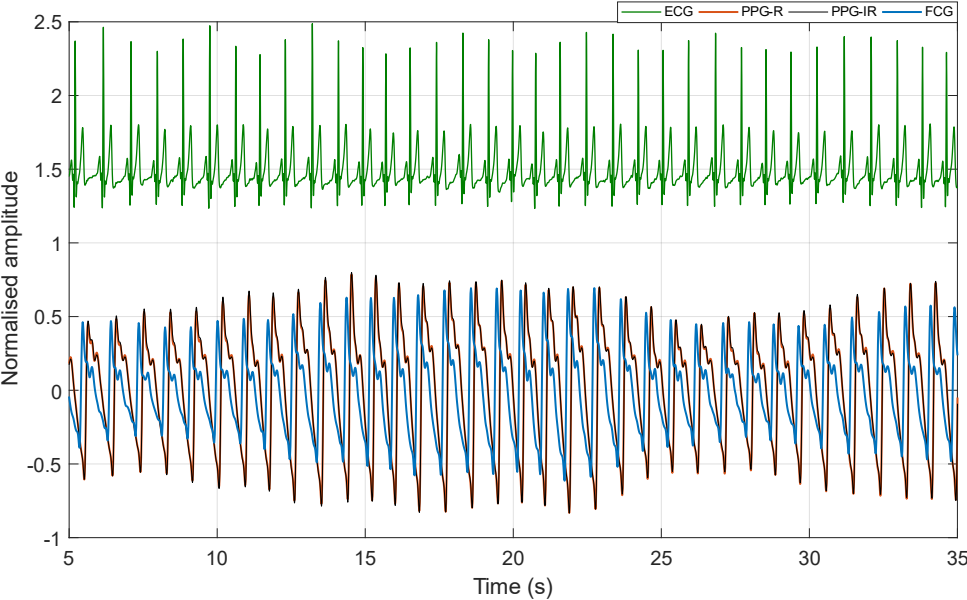
Figure 90 shows 5-second segments of the original PW signals acquired from subjects #1 and #3, along with the first and second derivatives.

Table 21. Mean and SD of time delays (in milliseconds) between PW fiducial markers of FCG and PPG.

Subject #	Foot		Systolic Peak		Dicrotic Notch		Diastolic Peak	
	PPG-R	PPG-IR	PPG-R	PPG-IR	PPG-R	PPG-IR	PPG-R	PPG-IR
1	163 ± 1.12	165 ± 1.15	168 ± 4.39	170 ± 4.77	166 ± 1.52	168 ± 1.33	164 ± 3.66	166 ± 3.94
2	162 ± 2.58	164 ± 2.18	162 ± 8.77	166 ± 11.3	167 ± 6.27	171 ± 6.36	167 ± 6.27	171 ± 6.36
3	163 ± 4.44	165 ± 4.53	174 ± 5.38	177 ± 6.17	178 ± 26.3	183 ± 26.3	166 ± 8.77	168 ± 8.61
4	165 ± 11.3	166 ± 15.7	170 ± 5.92	171 ± 5.72	169 ± 3.20	171 ± 2.91	167 ± 4.30	170 ± 4.03
5	164 ± 2.35	165 ± 2.42	165 ± 6.67	165 ± 5.79	163 ± 4.94	166 ± 4.99	162 ± 6.30	163 ± 6.47



(a)



(b)

8.4 SIGNAL PROCESSING AND ANALYSIS

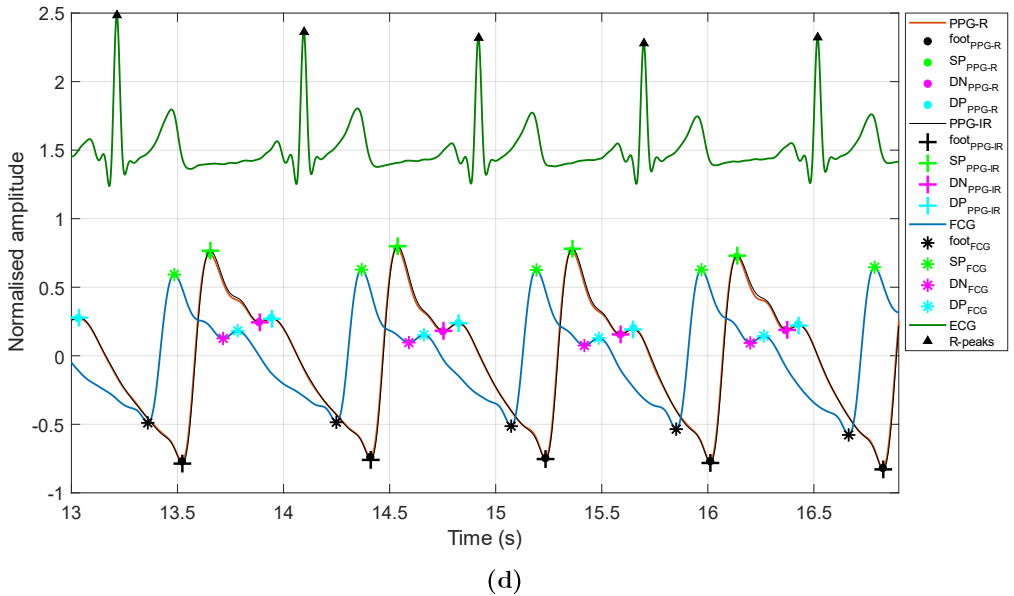
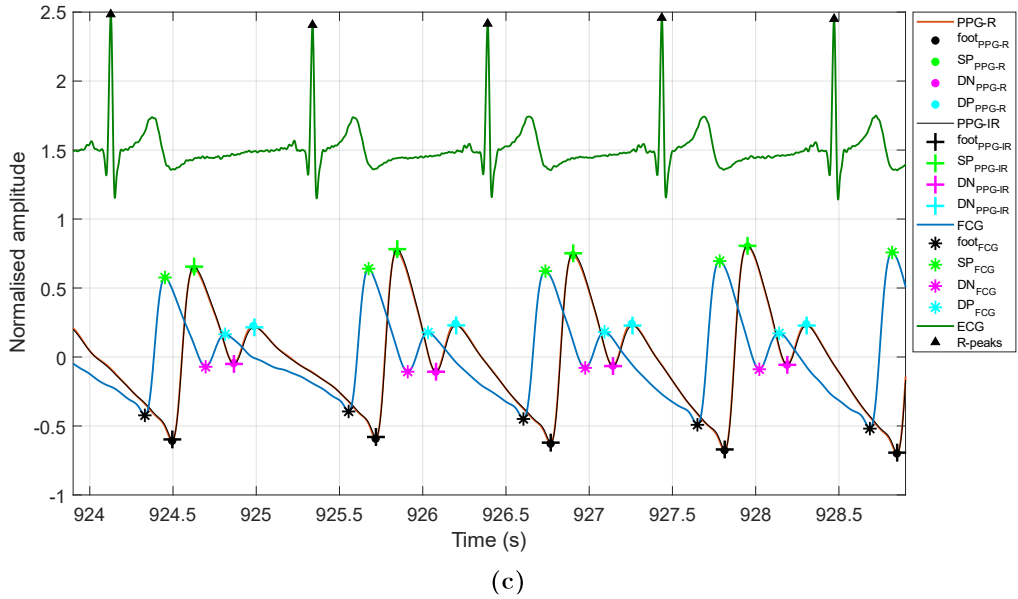
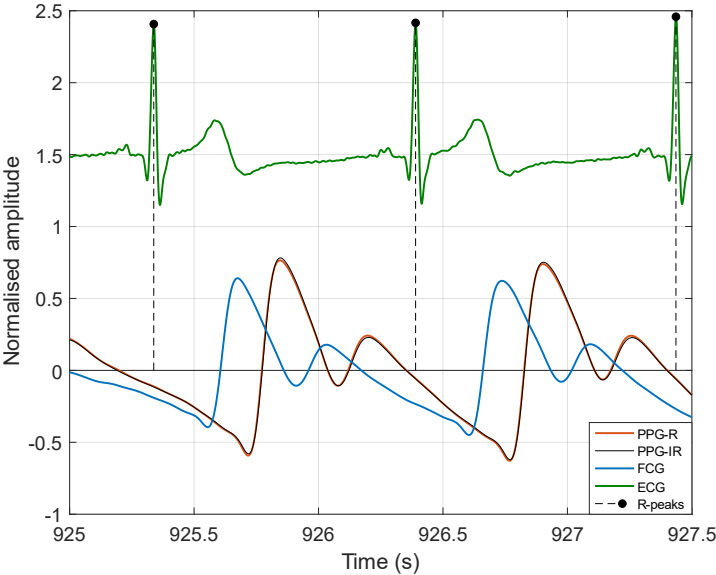
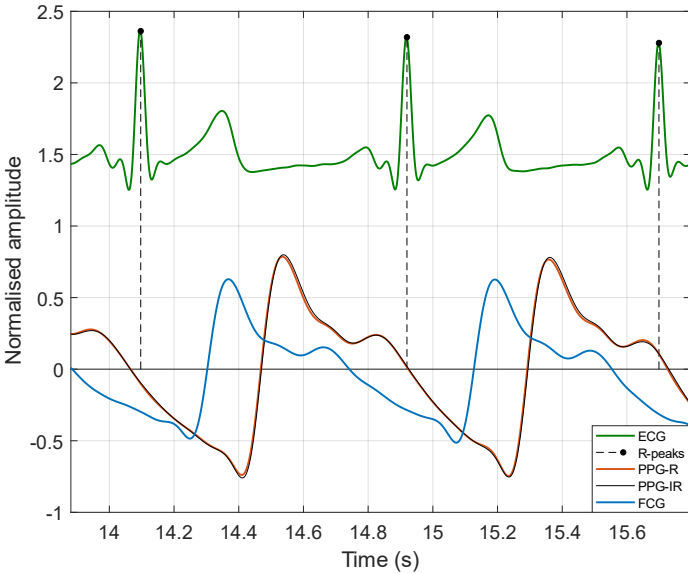


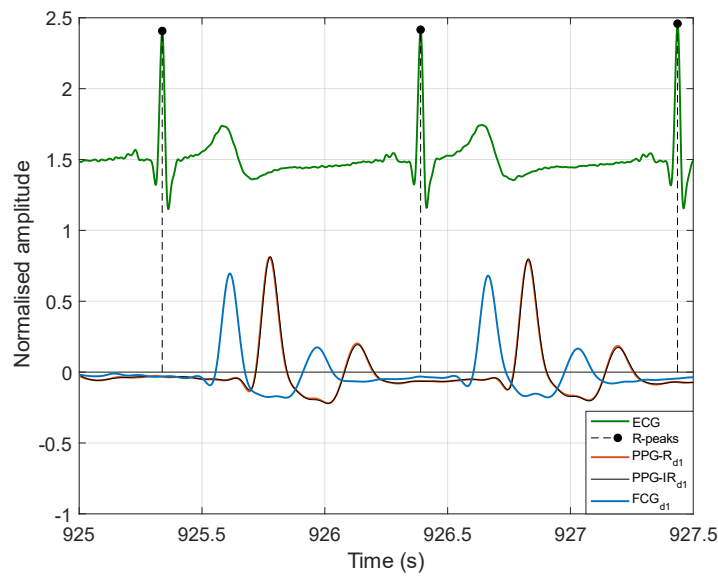
Figure 89. Example of PW signals acquired by the PPG sensor (red and infrared) and the piezoelectric FCG sensor, along with the concurrently acquired ECG lead I. ECG R-peaks and the four fiducial markers located in PW signals are also depicted. A delay between the PPG and FCG sensor signals can be clearly observed. (a) Signals acquired in subject #1; (b) signals acquired in subject #3; (c) detail on four heartbeats from the signal shown in panel (a) with the localized fiducial markers; (d) detail on four heartbeats from the signal shown in panel (b) with the localized fiducial markers.



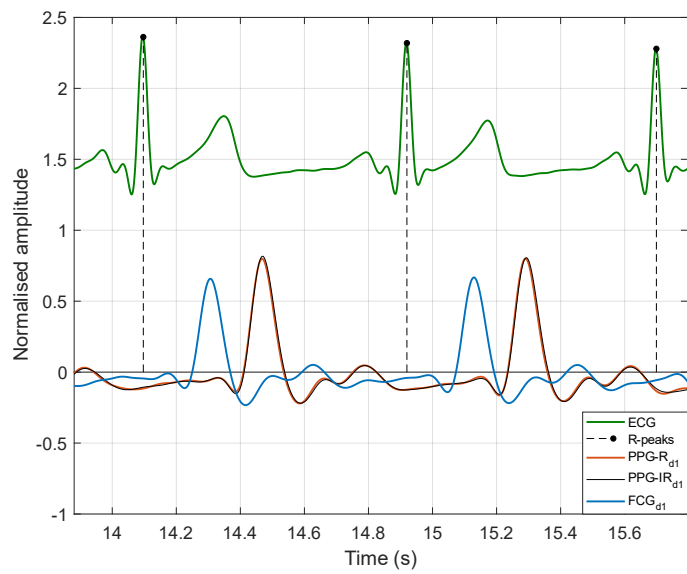
(a)



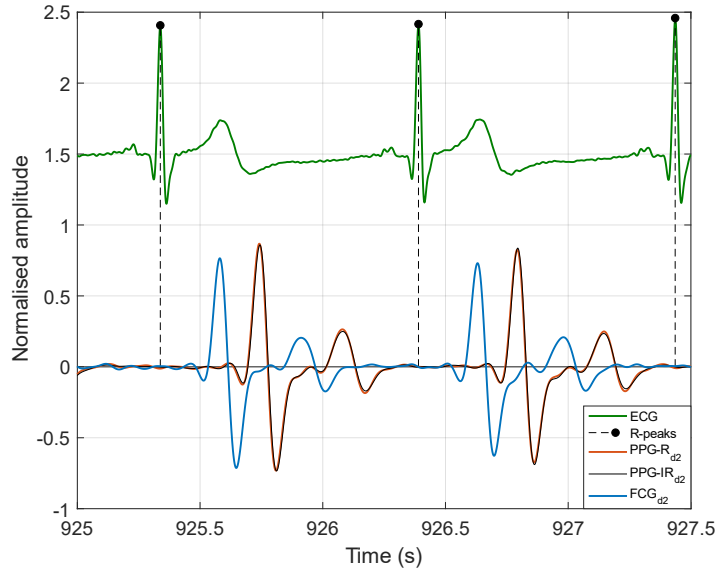
(b)



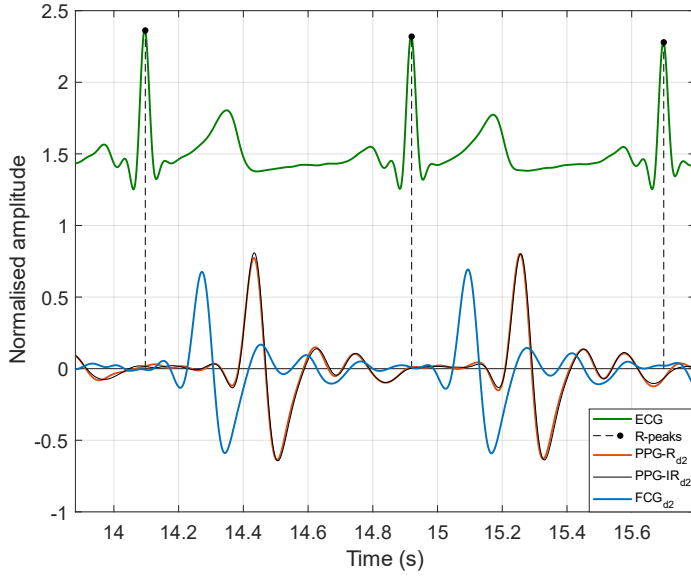
(c)



(d)



(e)



(f)

Figure 90. Comparison of PW signals and related first and second derivatives, acquired by the PPG sensor (red and infrared photodetectors) and the piezoelectric FCG sensor, along with the concurrently acquired ECG lead I. Signals acquired in subjects #1 and #3 are depicted in the first and second columns, respectively. The original PW signal, first derivative, and second derivative of both subjects are depicted in the first (a),(b), second (c),(d), and third (e),(f) rows, respectively.

8.4.4 Normalized cross-correlation

The morphological similarity between the PW signals provided by the PPG and FCG sensors was quantitatively assessed by evaluating their NCC. In particular, NCC was computed both between single corresponding heartbeats and between whole signal segments. While the former gives information about beat-by-beat morphological variations in PW signal similarity regardless of amplitude variations, the latter also takes into account the amplitude modulations that are usually observed over time in PW signals [175]-[177].

Single heartbeats were segmented in each PW signal by considering the time intervals between two consecutive feet. Then, the NCC function (NCCF) of PW signals provided by FCG and PPG sensors was computed between segments corresponding to the same heart beats. Afterwards, the NCC was obtained as the maximum of the NCC function. For whole signal segments, the NCCF was first computed; then, the maximum of the NCCF was located. Its value corresponded to the NCC, while its position gave information on the average time lag between the analysed signals.

The NCC between piezoelectric PW signals and optical PW signals was first computed for each single heartbeat. The means and SDs of the computed beat-by-beat NCC are reported in **Table 22**. **Table 23** instead reports the NCC computed between the whole piezoelectric and optical PW signals, along with the related time lags. As expected, the NCC time lags were in very good agreement with those computed between corresponding PW fiducial markers (see **Table 21**).

8.4.5 Statistical analyses on morphological parameters

Regression, correlation and Bland–Altman [150]-[151] analyses were carried out via the MATLAB® function “bland-altman-and-correlation-plot” [152] to compare the morphological parameters extracted from PW signals acquired by the FCG sensor and the PPG sensor. These statistical analyses were performed either on the dataset of parameters acquired from each single subject or on a combined dataset obtained by joining the parameters of all subjects.

The means and SDs of the morphological parameters extracted from the optical and piezoelectric PW signals are reported, for each subject, in **Table 24**. **Table 25** and **Table 26** outline, for each subject, the results of the regression, correlation, and Bland–Altman analyses. **Table 27** and **Table 28** show the results achieved by performing the same statistical analyses on the combined-parameters dataset.

Table 22. Mean and SD of beat-by-beat NCCs between PW signals acquired by FCG and PPG-R sensors.

Subject #	Original PW	First Derivative of PW	Second Derivative of PW
1	0.991 ± 0.004	0.995 ± 0.003	0.995 ± 0.005
2	0.996 ± 0.005	0.994 ± 0.004	0.990 ± 0.007
3	0.983 ± 0.009	0.987 ± 0.007	0.991 ± 0.004
4	0.991 ± 0.007	0.988 ± 0.009	0.981 ± 0.012
5	0.989 ± 0.008	0.990 ± 0.007	0.984 ± 0.011

Table 23. NCCs and time lags between whole PW signals acquired by FCG and PPG-R sensors.

Subject #	Original PW		First Derivative of PW		Second Derivative of PW	
	NCC	Lag (ms)	NCC	Lag (ms)	NCC	Lag (ms)
1	0.991	167	0.991	163	0.991	161
2	0.990	163	0.990	161	0.986	161
3	0.981	168	0.981	162	0.984	160
4	0.975	165	0.974	165	0.970	166
5	0.981	165	0.980	161	0.975	160

Table 24. Morphological parameters extracted from PW signals acquired by FCG and PPG sensors.

Subject #		t_{up} (ms)	t_i (ms)	T (ms)	t_{up}/T	h_2/h_1	h_3/h_1
1	PPG-	136 \pm	366 \pm	965 \pm	0.143 \pm	0.393 \pm	0.600 \pm
	R	4.88	7.47	106	0.0167	0.0594	0.0482
	PPG-	137 \pm	367 \pm	965 \pm	0.143 \pm	0.390 \pm	0.589 \pm
	IR	5.11	7.46	106	0.0168	0.0577	0.0447
	PIEZO	131 \pm	363 \pm	965 \pm	0.138 \pm	0.302 \pm	0.525 \pm
		6.18	7.48	106	0.0172	0.0545	0.0461
2	PPG-	122 \pm	374 \pm	995 \pm	0.125 \pm	0.631 \pm	0.739 \pm
	R	6.66	7.35	121	0.0165	0.0583	0.0733
	PPG-	125 \pm	376 \pm	995 \pm	0.128 \pm	0.650 \pm	0.751 \pm
	IR	9.05	7.59	122	0.0175	0.0592	0.0743
	PIEZO	123 \pm	373 \pm	995 \pm	0.126 \pm	0.593 \pm	0.694 \pm
		8.30	9.09	121	0.0175	0.0684	0.0787
3	PPG-	127 \pm	359 \pm	894 \pm	0.143 \pm	0.671 \pm	0.699 \pm
	R	3.34	8.45	70.8	0.0099	0.0515	0.0545
	PPG-	129 \pm	362 \pm	894 \pm	0.145 \pm	0.666 \pm	0.688 \pm
	IR	3.26	8.17	70.8	0.0100	0.0486	0.0509
	PIEZO	119 \pm	353 \pm	894 \pm	0.134 \pm	0.546 \pm	0.589 \pm
		3.79	9.17	71.0	0.0109	0.0412	0.0426
4	PPG-	121 \pm	339 \pm	863 \pm	0.142 \pm	0.190 \pm	0.490 \pm
	R	8.54	11.4	81.3	0.0159	0.0787	0.110
	PPG-	121 \pm	340 \pm	863 \pm	0.142 \pm	0.185 \pm	0.488 \pm
	IR	7.96	11.1	81.2	0.0158	0.0754	0.104
	PIEZO	125 \pm	335 \pm	863 \pm	0.146 \pm	0.137 \pm	0.505 \pm
		10.9	12.5	80.7	0.0198	0.0809	0.0549
5	PPG-	131 \pm	334 \pm	903 \pm	0.147 \pm	0.531 \pm	0.685 \pm
	R	6.60	8.09	92.9	0.0165	0.0842	0.0530
	PPG-	130 \pm	335 \pm	903 \pm	0.145 \pm	0.510 \pm	0.659 \pm
	IR	5.28	7.94	93.0	0.0156	0.0762	0.0502
	PIEZO	130 \pm	334 \pm	903 \pm	0.145 \pm	0.434 \pm	0.583 \pm
		4.39	8.35	92.8	0.0153	0.0659	0.0472

Table 25. Results of the regression, correlation, and Bland–Altman analyses that were carried out to compare the morphological parameters of PW signals provided by FCG and PPG sensors for each subject. Intercept, bias, and LoA for t_{up} , t_i , and T are expressed in milliseconds. Non-significant bias is indicated as “NS”.

Subject #	Parameter	tup		ti		T	
		R	IR	R	IR	R	IR
1	Slope	0.910	0.820	0.975	0.980	1.000	1.000
	Intercept	7.13	19.2	6.21	3.7	−0.377	−0.632
	R2	0.516	0.46	0.949	0.955	1.000	1.000
	Bias	−5.18	−5.39	−2.90	−3.63	NS	NS
	p-value	c***	c***	c***	c***	0.885	0.890
	LoA	±8.47	±9.08	±3.34	±3.13	±2.92	±3.05
2	Slope	0.260	0.0765	1.01	0.966	0.993	0.995
	Intercept	91.3	113	−4.78	10.4	6.80	4.90
	R2	0.044	0.007	0.671	0.651	1.000	1.000
	Bias	0.774	−2.24	−0.415	−2.45	NS	NS
	p-value	a*	c***	a*	c***	0.955	0.964
	LoA	18.6	23.1	10.2	10.5	4.44	4.19
3	Slope	0.632	0.501	0.956	0.982	1.00	1.00
	Intercept	38.6	54.2	9.88	−2.67	−2.3	−2.51
	R2	0.31	0.186	0.778	0.767	1.000	1.000
	Bias	−8.25	−10.1	−5.86	−9.15	NS	NS
	p-value	c***	c***	c***	c***	0.957	0.953
	LoA	6.62	7.42	8.5	8.68	2.62	2.44
4	Slope	0.98	1.1	1.02	1.07	0.993	0.993
	Intercept	5.9	−7.94	−12.6	−27.2	6.25	5.89
	R2	0.589	0.639	0.873	0.896	0.999	0.999
	Bias	3.48	3.61	−4.38	−4.95	0.0523	0.0392
	p-value	c***	c***	c***	c***	0.808	0.860
	LoA	13.7	12.9	8.75	8.05	5.22	5.38
5	Slope	0.248	0.302	0.835	0.845	0.998	0.997
	Intercept	97.3	90.7	55.5	51.3	1.93	2.53
	R2	0.14	0.132	0.655	0.646	0.999	0.999
	Bias	−1.28	NS	NS	−0.768	NS	NS
	p-value	a*	0.247	0.190	a*	0.940	0.956
	LoA	12.6	10.8	9.96	10	6.26	6.45

^a $p < 0.05$; ^b $p < 0.001$; ^c $p < 0.00011$.

Table 26. Results of the regression, correlation, and Bland–Altman analyses that were carried out to compare the morphological parameters of PW signals provided by FCG and PPG sensors for each subject.

Subject #	Parameter	t_{up}/T		h_2/h_1		h_3/h_1	
		R	IR	R	IR	R	IR
1	Slope	0.996	0.980	0.868	0.879	0.905	0.945
	Intercept	−0.005	−0.003	−0.039	−0.041	−0.018	−0.031
	R ²	0.928	0.916	0.893	0.866	0.894	0.839
	Bias	−0.005	−0.006	−0.091	−0.088	−0.075	−0.064
	p-value	c***	c***	c***	c***	c***	c***
	LoA	±0.009	±0.01	±0.04	±0.04	±0.03	±0.04
2	Slope	0.886	0.769	0.913	0.869	0.751	0.739
	Intercept	0.015	0.027	0.017	0.029	0.139	0.139
	R ²	0.695	0.590	0.606	0.564	0.489	0.487
	Bias	0.001	−0.002	−0.037	−0.056	−0.045	−0.057
	p-value	a*	c***	c***	c***	c***	c***
	LoA	0.019	0.023	0.085	0.090	0.116	0.117
3	Slope	1.04	1.01	0.644	0.689	0.689	0.738
	Intercept	−0.015	−0.013	0.114	0.088	0.108	0.082
	R ²	0.897	0.867	0.65	0.661	0.78	0.779
	Bias	−0.009	−0.011	−0.125	−0.12	−0.109	−0.099
	p-value	c***	c***	c***	c***	c***	c***
	LoA	0.007	0.008	0.060	0.056	0.051	0.047
4	Slope	1.15	1.17	0.949	1	0.465	0.493
	Intercept	−0.017	−0.020	−0.043	−0.048	0.277	0.264
	R ²	0.852	0.877	0.852	0.872	0.877	0.877
	Bias	0.004	0.005	−0.053	−0.048	0.014	0.016
	p-value	c***	c***	c***	c***	c***	c***
	LoA	0.016	0.015	0.062	0.057	0.122	0.110
5	Slope	0.836	0.905	0.74	0.815	0.794	0.822
	Intercept	0.0225	0.0142	0.0411	0.0186	0.0387	0.041
	R ²	0.812	0.847	0.893	0.887	0.794	0.766
	Bias	−0.001	0.0004	−0.097	−0.076	−0.103	−0.076
	p-value	b**	0.278	c***	c***	c***	c***
	LoA	0.014	0.012	0.060	0.051	0.047	0.048

^a $p < 0.05$; ^b $p < 0.001$; ^c $p < 0.00011$.

Table 27. Results of the regression, correlation, and Bland–Altman analyses that were carried out to compare the morphological parameters of PW signals provided by FCG and PPG sensors for all subjects. Intercept, bias, and LoA for t_{up} , t_i , and T are expressed in milliseconds. Non-significant bias is indicated as “NS”.

Parameter	t_{up}		t_i		T	
	R	IR	R	IR	R	IR
Slope	0.472	0.304	1.010	0.989	0.996	0.997
Intercept	65.5	86.1	−5.78	0.762	4.10	3.06
R^2	0.210	0.098	0.921	0.915	1.000	1.000
Bias	−0.915	−2.52	−1.48	−3.24	NS	NS
p-value	c***	c***	c***	c***	0.919	0.934
LoA	±16.8	±19.5	±10.2	±10.5	±4.55	±4.48

^a $p < 0.05$; ^b $p < 0.001$; ^c $p < 0.00011$.

Table 28. Results of the regression, correlation, and Bland–Altman analyses that were carried out to compare the morphological parameters of PW signals provided by FCG and PPG sensors for all subjects.

Parameter	t_{up}/T		h_2/h_1		h_3/h_1	
	R	IR	R	IR	R	IR
Slope	0.887	0.868	0.999	0.969	0.788	0.784
Intercept	0.014	0.015	−0.062	−0.051	0.087	0.090
R^2	0.775	0.711	0.905	0.927	0.680	0.736
Bias	−0.001	−0.003	−0.063	−0.069	−0.059	−0.059
p-value	c***	c***	c***	c***	c***	c***
LoA	±0.018	±0.020	±0.096	±0.085	±0.117	±0.109

^a $p < 0.05$; ^b $p < 0.001$; ^c $p < 0.00011$.

8.5 Discussion

This study addressed, for the first time in the literature, the simultaneous measurement of finger-pulse waveforms via a true multimodal sensor, realized by integrating a reflectance-mode PPG and a piezoelectric FCG sensor, which acquire PW signals from the same site. The preliminary results of this study unveiled the existence of a time delay between the PW signals recorded by a reflectance-mode

optical sensor and a piezoelectric sensor, which has also not been previously described in the literature. Therefore, these preliminary results suggest that the changes in blood vessels' lumens and in the optical reflectance of tissues, due to local changes in blood pressure in the finger, have different time dynamics. However, the actual mechanisms behind this phenomenon are still unclear, and undoubtedly deserve deeper investigation, which was outside of the scope of this study.

The results also showed, for the first time, that PW signals acquired by a PPG sensor and a piezoelectric FCG sensor from the same site share very similar morphology, as they had very high NCC scores. Indeed, the beat-by-beat NCCs turned out to be 0.990 ± 0.005 , and always in excess of 0.98 for all subjects, thus indicating very high and stable morphological similarity between PWs provided by FCG and PPG sensors. The NCCs computed between whole signals turned out to be 0.984 ± 0.007 , and always in excess of 0.98, except for subject #4 ($\text{NCC} > 0.97$), thus showing that the amplitude modulations exhibited by PW signals acquired via different sensors were also very similar.

Reasonable agreement was generally found between the PW parameters extracted from FCG and PPG sensors signals, apart from the time interval between the feet and the systolic peaks (t_{up} parameter), for which the greatest disagreement was observed. In particular, a statistically significant bias ($p < 0.0001$) was found for the diastolic-to-systolic peak ratio (h_3/h_1) and the dicrotic notch-to-systolic peak ratio (h_2/h_1), which turned out to be consistently lower in PW signals acquired by the piezoelectric FCG sensor with respect to signals acquired by the PPG sensor. This suggests that the relative height of the systolic peak was higher in piezoelectric PW signals, which could also be qualitatively assessed via visual inspection of the signals in **Figure 89**.

As a preliminary investigation, this study has some limitations, which will be the subject of future studies. Only a small cohort of healthy volunteers was considered for this study, and its preliminary results need to be confirmed on a larger cohort, also including actual patients; this would enable to verify if hemodynamic changes, both physiological and pathological, produce the same effects on the morphology of PW signals acquired by PPG and piezoelectric FCG sensors. In addition, only PW acquired from the finger were analysed. The performance assessment of the proposed

multimodal PW sensor could also be extended to PWs acquired from radial, brachial, carotid, iliac, and femoral arteries. The unexpected delay observed between the PW signals acquired by PPG and FCG sensors must be further investigated by using different PPG sensors (reflective and transmissive types) and identifying potential physical mechanisms that can explain the experimental data. The acquisition of PW signals was limited to subjects at rest, so as to analyse the multimodal PW sensor performances in the best experimental conditions. Sensor performances should also be assessed in subjects undergoing stress testing, such as the cold pressor test [248], mental arithmetic test [249], Valsalva maneuver [250], and various physical exercises, which are commonly adopted to elicit various hemodynamic changes. Finally, extending the analysis to subjects performing various physical exercises is also important to assess the robustness to motion artifacts of PPG and piezoelectric FCG sensors integrated in the proposed multimodal PW sensor. All these analyses could also lead to deeper comprehension of the strengths and weaknesses of these sensors and highlight opportunities for the development of sensor fusion strategies; these would be aimed at exploiting the multimodal nature of the proposed sensor to overcome the current limitations of existing PW sensing technologies and achieve superior accuracy, reliability, and reproducibility.

Conclusions

The results of this thesis demonstrated that FCG allows to acquire signals with much richer information content as compared to the well-established SCG. Indeed, the raw signal provided by the FCG sensor consists of a very low-frequency component, like a large baseline oscillation, closely related to the respiratory activity, i.e., the FRG, and a superimposed, much smaller component related to the cardiac activity, i.e., the actual Forcecardiogram. The FRG provides accurate measurement of inter-breath intervals, by clearly capturing the chest expansion and release forces during breathing. On the other hand, the Forcecardiogram appears roughly as a repetition of short, oscillatory patterns corresponding to heartbeats.

As already described in [21], the Forcecardiogram can be further divided into three frequency components, i.e., the LF-FCG, HF-FCG and HS-FCG, which carry information about multiple aspects of cardiac mechanics. The HF-FCG has been found to share a very high similarity with the SCG signal, to precisely identify the timings of important cardiac cycle events (i.e., AO and AC) and to provide accurate estimates of related CTIs (i.e., inter-beat interval, PEP and LVET). CTIs are clinically relevant parameters since they support the diagnosis of various CVDs. Several studies reported that changes in CTIs may be associated with pathological conditions [30]-[32],[75]-[79]. To date, ECHO is regarded as the gold-standard for CTIs evaluation. By this approach, CTIs measurements are limited to sporadic clinical examinations, which must be performed by trained personnel. FCG could offer an easy, low-cost, and comfortable alternative to continuously monitor patients

during daily life or in hospital. For this reason, a comparison with ECHO must be carried out soon to straight validate the localization of meaningful signal characteristics (e.g., FCG signal peaks and valleys) and the estimation of CTIs against gold-standards. Moreover, a larger cohort of subjects, including patients, must be enrolled to investigate the ability of FCG to discriminate some CVDs.

The HF-FCG has been shown to provide very accurate measurements of inter-beat intervals without the need of the ECG. Therefore, FCG could be used as an accurate HR monitor for continuous, long-term applications. Potentially, all the indices of the HRV analyses can be obtained without using an ECG lead. The LF-FCG, instead, reflects the forces impressed onto the chest wall due to the emptying and filling of the heart chambers, thus potentially carrying information on heart muscle contractility, synchronicity, SV variations, etc. This low-frequency component recovers the information captured by the ACG and could support a comprehensive evaluation of the heart mechanical function, both under physiological and pathological conditions. However, the relationship between LF-FCG and heart walls motion must be confirmed via the comparison with ECHO. If confirmed, this component could allow the evaluation of SV, CO, LVEF and therefore the diagnosis of CVDs, such as heart failure, also by distinguishing between diastolic heart failure (i.e., with preserved ejection fraction) or systolic heart failure (i.e., with reduced ejection fraction).

The HS-FCG, i.e., the heart sounds, can provide the well-known diagnostic information related to auscultation, with the advantage of being able to obtain long recordings during all daily actions [22]-[23],[63].

Respiration has been found to affect the cardiac components of FCG signals. Particularly, it causes amplitude modulation of both LF-FCG and HF-FCG, as well as changes in two parameters of heartbeat morphology, i.e., the LVET and MSi. This is in line with the well-known phenomena of changes in heart sounds with respiration, such as at the S₂ split. At present, however, no studies have been undertaken on HS-FCG and it is hoped that they will be carried out in the future. Nonetheless, FCG could be employed in the study of cardio-respiratory interactions. In conclusion, FCG sensors are able to capture respiration, infrasonic cardiac vibrations and heart sounds, all simultaneously from a single contact point on the chest. For this reason, the FCG stands as a valuable tool for non-invasive cardio-

respiratory monitoring. This suggests the use of FCG sensors as effective, cheap, lightweight, and unobtrusive devices for continuous, long-term monitoring of cardio-respiratory function of patients and paves the way for a wide range of potential applications. FCG sensors, for example, could be employed in elderly long-term monitoring, the search for arrhythmias, the study of cardio-respiratory response to physical activity, heart failure monitoring, athlete monitoring, sleep analysis, accident and emergency healthcare delivery, etc. Moreover, the small, non-invasive, passive FCG sensors are particularly suitable for the remote and continuous management of cardio-pulmonary diseases via pervasive wearable monitoring and telemedicine. FCG sensors could be used for continuous, managing elderly subjects or chronic patients at home, for the diagnosis and monitoring of sleep apnea and many other telemonitoring applications. Early detection of threatening conditions would result in timely intervention and reduced healthcare costs.

Future studies have been planned to analyse FCG recordings acquired in different experimental conditions, such as subjects in standing or supine positions, while performing voluntary tachypnea or bradypnea, engaging in physical activities (e.g., walking, running) or sport exercises, accomplishing heavy works, etc., by fostering the use of FCG sensors in other applications, such as sport and fitness, exercise testing, rehabilitation protocols. However, the robustness of FCG with respect to motion artifacts still need to be evaluated.

Moreover, multichannel measurements could be performed in the future by using FCG sensor matrices to provide a more detailed insight of heart activity. Finite element mechanical models of the human torso could also help in these kinds of studies and shed a light on cardio-mechanical waves generation and propagation across tissues.

As reported in the thesis, a preliminary investigation showed that FCG sensor can accurately monitor finger pulse waves. Indeed, the FCG sensor is capable of recording sphygmocardi waves over the almost entire body surface. This opens the way for the sensor to be used to study sphygmocardi wave propagation in blood vessels. One of the most interesting applications is the non-invasive, continuous monitoring of blood pressure by exploiting the calculation of PTT over the aorta artery. This measurement requires the use of two sensors placed at a certain distance along the aorta and recording the speed of propagation of the sphygmocardi wave: the higher the

blood pressure, the greater the stiffness of the aorta and the shorter the transit time will be.

In conclusion, the new FCG technique can potentially offer broad practical applications for widespread diseases, provide unprecedented, continuous and pervasive monitoring of cardio-respiratory function, and enable new paradigms for health care.



Bibliography

- [1] World Heart Federation. Trends in cardiovascular disease. <https://worldheartobservatory.org/trends/> (accessed on September 10, 2022)
- [2] World Heart Federation. World heart vision 2030: driving policies change <https://world-heart-federation.org/resource/world-heart-vision-2030-driving-policy-change/> (accessed on December 13, 2022)
- [3] Nazeran, H. "Electrocardiography, computers in," In Encyclopedia of Medical Devices and Instrumentation, 2nd ed.; Webster, J.G., Ed.; John Wiley & Sons, Inc.: Hoboken, NJ, USA, pp. 34-51, 2006.
- [4] Packer, M.; Abraham, W.T.; Mehra, M.R.; Yancy, C.W.; Lawless, C.E.; Mitchell, J.E.; Smart, F.W.; Bijou, R.; O'Connor, C.M.; Massie, B.M.; Pina, I.L.; Greenberg, B.H.; Young, J.B.; Fishbein, D.P.; Hauptman, P.J.; Bourge, R.C.; Strobeck, J.E.; Murali, S.; Schocken, D.; Teerlink, J.R.; Levy, W.C.; Trupp, R.J.; Silver, M.A. Utility of Impedance Cardiography for the Identification of Short-Term Risk of Clinical Decompensation in Stable Patients With Chronic Heart Failure. *Journal of the American College of Cardiology*, 2006, 47(11), pp. 2245-2252.
- [5] Olson, W.H. "Electrical safety," In Medical Instrumentation Application and Design, 4th ed.; Webster, J.G., Ed.; John Wiley & Sons, Inc.: Hoboken, NJ, USA, pp. 638-674, 2009.
- [6] Vermarien, H. "Phonocardiography," In Encyclopedia of Medical Devices and Instrumentation, 2nd ed.; Webster, J.G., Ed.; John Wiley & Sons: Hoboken, NJ, USA, pp. 278-289, 2006.
- [7] Dimond, E.G.; Benchimol, A. Phonocardiography. *Calif Med*, 1961, 94(3), pp. 139-146.
- [8] Tippit, H.; Benchimol, A. The Apex Cardiogram. *JAMA*, 1967, 201(7), 549.
- [9] Benchimol, A.; Dimond, E.G. The apex cardiogram in ischaemic heart disease. *Br Heart J*, 1962, 24(5), pp. 581-594.
- [10] Inan, O.T. Recent advances in cardiovascular monitoring using ballistocardiography. *Annu Int Conf IEEE Eng Med Biol Soc.* 2012, pp. 5038-5041.

- [11] Inan, O.T.; Migeotte, P.F.; Park, K.S.; Etemadi, M.; Tavakolian, K.; Casanella, R.; Zanetti, J.; Tank, J.; Funtova, I.; Prisk, G.K.; Di Rienzo, M. Ballistocardiography and seismocardiography: a review of recent advances. *IEEE J Biomed Health Inform*, 2015, 19(4), pp. 1414-1427.
- [12] Salerno, D.M.; Zanetti, J. Seismocardiography: a new technique for recording cardiac vibrations: concept, method and initial observations. *J Cardiovasc Technol*, 1990, 9, pp. 111-118.
- [13] Taebi, A.; Solar, B.E.; Bomar, A.J.; Sandler, R.H.; Mansy, H.A. Recent Advances in Seismocardiography. *Vibration*, 2019, 2(1), pp. 64-86.
- [14] Rahko, P.S. "Echocardiography and Doppler Echocardiography," In *Encyclopedia of Medical Devices and Instrumentation*, 2nd ed.; Webster, J.G., Ed.; John Wiley & Sons: Hoboken, NJ, USA, pp. 1-23, 2006.
- [15] Jafari Tadi, M.; Lehtonen, E.; Saraste, A.; Tuominen, J.; Koskinen, J.; Teräs, M.; Airaksinen, J.; Pänkäälä, M.; Koivisto, T. Gyrocardiography: A New Non-invasive Monitoring Method for the Assessment of Cardiac Mechanics and the Estimation of Hemodynamic Variables. *Sci Rep*, 2017, 7(1): 6823.
- [16] Sieciński, S.; Kostka, P.S.; Tkacz, E.J. Gyrocardiography: A Review of the Definition, History, Waveform Description, and Applications. *Sensors*, 2020, 20(22), 6675.
- [17] D'Mello, Y.; Skoric, J.; Xu, S.; Roche, P.J.R.; Lortie, M.; Gagnon, S.; Plant, D.V. Real-Time Cardiac Beat Detection and Heart Rate Monitoring from Combined Seismocardiography and Gyrocardiography. *Sensors*, 2019, 19, 3472.
- [18] Munck, K.; Sørensen, K.; Struijk, J.J.; Schmidt, S.E. Multichannel seismocardiography: an imaging modality for investigating heart vibrations. *Physiol Meas*, 2020, 41(11), 115001.
- [19] Hossein, A.; Rabineau, J.; Gorlier, D.; Del Rio, J.I.J.; van de Borne, P.; Migeotte, P.F.; Nonclercq, A. Kinocardiography Derived from Ballistocardiography and Seismocardiography Shows High Repeatability in Healthy Subjects. *Sensors*, 2021, 21, 815.
- [20] Andreozzi, E.; Fratini, A.; Esposito, D.; Naik, G.; Polley, C.; Gargiulo, G.D.; Bifulco, P. Forcecardiography: A Novel Technique to Measure Heart Mechanical Vibrations onto the Chest Wall. *Sensors*, 2020, 20, 3885.

- [21] Andreozzi, E.; Gargiulo, G.D.; Esposito, D.; Bifulco, P. A Novel Broadband Forcecardiography Sensor for Simultaneous Monitoring of Respiration, Infrasonic Cardiac Vibrations and Heart Sounds. *Front Physiol*, 2021, 12:725716.
- [22] Iaizzo, P.A. *Handbook of Cardiac Anatomy, Physiology, and Devices*, 1st edition. Humana Press, Totowa, NJ, 2005.
- [23] OpenStax College. *Anatomy & Physiology*. Chapters 19, 20. OpenStax, 2013. <http://cnx.org/content/col11496/latest/>
- [24] *Anatomy and Physiology of the Cardiovascular System*, Chapter 5. Jones & Bartlett Learning, LLC
- [25] “The Cardiac Position and Axis Orientation”, In: *Echocardiographic Anatomy in the Fetus*. Springer, Milano, 2008.
- [26] https://commons.wikimedia.org/wiki/File:Blausen_0451_Heart_Anterior.png
- [27] https://commons.wikimedia.org/wiki/File:Blausen_0456_Heart_Posterior.png
- [28] https://en.wikipedia.org/wiki/Wiggers_diagram#/media/File:Wiggers_Diagram_2.svg
- [29] Chambers, D.; Huang, C.; Matthews, G. “Arterial pressure waveforms”, In *Basic Physiology for Anaesthetists*, pp. 150-152. Cambridge: Cambridge University Press, 2005.
- [30] Weissler, A.M.; Harris, W.S.; Schoenfeld, C.D. Systolic Time Intervals in Heart Failure in Man. *Circulation*, 1968, 37, 149-159.
- [31] Cardus, D.; Vera, L. Systolic Time Intervals at Rest and during Exercise. *Cardiology*, 1974, 59, pp. 133-153.
- [32] D'Angelo, R.; Shah, N.; Rubler, S. Diastolic time intervals in ischemic and hypertensive heart disease: A comparison of isovolumic relaxation time and rapid filling time with systolic time intervals. *Chest*, 1975, 68(1), pp. 56-61.
- [33] Rai, D.; Thakkar, H.K.; Rajput, S.S.; Santamaria, J.; Bhatt, C.; Roca, F. A Comprehensive Review on Seismocardiogram: Current Advancements on Acquisition, Annotation, and Applications. *Mathematics*, 2021, 9, 2243.
- [34] Kolodziej, Andrew, Falls, Candice. “The Cardiovascular System. Chapter 2”, In. Editors Boling, Bryan, Hatton, Kevin, Hartjes, Tonja, 2020

- [35] Towe, B.C. "Bioelectricity and its measurement," In Biomedical Engineering and Design Handbook, 2nd ed; Kutz, M., Ed.; McGraw-Hill Education: New York, NY, USA, pp. 517-519, 2009.
- [36] Berbari, E.J. "Principles of Electrocardiography," In Biomedical Engineering Handbook; Bronzino, J.D., Ed.; CRC Press: Boca Raton, FL, USA, pp. 231-240, 1999.
- [37] https://www.pngkey.com/download/u2y3a9r5w7u2w7r5_einthovens-triangle/
- [38] Dehkordi, P.; Khosrow-Khavar, F.; Di Rienzo, M.; Inan, O.T.; Schmidt, S.E.; Blaber, A.P.; Sørensen, K.; Struijk, J.J.; Zakeri, V.; Lombardi, P.; Shandhi, M.M.H.; Borairi, M.; Zanetti, J.M.; Tavakolian, K. Comparison of Different Methods for Estimating Cardiac Timings: A Comprehensive Multimodal Echocardiography Investigation. *Front Physiol*, 2019, 10, 1057.
- [39] Kubicek, W.G.; Patterson, R.P.; Witsoe, D.A. Impedance cardiography as a noninvasive method of monitoring cardiac function and other parameters of the cardiovascular system. *Annals of the New York Academy of Sciences*, 1970, 170, 2, pp. 724-732.
- [40] Malmivuo, J.; Plonsey, R. "Impedance Plethysmography," In Bioelectromagnetism: Principles and Applications of Bioelectric and Biomagnetic Fields; Oxford University Press, UK, pp. 405-419, 1995.
- [41] Sherwood, A.; Allen, M.T.; Fahrenberg, J.; Kelsey, R.M.; Lavallo, W.R.; van Doornen, L.J. Methodological guidelines for impedance cardiography. *Psychophysiology*, 1990, 27(1), pp. 1-23
- [42] Tavakolian, K. Characterization and analysis of seismocardiogram for estimation of hemodynamic parameters, 2010.
- [43] Robinson, T.F.; Factor, S.M.; Sonnenblick, E.H. The Heart as a Suction Pump. *Sci Am*, 1986, 254, pp. 84-91.
- [44] Ranganathan, N.; Sivaciyan, V.; Saksena, F.B. "Precordial Pulsations," in The Art and Science of Cardiac Physical Examination. Contemporary Cardiology. Ranganathan, N., Sivaciyan, V., Saksena, F.B. (eds), Humana Press: Totowa, NJ, pp. 113-139, 2006.
- [45] Haycraft, J.B.; Paterson, D.R. The Changes in Shape and in Position of the Heart during the Cardiac Cycle. *J Physiol*, 1896, 19(5-6), pp. 496-506.

- [46] Hawthorne E.W. Dynamic geometry of the left ventricle. *Am J Cardiol*, 1966, 18(4), pp. 566-573.
- [47] Krasny, R.; Kammermeier, H.; Köhler, J. Biomechanics of valvular plane displacement of the heart. *Basic Res Cardiol*, 1991, 86, pp. 572-581.
- [48] Pinsky, M.R. Cardiopulmonary Interactions: Physiologic Basis and Clinical Applications. *Ann Am Thorac Soc*, 2018, 15(1), pp. S45-S48.
- [49] Mahmood, S.S.; Pinsky, M.R. Heart-lung interactions during mechanical ventilation: the basics. *Ann Transl Med*, 2018, 6(18), 349.
- [50] Williams, E.A.; Whitney, G.M. Cardiopulmonary interactions. *SAJCC* 2006, 22(1), pp. 28-35.
- [51] Cheyne, W.S.; Harper, M.I.; Gelinas, J.C.; Sasso, J.P.; Eves, N.D. Mechanical cardiopulmonary interactions during exercise in health and disease. *J Appl Physiol* (1985), 2020,128(5), pp. 1271-1279.
- [52] Van Leeuwen, P.; Kuemmel, H.C. Respiratory modulation of cardiac time intervals. *Br Heart J*, 1987, 58(2), pp. 129-135.
- [53] Caiani, E.G.; Turiel, M.; Muzzupappa, S.; Colombo, L.P.; Porta, A.; Baselli, G. Noninvasive quantification of respiratory modulation on left ventricular size and stroke volume. *Physiol Meas*, 2002, 23(3), pp. 567-580.
- [54] Bendjelid, K.; Suter, P.M.; Romand, J.A. The respiratory change in preejection period: a new method to predict fluid responsiveness. *J Appl Physiol* (1985), 2004, 96(1), pp. 337-342.
- [55] Magder, S. Heart-Lung interaction in spontaneous breathing subjects: the basics. *Ann Transl Med*, 2018, 6(18), 348.
- [56] Elstad, M.; O'Callaghan, E.L.; Smith, A.J.; Ben-Tal, A.; Ramchandra, R. Cardiorespiratory interactions in humans and animals: rhythms for life. *Am J Physiol Heart Circ Physiol*, 2018, 315(1), pp. H6-H17.
- [57] Rosenkranz, S.; Bauersachs, J. Cardiopulmonary interaction in heart or lung disease: physiology, disturbances, and their clinical implications. *Herz*, 2019, 44, pp. 475-476.
- [58] Huang, Y.C.; Lin, T.Y.; Wu, H.T. Chang, P.J.; Lo, C.Y.; Wang, T.Y.; Kuo, C.S.; Lin, S.M.; Chung, F.T.; Lin, H.C.; Hsieh, M.H.; Lo YL. Cardiorespiratory

- coupling is associated with exercise capacity in patients with chronic obstructive pulmonary disease. *BMC Pulm Med*, 2021, 21(1), 22.
- [59] Radovanović, N.N.; Pavlović, S.U.; Milašinović, G.; Kirćanski, B.; Platiša, M.M. Bidirectional Cardio-Respiratory Interactions in Heart Failure. *Front Physiol*, 2018, 9, 165.
 - [60] Iliopoulos, I.; Nelson, D.P. Cardiopulmonary interactions in adults and children with congenital heart disease. *Prog Pediatr Cardiol*, 2015, 39(2), pp. 151-156.
 - [61] Atkinson, D.; Burcher, M.; Declerck, J.; Noble, J.A. Respiratory motion compensation for 3-D freehand echocardiography. *Ultrasound Med Biol*, 2001, 27, pp. 1615-1620.
 - [62] Wang, Y.; Riederer, S.J.; Ehman, R.L. Respiratory motion of the heart: Kinematics and the implications for the spatial resolution in coronary imaging. *Magn Reson Med*, 1995, 33, pp. 713-719.
 - [63] Greenstein, J. Phonocardiography; its application to clinical medicine. *S Afr Med J*, 1955, 29(6), pp. 123-134.
 - [64] Boyer, N.H.; Eckstein, R.W.; Wiggers, C.J. The characteristics of normal heart sounds recorded by direct methods. *American Heart Journal*, 1940, 19, pp. 257-274.
 - [65] Giordano, N.; Knaflitz, M. A Novel Method for Measuring the Timing of Heart Sound Components through Digital Phonocardiography. *Sensors*, 2019, 19(8), 1868.
 - [66] Benchimol, A.; Dimond, E.G. The normal and abnormal apexcardiogram. Its physiologic variation and its relation to intracardiac events. *Am J Cardiol*, 1963, 12, pp. 368-381.
 - [67] <https://it.wikipedia.org/wiki/File:Apex-cardiogram.JPG>
 - [68] Coulshed, N.; Epstein, E.J. The apex cardiogram: its normal features explained by those found in heart disease. *Br Heart J*, 1963, 25(6), pp. 697-708. DOI: 10.1136/hrt.25.6.697.
 - [69] Benchimol, A.; Dimond, E.G.; Carson, J.C. The value of the apex cardiogram as a reference tracing in phonocardiography. *Am Heart J*, 1961, 61(4), pp. 485-493.

- [70] Dimond, E.G.; Duenas, A.; Benchimol, A. Apex Cardiography. *Am Heart J*, 1966, 72(1), pp. 124-130.
- [71] Benchimol, A.; Dimond, E.G. The apexcardiogram in normal older subjects and in patients with arteriosclerotic heart disease. Effect of exercise on the "a" wave. *Am Heart J*, 1963, 65, pp. 789-801.
- [72] Costeas, F.; Kardalinos, A. The Right Apex Cardiogram in Patients With Reactive Pulmonary Hypertension. *Angiology*, 1971, 22(10), pp. 561-567.
- [73] Rios, J.C.; Massumi, R.A. Correlation between the apex cardiogram and left ventricular pressure. *Am J Cardiol*, 1965, 15(5), pp. 647-655.
- [74] Jain, S.R.; Lindahl, J. Apex cardiogram and systolic time intervals in acute myocardial infarction. *Br Heart J*, 1971, 33(4), pp. 578-84.
- [75] Weissler, A.M.; Peeler, R.G.; Roehll, W.H. Jr. Relationships between left ventricular ejection time, stroke volume, and heart rate in normal individuals and patients with cardiovascular disease. *Am Heart J*, 1961, 62, pp. 367-378.
- [76] Harris, W.S.; Schoenfeld, C.D.; Weissler, A.M. Effects of adrenergic receptor activation and blockade on the systolic preejection period, heart rate, and arterial pressure in man. *J Clin Invest*, 1967, 46(11), pp. 1704-1714.
- [77] Cokkinos, D.V.; Heimonas, E.T.; Demopoulos, J.N.; Harralambakis, A.; Tsartsalis, G.; Gardikas, C.D. Influence of heart rate increase on uncorrected pre-ejection period/left ventricular ejection time (PEP/LVET) ratio in normal individuals. *Br Heart J*, 1976, 38(7), pp. 683-688.
- [78] Lewis, R.P.; Rittogers, S.E.; Froester, W.F.; Boudoulas, H. A critical review of the systolic time intervals. *Circulation*, 1977, 56(2), pp. 146-158.
- [79] Wikstrand, J.; Berglund, G.; Wilhelmsen, L.; Wallentin, I. Value of systolic and diastolic time intervals. Studies in normotensive and hypertensive 50-year-old men and in patients after myocardial infarction. *Br Heart J*, 1978, 40(3), pp. 256-267.
- [80] Ferro, G.; Ricciardelli, B.; Saccá, L.; Chiariello, M.; Volpe, M.; Tari, M.G.; Trimarco, B. Relationship between systolic time intervals and heart rate during atrial or ventricular pacing in normal subjects. *Jpn Heart J*, 1980, 21(6), pp. 765-771.

- [81] Mertens, H.M.; Mannebach, H.; Trieb, G.; Gleichmann, U. Influence of heart rate on systolic time intervals: effects of atrial pacing versus dynamic exercise. *Clin Cardiol*, 1981, 4(1), pp. 22-27.
- [82] Mäntysaari, M.; Antila, K.; Peltonen, T. Relationship between systolic time intervals and heart rate during four circulatory stress tests. *Eur J Appl Physiol Occup Physiol*, 1984, 52(3), pp. 282-286.
- [83] Van Leeuwen, P.; Kümmell, H.C. Effects of Posture on Cardiac Time Intervals. *Am J Noninvas Cardiol*, 1991, 5, pp. 125-128.
- [84] Henderson, Y. The mass-movements of the circulation as shown by a recoil curve. *Am J Physiol*, 1905, 14(3), pp. 287-298.
- [85] Gordon, JW. On Certain Molar Movements of the Human Body produced by the Circulation of the Blood. *J Anat Physiol*, 1877; 11(3), pp. 533-536.
- [86] Starr, I.; Rawson, A.J.; Schroeder, H.A.; Joseph, N.R. Studies on the estimation of cardiac output in man, and of abnormalities in cardiac function, from the heart's recoil and the blood's impacts; the Ballistocardiogram. *Am J Physiol*, 1939, 127(1), pp. 1-28.
- [87] Knoop, A.A. Experimental Investigations on Ultra-Low Frequency Displacement Ballistocardiography. NASA TT F-269. NASA Contract Rep. NASA CR. National Aeronautics and Space Administration: Washington, DC, USA, 1965; pp. 1-107.
- [88] Pollock P. Ballistocardiography: a clinical review. *Can Med Assoc J*, 1957, 76(9), pp. 778-783.
- [89] Nickerson, J.L.; Warren, J.V.; Brannon, E.S. The cardiac output in man: studies with the low frequency, critically-damped ballistocardiograph, and the method of right atrial catheterization. *J Clin Invest* 1947, 26(1), pp. 1-10.
- [90] Dock, W.; Taubman, F. Some technics for recording the ballistocardiogram directly from the body. *Am J Med*, 1949, 7(6), pp. 751-755.
- [91] Starr, I. The relation of the ballistocardiogram to cardiac function. *Am J Cardiol*, 1958, 2(6), pp. 737-747.
- [92] Starr I. Progress towards a physiological cardiology: a second essay on the ballistocardiogram. *Ann Intern Med*, 1965, 63(6), pp.1079-1105.

- [93] Noordergraaf, A.; Horeman, H.W. The prediction of the Ballistocardiogram from physiological and anatomical data. *Cardiologia*, 1957, 31(5), pp. 416-420.
- [94] Noordergraaf, A.; Heynekamp, C.E. Genesis of displacement of the human longitudinal ballistocardiogram from the changing blood distribution. *Am J Cardiol*, 1958, 2(6), pp. 748-756.
- [95] Noordergraaf, A. Further Studies on a Theory of the Ballistocardiogram. *Circulation*, 1961, 23(3), pp. 413-425.
- [96] Scarborough, W.R.; Talbot, S.A. Proposals for ballistocardiographic nomenclature and conventions: revised and extended report of Committee on Ballistocardiographic Terminology. *Circulation*, 1956, 14(3), pp. 435-450.
- [97] Sadek, I.; Biswas, J.; Abdulrazak, B. Ballistocardiogram signal processing: a review. *Health Inf Sci Syst*, 2019, 7(1), 10.
- [98] Santucci, F.; Lo Presti, D.; Massaroni, C.; Schena, E.; Setola, R. Precordial Vibrations: A Review of Wearable Systems, Signal Processing Techniques, and Main Applications. *Sensors* 2022, 22, 5805.
- [99] Mounsey, P. Praecordial ballistocardiography. *Br Heart J*, 1957, 19(2), pp. 259-271.
- [100] Zanetti, J.M.; Salerno, D.M. Seismocardiography: a technique for recording precordial acceleration. In *Proceed of 1991 Computer-Based Medical Systems@m_Proceedings of the Fourth Annual IEEE Symposium*, 1991, pp. 4-9.
- [101] Salerno, D.M.; Zanetti, J. Seismocardiography for monitoring changes in left ventricular function during ischemia. *Chest*, 1991, 100(4), pp. 991-993.
- [102] Wilson, R.A.; Bamrah, V.S.; Lindsay, J.; Schwaiger, M.; Morganroth, J. Diagnostic accuracy of seismocardiography compared with electrocardiography for the anatomic and physiologic diagnosis of coronary artery disease during exercise testing. *Am J Cardiol*, 1993, 71(7), pp. 536-545.
- [103] Crow, R.S.; Hannan, P.; Jacobs, D.; Hedquist, L.; Salerno, D.M. Relationship between Seismocardiogram and Echocardiogram for Events in the Cardiac Cycle. *Am J Noninvas Cardiol*, 1994, 8, pp. 39-46.
- [104] Lin, W.; Chou, W.; Chang, P.; Chou, C.; Wen, M.; Ho, M.; Lee, M. Identification of Location Specific Feature Points in a Cardiac Cycle Using a

- Novel Seismocardiogram Spectrum System. *IEEE J. Biomed Health Inform*, 2018, 22, pp. 442–449.
- [105] Korzeniowska-Kubacka, I.; Kuśmierczyk-Droszcz, B.; Bilińska, M.; Dobraszkiewicz-Wasilewska, B.; Mazurek, K.; Piotrowicz, R. Seismocardiography - a non-invasive method of assessing systolic and diastolic left ventricular function in ischaemic heart disease. *Folia Cardiol*, 2006, 13(4), pp. 319-325.
 - [106] Tavakolian, K.; Blaber, A.P.; Ngai, B.; Kaminska, B. Estimation of hemodynamic parameters from seismocardiogram. In *Proceed of 2010 Computing in Cardiology*, 2010, pp. 1055-1058.
 - [107] Tavakolian, K.; Portacio, G.; Tamddondoust, N.R.; Jahns, G.; Ngai, B.; Dumont, G.A.; Blaber, A.P. Myocardial contractility: a seismocardiography approach. In *Proceed of 2012 Annu Int Conf IEEE Eng Med Biol Soc*, 2012, pp. 3801-3804.
 - [108] İşilay Zeybek, Z.M.; Racca, V.; Pezzano, A.; Tavanelli, M.; Di Rienzo, M. Can Seismocardiogram Fiducial Points Be Used for the Routine Estimation of Cardiac Time Intervals in Cardiac Patients? *Front Physiol*, 2022, 13, 825918.
 - [109] Di Rienzo, M.; Vaini, E.; Castiglioni, P.; Merati, G.; Meriggi, P.; Parati, G.; Faini, A.; Rizzo, F. Wearable seismocardiography: towards a beat-by-beat assessment of cardiac mechanics in ambulant subjects. *Auton Neurosci*, 2013, 178(1-2), pp. 50-59.
 - [110] Inan, O.T.; Pandia, K.; Giovangrandi, L.; Zamanian, R.T.; Kovacs, G.T. A preliminary study investigating the quantification of beat-to-beat in seismocardiogram signals. In *Proceed of 2013 Annu Int Conf IEEE Eng Med Biol Soc*, 2013, pp. 7286-7289.
 - [111] Laurin, A.; Blaber, A.; Tavakolian, K. Seismocardiograms return valid heart rate variability indices. *Computing in Cardiology 2013*, 2013, pp. 413-416.
 - [112] Zanetti, J.M.; Tavakolian, K. Seismocardiography: past, present and future. In *Proceed of 2013 Annu Int Conf IEEE Eng Med Biol Soc*, 2013, pp. 7004-7007.
 - [113] Tadi, M.J.; Lehtonen, E.; Koivisto, T.; Pänkäälä, M.; Paasio, A.; Teräs, M. Seismocardiography: Toward heart rate variability (HRV) estimation. In

Proceed of 2015 IEEE International Symposium on Medical Measurements and Applications (MeMeA), 2015, pp. 261-266.

- [114] Tadi, M.J.; Koivisto, T.; Pänkäälä, M.; Paasio, A.; Knuutila, T.; Teräs, M.; Hänninen, P. A new algorithm for segmentation of cardiac quiescent phases and cardiac time intervals using seismocardiography, In Proceed of SPIE 9443, Sixth International Conference on Graphic and Image Processing (ICGIP 2014), 94432K (4 March 2015).
- [115] Laurin, A.; Khosrow, F.; Blaber, A.; Tavakolian, K. Accurate and consistent automatic seismocardiogram annotation without concurrent ECG. In Proceed of 2015 Computing in Cardiology Conference (CinC), 2015, pp. 25-28.
- [116] Lin, W.Y.; Chou, W.C.; Chang, P.C.; Chou, C.C.; Wen, M.S.; Ho, M.Y.; Lee, W.C.; Hsieh, M.J.; Lin, C.C.; Tsai, T.H.; Lee, M.Y. Identification of Location Specific Feature Points in a Cardiac Cycle Using a Novel Seismocardiogram Spectrum System. IEEE J Biomed Health Inform, 2018, 22(2), pp. 442-449.
- [117] Khosrow-Khavar, F.; Tavakolian, K.; Blaber, A.; Menon, C. Automatic and Robust Delineation of the Fiducial Points of the Seismocardiogram Signal for Non-invasive Estimation of Cardiac Time Intervals. IEEE Trans Biomed Eng, 2017, 64(8), pp. 1701-1710.
- [118] Choudhary, T.; Sharma, L.N.; Bhuyan, M.K. Automatic Detection of Aortic Valve Opening Using Seismocardiography in Healthy Individuals. IEEE J Biomed Health Inform, 2019, 23(3), pp. 1032-1040.
- [119] Sørensen, K.; Schmidt, S.E.; Jensen, A.S.; Søggaard, P.; Struijk, J.J. Definition of Fiducial Points in the Normal Seismocardiogram. Sci Rep, 2018, 8, 15455.
- [120] Choudhary, T.; Bhuyan, M.K.; Sharma, L.N. A Novel Method for Aortic Valve Opening Phase Detection Using SCG Signal. IEEE Sensors Journal, 2020, 20(2), pp. 899-908.
- [121] Choudhary, T.; Bhuyan, M.K.; Sharma, L.N. Delineation and Analysis of Seismocardiographic Systole and Diastole Profiles. IEEE Trans Instrum Meas, 2021, 70, pp. 1-8.
- [122] Mora, N.; Cocconcelli, F.; Matrella, G.; Ciampolini, P. Fully Automated Annotation of Seismocardiogram for Noninvasive Vital Sign Measurements. IEEE Trans Instrum Meas, 2020, 69(4), pp. 1241-1250.

- [123] Ashouri, H.; Inan, O.T. Automatic detection of seismocardiogram sensor misplacement for robust pre-ejection period estimation in unsupervised settings. *IEEE Sens J*, 2017, 17, pp. 3805-3813.
- [124] Zia, J.; Kimball, J.; Hersek, S.; Shandhi, M.M.H.; Semiz, B.; Inan, O.T. Unified Framework for Quality Indexing and Classification of Seismocardiogram Signals. *IEEE J Biomed Health Inform*, 2020, 24(4), pp. 1080-1092.
- [125] Zia, J.S.; Kimball, J.; Hersek, S.; Inan, O.T. Modeling Consistent Dynamics of Cardiogenic Vibrations in Low-Dimensional Subspace. *IEEE J Biomed Health Inform*, 2020, 24, pp. 1887-1898.
- [126] Zia, J.S.; Kimball, J.; Rozell, C.J.; Inan, O.T. Harnessing the Manifold Structure of Cardiomechanical Signals for Physiological Monitoring during Hemorrhage. *IEEE Transac Biomed Eng*, 2020, 68, pp. 1759-1767.
- [127] Gurev, V.; Tavakolian, K.; Constantino, J.; Kaminska, B.; Blaber, A.P.; Trayanova, N.A. Mechanisms Underlying Isovolumic Contraction and Ejection Peaks in Seismocardiogram Morphology. *J Med Biol Eng*, 2012, 32(2), pp. 103-110.
- [128] Hassan, T.; Rahman, B.; Sandler, R.H.; Mansy, H.A. Effect of Normal Breathing and Breath Holding on Seismocardiographic Signals and Heart Rate. In *Proceed of 2021 IEEE Signal Processing in Medicine and Biology Symposium (SPMB)*, 2021, pp. 1-6.
- [129] Pandia, K.; Inan, O.T.; Kovacs, G.T. A frequency domain analysis of respiratory variations in the seismocardiogram signal. In *Proceeding of 2013 35th Annual International Conference of the IEEE Engineering in Medicine and Biology Society (EMBC)*, Osaka, Japan, 9-7 July 2013, pp. 6881-6884.
- [130] Pandia, K.; Inan, O.T.; Kovacs, G.T.; Giovangrandi, L. Extracting respiratory information from seismocardiogram signals acquired on the chest using a miniature accelerometer. *Physiol Meas*, 2012, 33(10), pp. 1643-1660.
- [131] Azad, K.; Gamage, P.T.; Sandler, R.H.; Mansy, H.A. Detection of respiratory phase and rate from chest surface measurements. *J. Appl. Biotechnol Bioeng*, 2018, 5(6), pp. 359-362.
- [132] Taebi, A.; Mansy, H.A. Grouping similar seismocardiographic signals using respiratory information. In *Proceeding of 2017 IEEE Signal Processing in*

Medicine and Biology Symposium (SPMB), Philadelphia, PA, USA, 2 December 2017, pp. 1-6.

- [133] Zakeri, V.; Akhbardeh, A.; Alamdari, N.; Fazel-Rezai, R.; Paukkunen, M.; Tavakolian, K. Analyzing Seismocardiogram Cycles to Identify the Respiratory Phases. *IEEE Trans Biomed Eng*, 2017, 64(8), pp. 1786-1792.
- [134] Berntson, G.G.; Cacioppo, J.T.; Quigley, K.S. Respiratory sinus arrhythmia: autonomic origins, physiological mechanisms, and psychophysiological implications. *Psychophysiology*, 1993, 30, pp. 183-196.
- [135] Leighton, R.F. Right and left ventricular systolic time intervals: effects of heart rate, respiration and atrial pacing. *Am J Cardiol*, 1971, 27(1), pp. 66-72.
- [136] Sakamoto, T. Hemodynamic determinants of the amplitude of the first heart sound. *Circ Res*, 1965, 16, pp. 45-67.
- [137] Kusakawa, R. Hemodynamic determinants of the amplitude of the second heart sound. *J Appl Physiol*, 1966, 21, pp. 938-946.
- [138] Tadi, M.J.; Lehtonen, E.; Pankaala, M.; Saraste, A.; Vasankari, T.; Teras, M.; Koivisto, T. Gyrocardiography: a new non-invasive approach in the study of mechanical motions of the heart. Concept, method and initial observations. In *Proceeding of Annu Int Conf IEEE Eng Med Biol Soc.* 2016, 2016, pp. 2034-2037.
- [139] Yang, C.; Tavassolian, N. Combined Seismo- and Gyro-Cardiography: A More Comprehensive Evaluation of Heart-Induced Chest Vibrations. *IEEE J Biomed Health Inform*, 2018, 22(5), pp. 1466-1475.
- [140] Hossein, A.; Mirica, D.C.; Rabineau, J.; Del Rio, J.I.J.; Morra, S.; Gorlier, D.; Nonclercq, A.; van de Borne, P.; Migeotte, P.F. Accurate Detection of Dobutamine-induced Haemodynamic Changes by Kino-Cardiography: A Randomised Double-Blind Placebo-Controlled Validation Study. *Sci Rep*, 2019, 9, 10479.
- [141] Paredes-Madrid, L.; Matute, A.; Bareño, J.O.; Parra Vargas, C.A.; Gutierrez Velásquez, E.I. Underlying Physics of Conductive Polymer Composites and Force Sensing Resistors (FSRs). A Study on Creep Response and Dynamic Loading. *Materials*, 2017, 10, 1334.

- [142] Paredes-Madrid, L.; Palacio, C.; Matute, A.; Parra Vargas, C. Underlying Physics of Conductive Polymer Composites and Force Sensing Resistors (FSRs) under Static Loading Conditions. *Sensors*, 2017, 17, 2108.
- [143] Esposito, D.; Andreozzi, E.; Fratini, A.; Gargiulo, G.D.; Savino, S.; Niola, V.; Bifulco, P. A Piezoresistive Sensor to Measure Muscle Contraction and Mechanomyography. *Sensors*, 2018, 18, 2553.
- [144] Esposito, D.; Andreozzi, E.; Gargiulo, G.D.; Fratini, A.; D'Addio, G.; Naik, G.R.; Bifulco, P. A Piezoresistive Array Armband With Reduced Number of Sensors for Hand Gesture Recognition. *Front. Neurobotics*, 2020, 13, 114.
- [145] Jayarathna, T.; Gargiulo, G.D.; Breen, P.P. Continuous Vital Monitoring During Sleep and Light Activity Using Carbon-Black Elastomer Sensor. *Sensors*, 2020, 20, 1583.
- [146] Schriger, L. Approach to the patient with abnormal vital signs. In *Goldman's Cecil Medicine*; Elsevier: Amsterdam, The Netherlands, pp. 27-30, 2012.
- [147] Bailòn, R.; Sörnmo, L.; Laguna, P. A robust method for ECG-based estimation of the respiratory frequency during stress testing. *IEEE Trans Biomed Eng*, 2006, 53, pp. 1273-1285.
- [148] Gao, Y.; Yan, H.; Xu, Z.; Xiao, M.; Song, J. A principal component analysis based data fusion method for ECG-derived respiration from single-lead ECG. *Australas Phys Eng Sci Med*, 2018, 41, pp. 59-67.
- [149] Sedghamiz, H. BioSigKit: A Matlab Toolbox and Interface for Analysis of BioSignals. *J. Open Source Softw.* 2018, 3, 671.
- [150] Altman, D.G.; Bland, J.M. Measurement in medicine: the analysis of method comparison studies. *The Statistician* 32, 1983, pp. 307-317.
- [151] Giavarina, D. Understanding Bland Altman analysis. *Biochemia medica*, 2015, 25(2), pp. 141-151.
- [152] Ran, K. Bland-Altman and Correlation Plot, MATLAB Central File Exchange. 2020. Available online: <https://www.mathworks.com/matlabcentral/fileexchange/45049-bland-altman-and-correlation-plot> (accessed on 28 May 2020).
- [153] Yu, S.; Liu, S. A Novel Adaptive Recursive Least Squares Filter to Remove the Motion Artifact in Seismocardiography. *Sensors*, 2020, 20, 1596.

- [154] Yang, C.; Tavassolian, N. An Independent Component Analysis Approach to Motion Noise Cancellation of Cardio-Mechanical Signals. *IEEE Trans Biomed Eng*, 2018, 66, 784-793.
- [155] Javaid, A.Q.; Ashouri, H.; Dorier, A.; Etemadi, M.; Heller, J.A.; Roy, S.; Inan, O.T. Quantifying and Reducing Motion Artifacts in Wearable Seismocardiogram Measurements During Walking to Assess Left Ventricular Health. *IEEE Trans Biomed Eng*, 2017, 64, 1277-1286.
- [156] Luu, L.; Dinh, A. Artifact Noise Removal Techniques on Seismocardiogram Using Two Tri-Axial Accelerometers. *Sensors*, 2018, 18, 1067.
- [157] Savitzky, A.; Golay, M.J.E. Smoothing and Differentiation of Data by Simplified Least Squares Procedures. *Anal Chem*, 1964, 36, 1627-1639.
- [158] Kozia, C.; Herzallah, R. Advanced Fusion and Empirical Mode Decomposition-Based Filtering Methods for Breathing Rate Estimation from Seismocardiogram Signals. *Information*, 2021, 12, 368.
- [159] Solar, B.E.; Taebi, A.; Mansy, H.A. Classification of seismocardiographic cycles into lung volume phases. In *Proceedings of the 2017 IEEE Signal Processing in Medicine and Biology Symposium (SPMB)*, Philadelphia, PA, USA, 2 December 2017.
- [160] Amit, G.; Shukha, K.; Gavriely, N.; Intrator, N. Respiratory modulation of heart sound morphology. *Am J Physiol Heart Circ Physiol*, 2009, 296, pp. H796-H805.
- [161] Ishikawa, K.; Tamura, T. Study of respiratory influence on the intensity of heart sound in normal subjects. *Angiology*, 1979, 30, pp. 750-755.
- [162] Tang, H.; Gao, J.; Ruan, C.; Qiu, T.; Park, Y. Modeling of heart sound morphology and analysis of the morphological variations induced by respiration. *Comput Biol Med*, 2013, 43, pp. 1637-1644.
- [163] Lu, X.; Azevedo Coste, C.; Nierat, M.C.; Renaux, S.; Similowski, T.; Guiraud, D. Respiratory Monitoring Based on Tracheal Sounds: Continuous Time-Frequency Processing of the Phonospirogram Combined with Phonocardiogram-Derived Respiration. *Sensors*, 2020, 21, 99.
- [164] Bao, X.; Gall, N.; Deng, Y.; Kamavuako, E.N. Analysis of ECG and PCG Time Delay around Auscultation Sites. In *Proceedings of the 13th International*

Joint Conference on Biomedical Engineering Systems and Technologies, Valletta, Malta, 24–26 February 2020, Volume 4, pp. 206-213.

- [165] Su, H.M.; Lin, T.-H.; Hsu, P.C.; Chu, C.Y.; Lee, W.H.; Chen, S.C.; Lee, C.S.; Voon, W.C.; Lai, W.T.; Sheu, S.H. A Comparison between Brachial and Echocardiographic Systolic Time Intervals. *PLoS ONE*, 2013, 8, e55840.
- [166] Noda, K.; Endo, H.; Kadosaka, T.; Nakata, T.; Watanabe, T.; Terui, Y.; Kajitani, S.; Monnma, Y.; Sato, K.; Kanazawa, M.; Nakajima, S.; Kondo, M.; Takahashi, T.; Nakamura, A.; Nozaki, E. Comparison of the measured pre-ejection periods and left ventricular ejection times between Echocardiography and impedance cardiography for optimizing cardiac resynchronization therapy. *J Arrhythmia*, 2017, 33, 130-133.
- [167] Tavel, M.E.; Campbell, R.W.; Feigenbaum, H.; Steinmetz, E.F. The apex cardiogram and its relationship to haemodynamic events within the left heart. *Heart*, 1965, 27, pp. 829-839.
- [168] Voigt, G.C.; Friesinger, G.C. The Use of Apexcardiography in the Assessment of Left Ventricular Diastolic Pressure. *Circulation*, 1970, 41, pp. 1015-1024.
- [169] Willems, J.L.; De Geest, H.; Kesteloot, H. On the value of apex cardiography for timing intracardiac events. *Am J Cardiol*, 1971, 28, pp. 59-66.
- [170] Manolas, J.; Rutishauser, W.; Wirz, P.; Arbenz, U. Time relation between apex cardiogram and left ventricular events using simultaneous high-fidelity tracings in man. *Heart*, 1975, 37, pp. 1263-1267.
- [171] Manolas, J.; Krayenbuehl, H.P. Comparison between apexcardiographic and angiographic indexes of left ventricular performance in patients with aortic incompetence. *Circulation*, 1978, 57, pp. 692-698.
- [172] Manolas, J.; Rutishauser, W. Diastolic amplitude time index: A new apexcardiographic index of left ventricular diastolic function in human beings. *Am J Cardiol*, 1981, 48, pp. 736-745.
- [173] Thong, Y.K.; Woolfson, M.S.; Crowe, J.A.; Hayes-Gill, B.R.; Jones, D.A. Numerical double integration of acceleration measurements in noise. *Measurement*, 2004, 36, pp. 73-92.
- [174] Migeotte, P.-F.; Mucci, V.; Delière, Q.; Lejeune, L.; van de Borne, P. Multi-dimensional Kineticardiography a New Approach for Wearable Cardiac Monitoring Through Body Acceleration Recordings. In *Proceedings of the XIV*

- Mediterranean Conference on Medical and Biological Engineering and Computing 2016, MEDICON 2016, Paphos, Cyprus, 31 March–2 April 2016; Springer International Publishing: Cham, Switzerland, 2016; pp. 1119-1124.
- [175] Park, J.; Seok, H.S.; Kim, S.S.; Shin, H. Photoplethysmogram Analysis and Applications: An Integrative Review. *Front Physiol*, 2022, 12, 808451.
 - [176] Meng, K.; Xiao, X.; Wei, W.; Chen, G.; Nashalian, A.; Shen, S.; Xiao, X.; Chen, J. Wearable Pressure Sensors for Pulse Wave Monitoring. *Adv Mater*, 2022, 34, 21, e2109357.
 - [177] Wang, H.; Wang, L.; Sun, N.; Yao, Y.; Hao, L.; Xu, L.; Greenwald, S.E. Quantitative Comparison of the Performance of Piezoresistive, Piezoelectric, Acceleration, and Optical Pulse Wave Sensors. *Front Physiol*, 2020, 14, 1563.
 - [178] Challoner, A. Photoelectric plethysmography for estimating cutaneous blood flow. *Non-Invasive Physiol Meas*, 1979, 1, pp. 125-151.
 - [179] Lindberg, L.-G.; Oberg, P.A. Optical properties of blood in motion. *Opt Eng*, 1993, 32, pp. 253-258.
 - [180] Kamal, A.; Harness, J.; Irving, G.; Mearns, A. Skin photoplethysmography—A review. *Comput Methods Programs Biomed*, 1989, 28, pp. 257-269.
 - [181] De Trafford, J.; Lafferty, K. What does photoplethysmography measure? *Med Biol Eng Comput*, 1984, 22, pp. 479-480.
 - [182] Ruggiero, E.; Alonso-De Castro, S.; Habtemariam, A.; Salassa, L. Upconverting nanoparticles for the near infrared photoactivation of transition metal complexes: New opportunities and challenges in medicinal inorganic photochemistry. *Dalton Trans*, 2016, 45, pp. 13012-13020.
 - [183] Spigulis, J.; Gailite, L.; Lihachev, A.; Ertz, R. Simultaneous recording of skin blood pulsations at different vascular depths by multiwavelength photoplethysmography. *Appl Opt*, 2007, 46, pp. 1754-1759.
 - [184] Liu, J.; Yan, B.P.; Zhang, Y.-T.; Ding, X.-R.; Su, P.; Zhao, N. Multi-wavelength photoplethysmography enabling continuous blood pressure measurement with compact wearable electronics. *IEEE Trans Biomed Eng*, 2018, 66, pp. 1514-1525.
 - [185] Jones, D.P. Medical electro-optics: Measurements in the human microcirculation. *Phys Technol*, 1987, 18, 79.

- [186] Li, S.; Liu, L.; Wu, J.; Tang, B.; Li, D. Comparison and noise suppression of the transmitted and reflected photoplethysmography signals. *BioMed Res Int*, 2018, 4523593.
- [187] Millasseau, S.C.; Ritter, J.M.; Takazawa, K.; Chowienczyk, P.J. Contour analysis of the photoplethysmographic pulse measured at the finger. *J Hypertens*, 2006, 24, pp. 1449-1456.
- [188] Allen, J.; Murray, A. Age-related changes in peripheral pulse timing characteristics at the ears, fingers and toes. *J Hum Hypertens*, 2002, 16, pp. 711-717.
- [189] Stern, R.M. Ear lobe photoplethysmography. *Psychophysiology*, 1974, 11, pp. 73-75.
- [190] Choi, B.; Park, C.; Lee, Y.; Shin, H.; Lee, S.; Jeong, S.; Noh, G.J.; Lee, B. Development of a new analgesic index using nasal photoplethysmography. *Anaesthesia*, 2018, 73, pp. 1123-1130.
- [191] Sabbadini, R.; Di Tocco, J.; Massaroni, C.; Schena, E.; Carassiti, M. A smart face mask based on photoplethysmography for cardiorespiratory monitoring in occupational settings. In *Proceedings of the IEEE International Symposium on Medical Measurements and Applications (MeMeA)*, Lausanne, Switzerland, 23-25 June 2021; pp. 1-6.
- [192] Kyriacou, P.; Powell, S.; Langford, R.; Jones, D. Investigation of oesophageal photoplethysmographic signals and blood oxygen saturation measurements in cardiothoracic surgery patients. *Physiol Meas*, 2002, 23, 533.
- [193] Barnes, R.W.; Clayton, J.M.; Bone, G.E.; Slaymaker, E.E.; Reinertson, J. Supraorbital photoplethysmography. Simple, accurate screening for carotid occlusive disease. *J Surg Res*, 1977, 22, pp. 319-327.
- [194] Stone, K.; Fryer, S.; Faulkner, J.; Meyer, M.L.; Zieff, G.; Paterson, C.; Burnet, K.; Kelsch, E.; Credeur, D.; Lambrick, D.; et al. Acute Changes in Carotid-Femoral Pulse-Wave Velocity Are Tracked by Heart-Femoral Pulse-Wave Velocity. *Front Cardiovasc Med*, 2021, 7, 592834.
- [195] Wannenburg, J.; Malekian, R. Body sensor network for mobile health monitoring, a diagnosis and anticipating system. *IEEE Sens J*, 2015, 15, pp. 6839-6852.

- [196] Venema, B.; Blanik, N.; Blazek, V.; Gehring, H.; Opp, A.; Leonhardt, S. Advances in reflective oxygen saturation monitoring with a novel in-ear sensor system: Results of a human hypoxia study. *IEEE Trans Biomed Eng*, 2012, 59, pp. 2003-2010.
- [197] Mahmud, S.; Ibtehaz, N.; Khandakar, A.; Tahir, A.M.; Rahman, T.; Islam, K.R.; Hossain, M.S.; Rahman, M.S.; Musharavati, F.; Ayari, M.A.; et al. A Shallow U-Net Architecture for Reliably Predicting Blood Pressure (BP) from Photoplethysmogram (PPG) and Electrocardiogram (ECG) Signals. *Sensors*, 2022, 22, 919.
- [198] Mousavi, S.S.; Firouzmand, M.; Charmi, M.; Hemmati, M.; Moghadam, M.; Ghorbani, Y. Blood pressure estimation from ap-propriate and inappropriate PPG signals using A whole-based method. *Biomed Signal Process Control*, 2019, 47, pp. 196-206.
- [199] Wang, G.; Atef, M.; Lian, Y. Towards a continuous non-invasive cuffless blood pressure monitoring system using PPG: Systems and circuits review. *IEEE Circuits Syst Mag*, 2018, 18, pp. 6-26.
- [200] Nabeel, P.; Jayaraj, J.; Mohanasankar, S. Single-source PPG-based local pulse wave velocity measurement: A potential cuffless blood pressure estimation technique. *Physiol Meas*, 2017, 38, 2122.
- [201] He, X.; Goubran, R.A.; Liu, X.P. Secondary peak detection of PPG signal for continuous cuffless arterial blood pressure measurement. *IEEE Trans Instrument Meas*, 2014, 63, pp. 1431-1439.
- [202] Ma, H.T. A blood pressure monitoring method for stroke management. *BioMed Res Int*, 2014, 2014, 571623.
- [203] Mase, M.; Mattei, W.; Cucino, R.; Faes, L.; Nollo, G. Feasibility of cuff-free measurement of systolic and diastolic arterial blood pressure. *J Electrocardiol*, 2011, 44, pp. 201-207.
- [204] Wong, M.Y.-M.; Poon, C.C.-Y.; Zhang, Y.-T. An evaluation of the cuffless blood pressure estimation based on pulse transit time technique: A half year study on normotensive subjects. *Cardiovasc Eng*, 2009, 9, pp. 32-38.
- [205] Baek, H.J.; Kim, K.K.; Kim, J.S.; Lee, B.; Park, K.S. Enhancing the estimation of blood pressure using pulse arrival time and two confounding factors. *Physiol Meas*, 2009, 31, 145.

- [206] Chen, W.; Kobayashi, T.; Ichikawa, S.; Takeuchi, Y.; Togawa, T. Continuous estimation of systolic blood pressure using the pulse arrival time and intermittent calibration. *Med Biol Eng Comput*, 2000, 38, pp. 569-574.
- [207] Korkalainen, H.; Aakko, J.; Duce, B.; Kainulainen, S.; Leino, A.; Nikkonen, S.; Afara, I.O.; Myllymaa, S.; Töyräs, J.; Leppänen, T. Deep learning enables sleep staging from photoplethysmogram for patients with suspected sleep apnea. *Sleep*, 2020, 43, zsaa098.
- [208] Dall'Olio, L.; Curti, N.; Remondini, D.; Harb, Y.S.; Asselbergs, F.W.; Castellani, G.; Uh, H.-W. Prediction of vascular aging based on smartphone acquired PPG signals. *Sci Rep*, 2020, 10, 19756.
- [209] Yousef, Q.; Reaz, M.; Ali, M.A.M. The analysis of PPG morphology: Investigating the effects of aging on arterial compliance. *Meas Sci Rev*, 2012, 12, pp. 266-271.
- [210] Millasseau, S.C.; Kelly, R.P.; Ritter, J.M.; Chowienczyk, P.J. The vascular impact of aging and vasoactive drugs: Comparison of two digital volume pulse measurements. *Am J Hypertens*, 2003, 16, pp. 467-472.
- [211] Bortolotto, L.A.; Blacher, J.; Kondo, T.; Takazawa, K.; and Safar, M.E. Assessment of vascular aging and atherosclerosis in hypertensive subjects: Second derivative of photoplethysmogram versus pulse wave velocity. *Am J Hypertens*, 2000, 13, pp. 165-171.
- [212] Takazawa, K.; Tanaka, N.; Fujita, M.; Matsuoka, O.; Saiki, T.; Aikawa, M.; Tamura, S.; Ibukiyama, C. Assessment of vasoactive agents and vascular aging by the second derivative of photoplethysmogram waveform. *Hypertension*, 1998, 32, pp. 365-370.
- [213] Allen, J.; Liu, H.; Iqbal, S.; Zheng, D.; Stansby, G. Deep learning-based photoplethysmography classification for peripheral arterial disease detection: A proof-of-concept study. *Physiol Meas*, 2021, 42, 054002.
- [214] Bentham, M.; Stansby, G.; Allen, J. Innovative multi-site photoplethysmography analysis for quantifying pulse amplitude and timing variability characteristics in peripheral arterial disease. *Diseases*, 2018, 6, 81.
- [215] Alnaeb, M.E.; Alobaid, N.; Seifalian, A.M.; Mikhailidis, D.P.; Hamilton, G. Optical techniques in the assessment of peripheral arterial disease. *Curr Vasc Pharmacol*, 2007, 5, pp. 53-59.

- [216] Allen, J., Murray, A. Development of a neural network screening aid for diagnosing lower limb peripheral vascular disease from photoelectric plethysmography pulse waveforms. *Physiol Meas*, 1993, 14, 13.
- [217] Cannesson, M.; Besnard, C.; Durand, P.G.; Bohé, J.; Jacques, D. Relation between respiratory variations in pulse oximetry plethysmographic waveform amplitude and arterial pulse pressure in ventilated patients. *Crit Care*, 2005, 9, R562.
- [218] Monnet, X.; Lamia, B.; Teboul, J.-L. Pulse oximeter as a sensor of fluid responsiveness: Do we have our finger on the best solution? *Crit Care*, 2005, 9, 429.
- [219] Lazazzera, R.; Deviaene, M.; Varon, C.; Buyse, B.; Testelmans, D.; Laguna, P.; Gil, E.; Carrault, G. Detection and classification of sleep apnea and hypopnea using PPG and SpO2 signals. *IEEE Trans Biomed Eng*, 2020, 68, pp. 1496-1506.
- [220] Hilmisson, H.; Berman, S.; Magnúsdóttir, S. Sleep apnea diagnosis in children using software-generated apnea-hypopnea index (AHI) derived from data recorded with a single photoplethysmogram sensor (PPG). *Sleep Breath*, 2020, 24, pp. 1739-1749.
- [221] Park, K.S.; Choi, S.H. Smart technologies toward sleep monitoring at home. *Biomed Eng Lett*, 2019, 9, pp. 73-85.
- [222] Behar, J.; Roebuck, A.; Shahid, M.; Daly, J.; Hallack, A.; Palmius, N.; Stradling, J.; Clifford, G.D. SleepAp: An automated obstructive sleep apnoea screening application for smartphones. *IEEE J Biomed Health Inform*, 2014, 19, pp. 325-331.
- [223] Liu, S.H.; Li, R.X.; Wang, J.J.; Chen, W.; Su, C.H. Classification of photoplethysmographic signal quality with deep convolution neural networks for accurate measurement of cardiac stroke volume. *Appl Sci*, 2020, 10, 4612.
- [224] Liu, S.H.; Wang, J.J.; Chen, W.; Pan, K.L.; Su, C.H. Classification of photoplethysmographic signal quality with fuzzy neural network for improvement of stroke volume measurement. *Appl Sci*, 2020, 10, 1476.
- [225] Lee, Q.Y.; Redmond, S.J.; Chan, G.S.; Middleton, P.M.; Steel, E.; Malouf, P.; Critoph, C.; Flynn, G.; O'Lone, E.; Lovell, N.H. Estimation of cardiac output and systemic vascular resistance using a multivariate regression model with

- features selected from the finger photoplethysmogram and routine cardiovascular measurements. *Biomed Eng Online*, 2013, 12, 19.
- [226] Wang, L.; Poon, C.; Zhang, Y. The non-invasive and continuous estimation of cardiac output using a photoplethysmogram and electrocardiogram during incremental exercise. *Physiol Meas*, 2010, 31, pp. 715-726.
- [227] Sabbadini, R.; Riccio, M.; Maresca, L.; Irace, A.; Breglio, G. Atrial Fibrillation Detection by Means of Edge Computing on Wearable Device: A Feasibility Assessment. In *Proceedings of the 2022 IEEE International Symposium on Medical Measurements and Applications (MeMeA)*, Messina, Italy, 22-24 June 2022; pp. 1-6.
- [228] Lee, C.; Shin, H.S.; Lee, M. Relations between ac-dc components and optical path length in photoplethysmography. *J Biomed Opt*, 2011, 16, 077012.
- [229] Yuan, H.; Memon, S.F.; Newe, T.; Lewis, E.; Leen, G. Motion artefact minimization from photoplethysmography based non-invasive hemoglobin sensor based on an envelope filtering algorithm. *Measurement*, 2018, 115, pp. 288-298.
- [230] Lakshmanan, S.; Chatterjee, D.; Muniyandi, M. “Noninvasive assistive method to diagnose arterial disease-takayasu’s arteritis”. In *Computational Vision and Bio Inspired Computing*; Hemanth, D.J., Smys, S., Eds.; Springer: Berlin, Germany; pp. 384-398.
- [231] Bentham, M.; Stansby, G.; Allen, J. Innovative multi-site photoplethysmography analysis for quantifying pulse amplitude and timing variability characteristics in peripheral arterial disease. *Diseases*, 2018, 6, 81.
- [232] Pimentel, M.A.; Charlton, P.H.; Clifton, D.A. “Probabilistic estimation of respiratory rate from wearable sensors”. In *Wearable Electronics Sensors*; Mukhopadhyay, S. C., Ed.; Springer: Berlin, Germany, 2015; pp. 241-262.
- [233] McKay, N.D.; Griffiths, B.; Di Maria, C.; Hedley, S.; Murray, A.; Allen, J. Novel photoplethysmography cardiovascular assessments in patients with Raynaud’s phenomenon and systemic sclerosis: A pilot study. *Rheumatology*, 2014, 53, pp. 1855-1863.
- [234] Reisner, A.; Shaltis, P.A.; McCombie, D.; Asada, H.H. Utility of the photoplethysmogram in circulatory monitoring. *Anesthesiol*, 2008, 108, pp. 950-958.

- [235] Shelley, K.H. Photoplethysmography: Beyond the calculation of arterial oxygen saturation and heart rate. *Anesth Analg*, 2007, 105, pp. S31-S36.
- [236] Allen, J. Photoplethysmography and its application in clinical physiological measurement. *Physiol Meas*, 2007, 28, R1.
- [237] Shelley, K.H.; Jablonka, D.H.; Awad, A.A.; Stout, R.G.; Rezkanna, H.; Silverman, D.G. What is the best site for measuring the effect of ventilation on the pulse oximeter waveform? *Anesth Analg*, 2006, 103, pp. 372-377.
- [238] Nitzan, M.; Faib, I.; Friedman, H. Respiration-induced changes in tissue blood volume distal to occluded artery, measured by photoplethysmography. *J Biomed Opt*, 2006, 11, 040506.
- [239] Xu, L.; Cheng, J.; Chen, X. Illumination variation interference suppression in remote PPG using PLS MEMD. *Electron Lett*, 2017, 53, pp. 216-218.
- [240] Allen, J.; Murray, A. Similarity in bilateral photoplethysmographic peripheral pulse wave characteristics at the ears, thumbs toes. *Physiol Meas*. 2000, 21, 369.
- [241] Senay, L.C.Jr.; Prokop, L.D.; Cronau, L.; Hertzman, A.B. Relation of local skin temperature local sweating to cutaneous blood flow. *J Appl Physiol*, 1963, 18, pp. 781-785.
- [242] Hertzman, A.B.; Roth, L.W. The absence of vasoconstrictor reflexes in the forehead circulation. Effects of cold. *Am J Physiol-Leg Content*, 1942, 136, pp. 692-697.
- [243] Hertzman, A.B.; Dillon, J.B. Applications of photoelectric plethysmography in peripheral vascular disease. *Am Heart J*, 1940, 20, pp. 750-761.
- [244] Krishnaswamy, A.; Baranoski, G.V. A biophysically-based spectral model of light interaction with human skin. *Comput Graph Forum*, 2004, 23, pp. 331-340.
- [245] Zhang, Q.; Lindberg, L.-G.; Kadefors, R.; Styf, J. A non-invasive measure of changes in blood flow in the human anterior tibial muscle. *Eur J Appl Physiol*, 2001, 84, pp. 448-452.
- [246] Sondej, T.; Sieczkowski, k.; Olszewski, R.; Dobrowolski, A. Simultaneous multi-site measurement system for the assessment of pulse wave delays. *Biocybern Biomed Eng*, 2019, 39, pp. 488-502.

- [247] Rajala, S.; Ahmaniemi, T.; Lindholm, H.; Taipalus, T. Pulse arrival time (PAT) measurement based on arm ECG and finger PPG signals-comparison of PPG feature detection methods for PAT calculation. In Proceedings of the 2017 39th Annual International Conference of the IEEE Engineering in Medicine and Biology Society (EMBC), Jeju, Korea, 11-15 July 2017.
- [248] Lamotte, G.; Boes, C.J.; Low, P.A.; Coon, E.A. The expanding role of the cold pressor test: A brief history. *Clin Auton Res*, 2021, 31, pp. 153-155.
- [249] Falkner, B.; Onesti, G.; Angelakos, E.T.; Fernandes, M.; Langman, C. Cardiovascular response to mental stress in normal adolescents with hypertensive parents. *Hemodynamics and mental stress in adolescents. Hypertension*, 1979, 1, pp. 23-30.
- [250] Gelfman, D.M. The Valsalva Maneuver, Set in Stone. *Am J Med*, 2021, 134, 6, pp. 823-824.



Author's Publications

1. Centracchio, J.; Sarno, A.; Esposito, D.; Andreozzi, E.; Pavone, L.; Di Gennaro, G.; Bartolo, M.; Esposito, V.; Morace, R.; Casciato, S.; Bifulco, P. Efficient automated localization of ECoG electrodes in CT images via shape analysis. *Int J CARS* 2021, 16, pp. 543-554. <https://doi.org/10.1007/s11548-021-02325-0>
2. Andreozzi, E.; Centracchio, J.; Punzo, V.; Esposito, D.; Polley, C.; Gargiulo, G.D.; Bifulco, P. Respiration Monitoring via Forcecardiography Sensors. *Sensors* 2021, 21, 3996. <https://doi.org/10.3390/s21123996>
3. Esposito, D.; Centracchio, J.; Andreozzi, E.; Gargiulo, G.D.; Naik, G.R.; Bifulco, P. Biosignal-Based Human–Machine Interfaces for Assistance and Rehabilitation: A Survey. *Sensors* 2021, 21, 6863. <https://doi.org/10.3390/s21206863>
4. Polley, C.; Jayarathna, T.; Gunawardana, U.; Naik, G.; Hamilton, T.; Andreozzi, E.; Bifulco, P.; Esposito, D.; Centracchio, J.; Gargiulo, G. Wearable Bluetooth Triage Healthcare Monitoring System. *Sensors* 2021, 21, 7586. <https://doi.org/10.3390/s21227586>
5. Esposito, D.; Centracchio, J.; Andreozzi, E.; Savino, S.; Gargiulo, G.D.; Naik, G.R.; Bifulco, P. Design of a 3D-Printed Hand Exoskeleton Based on Force-Myography Control for Assistance and Rehabilitation. *Machines* 2022, 10, 57. <https://doi.org/10.3390/machines10010057>
6. Centracchio, J.; Andreozzi, E.; Esposito, D.; Gargiulo, G.D.; Bifulco, P. Detection of Aortic Valve Opening and Estimation of Pre-Ejection Period in Forcecardiography Recordings. *Bioengineering* 2022, 9, 89. <https://doi.org/10.3390/bioengineering9030089>
7. Andreozzi, E.; Centracchio, J.; Esposito, D.; Bifulco, P. A Comparison of Heart Pulsations Provided by Forcecardiography and Double Integration of Seismocardiogram. *Bioengineering* 2022, 9, 167. <https://doi.org/10.3390/bioengineering9040167>

8. Centracchio, J.; Andreozzi, E.; Esposito, D.; Gargiulo, G.D. Respiratory-Induced Amplitude Modulation of Forcecardiography Signals. *Bioengineering* 2022, 9, 444. <https://doi.org/10.3390/bioengineering9090444>
9. Andreozzi, E.; Sabbadini, R.; Centracchio, J.; Bifulco, P.; Irace, A.; Breglio, G.; Riccio, M. Multimodal Finger Pulse Wave Sensing: Comparison of Forcecardiography and Photoplethysmography Sensors. *Sensors* 2022, 22, 7566. <https://doi.org/10.3390/s22197566>
10. Esposito, D.; Centracchio, J.; Andreozzi, E.; Bifulco, P.; Gargiulo, G.D. Design and Evaluation of a Low-Cost Electromechanical System to Test Dynamic Performance of Force Sensors at Low Frequencies. *Machines* 2022, 10, 1017. <https://doi.org/10.3390/machines10111017>
11. Centracchio, J.; Esposito, D.; Gargiulo, G.D.; Andreozzi, E. Changes in Forcecardiography Heartbeat Morphology Induced by Cardio-Respiratory Interactions. *Sensors* 2022, 22, 9339. <https://doi.org/10.3390/s22239339>
12. Centracchio, J.; Muto, M. Heartbeats Localization in Forcecardiography Signals Via Template Matching. In *Proceeding of 2022 E-Health and Bioengineering Conference (EHB)*, Iași, Romania, 17-18 November 2022, pp. 1-4, DOI: 10.1109/EHB55594.2022.9991505.
13. Centracchio, J. A New Piezoelectric Sensor for Forcemycography Application. In *Proceeding of 2022 E-Health and Bioengineering Conference (EHB)*, Iași, Romania, 17-18 November 2022, pp. 1-4, DOI: 10.1109/EHB55594.2022.9991364.

